Development of the Spatial Atomic Layer Deposition (SALD) technique for the fabrication of p-type thin films of highly conductive copper (I) oxide

César, Arturo Masse de La Huerta

▶ To cite this version:

César, Arturo Masse de La Huerta. Development of the Spatial Atomic Layer Deposition (SALD) technique for the fabrication of p-type thin films of highly conductive copper (I) oxide. Materials Science [cond-mat.mtrl-sci]. Université Grenoble Alpes, 2019. English. NNT : 2019GREAI067 . tel-03362690

HAL Id: tel-03362690

https://theses.hal.science/tel-03362690v1

Submitted on 2 Oct 2021

THÈSE

Pour obtenir le grade de

DOCTEUR DE LA

COMMUNAUTE UNIVERSITE GRENOBLE ALPES

Spécialité : 2MGE : Matériaux, Mécanique, Génie civil, Electrochimie

Arrêté ministériel : 25 mai 2016

Présentée par

César Arturo MASSE DE LA HUERTA

Thèse dirigée par **David MUNOZ-ROJAS**, Chargé de Recherches, Communauté Université Grenoble Alpes
et codirigée par **Daniel BELLET**, Professeur, G-INP
et **Maria del Carmen JIMENEZ AREVALO**, Ingénieur de recherche, CNRS

préparée au sein du **Laboratoire Laboratoire des matériaux et du génie physique**
dans **l'École Doctorale I-MEP2 - Ingénierie - Matériaux, Mécanique, Environnement, Energétique, Procédés, Production**

Développement de la technique dépôt par couche atomique spatiale (SALD) pour la fabrication de couches minces type P d'oxyde de cuivre (I) conductrices

Development of the Spatial Atomic Layer Deposition (SALD) technique for the fabrication of p-type thin films of highly conductive copper (I) oxide

Thèse soutenue publiquement le **26 novembre 2019**,
devant le jury composé de :

Monsieur David MUNOZ-ROJAS,
CHARGE DE RECHERCHE HDR, CNRS DELEGATION ALPES, Directeur de thèse
Madame DANIELE BLANC-PELISSIER
CHARGE DE RECHERCHE HDR, CNRS DELEGATION RHONE AUVERGNE, Rapporteur
Madame FREDERIQUE DONSANTI
INGENIEUR DE RECHERCHE, EDF R&D - PALAISEAU, Examinateur
Monsieur ALAIN ESTEVE
DIRECTEUR DE RECHERCHE, CNRS DELEGATION OCCITANIE OUEST, Rapporteur
Monsieur CHRISTOPHE VALLEE
PROFESSEUR DES UNIVERSITES, UNIVERSITE GRENOBLE ALPES, Examinateur
Monsieur GERMAN DE LA FUENTE
PROFESSEUR, CSIC - ESPAGNE, Examinateur

Acknowledgements

Every chapter of everyone's life is marked by numerous experiences and by countless individuals that influence on one's professional and personal growth. In the case of the project here presented, the lab and the people met along the way meant an even greater growth in all levels than what was remotely expected by the author.

It's no surprise that the first person to acknowledge and express gratitude to is my thesis supervisor Dr. David Muñoz Rojas who gave me the opportunity and the confidence on developing a great tool that forms such an important part of the LMGP. Dr Muñoz Rojas provided so much knowledge and insights on the science and nanotechnology instrumentation and his support was invaluable. There's no doubt that the creative nature and excitement about innovation of Dr. Muñoz Rojas and the whole SALD team will lead to great and impactful advances on the scientific community.

I, of course, thank my co-supervisors Carmen Jiménez and Daniel Bellet for their continuous support and the fruitful scientific discussions that gave me guide and eased the path for the thesis project here shown. It is certain that the excellence obtained by LMGP and that the great scientific advancements achieved by the laboratory are the result of a great leadership and motivation.

One of the best experiences during the PhD was being part of the InnoEnergy PhD school, which has as alumni some of the most talented persons and impressive people I've met. Although it's difficult to name them all, I deeply thank my colleagues and the courses that the InnoEnergy team provided, for they represented an enormous advancement in my knowledge that will certainly be useful for life. Thank you to all the team of the InnoEnergy PhD school, specially Isabelle Schuster, who always gave me her support. Thank you also to the all the InnoEnergy students for the great moments.

During the internship at Zaragoza, I couldn't be more thankful for the warm welcome I received and for the great experiments and scientific discussions we enjoyed during those times. The expertise of Prof. Germán de la Fuente is impressive, and I am extremely thankful I had the opportunity to share experiments and discussions up-close with him, along with Dr. Luis Alberto Angurel. I also thank Dr. Héctor Santos for the shared scientific time and the morning coffees. Thank you to the whole team of the Institute of Material Science of Aragón (ICMA) for the great hosting and for the opportunity to discover the amazing Spanish culture.

I would like to thank Serge Quessada, Matthieu Jouvert, Herve Roussel, Odette Chaix, Michèle San Martin, Josiane Viboud, Virginie Charrière, and all the LMGP permanent people for their technical and administrative support during the thesis. Special thanks to Dr. Dominique De Barros for his guidance and shared knowledge. It was so rewarding to work with him and to learn from his wide experience. I am thankful for the knowledge shared from him since it will surely be useful for my professional future. Special thanks as well to Jean Marc Dedulle for the fruitful guidance with the simulation tools.

It is impossible to achieve great things without the support from friends. This thesis was no exception, and I feel deeply thankful for the great times that all my PhD colleagues had at the LMGP. Thanks to Dr. Viet H. Nguyen for his fruitful help on the experiments and his scientific suggestions. I'd also like to thank Lukas Fusek for the work done, which helped me greatly on the advancement of my thesis, I'm sure a brilliant scientific future awaits for him. Thanks to the whole SALD team for their amazing help and specially Abdou and Chiara for the nice time during experiments. Thanks also to Raquel, Dorina, Antalya, Morgane, Fanny, Damir, Caroline, Evgeni for the great moments at LMGP. Thanks to Sara, Klaasjan, Joao and Mirasbek for the long discussions around deep and crazy topics.

I'd like to acknowledge and thank the support CONACYT for the economic support received for my thesis project, which allowed me to complete the tasks successfully.

Last but of course not least, I'd like to thank my family for their unconditional support. My mother and my father provided all the support possible for me to be where I am, and for that I cannot be more grateful. There's absolutely no doubt that they provided for the best guidance and the best role model for me to follow, and I can only hope that I can be half as successful as they have been. I am also incredibly grateful for the support and guidance from my brother. I admire his skills and I couldn't be prouder of having guidance from someone as incredible as him. Really deep thanks to Taughi, who tolerated me in the best and worst moments and still had the strength to push me through the struggles. Everything is easier with them by my side and for that I am extremely grateful.

With that, I thank the scientific community for the benefit to mankind and I am grateful I had the chance to provide my skills to give advances, however small, to the creation of knowledge and development of humanity. And finally, I thank you, reader, for reading this work and I hope you enjoy it and find it useful.

Abstract

Future trends in materials and devices are strongly based on novel fabrication methods that allow for mass production with low cost and high throughput. Such methods must be finely optimized to achieve nanometric control without incurring in high costs. This can be achieved by developing a process that reduces the number of steps required, as well as by reducing the amount of human involvement in the process, which would increase the quality and reproducibility of the output. But the improvement of fabrication technologies cannot be optimized without considering the materials desired, along with its most fundamental chemical and physical properties. Hence, to successfully design the instrumentation needed for novel fabrication technologies with nanometric precision, the design methodology must consider multiple different subjects related to the chemistry, physics, mechanics, electronics and automation, all working together to achieve the desired objective. In this doctoral work, such design methodology was implemented with a diverse number of tools and approaches to successfully optimize a nanofabrication method called Spatial Atomic Layer Deposition (SALD) to deposit thin films of a material that has potential applications as a component of non-silicon solar energy devices, photoelectrochemical water splitting devices, and thin film transparent electronics, among others: cuprous oxide (Cu_2O).

Regarding the fabrication technology and the mechatronic design, SALD is a promising fabrication technique that allows fabrication of thin films with nanometric precision and with the ability to control their mechanical, electrical and crystallographic properties. Furthermore, the SALD approach used in this thesis and in the Laboratoire des Matériaux et du Génie Physique (LMGP) works in the open-air (no deposition chamber), and thus is potentially an industrial-compatible approach for large area, homogeneous thin film fabrication with a high throughput. Additionally, SALD can be used with conditions that make it compatible with flexible substrates and with roll-to-roll (R2R) approaches. Finally, SALD provides flexibility on the deposition process so that it can be tuned to obtain different properties on the films fabricated with minimal change in the instrumentation. In this thesis, some of the potential benefits of the flexible parameters of the SALD system are explored and the impact of some of them on fabricated films is presented.

Using Computational Fluid Dynamics (CFD) simulations, the fluid mechanics phenomena that occur during the deposition process in the SALD system were analyzed for different configurations of the reactor. The influence on the film properties were studied and validation with experimental depositions were performed. Afterwards, using the knowledge and guidelines obtained with the CFD simulations, and in order to lower the cost and complexity of modifying some of the mechanical components of the system, a workflow including Computer Aided Design (CAD) and additive manufacturing (also known as 3D printing) was established at the LMGP for the fabrication of one of the main components of the SALD system at LMGP: the deposition head. The use of additive manufacturing has followed a rapid increase on applications, and, in this work,

it is the first time that such innovative fabrication technique is applied to thin-film nanofabrication processes, providing numerous potential applications in the field. In this thesis, such workflow is shown and explained, and the guidelines learned, and limitations discovered are presented as well.

Finally, after making some modifications on the system and adding the necessary components such as new heating systems and containers for the needed precursor, Cu_2O was successfully deposited with the SALD method. Cu_2O is one of the few materials with promising electronic properties as a p-type transparent semiconductor. It is also a material that allows for mass production, if coupled with an industrial-compatible fabrication method (such as SALD), thanks to its non-toxicity, its chemical and environmental stability and its earth abundance. Here, the fabricated Cu_2O films using the SALD system at LMGP are reported, and their p-type conductivity and crystallography are analyzed.

In the work done during this doctoral project, a systematic approach was used to analyze, adapt and optimize the SALD system at LMGP for the deposition of Cu_2O. Using CFD simulations, CAD tools, 3D printing and automation, the whole process was successfully installed in the system and highly conductive Cu_2O films can be now deposited their further study or for their integration in numerous types of devices.

Furthermore, the results of this work provide initial guidelines for the industrial design of an SALD-based high-throughput fabrication system, in which the design of its components is optimized for each material desired. Such design approach, combined with the flexibility and low cost of the SALD, the flexibility of the mechanical design and fabrication of some of its components, and the speed of the deposition procedure, make this work also useful to further increase the amount of materials compatible with SALD, as well as to further develop the SALD methodology into innovative fabrication processes of materials and devices.

Table of Contents

List of Figures

List of Tables

Chapter 1

Introduction and background

Within the materials science community, metal oxides (ME-Ox) provide a promising horizon for materials research and industry. These materials have a wide range of applications due to their interesting electrical, catalytic, optical and mechanical properties, which can furthermore be tuned. These applications range from gas and biological sensors, catalysis, or photoelectrochemical water splitting, to electronic applications such as transparent conductive and semi-conductive oxides, resistive RAM, photovoltaics, thin film transistors and transparent electronics. In each of these applications, ME-Ox materials provide a key functionality that makes them essential, making their research an attractive challenge.

Within all applications of Me-Ox materials, one in which their properties provide the most disruptive applications is on transparent conductive oxides (TCO). TCOs have found their way to provide innovative applications with devices like all-oxide transparent electronics [1], photovoltaics [2], flexible electronic devices [3], memristors[4], smart windows [5], and energy-efficient, high resolution displays [6]. TCOs are commercially used in numerous industrial applications such as, e.g. indium tin oxide (ITO) for tactile displays in mobile devices. They present electrical conduction with both n-type and p-type carriers, but the electrical performance of the former is largely superior to those with the latter type. N-type TCOs have been well developed and their good electrical and optical properties is what have paved their way into commercial applications as conductive materials. The next innovative applications, such as the mentioned transparent electronics, become promising with these materials but to date, the availability of p-type TCOs with the required electrical performance is limited [7], [8]. In order to achieve a material that is complementary to the n-type TCOs available, p-type TCOs with good electronic properties are needed. If they become available, they would enable a large variety of energy-efficient and more complex transparent devices, driving the electronics market towards the next era of oxide-based applications [9].

The reason for the lack of p-type TCOs with similar electronic properties to n-type ones is due to the mechanism of charge carriers formation. In p-type oxides, the creation of charge carriers is complex since in the material, the cation vacancies, which are the responsible to provide the charge carriers (holes), present usually a high formation energy, while the native donors creation in the material, which act as hole annihilators and consist mainly on anion vacancies, have a low formation energy. Furthermore, even when there is an important concentration of holes, the valence band maximum consists on localized oxygen 2p orbitals, which traduces into low hole mobility values [10]–[12].

Promising candidates for p-type oxides include SnO, due to the dominating 5s orbitals in its valence band maximum and which has been successfully applied to thin film transistors (TFTs), and cuprous oxide (Cu_2O), which has been fabricated with mobility values exceeding 100 $cm^2V^{-1}s^{-1}$ [13], and has been used for the fabrication of devices such as p-n junctions, TFTs and hole transport layers (HTL) in solar cells [13], [14]. Nevertheless, p-type oxides still need to be improved for higher mobility and lower interfacial defects, and the strategies to do so include dopant incorporation, strain engineering and microstructure control, along with novel processing technologies such as atomic layer deposition (ALD) [9].

Cuprous oxide is a promising candidate as a p-type oxide [15] and, if we consider that copper is an earth-abundant element [16], [17], non-toxic, and an environmentally friendly material since it occurs also in nature, it is wise to say that Cu_2O holds true potential for new disruptive commercial applications. In this thesis, we combine the promising properties of Cu_2O as a p-type oxide with a novel low-cost, industry-compatible method known as Spatial Atomic Layer Deposition (SALD) to fabricate high-mobility cuprous oxide thin films.

In this chapter the properties of cuprous oxides are presented. The fabrication methods and the properties they can achieve are reported and compared, and an overview of the perspectives for low-cost fabrication is discussed. Then, the ALD method is presented and compared to the novel SALD method, and the basics of this technology is explained. The objective of this thesis is explained and, finally, an overview of the structure and contents of this thesis is listed.

1.1 Cuprous Oxides

Copper oxides have two stable forms: cuprous oxide (Cu_2O) and cupric oxide (CuO). Both are reported to be intrinsically p-type. In this thesis, we will study the case of cuprous oxide.

The almost exclusive p-type conductivity of Cu_2O, obtained with most fabrication methods, makes it appropriate for applications such as an electron blocking or hole transport layer in solar cell. Moreover, Cu_2O can be deposited at low temperatures with a soft chemical process, making it attractive for its deposition on sensitive materials and substrates, such as ITO (which electrical and optical properties degrade at temperatures from 250 to 400 °C [18]), non-Si solar cells, and on flexible substrates such as PEN or PET. The latter is especially interesting for the large area fabrication technique known as roll-to-roll (R2R).

The theoretical solar cell efficiency (the Shockley–Queisser limit) for a Cu_2O homojunction could achieve more than 20% of solar conversion efficiency [19], [20]. However, obtaining a Cu_2O

homojunction is a difficult task since Cu_2O grows intrinsically as a p-type oxide. Thus, Cu_2O has been used as a p-type absorber for heterojunctions usually in combination with doped ZnO achieving 2.3% efficiency [21]. Other studies have been performed with a combination of ZnO and Ga_2O_3 reaching an efficiency of 5.3% [22], [23]. Another team fabricated a full perovskite solar cell, achieving 13% of solar conversion efficiency with a Cu_2O layer used as a hole transport layer [24].

1.1.1 *Crystal parameters*

The crystal lattice of cuprous oxide, known as well as cuprite, is composed of two sublattices: The O atoms, which form a BCC lattice at (0,0,0) in a local coordinate system, and the Cu atoms, which form a FCC sublattice, shifted by ¼ of the lattice constant. This forms a diamond-like oxygen and copper networks. Together they form a cubic crystal structure with space group Pn(-3)m and a lattice parameter of 4.27 Å. Figure 1-1 shows a unit cell of Cu_2O. Cu_2O is one of the few oxides that present a linear coordination O-Cu-O (only few other materials such as Ag_2O and Pb_2O present linear coordination when the silver and lead is in a cation form) [25]. The Cu atoms have an atomic radius of 140 pm, while atoms of O have an atomic radius of 74 pm. Since it is a binary compound, Cu_2O presents different surface (planar) properties depending on the growth orientation [26]. The density of Cu_2O is 6.1 g/cm^3.

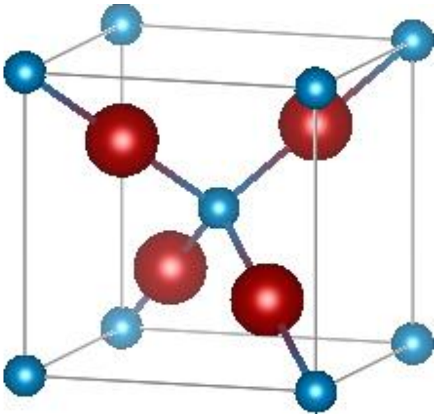

Figure 1-1. *Unit cell of Cu_2O where the red spheres correspond to Cu atoms and the blue spheres correspond to oxygen atoms.*

1.1.2 *Electrical properties*

Regarding the electrical properties, a direct bandgap of around 2.09 eV is accepted for a bulk material. However, for thin films, the electrical properties of Cu_2O change as a function of film local stoichiometry (local coordination, local electrical defect density, surface effects, grain boundaries existence, CuO inclusions, etc.) [27], [28]. Relevant reviews on the topic were reported in [29], [30] and [31]. Hence, the fabrication method of thin film used is determinantal for quasi-homogenous electrical properties, where microstructure of the film should be controlled at the atomic level.

The intrinsic p-type characteristic of Cu_2O is attributed to the formation of copper vacancies (V_{Cu}) and to the hybridization of the 3d orbital in Cu and the 2p orbital in O. This hybridization is shown in reference [32], and it is an important characteristic of Cu_2O because it provides Cu_2O with a high charge carrier mobility, differentiating it from other p-type oxides where the low mobility is attributed to the localized 2p orbital in O. Moreover, the top of the valence band maximum is composed mainly of Cu d states, creating a good pathway for the hole-transport [29].

It has been widely accepted in the research community that the V_{Cu} formation energy decreases in O-rich condition [33] as shown in reference [32]. These defects are negatively charged and thus, they attract positive charge carriers, i.e. holes.

The density of V_{Cu} is theoretically high in Cu_2O (10^{18} to 10^{20} cm^{-3}) and they introduce a shallow state at 0.2-0.3 eV. However, these states are only partially activated at room temperature and, usually, less carrier concentration is present in the material, which depends also on the fabrication method, achieving values as low as 10^{13} cm^{-3} [34]. The p-type conductivity is also promoted by the fact that charge carrier effective mass in Cu_2O is 60-50% lower than that of the electron [35]. This gives holes a high mobility in the bulk material, achieving values as high as 256 $cm^2V^{-1}s^{-1}$, for a sample fabricated at 600 °C with radio frequency magnetron sputtering [14].

For all electronics applications, the Cu_2O electronic properties such as charge carrier mobility and carrier concentration are important. According to [36], TFTs require carrier mobility above 5 $cm^2V^{-1}s^{-1}$ and carrier concentration above 10^{17} cm^{-3}. In the case of photovoltaics, a carrier concentration of 10^{16} cm^{-3} is needed to achieve full depletion layer width of several hundreds of nanometers, a thickness suitable for thin films fabrication methods. The depletion width is roughly inversely proportional to the carrier concentration and it has to be fully achieved in a nanostructure device to allow for complete charge collection and limit recombination losses [21]. The challenge for Cu_2O lies on the fact that the fabrication of monocrystalline Cu_2O is technically challenging. In fact, only one report is usually cited on the growth of monocrystalline Cu_2O [37] since it is too resource-demanding, too slow and works at too high temperatures for usual TCO applications. Since usually Cu_2O films are polycrystalline, the grain boundaries play an important factor for the conduction in Cu_2O thin films, even when there is a preferred orientation of the growth, which indeed applies to thin films of any material. Hence, bigger grains are preferred since the mobility will be higher due to the decrease of the influence of gran boundary scattering [36], [38], [39]. Nevertheless, it is known that the carrier concentration is inversely proportional to the carrier mobility since more carriers imply more scattering, thus causing a lower mobility. [40], [41] Moreover, the fabrication window is rater narrow and eventual inclusions of CuO and Cu are possible, degrading even further the electrical properties of Cu_2O. [27], [28]

1.1.3 *Absorption*

One of the most important parameters for Cu_2O, especially for photovoltaic applications, but also for photoelectrochemical water splitting, is its absorbance in the solar spectrum.

Although Si absorbs rather wide range of solar spectrum, the fact that it has an indirect bandgap implies that it also has a lower absorption coefficient. Hence, to obtain high efficiency solar cells with crystalline Si, thick (more than 1 µm) Si absorbers are needed. Moreover, the reflectance of Si is usually reduced by texturing the Si surface. However, to overcome the limits of standard Si solar cells, a so-called tandem solar cell can be used, where a crystalline Si sub-cell is combined with another type of absorber having a higher absorption coefficient at lower wavelengths of Air Mass 1.5 global conditions solar spectrum (AM 1.5G solar spectrum). See Figure 1-2 for an example of a tandem solar cell with a top sub-cell made with a ZnO/Cu_2O device [42]. Cu_2O presents a suitable option to use as a solar absorber in the visible range, i.e. wavelengths below 550 nm [36], and this can be potentially exploited to create tandem solar cells with crystalline Si [43] or perovskite materials [19], [20]. These wavelengths are in accordance to the optical bandgap of Cu_2O, which has been reported to be 2.1 – 2.6 eV [44], whereas CuO presents an optical bandgap of around 1.9 eV. The refraction index on Cu_2O is around 2.3 for a 400 nm wavelength [45].

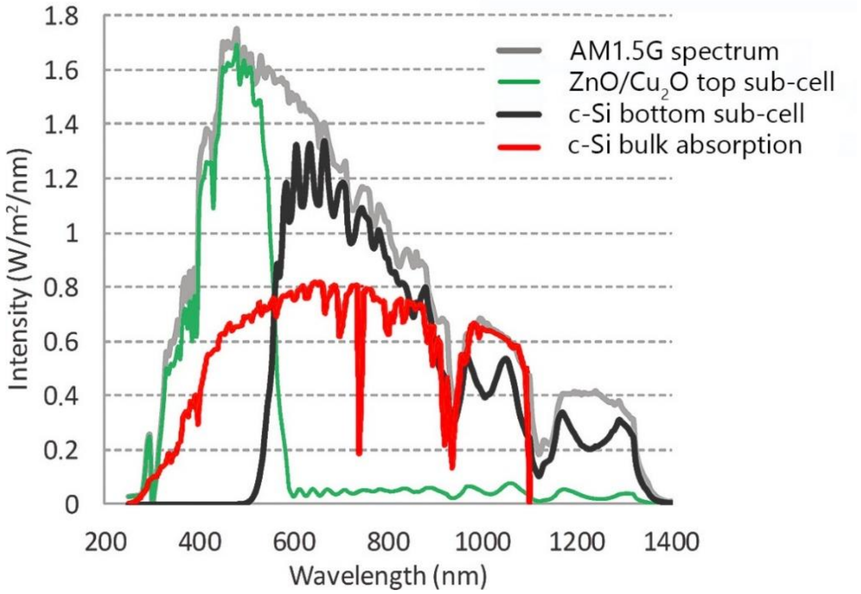

Figure 1-2 *Plot showing the solar AM 1.5 G solar spectrum and the absorption of a tandem solar device with a ZnO/Cu_2O junction as a top sub-cell (green) and a c-Si bottom sub-cell (black). In red, the absorption of a bulk c-Si of at least 1 mm thickness. Graph adapted from [42] and [46].*

1.2 Fabrication of Cu_2O

Numerous groups have published the fabrication of Cu_2O films or nanostructures by multiple methods. From the physical deposition methods, Pulsed Layer Deposition (PLD) [14], [47], [48], (Radio Frequency) Magnetron Sputtering [13], [49], [50], are the techniques that have presented the best mobility. On the chemical methods, Thermal oxidation (TO) [44], [51], [52], electrodeposition [53], spin coating [54], spray coating [55], molecular beam epitaxy [56], ink printing [57], Chemical Vapor Deposition (CVD) [27], [58], and Atomic Layer Deposition (ALD) [36], [59] have been reported.

RF-Magnetron sputtering has achieved a surprising Hall mobility of 256 $cm^2V^{-1}s^{-1}$ with films deposited at 600 °C by adding a low temperature buffer Cu_2O layer that controlled the grain size, as well as the growth mode to (111) films orientation [13]. In PLD, a Hall mobility of 90 $cm^2V^{-1}s^{-1}$ was achieved on thin films with (110) orientation grown on MgO substrates, by controlling the oxygen partial pressure in the chamber. In another study, a mobility of 107 $cm^2V^{-1}s^{-1}$ was achieved at a temperature of 500 °C by Pulsed Laser Deposition (PLD) in pure O_2, i.e., in an oxygen-rich environment. [60] These results provide optimism on high mobility Cu_2O, but their method of fabrication is a complex one, requiring a high thermal budget and high vacuum and, therefore, increasing the cost of the process and limiting the compatibility with other active materials or substrates. This impedes their scalability and their introduction into commercial devices.

Alternative fabrication methods include ALD with post-deposition annealing at 200 °C [49], MOCVD with a heated substrate (300-400 °C) [61], Cu_2O growth on ZnO via metal-organic (MO) CVD [62], or the sol-gel method followed by sequential thermal treatments in oxygen and nitrogen [63], [64]. All these methods achieve a high mobility of 18.5, >30, 35 and 31.7 $cm^2V^{-1}s^{-1}$, respectively, but the charge carrier concentration is low, ranging at around 10^{14} - $10^{15}cm^{-3}$.

Table 1-1 presents a comparison of different fabrication methods of Cu_2O that have been reported, along with their relevant electrical properties.

__Table 1-1__. Comparison of deposition methods for the fabrication of Cu_2O films, and their relevant electrical properties.

DEP. METHOD	**Subs**	**T. Dep. (°C)**	**P. Dep. (Pa)**	**Thickness (nm)**	**Gr. Rate (nm/min)**	**μHall (cm^2/Vs)**	**n_p (cm^{-3})**	**ρ (Ω.cm)**	**Ref**
TO	Glass, ITO	400	10^{-5}	223	-	6.1	10^{15}	333	[65]
	Cu	1015	-	-	-	100	10^{13-16}	10^3 - 10^{-2}	[51]
ECD	ITO	60	10^5	3 x 10^3	-	2.1 - 28.5	10^{13}	10^5 - 10^4	[34]
	Glass/ZnO	30-70	10^5	2 x 10^3	-	1.8	10^{14}	10^6	[66]
RF-MAG. SPUTTER.	Glass	200	-	115	-	0.39	10^{17}	32.7	[67]
	Glass	600	10^{-6}	1 x 10^3	-	256	10^{14}	~100	[13]
PLD	MgO (crystal)	650-850	10^{-3} - 1	100	6	90	10^{15}	-	[14]
	Si/SiO_2	RT + anneal 300	10^{-5}	-	-	2.1	10^{16}	-	[47]
CVD	Al_2O_3, MgO	175	10^3	60-90	0.41	5-8	10^{16}	100-250	[68]
MIST CVD	Glass	350-450	10^5	600	5	19	10^{15}	280	[69]
AA-MOCVD	Glass	290-365	~105	1 x 10^3	1.5-4.5	2-17	10^{15}	60-110	[38]
MOCVD	Glass/ ZnO	350	-	~200-500	-	35	10^{14}	3-9	[70]
ALD	Si NW	140-160	-	30	0.013	8	10^{15}	-	[62]
(PE)ALD	Glass, Si	100	-	50	0.003	37	10^{14}	192	[71]
SALD	Glass, PEN	150-300	105	50-150	0.025	5	10^{16}	11-125	[36]
SPRAY PYROL.	Glass	280	10^5	~ 250	-	-	-	100	[72]

On a parallel note, the parameters of Cu_2O can be also tuned by doping with Sr [73], Mg [74], Na [23], N [75], Cl [76], Sb [77].The scope of this work, however, involved the deposition of undoped layers.

1.3 A path towards industrialized fabrication

As it can be seen, Cu_2O provides several advantages as a p-type oxide and numerous research groups are actively investigating its growth as a thin film. Cu_2O may enable the fabrication of disruptive electronic devices, the development of a novel era of transparent electronics, the enhancement of solar cell energy conversion and even a new way of generating hydrogen via water splitting. All these applications seem interesting but, to achieve full market adoption, industries must ensure that the fabrication of Cu_2O is cost-effective. This requires addressing the issue of the fabrication method.

Soft chemical methods are useful for scalability, but films deposited by these techniques tend to have low electrical properties. In the case of Cu_2O, and as mentioned before, low mobility and high number of defects are usual with these techniques [9]. On the other hand, RF Magnetron sputtering and conventional ALD provide good results in terms of film quality, but they are techniques that rely on vacuum. This makes them difficult to scale-up to an industrial fabrication level and increase their cost. Furthermore, RF magnetron sputtering requires high temperatures (~600 °C) for processing, while good ALD films require thermal post-deposition treatments for periods raging tenths of hours. This creates a thermal budget that also increases the cost and hinders their industrialization.

To recall the requirements needed for Cu_2O -based devices, the mobility and the carrier concentration of films of this material need to be tuned to achieve good performance on the device for each application. In this thesis, we concentrate on improving the Cu_2O films deposited by exploring a very promising technique that has recently gained momentum in thin film fabrication: Spatial Atomic Layer Deposition (SALD) [78].

1.4 SALD technology

SALD is a thin film fabrication method that takes its principles from the more known, conventional ALD method. Here we will present the ALD method fundamental concepts and then we will introduce the SALD as an innovative variation of ALD, presenting its main differences against other fabrication methods and discussing its applicability in industrial environments.

1.4.1 *Basics of ALD*

ALD is a material deposition process that allows for a homogeneous, conformal thin film deposition with a nanometric thickness control. ALD is indeed a variation of a CVD process, characterized by self-limited surface reactions.

In Metal-Organic CVD (MOCVD) processes, two gaseous reactants (a precursor and a reacting gas) are injected into a chamber where the substrate to be coated is present. Such gaseous precursor is often composed by a metallic atom, surrounded by one or many organic molecules, known as metal-organic (MO) precursor. The use of MO ligands is due to several reasons: to keep a good reactivity of the molecule, to prevent the metallic atoms to interact among themselves which would create a deposition in the container, and finally, to increase the volatility of the molecules. In such CVD process, as simultaneous presence of the two reactants in the chamber takes place, the precursors give rise to gas phase reactions on top of the surface which creates the deposited film. These CVD reactions happen rapidly, and their control becomes difficult. Usually, a CVD process is mainly driven by the control of pressure in the chamber, the partial pressure of the gaseous reactants in the same, the substrate temperature and, in more complex setups, the introduction of other energy sources, such as a plasma agent or a hot filament, to enhance the reaction. Typical growth rates can achieve from tenths to hundredths of $\mu m \cdot h^{-1}$, depending on the growth conditions used [79].The previously mentioned control parameters are used to tune the growth rate of the process. As the deposition temperature increases, the CVD reaction rate in the surface increases as well. While this happens, the CVD growth mode is said to be in reaction-limited growth mode. When the temperature is high enough to ensure an optimal surface reaction rate, the growth mode then depends only on the concentration of reactants introduced in the chamber. When this happens, the CVD growth mode is said to be in mass-transport-limited growth mode. In this way, and by controlling the time of the CVD process, the thickness can be controlled, although, due to the high growth rate it has, this control is accurate only to some microns; sub-micron and nanometer thicknesses are difficult to reproduce with high precision with this technique.

ALD, in contrast to a CVD process, exposes the substrate to reactants in a sequential manner, instead of exposing it to both reactants at once. A whole sequence of such exposures is called an ALD cycle and it consists of a series of exposures separated from each other. Figure 1-3 shows a schematic of a typical ALD cycle. An ALD cycle usually starts with an exposure step, where the surface of the substrate is exposed to the gaseous reagent and is saturated with the reagent. Thus, a half chemical reaction with the active sites occurs. This requires for the surface to have, in the first place, presence of active sites on which the reactive molecule could react with; usually hydroxyl terminations are preferred. This step prepares the surface for its exposure to the next reactant, not without first performing a purging step either by filling the chamber with inert gas, or by pumping out all gaseous contents from the reaction chamber. This is performed to remove the remnants of the reaction and the surplus of the first reactant. Then, a pulse of the second gaseous reactant is introduced. This second reactant will finish the chemical reaction on the surface, reacting with all surface sites available, creating then the film of the material desired. Finally, a last step of purging with inert gas is performed to remove remnants and byproducts of the second half of the chemical reaction. Shown in Figure 1-3a, this process ensures that the reactants react exclusively with the surface of the substrate, and not in the gas phase. During each exposure step, once the surface sites available on the surface have reacted with a precursor molecule, no more reaction can happen; the surface sites are said to be occupied [80]. Due to this effect, ALD depositions have a so-called surface-limited nature, which ideally creates a monolayer of the material in each cycle. It suffices then to repeat the cycle for the number of times desired to obtain the desired thickness; and since every cycle creates a monolayer, the control of such process can achieve nanometric layers. The rate at which an ALD process increases the thickness of the layer depends on the surface chemistry of the reactants, the temperature of the surface in which the deposition is carried out, and the geometry of the reactor. This value is commonly known as growth per cycle (GPC) and ranges about 0.1 Å/cycle. If we consider that the time that every step in the cycle requires is from one to several seconds, the growth rate of films range around 0.1-0.3 nm/min [78], [81].

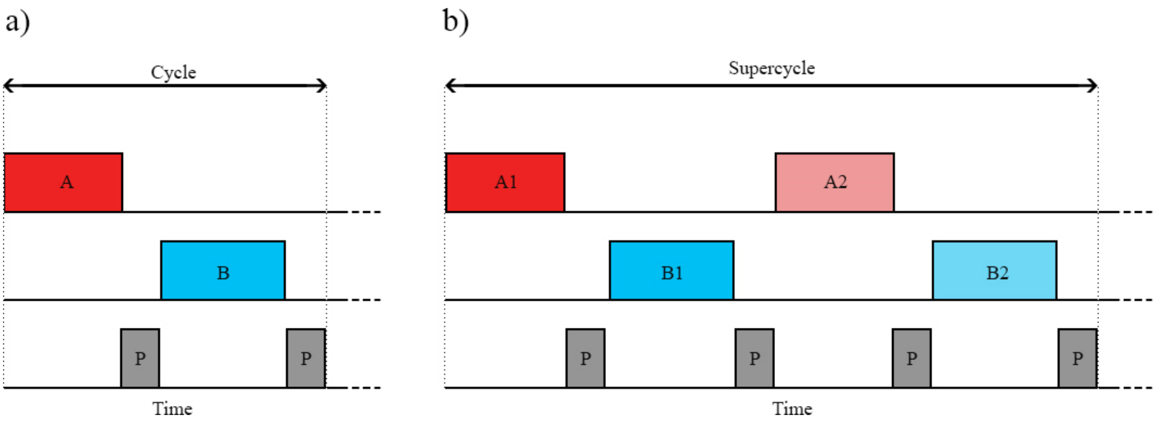

Figure 1-3. *Schematic of the pulses of an ALD process. a) A conventional cycle of an ALD process includes a pulse of reactant A (in red), a purging step (gray), a pulse of reactant B (blue) and a second purging step. b) More complex deposition cycle processes can be achieved. These complex pulse sequences are called supercycles.*

More complex sequences of ALD deposition can be achieved by creating a set of different sequences that have predefined pulse sequences themselves. This cycles are usually called "supercycles" and they can be used for more complex ALD processes that introduce extra steps during the film growth [82], [83]. A schematic of one type of supercycle can be seen in Figure 1-3b, although there may be any amount of variation to create supercycles.

Compared to CVD growth, this process is quite slow, which makes it less convenient to scale to industrial levels. Nevertheless, ALD deposition gives other advantages regarding the quality of the grown films. Since the process is optimized to saturate the surface being coated, films deposited by ALD yield a high density and high adhesion. Moreover, as each cycle is in theory one-atom thick along the whole surface, the film is grown at the same deposition rate, regardless of its shape or aspect ratio. Commonly, it is said that the deposited film has good conformality. This is especially useful for coating nano-sized geometries, such as nanowires or nanorods, with a nanometric control of the thickness. The good conformality achieved with ALD is unique amongst other film deposition techniques and, along with the density of the film and the low concentration of defects, it's what makes it stand out as one of the most promising deposition techniques for future nanofabrication. Figure 1-4 shows the concept of conformity: Figure 1-4a shows a non-conformal deposition characteristic of fast CVD processes, usually happening in high-aspect ratios present in nanostructures. On the other hand, Figure 1-4b shows a conformal deposition along the whole geometry and with a controlled thickness. This is characteristic of ALD process, and it can achieve this conformality even in nanostructures with high aspect-ratios, reaching values up to 1:3000 [84].

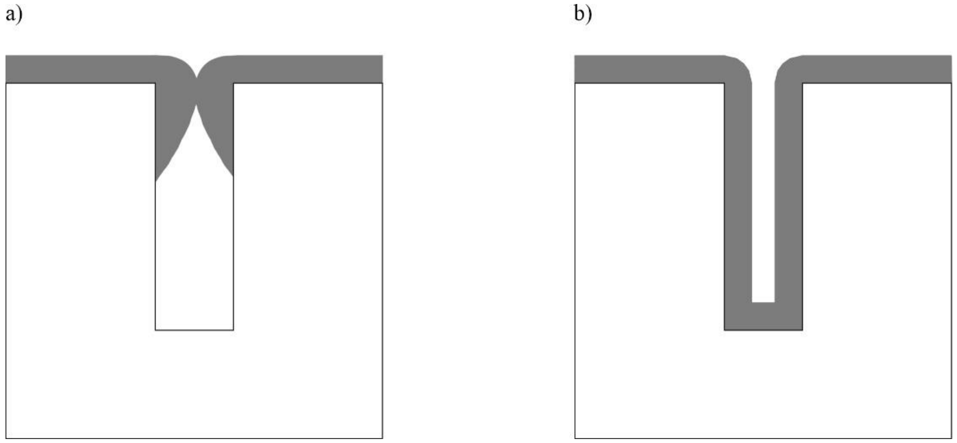

__Figure 1-4__. Schematic to illustrate the concept of conformality of a thin film deposition. a) deposition in which the film (gray) does not cover the entirety of the geometry (in this case a well); this deposition is non-conformal b) deposition in which the thickness of the films is homogeneous along the whole geometry; this deposition is conformal.

On the other hand, a current limitation of the ALD technique is that, since its working principle is based on filling a chamber to ensure surface coverage, the depositions of ALD cannot be selective on certain areas. This selective area deposition with ALD is one of the most important directions of research in the topic. [85]–[88]

Moreover, while CVD processes usually employ temperatures around 800 - 1300 °C [89], [90], making them unsuitable for certain substrates such as polymers and glass, ALD can achieve high quality thin-film formation at much lower temperatures of around 200 °C, which enables high-quality thin-film fabrication even on temperature sensitive substrates, and thus enabling processes for, e.g., flexible electronics.

A thorough reading list of the origins and principles of ALD can be found in [91]

1.4.2 *SALD contribution: spatial separation of chemical reactants*

To address the issue of the slow deposition of ALD, and with the objective to make the deposition more industrial-compatible, a variation of the deposition method called Spatial Atomic Layer Deposition (SALD) has been explored [78]. SALD is gaining momentum in the materials research community since it can achieve fast deposition rates of around 20-40 nm/min and is has the potential to be performed as a large-area deposition technique at atmospheric pressure (and even in the open air) [92], [93], achieving higher throughputs than ALD. These advantages can be reached working at low deposition temperatures as in conventional ALD.

All these features make SALD appealing for industrial processes. In addition, as we will study in this thesis, it offers the possibility of area-selective deposition, with relatively simple instrumentation. Since SALD relies on the same basic mechanisms than ALD, it can theoretically deposit virtually the same number of materials than conventional ALD and it has been the focus of the group at LMGP. [92], [94], [95]

In SALD, the deposition takes the same basic principle: the substrate must be exposed to one reactant, then purged away from remnants and by products, then exposed to the second reactant, and finally purged again. This creates a cycle that must be repeated for a desired amount of times. The difference of SALD with respect to conventional ALD resides on the way the steps of each cycle are achieved. In conventional ALD, each reactant is injected into a chamber at different times, thus avoiding intermixing of reactants. This approach to achieve gaseous separation is called temporal separation, and the time of each pulse controls the surface saturation of the substrate. In SALD, in contrast, the flow of gaseous agents is constant in time, but they are injected on different locations in space. The substrate is then displaced to each region in a cyclic way, so as to emulate the ALD conventional cycles. This spatially separated exposure of the substrate can be compared with the temporal ALD cycles and it has been proven to achieve comparable film properties, even when the materials deposited are not sensitive to the atmosphere [94].

SALD has been tested before by several groups to deposit a wide variety of functional oxides in a homogeneous and conformal manner, in many cases taking place at atmospheric pressure. [96]–[98]

To achieve the alternated exposure of the substrate to the different regions, numerous approaches have been explored [99]–[101]. It is important to consider the need to avoid intermixing of the gaseous precursors in the gas phase during deposition, which is the most challenging parameter to control.

At LMGP, the approach used to successfully separate the reactants is based on a method patented by Kodak [102] and later published by the same team [103]. The principle of gaseous separation is based on controlling the diffusion of the reactants by a separation gas barrier. This can be done with an injection head placed at a close-proximity to the substrate. The substrate should thus be moved linearly in a back-and-forth motion to create the cycles needed for the SALD deposition. The concept and the technical details of the instrumentation of the SALD system used in this thesis are explained in detail in chapter 2. Figure 1-5 shows a schematic of the principle of SALD, as well as a cross section of the deposition head used for the SALD system at LMGP.

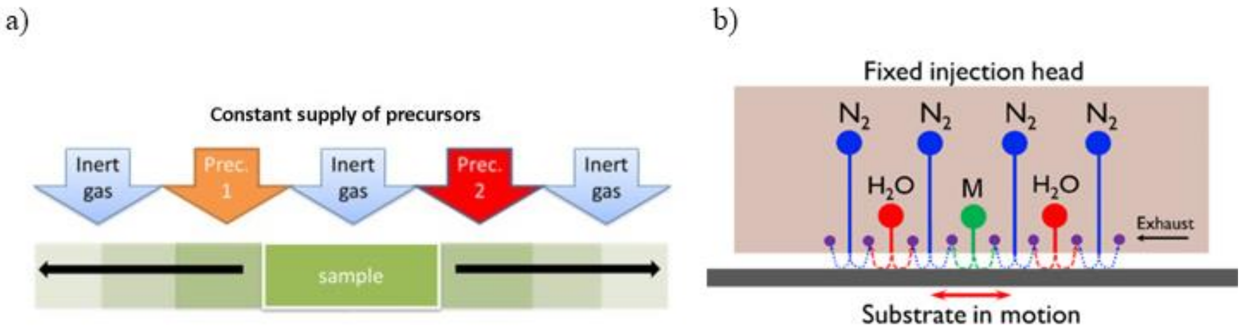

Figure 1-5.*a) Concept of the SALD technique. The gaseous reactants are injected continuously, whereas the sample is scanned. b) Schematic of the cross-section of the deposition head in the spatial atomic layer deposition (SALD) system at the Laboratoire des Matériaux et du Génie Physique (LMGP). These two are separated by a space that corresponds to the deposition gap. Image adapted from [92].*

The spatial, rather than temporal, separation of precursors in SALD gives it many advantages over conventional ALD. Even though SALD is based on the same principles as conventional ALD, the mechanisms of film deposition are inherently different. In ALD, for instance, the exposure happens inside a closed chamber, usually under vacuum. This limits the size of the sample to be coated, but it also ensures a perfect reactant separation and a complete surface coverage. It also simplifies the process of coating by preventing physical phenomena, such as the flow dynamics of the gaseous reactants, from influencing the deposition. SALD, in contrast, works with continuous flows, often without the use of vacuum, i.e. at atmospheric pressure, and, in some cases, even in open air conditions. This main difference with conventional ALD is what makes the SALD equipment more industry-compatible and, as mentioned before, provides the benefit of working with low-cost operation, and with large area surface coverage, since it suffices to displace the substrate in a proper way or modify the size of the gas injection mechanism. However, it also introduces many more physics phenomena into the process. The gas separation relies then on the mass transfer of the concentration of the reactants, which is itself dependent on the convective and diffusive processes within the gas. These processes are dependent themselves on the velocity field that the flow creates at the moment of deposition, which is controlled by the mass flow on the system and the size of the piping and gas injection mechanisms. Temperature also influences such mass transfer phenomena, not only by enhancing the reaction with the surface, but also by modifying the gas concentration diffusion. Finally, as the deposition relies on the movement of the substrate, such movement is expected to increase the convective diffusion of the reactant concentration as well.

Out of the deposition mechanism difference between SALD and ALD, it is key to highlight the conceptual difference between "growth rate", usually given in nm/min (µm/hr in the case of industrial CVD processes), and "growth per cycle" (GPC). GPC is a key parameter often used to study and optimize ALD processes. Its units are nm/cycle (or even pm/cycle for processes with low-reactive or low-volatile precursors), where the cycles represent a full sequence of the usual four temporal-separated steps in ALD mentioned before. Thus, due to the self-limited characteristic of ALD reactions, a limited amount of material, and thus thickness, can be deposited with each cycle. Therefore, the overall growth rate (in nm/min) is dependent on the duration of the ALD cycle itself, which can vary for the different ALD systems or approaches.

In the case of SALD, the GPC is similar to the one obtained in ALD, since the basic principle of surface reactions, as well as the precursors used, are the same. Nevertheless, the time needed to perform a full ALD cycle is greatly reduced in SALD, passing from 2-3 cycles per minute in ALD to 20-100 cycles per minute in SALD. The way to control the cycle time in SALD is directly controlled by the speed in which the substrate is displaced from region to region. As an example, typical values of displacement speed in the SALD system at the LMGP are 25-50 mm/min, which, depending on the reactor geometry, generate a full SALD cycle in around 1 second or less.

Continuing the comparison between ALD and SALD, when optimizing a deposition process in a conventional ALD equipment, one needs to optimize the time of each exposure pulse of the cycle for a fixed precursor flow, temperature and pressure in the chamber to ensure proper surface saturation, while keeping it as short as possible to avoid the waste of precursor that will not react with an already saturated surface. The time optimization is dependent on the precursors used, since its reactivity will determine the time needed to saturate the surface. Therefore, different times per precursor and purging pulses can be used. In SALD, the flows are constant, therefore a pulse time is not used. Instead, one needs to calculate the time of residence that the substrate will have at each region:

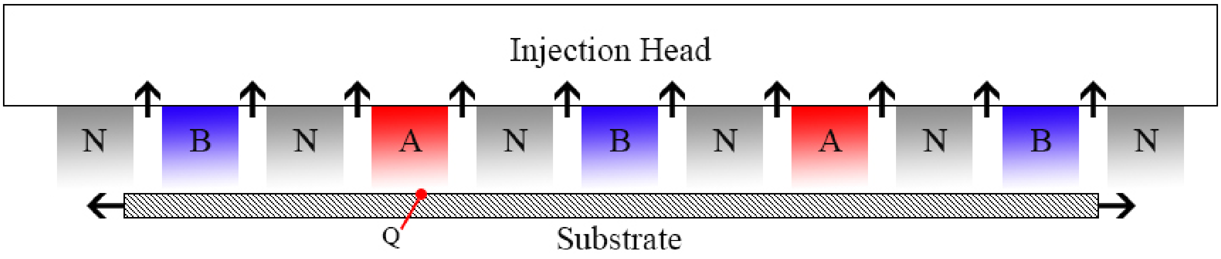

Figure 1-6. The different regions below the injection head produce the deposition as every point in the substrate (one of which is called here Q) passes through each of them. The arrows represent exhausts for the reactants and by-products of the surface reaction.

Figure 1-6 shows the mechanism of the SALD approach used at the LMGP. The spatial separation of reactants is obtained by the injection head, which generates different regions of reactants used to generate the SALD cycles as the substrate scans back and forth through each of them. They are depicted as N for the purging region, A and B for each gaseous reactant region. Black arrows represent the exhausts through which the remnants and by-products are evacuated. With each movement, the point Q travels under each region for a certain period, which will depend on the velocity of the movement and on the size of the region. This time is referred to as the residence time, and it is the SALD equivalent of the pulse times in ALD. Similarly, if we consider that said point Q is under the exhaust or the purge region, the size created by the purge region and the exhausts would be equivalent to the purge steps in conventional ALD. A deeper explanation of the SALD system at LMGP will be presented in chapter 2 of this thesis.

It can be concluded that the spatial attribute of SALD gives many advantages with respect to temporal ALD. SALD allows for an open-air, vacuum-free, fast deposition but, due to the complexity and the amount of the phenomena occurring at the same time during deposition, it usually requires a higher precision and control in its instrumentation than conventional ALD. Small adjustments to the geometry and mechanism of deposition will affect the outcome of the deposition regarding the physical, mechanical and electrical properties of the films deposited. Such adjustments include the positioning of the substrate with respect to the deposition head, the flows of the gaseous reaction, the geometry of the deposition head, and the speed of the substrate scanning. In the case of the SALD system in this thesis, the close-proximity approach is used to achieve separation of the reactants, and it is explained further in chapter 2. For this approach, a high mechanical and geometrical precision of the system needs to be carefully optimized. It is also important, to envision large-area depositions with these techniques, to ensure that the velocity and pressure of the flow along all the outlet is homogeneous, ensuring a film with homogeneous properties without hindering with the benefits SALD provides.

Therefore, to control and predict the materials deposited with SALD instruments, it is important to consider these aspects besides considering the usual chemical and physicochemical aspects of a surface reaction. Furthermore, industrial processes need to be considered when developing this fabrication method to bridge the gap between research and industrial thin film fabrication.

1.5 Variations and developments for the SALD deposition technique

1.5.1 *Large-area deposition*

With the high growth rate of SALD, it becomes apparent that SALD is a promising technique to perform large-area depositions. There would be two different approaches to fabricate thin films over large areas. The first approach would consist on simply enlarging the injection head to cover a larger area. With this approach, one could use the same deposition principles as smaller-scale deposition but enlarging the injection head would invariably result in the need of increasing the flows to ensure carrying the precursors homogeneously along the whole surface. Therefore, using close-proximity SALD would involve the study of the influence of the size of the injection head on, as well as an optimization of, the gaseous flow, the outlets, and, ultimately on the homogeneity of the deposition. The second approach would consist on sectional depositions with a head smaller than the area to coat. This approach is a simple one that wouldn’t complicate too much previous optimizations, allowing to deposit different sizes with the same flow parameters, although it would still need the high movement precision, and it would decrease the throughput of deposition. One would also have to consider the difference of properties on the overlap of the deposited sections.

1.5.2 *High throughput Roll-to-Roll technique*

Another technique of large area deposition that is exclusive to flexible substrates is the infamous roll-to-roll technique (R2R). This technique is available given the ability of SALD to deposit high-quality thin films at low temperatures (~200 °C). This technique would enable high throughput deposition, and it is especially interesting for low-cost photovoltaics and flexible electronics. Indeed, many groups have reported the use of R2R techniques in SALD systems, which is promising for the industrialization of the technique [104]–[107]

1.5.3 *Mask-less patterned deposition*

One of the key steps during the fabrication of microelectronic devices is the patterning step. Patterning is well known among microelectronic device researchers and manufacturers and it is used to transform deposited films into functional devices. The most used technique to achieve a good patterned deposition relies on the usage of masks and lithography steps. Although these steps achieve incredible resolution, they also increase the cost of the devices enormously. For consumer electronics devices, this may not be a deal-breaker, but for other applications, especially in energy-related applications like photovoltaics or water splitting, the cost-efficiency of the process is the most important parameter to control. An important research trend is the mask-less patterned deposition of high-quality materials. Multiple approaches have been explored; many of them include variations of conventional ALD and they are described in references [85]–[87], [108].

SALD is also a promising technique to achieve patterning of the deposited film. SALD can achieve this in a low-cost and simple way by exploiting the geometry of the injection head and its scanning movement. Usually, in SALD equipment (and in the research done in this thesis), substrates are scanned in a linear motion with respect to the deposition head to create a homogeneous film. Even when the substrate is rotated, the deposited area relies on a motion that is perpendicular to the gaseous outlets. Nevertheless, the movement of the SALD system is not (and should not) be constrained to a linear motion only. Instead, by combining movements on one linear head, or even using a system comprising more than one injection head (maybe even with each injection head using different materials), it is possible to envision much more complex functional materials deposition such as superlattices or subsequent patterned depositions with multiple layers of materials.

To achieve this, it would be again important to ensure the precise control of the flows and the concentration of reactants in the carrier gas, along with a precise movement of the injection head and/or the substrate to obtain homogeneous properties along the whole deposition. The diffusion of the concentrations would be key to achieve patterned depositions, but overall, using this technique seems quite promising.

1.5.3.1 Injection head geometry

Moreover, it is usual for SALD systems to use an injection head with simple geometries. This is usually the case since one of the limiting factors for a mechanical design of an injection head is the manufacturability of the piece, which uses conventional fabrication techniques such as computer numerical control (CNC) machining, milling and drilling on metal pieces. If conventional fabrication techniques are used, one is limited to simple geometries. However, from a mechanical design point of view, it is possible to come up with different geometries that would simplify the setup of the system, or that would even enable unconventional depositions by influencing the gaseous flows within it. As explored in this thesis, using innovative techniques such as additive manufacturing —also known as 3D printing— it is possible to imagine all number of different geometries that would enable different deposition patterns of that simply would integrate different parts of the system into one monolithic piece, lowering the complexity and the cost associated with the maintenance and setup of the equipment. In this thesis, we will introduce the utilization of additive manufacturing to simplify the deposition head previously used in the system. This also reduced the cost needed to test multiple prototypes for different geometries of deposition. Eventually, one of those prototypes was fabricated in metal additive manufacturing, that, although the cost was higher with respect to other additive manufacturing techniques, it still provided with the simplicity of use and the simplified maintenance for the system.

Moreover, as we will see also in this thesis, additional geometries were designed as prototype and as proof of concept to show the capabilities of 3D printing. This included a 2-in-1 deposition head for two different precursors, and a SALD "Pen", which can provide with free-form depositions; interesting for, e.g. building-integrated photovoltaics. This topic will be further discussed in chapter 4.

1.5.3.2 Atmosphere-controlled SALD

Considering the advances of SALD to date, it is imaginable that. Besides exploiting the spatial separation in ALD, one could also control the atmosphere in which the depositions occur. By doing this, one could explore the influence of humidity and the presence of oxygen on the films. This is particularly interesting when dealing with air-sensitive or humidity-sensitive materials, such as perovskites, or even n-type TCOs, where the presence of oxygen affects adversely to its electrical properties. Some experimental work has indeed already been done by Hoffman, L. [109]–[112] and it provides promising results for different type of materials deposited with this technique.

1.6 Overview and structure of this thesis

In this thesis, we explore the deposition of a promising p-type oxide that has the potential to be used in multiple applications and that would, if fabricated with the required properties, impact the electronics industry in great extent. For this, we use an innovative deposition technique that has gained momentum in the thin film deposition community, namely, Spatial Atomic Layer Deposition or SALD. This technique provides many advantages to the technique on which it is based, ALD, and decreases the gap between research and industry of ALD for materials fabrication.

The experimental work done in this thesis starts from a previously set SALD equipment in LMGP. Several adaptations were needed to enlarge the diversity of materials it can deposit, notably Cu_2O, although the adaptations were also used for deposition of other materials explored in the team's projects. These adaptations included mainly the creation of precursor containers that could be easily replaced, along with heating systems for such containers and their automated controllers. The description of the SALD equipment, the adaptations and the methods for characterization of the thin films deposited will be explained in chapter 2.

Afterwards, it is important to understand the physical phenomena present in the SALD deposition system. The fact that our system relies on a close-proximity deposition makes it important to understand and control the flows in the system, as well as the concentrations used for the depositions. Here, we used Computational Fluid Dynamics (CFD) simulations and coupled them with a surface reaction chemistry computation using Comsol Multiphysics® in order to model our SALD deposition system. This helped us study the influence of different parameters of the equipment of the SALD on the intermixing of the gaseous precursors. We explain the appearance of intermixture of gaseous reactants and demonstrate that, with a simple geometrical change on the reactor, it is possible to control the deposition regime of the system. This demonstrates the versatility of the SALD, but it also shows that, to obtain homogeneous properties, high mechanical precision of the movements and geometries is needed. This study will be presented on chapter 3.

On chapter 4 we explore how we used the innovative fabrication procedure known as additive manufacturing to enhance the usability of the system, while lowering the cost of the equipment. We explain the procedure to design and fabricate a monolithic system for the injection head that reduces the space and the need of maintenance. We use also CFD simulations to study the homogeneity for different design parameters, with the objective to provide insight on the scalability of the design. This demonstrates that functional prototypes are possible to be easily fabricated using additive manufacturing, enabling the fabrication of geometries that are not compatible with conventional fabrication techniques. We show that the technique used for the design prototyping, which was based on polymeric resins, can create functional prototypes that can achieve fabrication of films with comparable quality than those fabricated with the conventional injection head. We then present the disadvantages of the resin-based 3D printing, and we present the outcome of the depositions of one of the designs that was fabricated with 3D metal printing. Finally, we present the concepts that can be achievable with 3D printing, as examples and inspiration for future developments of this technique as a tool that allows unconventional film deposition processes.

Finally, on chapter 5 we present the results of the material depositions of Cu_2O, obtained with all the previously created knowledge and tools. We study the quality of the thin films obtained and their optical, electrical, and microstructural characterization. We demonstrate the ability to control the conductivity and carrier concentration of the p-type Cu_2O films, and present one of the best conductivities for such materials obtained with a low-cost and scalable deposition technique. We then provide our hypothesis on the resulting electrical properties. Finally, we present preliminary results on devices fabricated with Cu_2O as a p-type oxide and ZnO as a n-type oxide, and we provide the perspectives on SALD-based depositions for low-cost device fabrication.

Chapter 2

SALD Deposition equipment and characterization techniques

During this thesis, SALD was used for the deposition of Cu_2O thin films on different substrates. For this, certain modifications were needed on the original SALD system in order to make it more adapted to the inherent characteristics of the two different copper precursors used (See Chapter 5). Afterwards, the finite element method (FEM) was used in order to understand, predict and control the different phenomena taking place while performing depositions with the SALD reactor. Thus, different simulations were performed, which later led to the design and development of new versions of some components of the SALD system using innovative fabrication methods, namely additive manufacturing (AM). Lastly, the knowledge gained from the FEM simulations, coupled with the newly designed components were employed for the experimental deposition of thin films of copper (I) oxide (Cu_2O) on different substrates.

This chapter starts with an explanation of the working principle of the SALD deposition system in LMGP and its components, as well as the adaptations needed and performed for Cu_2O thin film deposition. Later, the tools for the FEM simulation of the complex SALD phenomena are presented. After that, the workflow and tools used for the design, optimization and AM fabrication of the designed components of the system are explained. Finally, the relevant characterization techniques used to study the SALD deposited films during this thesis are briefly explained.

2.1 Description of the SALD System in LMGP and the modifications performed during this work

As explained in Chapter 1, the SALD technique relies on a physical (rather than temporal) separation of reactants to obtain the same assets of ALD but with shorted deposition rates. This is achieved in our SALD thanks to a gas distribution system, i.e. a manifold head, coupled with the close-proximity between the gas outlets and the surface to be coated. The instrumentation needed to achieve such deposition process requires also a system to physically move the substrate through the regions containing different gaseous reactants, thus emulating the conventional ALD cycles. The instrumentation of the SALD at LMGP (designed and developed in-house) is explained in detail in the following sections.

2.2 Description of the original SALD system and its adaptations for Cu_2O deposition

The SALD system, shown in **Figure 2-1**, consists of three main parts: the automation system, the gas panel and the head-substrate system. The automation system includes all the electrical system and energy supply, sensors and actuators used during SALD deposition, as well as the automation needed to control them. The gas panel includes the well-known bubbler system used in conventional chemical vapor deposition (CVD) systems —including ALD— to carry certain concentration of reactants towards the surface to be coated, and which, in some cases, like in this thesis, needs external heating. The head-substrate system contains a “deposition head” that directs and spreads reactive gases along the substrate to obtain a homogeneous surface reaction, and a substrate holder in which the substrate to coat is placed and heated. In this thesis, all three parts were adapted for the deposition of Cu_2O, since the system was initially optimized for zinc oxide (ZnO) deposition with diethylzinc (DEZ) precursor. Such parts and modifications will now be explained in detail.

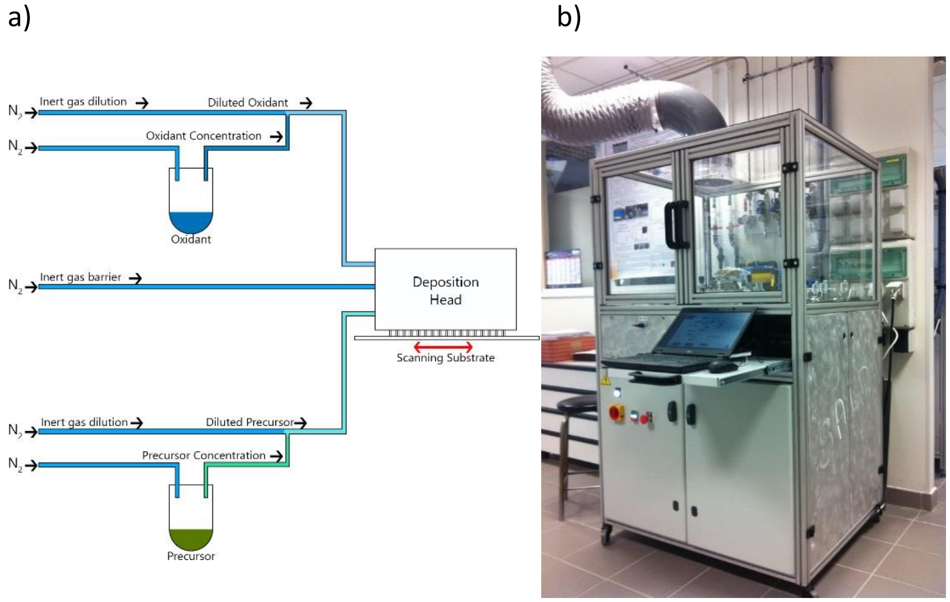

Figure 2-1. *a) Schematic of the working principle of the SALD system at LMGP. b) Picture of the SALD system at LMGP.*

2.2.1 *SALD deposition mechanism*

The principle of deposition of the close-proximity SALD in LMGP is achieved by a coordination of three parts of the system: the gas panel, used to extract certain concentration from the bubblers to create the required surface reactions; the head-substrate system, comprised of the deposition head with spatially separated and alternated reagent outlets; and, finally, the automated motion control system with which the substrate is scanned in a back-and-forth cycle, ensuring its exposure to the different regions, thus completing the surface reaction (**Figure 2-1a**).

In this work, the reagents used are metallic precursors that determine the layer material, water as an oxidant agent and inert gas barriers that ensure, along with the close-proximity gap, a spatial separation of the reactive gases, consequently working in ALD regime. The spatial regions with different reagents created by the head-substrate system. Furthermore, the number of cycles that the heated substrate scans under the deposition head will determine the thickness of the layer.

To modify and control the properties of the films deposited, parameters in each part of the system may be tuned. The mass flows going through the panel for each outlet, bubbler and dilution line can control the concentration of reagents sent to the substrate surface. The scan speed, acceleration and distance in the automated movement will have an impact on the “residence time” that the substrate passes in each region, the turbulence on the flow when changing scanning direction, and the area of layer deposited, respectively. The residence time has an influence on the growth rate on the film, since such residence time should be enough to allow for a complete surface coverage with each reagent, and it will be one of the parameters studied in Chapter 5. Finally, the geometry of the head-substrate system will ensure spatial separation of reagents, as well as a proper exhaust of remnants and by-products, making it important to control the deposition regime (ALD vs CVD) and, therefore, the properties of the deposition. All parameters mentioned here are inter-related and are co-dependent with each other, and thus must be properly controlled and optimized to obtain SALD films with the required homogeneity and properties.

A detailed description of the three main parts of the SALD system at LMGP will be now discussed.

2.2.2 *SALD automation system*

The automation system for the SALD equipment at LMGP consists of a Programmable Automation Controller (PAC) from Opto22® that controls all pneumatic valves, mass flow controllers, heating systems and motion controllers. It can control the gaseous flows in the gas panel (explained further in this section), the temperatures of each bubbler and of the substrate, and the movement of the substrate under a fixed deposition head, to perform the actual film deposition. Such movement needs to be optimized regarding speed, acceleration and distance, to achieve the desired deposition properties.

During this thesis, to achieve deposition of Cu_2O, additional mass flow controllers and heating systems for the bubblers were implemented and optimized using proportional-integral-differential (PID) controllers to enhance the volatility of the precursors utilized.

2.2.3 *Description of the precursor transport system: the gas panel and the bubbler*

For the transport of the reactants used for the deposition in the SALD, a gas panel uses an inert gas to function. In our system, nitrogen (N_2) gas is used to carry all reactants from their reservoirs to the surface of the substrate. More precisely, a container with certain liquid (or, in some cases, solid) precursor — colloquially named a “bubbler”— is subjected to a flow of nitrogen, called “carrier gas”, and the carrier gas is enriched with a certain concentration of molecules from said due to convective and diffusive mass transfer into the gas. The outflow of the bubbler is then transported to the pre-heated substrate surface. After a surface chemical reaction takes place, the remnants and by-products are taken away by a difference of pressure to an exhaust port where they should be treated properly. Even though a solid precursor would not create bubbles with a carrier gas flow, and even when the carrier gas sometimes does not actually create a bubble but rather only transports the vaporized molecules on the container, for simplicity, the name of the container stays the same.

Every reactant is stored separately in a distinct bubbler and the flow and temperature needed to saturate the carrier gas is different for each precursor. The chemical-physical characteristics of the precursor will determine these parameters but, in general, ALD-compatible precursors tend to have a high-volatility, high vapor pressure and chemical stability. Additionally, the gas panel allows for an inert carrier gas to dilute the concentration of the outflow of each bubbler with a so-called “dilution line”, allowing for a fine tune of the reactants injected towards the substrate surface.

Initially, the SALD system used had three bubblers installed, one containing DEZ to deposit ZnO, one containing trimethyl aluminum (TMA) to deposit aluminum oxide (Al_2O_3), and one containing water as an oxidant agent. During this thesis, an additional bubbler was fabricated and installed for the storage of the copper precursors, along with its dilution line and a high-precision heating system. Such new bubblers have a smaller size than the previously used ones, which allow for the path towards the substrate to be reduced, which is beneficial for low volatility precursors. **Figure 2-2** shows a schematic of the gas panel used in the SALD system. The whole panel has one input of carrier gas for all bubblers and it is then distributed to provide the gaseous reactants to the deposition head.

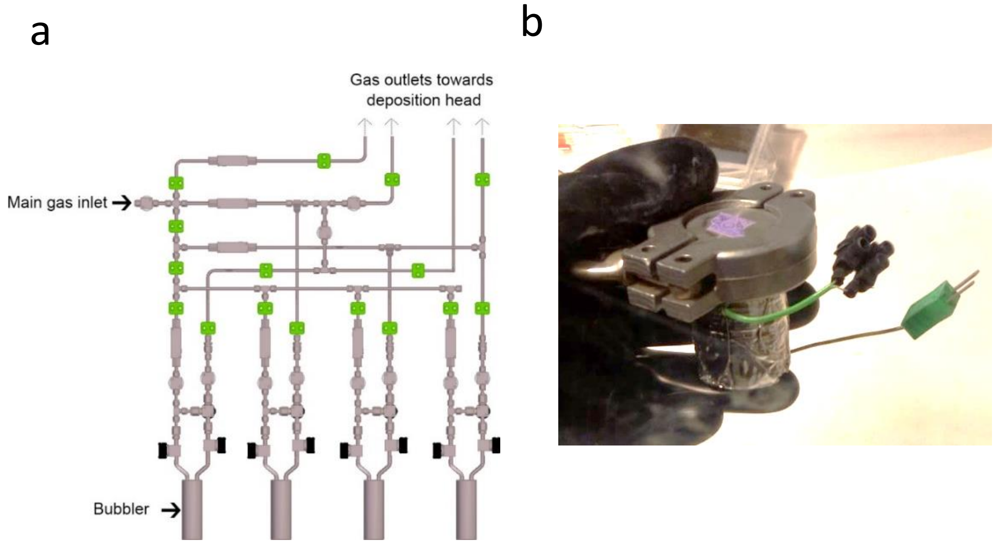

Figure 2-2. *a) Schematic of the gas panel in the SALD system, containing the bubbler used to store the reactive precursors. b) Picture of the new bubbler designed for the copper precursors.*

2.2.4 *Head-substrate system*

The spatial separation of the gaseous reactants extracted from the gas panel is achieved, in our SALD system, thanks to a deposition manifold head (**Figure 2-3**). This deposition head can take any form desired as long as the spatial separation of reagents is achieved. In a patent published by Kodak and a publication of 2008 by the same research team [102], the authors use a deposition head with rectangular slits that distribute the gaseous reagents and achieve spatial separation of gaseous reagents by placing it close to the substrate (at a separation of around 150 µm), thus giving these types of SALD the name of “close-proximity”.

The length of the deposition head used in LMGP previous to this thesis, as defined by the substrates we intended to deposit on, was 5 cm long and was inspired in Kodak-s initial design. **Figure 2-3** shows the geometry of the deposition head used in the initial tests and depositions of the SALD at LMGP. The first version of deposition head used in LMGP is comprised of many metallic parts: a piece to distribute the gases to their respective outlet, a piece to join the distribution piece with the main body, and the body which homogenizes such gases into the previously mentioned rectangular shape (**Figure 2-3a**).

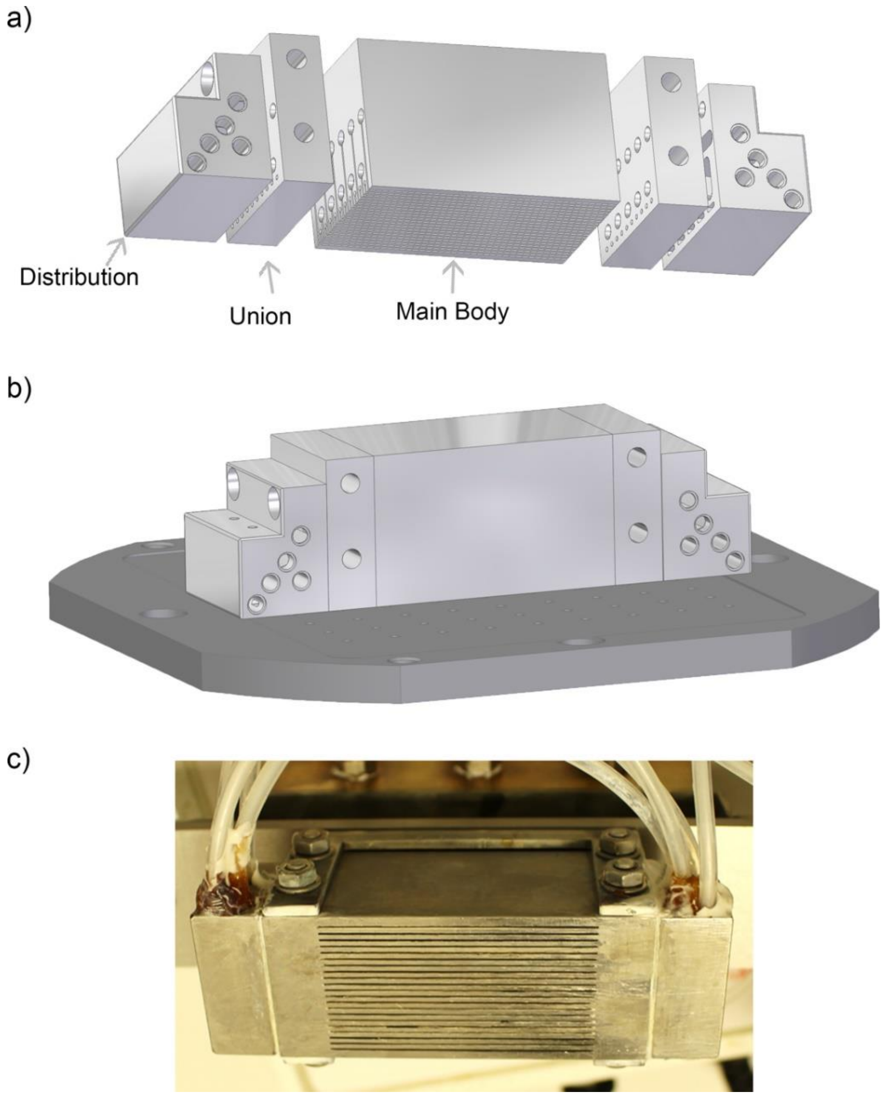

Figure 2-3. Design of the deposition head used previously to this thesis. a) Exploded view of the parts of the system, showing the distribution section, the joining section and the main body. b) Assembled view of the three section on top of the substrate holder. c) Photograph of the real deposition head in the SALD system.

This design was successfully used to deposit several materials such as ZnO, Al_2O_3 and aluminum doped ZnO [95], [113]. During this thesis, it was desired to avoid contamination of such deposition head. Therefore, one of the main achievements of this thesis is the establishment of a method to design, fabricate and install simpler, low-cost deposition heads to allow for the deposition of Cu_2O, while avoiding cross-contamination. Additionally, this method allowed the quick realization of head prototypes that in turn allowed for a rapid testing and improvement of the designs, and that were subsequently adapted to obtain different functionalities on the SALD system. The methods used for this (FEM simulation + AM) will be detailed further in this chapter, while a more in-depth explanation of the designed prototypes is presented in chapter 4.

2.2.4.1 Close-proximity to the substrate: the importance of the "gap"

As it has been described above, the "close-proximity" approach used with the SALD equipment at LMGP and throughout this thesis creates a deposition gap that, when small enough and with the help of the inert gas barrier, prevents gas-phase intermixing in the gap and maintains an ALD-like deposition regime. In **Figure 2-4a** schematic of the spatial separation principal is presented.

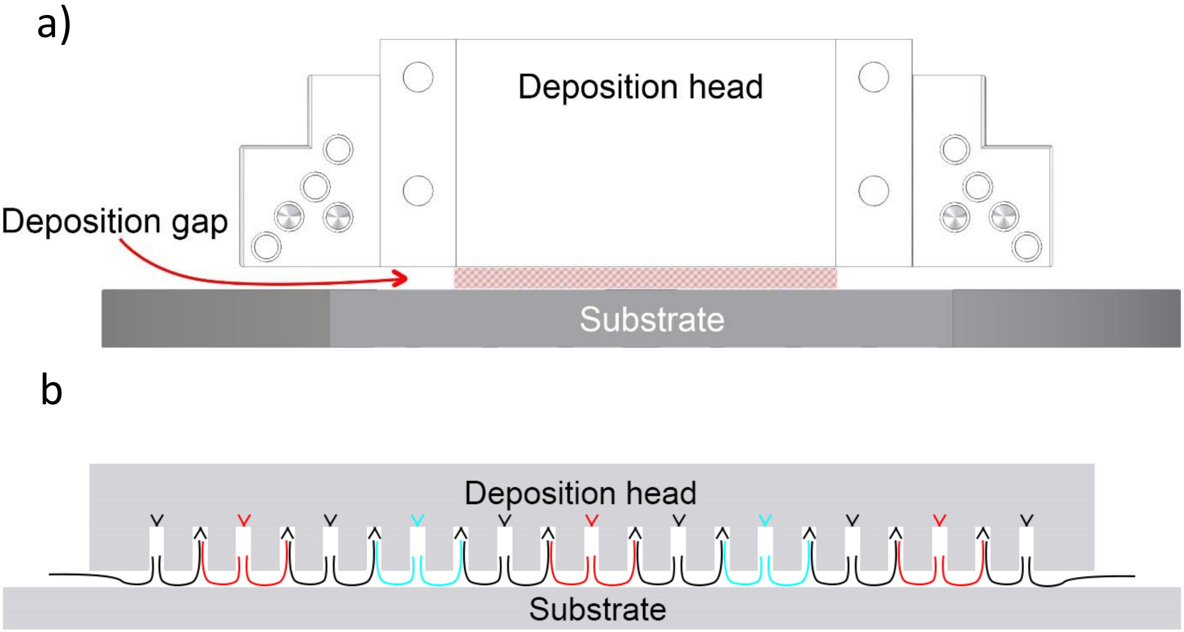

Figure 2-4. a) Schematic of the distance between the substrate and the deposition head, referred to in this thesis as deposition gap. b) Schematic of the principle of the spatial separation of gaseous reagents. The lines represent the flow of the gases used for deposition exiting the deposition head, into the two different reagents are shown in red and blue lines, whereas the inert gas barrier is shown with black lines.

The deposition gap plays a key role on the deposition regime, and, therefore, on the properties of the film deposited. Indeed, it has been shown that depositions made in a CVD regime can be obtained with such approach [114], [115]. A visual schematic of the gap is shown in **Figure 2-4b**. In this thesis a systematic computer simulation was created to predict and control the gap effect on the deposition regime, and it will be presented in detail in chapter 3.

2.3 ALD precursors formula, characteristics and chemistry

In this thesis, two materials were deposited on glass and silicon substrates: ZnO and Cu_2O. For the deposition of ZnO, the precursor used was diethylzinc (DEZ). This precursor is highly reactive and volatile and does not need to be heated. The deposition of ZnO from DEZ was previously optimized in the SALD system at LMGP in the thesis of V. H. Nguyen [116]. For the Cu_2O, the precursors will be presented in detail in chapter 5.

2.3.1 *Precursors for Copper Oxide Deposition*

For the deposition of Cu_2O, two precursors were studied: Copper hexafluoroacetylacetonate – trimethylvinylsilane (Cu(hfac)TMVS), more commonly referred to as Cupraselect, and Copper hexafluoroacetylacetonate ciclooctadiene (Cu(hfac)COD), called in this thesis Cu-COD. The precursors will be discussed in detail in chapter 5. The precursors were obtained from EpiValence Limited.

The low volatility of the copper precursors, in comparison to most ALD precursors, makes it necessary for the bubbler to be heated, as will be seen more in detail in chapter 5 as well. Hence, in order to obtain Cu_2O depositions, a heater system was fabricated for the bubbler, as well as for the delivery lines up until the deposition head, since it is needed to avoid undesired condensation happening in non-heated zones within the path of the hot, reactive gases. In this thesis, one of the main outcomes is the optimization of the temperature needed for the deposition on each precursor, as well as the influence on the material deposited.

A more in-depth analysis of the chemical properties of each precursor will be provided in chapter 5, where the experimental deposition of copper oxides is presented.

2.4 Computational Simulation of SALD Phenomena

As mentioned before, the SALD deposition technique relies on a surface-limited chemical half-reaction separated in space. Also let us remember that a close-proximity gap of around 150 µm is used to ensure the separation of reagents during the deposition. Indeed, all chemical reactions happen in the gap, essentially turning this gap into the actual reactor chamber. It is important then to qualitatively determine the value of the gap, its geometry and physical layout, so we can control the SALD deposition in a reproducible manner.

The phenomena present in the SALD system include diffusion of a diluted species within a gaseous flow, fluid dynamics, and chemical reactions, all happening at the same time. To simulate such coupling of different physics, the system is studied with a FEM software capable of simulating different physical equations and study their whole impact on the system. In this thesis, such multiphysics simulations were achieved by the software COMSOL® multiphysics.

COMSOL can achieve multiphysics coupling using a different module for each type of equations to be solved. Here, three physical models were used for our simulations: the fluid dynamics model with the Naiver-Stokes equation, the mass transport model via diffusion and convection using Fick's Law, and the chemical model for the kinetics of the reactions during deposition. The former two are included in the Computational Flow Dynamics (CFD) COMSOL module, while the latter is included in the Chemical COMSOL module. When coupled, the simulation involves a reactive flow and, when combined with the geometry simulated, a simulation of a surface chemical reaction can be obtained. The physics equations used in this thesis will be detailed in chapter 3.

2.5 Deposition Head Design and Fabrication

Since the SALD system is used to deposit different materials, to avoid cross-contamination, we decided to use a separate, independent deposition head for the deposition of Cu_2O in this thesis. Nevertheless, the architecture of the deposition head, as designed originally, had the inconveniences of being too complex to fabricate since it is comprised of many parts that require a time-consuming assembly, as well as being expensive due to the usage of conventional manufacturing techniques (milling, drilling, etc.) for high precision features. To avoid such complications, a new and innovative path was taken: the use of the emerging and growing technique known as additive manufacturing, also known as 3D printing.

2.5.1 *3D design and simulation of a new version of deposition head*

The design process of the new deposition head started with the objective of creating a simple yet functional part. We decided to design a single-piece deposition head containing all gas distribution within the geometry to reduce space and complexity of both the connection with the pipes coming from the gas panel, and the installation within the SALD cabinet. In parallel, different versions of deposition head were designed to add specific functions, such as the ability for selective area deposition (SAD) with SALD, a promising topic in the field. For this, we used a software called Solid Edge®, a computer aided design (CAD) software widely used in research and in industry.

Furthermore, in order to constantly improve the designs, CFD simulations were also used to maximize the homogeneity of the gas flows within the deposition head. Besides the previously mentioned software COMSOL®, an additional CFD simulation software, Autodesk CFD®, was used. Finally, thanks to the fast prototyping ability given by 3D printing, a continuous feedback from the experimental SALD depositions also influenced and improved each version of the design.

2.5.2 *3D fabrication methods*

Once a deposition head version was validated by simulation, additive manufacturing was used for its fabrication. In this thesis, the chosen additive manufacturing technique was stereolithography (SLA), which uses polymeric resins that can have a wide variety of interesting properties such as, e.g., high temperature resistance. Additionally, such techniques produce solid, leak-proof polymer printouts (in comparison with other techniques such as fused deposition modeling, FDM), well adapted to a gas flow.

Although SLA was the fabrication technique chosen for this thesis, in LMGP, two different printers were acquired: the Formlabs Form 2® for the SLA technique, and the Ultimaker 3 Extended® for FDM technique. Although the latter was not used for the deposition head, its lower cost justified its acquisition for the fabrication of smaller parts used in diverse ways, mostly mechanical adaptations, across the SALD instrumentation.

Once acquired, both printers were setup and calibrated accordingly. The designs then can be printed, not without going through a process of preparation for the printers. Each technology requires different considerations, and each has their own benefits and drawbacks. In additive manufacturing, a successful print file must follow certain guidelines, depending on the technique used. The use of supports for “overhanging” parts, as well as a good orientation for the piece are crucial for a successful print. To prepare the file, we make use of different software to adjust the print parameters for each machine; for SLA printing we make use of a software called PreForm®, while for FDM printing, we use CURA. Each technique has also post-processing steps to obtain the final piece. A more detailed explanation of the process needed to print, the guidelines and the limitations of each machine will be presented in chapter 4.

Regarding the materials used for 3D printing, during the setup of the LMGP 3D printing platform, several materials have been tested. For SLA, the materials tested include the standard “clear” resin, a resin with high mechanical resistance, a flexible resin and a high-temperature resistant resin, which is the main material used for the deposition head fabricated for the SALD due to the elevated temperatures of deposition used (~250 °C). For FDM, the materials available include polylactic acid (PLA) as well as acrylonitrile butadiene styrene (ABS).

After the design of the deposition head created was validated experimentally, such design was printed in Aluminum in a metal 3D printer by an external manufacturer, to increase its compatibility with high temperatures on the substrate holder.

2.6 Characterization methods

The deposited films with the SALD system were characterized to elucidate the effect of the parameters available in the system on the film properties. Here the main characterization techniques used in this thesis are briefly explained.

2.6.1 *Vibrational Spectroscopy Characterization*

Some of the main characterization techniques used during this thesis included vibrational spectroscopy techniques. They provide information on the vibrational modes of the bonds and molecules in the analyzed material.

Raman spectroscopy relies on inelastic scattering of the incoming radiation taken place in the studied material, giving rise to a molecular fingerprint of the same. Here, Cu_2O was studied with

Raman Spectroscopy to monitor the presence of CuO in the film, as well as to qualitatively determine the relative crystallinity of the films deposited. Raman spectroscopy was carried out with a Jobin Yvon/Horiba LabRam spectrometer with the use of different monochromatic lights. In this thesis, a 0.4 mW Argon laser with a 488 nm wavelength was used.

On the other hand, Fourier Transform Infrared Spectroscopy (FTIR) relies on the absorbance, transmission or reflection of a polychromatic infrared light beam by the material studied, giving information on vibrational modes of the bonds present in it. Here, we use a Bruker Vertex 70V spectrometer equipped with a CsI beam splitter working under vacuum in transmission mode. To obtain the spectra, Cu_2O was deposited on silicon substrates transparent to infrared light. This allows to detect the purity of the Cu_2O films.

2.6.2 *X-Ray Characterization*

The crystallography of the Cu_2O thin films deposited was deeply studied using X-Ray based techniques. X-Ray Diffraction (XRD) was used to obtain information on the crystallinity, phase and crystallographic orientation of the material.

Additionally, and with the same equipment, X-Ray Reflectivity (XRR) measurements were also performed to estimate the density, roughness and thickness of the thin films deposited. In XRR, the equipment is set in a parallel beam configuration

Here, for the XRD measurements, an XRD Diffractometer Bruker D8 Advance was used, which uses Cu-Kα radiation source (λ= 0.15406 nm). Measurements were made with a 2Θ range of 20°−80° with a step of 0.01° and a duration per step of 1 second.

Another technique based on X-Ray incident beam and used in this thesis is X-Ray Photoelectron Spectroscopy (XPS). In this case, an X-Ray beam is shined on the material to analyze, which in turn causes electrons to be ejected from their orbitals. The kinetic energy of each ejected electron (called photoelectron) is measured and compared with the incident beam energy to obtain the binding energy it had before its emission. Such binding energy provides information on the atomic composition of the film, the bonds present on the material, as well as the oxidation state of the atoms.

2.6.3 *Electron Microscopy Characterization*

To obtain information on the topography and to obtain information of the thickness of the films deposited in this thesis, Scanning Electron Microscopy (SEM) was used. SEM is a widely used microscopy technique based on an electron beam focused on the sample via a series of electronic lenses. The interaction between the incident electrons and the matter in the sample gives rise to secondary electrons (SE), backscattered electrons (BE) and X-Ray photons to be emitted from the sample. The detection of the secondary electrons gives information on the topography of the sample, analogous to an optical image obtained by an optical microscopy, but with a much larger resolution of about tenths of nanometers (in contrast with the optical microscope that has a resolution of >500 nm).

If instead the backscattered electrons are detected, an image containing information about the chemical contrast is obtained. This is especially useful in this thesis to clearly detect the thickness of a deposited films when obtaining an image of the cross-section of the sample.

Lastly, if the instrument has an X-Ray detector, a technique named Energy Dispersive Spectroscopy (EDS) is then used to obtain chemical information of the analyzed sample. The energies of the X-Ray photons measured correspond to the relaxation of electrons to lower energy shell electrons, as a result of their previous excitation caused by the incident electron beam. The spectrum obtained presents the number of times a photon with certain energy was detected. By knowing the energy of each energy level within an atom of an element, it is possible to verify the presence of an element in the sample observed, as well as an approximation of its chemical composition.

In this thesis, a FEI Quanta 250 MEB FEG ESEM tool was used to perform both secondary electrons and backscattered electrons SEM images, as well as to perform EDS on the Cu_2O and ZnO films deposited. The former two allow us to observe the grain size and the morphology of the layers, while the latter allows to detect the presence of other elements within the film.

2.6.4 *Optical Characterization*

As the deposited films in this thesis have a potential application on transparent electronics and TCOs, one of the important parameters to study is the transparency of the films. For this, Total Transmission measurements from ultraviolet to near-infrared wavelengths were conducted in a Lambda 950 spectrophotometer from Perkin Elmer, using an incident light wavelength from 250 nm to 2500 nm. Additionally, the total transmittance spectrum was used to calculate the optical bandgap, thanks to the Tauc Plot method [117].

2.6.5 *Electrical Characterization*

To analyze the electrical properties of the deposited films, two main measurements were carried. A technique called 4-point probe was used to quickly measure the resistivity of the deposited films. Such technique relies on 4 linearly aligned probes, of which the 2 outer ones create a current to flow through the film, while the voltage is measured with the 2 inner ones. With these measurements, it is possible to calculate a resistance value based on Ohm's law which can then provide a measurement of sheet resistance (R_{sh}) by multiplying by a constant that is determined by the instrument used. Finally, the resistivity of the material can be obtained by the equation:

$$\rho = R_{sh}t, \qquad (1)$$

where t corresponds to the thickness of the layer, which is obtained with XRR or cross-sectional SEM measurements.

Additionally, Hall-Effect measurements were performed to obtain a more precise measurement of the sheet resistance, as well as to calculate the nature of the charge carrier and the charge carrier density (N_d) and mobility (μ) of the film. Hall-Effect measurements rely on the measurement of a Hall Potential (V_H), perpendicular to an electric field applied to the substrate, caused by an external magnetic field applied to a sample in which the Van der Pauw configuration is set, which consists in 4 probes equidistantly placed in the perimeter of the sample (in contrast with the linear-placement 4PP measurements), allowing for a measurement that is independent of the measurement direction. See ref [118] for a description of the Van der Pauw method for resistivity in semiconductors.

The Hall-Effect measurements were made at room temperature with a Van der Pauw configuration in a RH2035 Hall effect measurement setup from Phys Tech, in presence of a magnetic field of 0,43 T.

2.7 Conclusion

In this chapter, the SALD system developed and mounted at LMGP was extensively presented. Its mechanism was explained as well as every part required for a thin film deposition of the desired material, homogeneous along the whole substrate both in its thickness and in its electrical, optical and microstructural properties. Likewise, the modifications to the system were presented and some of the main achievements of this thesis were mentioned. These include a COMSOL Multiphysics® FEM simulation to elucidate the effect of some parameters on the deposition regime of the SALD; the design, fabrication and installation of a monolithic deposition head fabricated with additive manufacturing methods to simplify the assembly and installation and to lower the cost associated with new deposition heads; and the setup of the 3D printing platform at LMGP with two different 3D printing techniques.

Furthermore, the characterization techniques used to study the deposited films were presented. Such characterization included molecular vibration measurements, X-Ray characterizations, electron microscopy characterization, as well as optical and electrical properties characterization.

In the next chapter, we explain in detail the computer simulation tasks performed during the thesis, the considerations taken for the FEM computer simulations in COMSOL Multiphysics®, as well as the capabilities of the simulated model, its results and the perspectives envisioned for computer simulations. We also dive into the phenomena that occurs within the SALD system and we discuss the possibilities to exploit them into innovative deposition processes.

Chapter 3

Numerical Simulations for SALD and Deposition Control: from outlets to substrate

SALD is based in the same physicochemical principles than conventional ALD, but the reactant spatial separation of SALD implies that the control of the film deposition requires the study and optimization of different parameters than in the case of conventional ALD. Such spatial separation, which is key for the SALD, can be achieved in multiple ways, but one of the most cost-effective ways is to work with a deposition head that continuously outputs the reactive gases in different spatial locations, and to displace the substrate from region to region (to mimic the conventional ALD cycles). As mentioned previously, in close-proximity SALD, the deposition should work at a close-proximity to the substrate, creating a gap between these two of around 150 µm. This is the approach used in the LMGP and during this thesis. Such spatial separation of reactants in SALD gives it numerous advantages against temporal ALD but, since the value for the gap needs to be small, to fully achieve a well-controlled deposition, a high mechanical and geometrical precision of the parts of the system and the cyclic movement of the substrate need to be carefully optimized. Additionally, the SALD system at LMGP works at open-air mode, thus, it does not rely on a chamber but rather on the deposition head distributing continuously the gaseous reactants on the surface of the substrate. All these features make the optimization of SALD depositions a challenging task and, to further understand and exploit the benefits of the system, a more detailed study of the SALD and the effect of each part on the deposition mechanism is needed.

It is the objective of the SALD technique to deposit high-quality thin films in a homogeneous, fast, and scalable manner. For this, we consider multiple phenomena happening simultaneously: the concentration extracted from the precursor bubblers, the distribution of the gaseous reactants, the spatial separation of the reactive concentration in each region, the surface reaction at the substrate, and the extraction of by-products and precursor remnants.

In this chapter, the CFD simulations of the SALD system are presented. The simulation was limited to the head-substrate region since this is the most critical part in the system. Comsol Multiphysics® was used to simulate the different phenomena and produce a systematic study of the deposition mechanism to observe the occurrence of a surface chemistry reaction at the surface of the substrate. Since close-proximity SALD allows to tune between CVD and ALD regime, in this work we studied the influence of different parameters on the intermixing of the gaseous reagents to quantify and understand the appearance and threshold between CVD and ALD deposition regime, which are also explained here. The Comsol® simulations are useful as guidelines for a controlled separation of species in the gap, and, therefore, to control the appearance of a CVD component in the deposition. Such type of simulations have indeed been reported in the past [1]-[2] and here, they have been specifically adapted to our system.

Additionally, flow simulations for different geometries of the deposition head in the SALD have been made to ensure a homogeneous deposition and flow at the outlets. The influence on the flow and on the diffusion of reagents was studied for modifications to the geometry of the deposition head, such as the size of the outlets and exhausts. This was made with the idea of decreasing the constraints needed for deposition and lowering complexity and cost of fabrication of the deposition head. These simulations provide guidelines and tolerances on the geometry and on the mechanical design of the system, serving as a guide towards an accurate mechanical design of future versions of the SALD adapted for diverse types and sizes of substrates, making it more versatile and reproducible. The results of the simulations here presented have been published in [119] and, in this chapter, the procedure for such simulations will be further detailed.

Moreover, we demonstrate the capability of controlling the deposition regime to have area-selective deposition with a close-proximity SALD by exploiting the inherent behavior of the deposition head used in the system, and providing experimental results with an experiment called “static deposition” to locally increase the reaction rate in some sections of the deposition gap, which will be explained further.

3.1 CVD vs ALD mode

In order to better understand the effect of the geometry of the deposition head and the deposition gap with the substrate in the deposited films, it is important to understand the main differences between a deposition in CVD regime and one made in ALD regime.

3.1.1 *CVD Deposition*

In a CVD deposition, the reactants are present in the reacting zone simultaneously, which will induce both a surface chemical reaction, due to both chemisorption and thermal activation of the reaction, and, at a lower rate, a gas-phase reaction. At the substrate surface, this CVD reaction will induce a competition among the reactants for the available surface sites. To describe this phenomenon, the Langmuir-Hinshelwood reaction rate equation can be used for surface reactions of each precursor (A and B) with the surface of the substrate:

$$R_{\mathrm{AB}} = \frac{\mathrm{k}_{\mathrm{react}}\mathrm{K}_{\mathrm{A}}\mathrm{K}_{\mathrm{B}}P_{\mathrm{A}}P_{\mathrm{B}}}{(1+\mathrm{K}_{\mathrm{A}}P_{\mathrm{A}}+\mathrm{K}_{\mathrm{B}}P_{\mathrm{B}})}, \tag{3.1}$$

where $\mathrm{k}_{\mathrm{react}}$, K_{A}, and K_{B} are reaction constants corresponding to the reaction that generates the thin film, and to the surface reaction of A and B with the surface, respectively. P_{A} and P_{B} are the partial pressures of each reactant [120]. To express the partial pressure of each reactant in terms of its concentration, we can assume an ideal gas behavior and express them as:

$$P_{\mathrm{A}} = \frac{n_{\mathrm{A}}}{n}P = x_{\mathrm{A}}P \tag{3.2}$$

And:

$$P_{\mathrm{B}} = \frac{n_{\mathrm{B}}}{n}P = x_{\mathrm{B}}P \tag{3.3}$$

where n_{A} and n_{B} are the number of moles of each reactant, n is the total number of moles of the solution and x_{A} and x_{B} are the partial fractions of each reactant. Hence, substituting in **equation 3.1**, we can obtain:

$$R_{\mathrm{AB}} = \frac{\mathrm{k}_{\mathrm{react}}\mathrm{K}_{\mathrm{A}}\mathrm{K}_{\mathrm{B}}x_{\mathrm{A}}x_{\mathrm{B}}P}{\left(\frac{1}{P}+\mathrm{K}_{\mathrm{A}}x_{\mathrm{A}}+\mathrm{K}_{\mathrm{B}}x_{\mathrm{B}}\right)} \tag{3.4}$$

In **equation 3.4**, the surface reaction rate for each reactant (A and B) is considered, as well as a reaction rate that corresponds to the creation of the thin film itself. This equation indicates that the reaction rate is not self-limited and will, therefore, continue as long as there is a non-zero concentration for any reactant. It also implies that if at any point the mass fraction of any of the reactants is zero, the reaction rate will also be zero and hence, no reaction would occur.

A CVD process yields a deposition that lacks the conformality and thickness control present in ALD, but it gives in turn a much faster deposition rate, easier to scale for large area depositions.

3.1.2 *ALD Deposition*

As mentioned at the beginning of this thesis, ALD is in fact a special case of CVD in which the reactants, instead of being present at the same time, they are separated sequentially, for the case of conventional ALD, or spatially, for the case of SALD studied here.

In the case of an ALD deposition, the film deposition occurs in two separated half-reactions on the surface. The amount of each half-reaction is limited to the surface sites available on the surface; this is the so-called self-limited characteristic inherent to an ALD deposition. In SALD, if we assume a total separation of the reactants, regardless of the residence time of the substrate in each reactant region (provided it is long enough), the concentration of chemisorbed reactant molecules in the surface should saturate the number of available reaction sites. The surface coverage (θ) can be explained with the Langmuir isotherm:

$$\theta = \frac{k_{ads}P}{k_{des} + k_{ads}P} = \frac{(\text{number of occupied sites})}{(\text{total number of sites})};\ 0 \le \theta \le 1 \qquad (3.5)$$

where k_{ads} and k_{des} represent the rate of adsorption/desorption of the reactant to/from the surface, respectively, and P is the precursor partial pressure [120].

In addition, the reaction probability depends on the calculated surface coverage, since, as more sites are occupied, the sticking probability β of a reactant diminishes:

$$\beta = \beta_0(1 - \theta) \qquad (3.6)$$

where β_0 is the "bare reaction probability" given by the intrinsic properties of the reactant. The saturation time of the available sites is then inversely proportional to the precursor partial pressure and to β_0 [80].

ALD deposition has extended its applications thanks to the advantages it provides in comparison to CVD: lower deposition temperatures, high-density films, conformal deposition in large aspect ratio geometries (suitable for nanofabrication) and precise control of thickness by controlling the number of cycles performed. Nevertheless, ALD is also well-known for the lack of scalability it provides due to the slow deposition rates achieved, the complexity for large area depositions and, for some systems, the vacuum in the reactor.

3.1.3 *Controlling of deposition regime in the SALD*

Considering both ends of the spectrum –CVD vs ALD deposition regime–, it is the purpose of the simulations here presented to understand where our SALD system is located, as well as how to control the depositions towards each of these regimes to obtain the most adequate deposition condition for the application in mind. Towards this end, one of the most influencing parameters in our close-proximity SALD is the gap between the deposition head and the substrate. Controlling the deposition gap can increase the flexibility of our SALD system, allowing the user to tune the process of deposition and the properties of the deposited film. Furthermore, this flexibility can be exploited in innovative ways since it may provide a versatility to tune the regime [121].

To understand the transition between CVD and ALD regime caused by a simple change in the deposition gap, the phenomena present in our SALD was introduced to Comsol® in a 2D simulation.

3.2 Finite Element Method and Multiphysics Simulations in the SALD System

Finite Element Method is a computational technique to solve equations in a defined system, which is divided in small parts called finite elements, using computer geometrical calculations, in a process called “meshing”. Known physics equations are then solved in every finite element to calculate the desired quantity and finally assembled into the original geometry to model the entire system. FEM simulations are widely used in science and engineering to model phenomena that would be infeasible to model analytically, and they provide the capability of optimizing a system even before prototyping.

Comsol Multiphysics® is a FEM simulation software that is oriented to couple different physical equations in the same system, allowing for a model that better approximates the real behavior of the phenomena. In the case of our SALD system, FEM simulations with Comsol Multiphysics® allowed us to better understand the flow, precursor concentration diffusion, and surface reaction to elucidate the transition between CVD and ALD mode.

3.2.1 *Introduction of SALD phenomena to a multiphysics simulation*

For the introduction of the SALD system phenomena into Comsol®, a 2D geometry corresponding to the cross-section of the deposition head architecture used in the beginning of this thesis (fig 6 in chapter 1) was created and introduced into the software.

Since the objective of the simulation is to understand the transition between CVD and ALD deposition regime, we need to understand the influence of the architecture of the deposition head, along with the close-proximity used, on the diffusion mechanisms of the reactants on the carrier gas. For this, a CFD is used to calculate the streamlines that the gaseous fluid follows during deposition. To this flow simulation, certain concentration of species is introduced, which may be transported along the surface of the substrate via diffusive (due to a difference of concentration) and convective transport (due to the velocity field the carrier gas has). In parallel, the kinetics of a CVD reaction between both precursors used is calculated, which is then used to calculate a surface reaction at the surface of the substrate. The physics behind each part will be explained in next sections.

3.2.2 *Explanation of the physics governing the phenomena of SALD*

3.2.2.1 Computational Fluid Dynamics: velocity and pressure of gaseous flow

CFD simulations are based on the Navier-Stokes equation and small variations of it. The Navier-Stokes equation is presented in **equation 3.7**,

$$\rho\left(\frac{\partial u}{\partial t}+u\cdot\nabla u\right)= -\nabla P+\mu\nabla^2, \tag{3. 7}$$

where u is the velocity of the flow, P is the pressure, ρ is the density of the fluid, μ is its dynamic viscosity, and ∇ is the gradient operator. The Navier-Stokes equation describes the motion of viscous fluids as a balance of pressure and viscous forces with the velocity of motion of the fluid. The solution of the equation yields the velocity of the fluid, which can then be used to calculate the pressure.

The Navier-Stokes equation can be generalized for incompressible flows, in which the divergence of velocity can be neglected ($\nabla\cdot v = 0$). This is a fair assumption even for a compressible fluid (such as gases) when working at very low Mach number, i.e. the ratio between the velocity of the flow and the sound of speed in the same medium, which is the case of the system here presented.

Another quantity important to choose the simulation model is the Reynolds Number (Re). The Reynolds number is dimensionless and represents the ratio between inertial versus viscous forces in the fluid and predicts its flow pattern. The Reynolds number can be calculated as seen in **equation 3.8**:

$$Re = \frac{uL}{\nu}, \tag{3. 8}$$

where ν is the kinematic viscosity of the fluid and L is the characteristic linear dimension of the path of the flow. In the case of the SALD system with the dimensions of the deposited head and a value of a gaseous inflow of carrier gas of $\sim$2000 sccm (which corresponds to the maximum value achievable by our gas panel), the Re is of $\sim$1, which corresponds to a value close to the limit for linear flow. Given that this number is close to the limit and that subtle sudden changes of the flow, such as the impact of the flow towards the substrate, may induce turbulence, the low-Re turbulent model provided by Comsol® was chosen for the simulation.

The solution of this section of the simulation is a velocity vector and a pressure magnitude at each point of the meshed geometry. With this information, the flow can be visualized as a 2D color map and/or as stream lines showing the path followed by the fluid.

3.2.2.2 Diffusion of concentrated species within the gaseous flow

With the velocity field calculated, we use mass transport equations to determine how the concentration of reactants is transported with the carrier gas. For this, Comsol® uses the well-known convection-diffusion equation:

$$\frac{\partial c}{\partial t} = \nabla \cdot (D\nabla c) - \nabla \cdot (uc) + R, \tag{3. 9}$$

where D is the diffusion coefficient of the diluted species, u is the velocity field of the flow, which in our simulation is calculated with the previously mentioned Navier-Stokes equation, c is the concentration of the species and the variable of interest, and R represents external sources of the concentration measured. With this equation we calculate the concentration at each point of the geometry simulated, caused by a diffusion of the concentration and by the convection created by the flow. The diffusion coefficient used for the reactants was in the order of magnitude of 10^{-5} m^2s^{-1}, which is the order of magnitude of diffusion of gas phase elements. [122]

3.2.2.3 Chemical Kinetics in Surface: film deposited in CVD regime

The chemical module in Comsol® calculates a concentration created as a product of a chemical reaction with certain reaction constant in a zero-dimensional space, i.e. a single point. In the simulation created for this thesis, such chemical reaction happens at the surface of the substrate and is used to calculate the concentration deposited as a consequence of the existence of a CVD regime. For this, the reaction rate shown in **equation 3.4** is used as a CVD reaction rate which, to recall, depends on the concentration of the reactants, and which will be zero if any concentration of the two reactants is zero. Hence, with this surfacic chemical reaction the concentration generated by a CVD chemical reaction can be calculated. If in the SALD system simulated, the separation of reagents is perfect, no CVD-deposited concentration should appear. Therefore, the concentration calculated in this last step is a direct indication of intermixing of species and, thus, of the existence of a CVD component in the deposition process.

3.2.3 *Architecture and geometry of SALD*

Once we have a coupled simulation in which we have calculated the vector flow, the concentration at each point of the flow (caused by the convection and diffusion of the reagents), and the chemical deposited concentration at the surface of the substrate (caused by a CVD regime), we can study the geometry of the reaction space (i.e. the gap and the deposition head) in the simulation, to observe their influence in the tuning of the appearance of a CVD component in the system.

As explained in Chapter 2, the deposition head contains 2 metallic precursor outlets, 3 oxidant reactants, 6 inert gas barrier outlets and 11 exhausts slits. The velocities used are fixed to values that are used experimentally in the SALD system: 300 sccm for the metallic precursor, 450 sccm for the oxidant, and 900 sccm for the inert gas barrier, which translates to a 125 sccm output per slit. The temperature of the substrate was set to 200 °C for the simulation. This temperature is taken into account for the surface chemical reaction, and no effect of this temperature on the fluid flows in the system is considered. These values were chosen to keep the parameters as close to the real deposition conditions as possible [94].

Regarding the geometry created by the deposition head and its separation to the substrate (the deposition gap), the initial dimensions were also taken from the deposition head used in the SALD system at LMGP: 0.5 mm for each outlet slit, as well as for the exhaust slit, all separated between each other by 0.5 mm. The simulated geometry is in fact a 2D shape corresponding to the cross-section of the deposition head. **Figure 3-1** shows a schematic of the deposition head with its outlets and exhausts, as well as the geometry used for the simulations here presented. In **Figure 3-1-a**, the letter I corresponds to the inert gas barrier, E corresponds to the exhaust slits, OP (in red) corresponds to the oxidant outlet, and MP (in blue) corresponds to the metallic precursor.

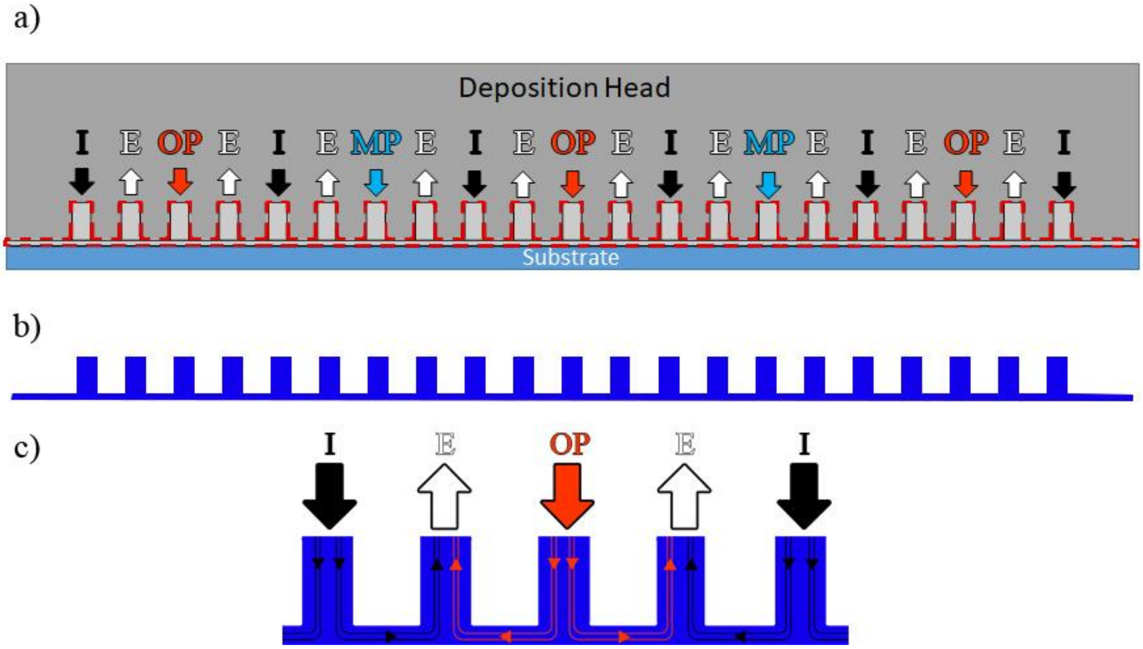

*Figure 3-1. (**a**) Schematic of the cross-section of the deposition head in the Spatial Atomic Layer Deposition (SALD) system at the Laboratoire des Matériaux et du Génie Physique (LMGP). The gray section represents the deposition head on the system, while the blue section below represents a substrate. These two are separated by a space that corresponds to the deposition gap. (**b**) Equivalent geometry used for simulations used to compute all the phenomena in SALD regarding flows, concentrations, and reactions. (**c**) Close-up to the region of the OP, showing the expected flow lines and directions of the gaseous mixture of the SALD. In*

the figure, the inert gas flow is represented with the letter I, the metallic and oxidant precursors are represented with the letters MP and OP, respectively, and the exhaust flow is represented with the letter E.

3.2.4 *Simulations and parameter considerations*

Finally, before discussing the results of the simulations, it is important to define the boundary conditions of the system and other considerations to take into account.

In the case of the CFD simulations, we consider inlets on the superior line of the corresponding gas outlet. The gas can flow freely along all geometry. The exhaust boundary condition, also placed on the superior line of the corresponding slit, is defined as atmospheric pressure, since in the SALD system, no extraction system is installed, and the outflow of gases happens due to the confinement within the gap (pumping could be implemented and simulated if necessary). On the lateral sides of the gap, also an atmospheric pressure is defined. The inferior line of the section defining the gap, corresponding to the surface of the substrate, is defined with a "slip" condition, which defines the normal velocity equal to zero, but the tangential velocity is non-zero. This was chosen to take into account the lateral diffusion of the concentration along the substrate surface. All other boundaries are defined as no-slip, where both normal and tangential velocities equal zero, and which is a common boundary condition in fluid simulations.

For the concentration, we use the mass fraction of concentration of each reactant. We define a mass fraction of reactant A equal to 1 and reactant B equal to zero in an outlet where reactant A is output. We do the inverse for an outlet where reactant B is output. We define as well both concentrations of reactant A and B equal to zero, where the inert gas barrier is output. Finally, the same lines used as exhausts boundary condition in the CFD section are used as an outflow of concentration.

The whole system is simulated only on one half of the system, with a symmetry condition at the line that divides the system, to simulate the whole system. This was done to reduce the computation time of the simulations.

Finally, it is shown below that the intermixing of reagents is not strongly affected by the movement of the substrate at the velocities used during a film deposition. For the simulations in which the velocity of the substrate is zero, i.e. a static substrate is considered, the deposition is said to be in "static mode". Even though the velocity of the substrate does not affect the intermixing of species, it does affect the effective size of the region with reagent concentration, modifying, along with the speed of the movement, the residence time of the substrate in each region. This will be explained below.

3.3 Results of Simulations

3.3.1 *Velocity Profile of the Gaseous Flows*

Figure 3-2 shows the velocity profile computed by the CFD simulation in which the gap was fixed at 150 µm. The velocity profile shows the expected flow from the inlets of gases to the exhausts. In the lateral sides of the gap, where we have a condition of atmospheric pressure, it is possible to see that the value of the velocity is not zero, indicating some amount of gas exiting laterally from the gap. This could indicate that the gap is not perfectly confined, although it remains to be seen if any concentration of reactants exits as well, or if only inert gas does. Nevertheless, it is an interesting first observations for future designs of deposition heads if confinement of the gases is needed; e.g. for isolation avoiding the in-diffusion of humidity or oxygen from the atmosphere around the reactor, for example.

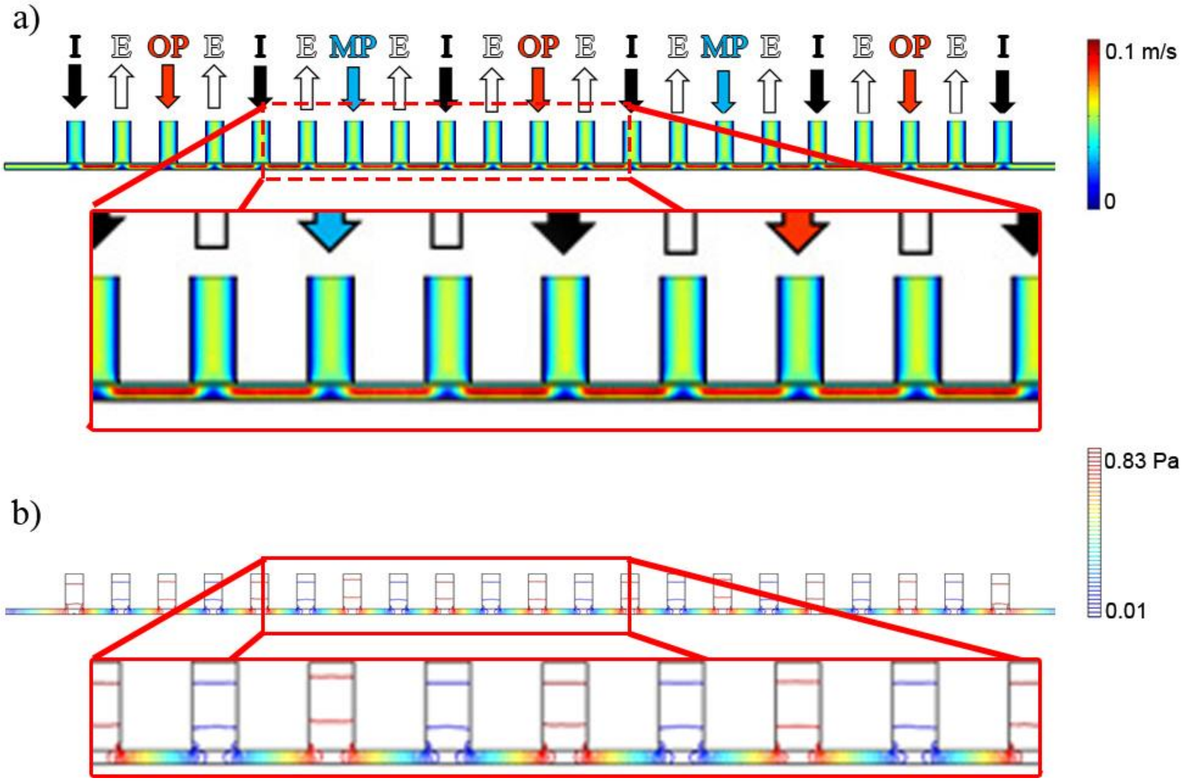

__Figure 3-2__ Computational Fluid Dynamics calculation made with Comsol Multiphysics® to represent the flow of the region of interest in the SALD geometry: (__a__) The gas velocity increases in the deposition gap, given the close-proximity, and (__b__) the pressure increases under each of the outlets as it enters the deposition gap.

The maximum value of gas velocity is around 0.1 m/s at the narrowest path on the flow, shown in **Figure 3-2a**. At the same place, we can observe in **Figure 3-2b** that the pressure is the highest just at the corners of the gas outlets, causing a pressure gradient from the gas outlets to the exhausts, hence, directing the flow towards the exhaust ports. This is beneficial for our system since the pressure gradient increases convective flow towards the exhausts, overwhelming the diffusion transport of the reagent concentration in the gap. In our system, this occurs contrary to previously published results by Pan et al. [123] where it is mentioned that at smaller gaps, more intermixing occurs. The main difference in our system, though, is the fact that we work at atmospheric pressure, whereas Pan et al. work at low pressure (∼10^{-1} Torr). The lower pressure in the system enhances diffusive processes, causing that, at small gap values, the high velocity values of the speed increase the diffusion, along with the convection, thus increasing intermixing of species. For this reason, working at atmospheric pressure is indeed desirable to prevent gas intermixing caused by high velocities, achieving a better spatial gaseous separation.

3.3.2 *Concentration Distribution of Gaseous Reactants in the Gap*

Once we have a flow profile, we introduce the mentioned "concentrated species", corresponding to the concentration of the reactants is our SALD, which is estimated using the vapor pressure of DEZ [124], and considering this value as the concentration extracted from the bubbler. Afterwards, some parameters are modified to observe their influence on the surface reaction created as a consequence of a CVD-regime.

3.3.2.1 Effect on Gap

In **Figure 3-3**, the difference in reactant concentration between simulations performed with a gap of 150 µm and 750 µm is shown. The linear graph corresponds to a plot of the mass fraction of each reactant on the surface of the substrate. Here, only the precursor concentration in the carrier gas is calculated. The lower 2D graph corresponds to the concentration along the whole simulated geometry. Finally, the close-up shows one precursor outlet, the exhausts and the inert gas barriers that surround it. In the 2D plot, the color red corresponds to the mass fraction of reactant. Note that there is no distinction on color between metallic precursor and the oxidant agent in the 2D plots.

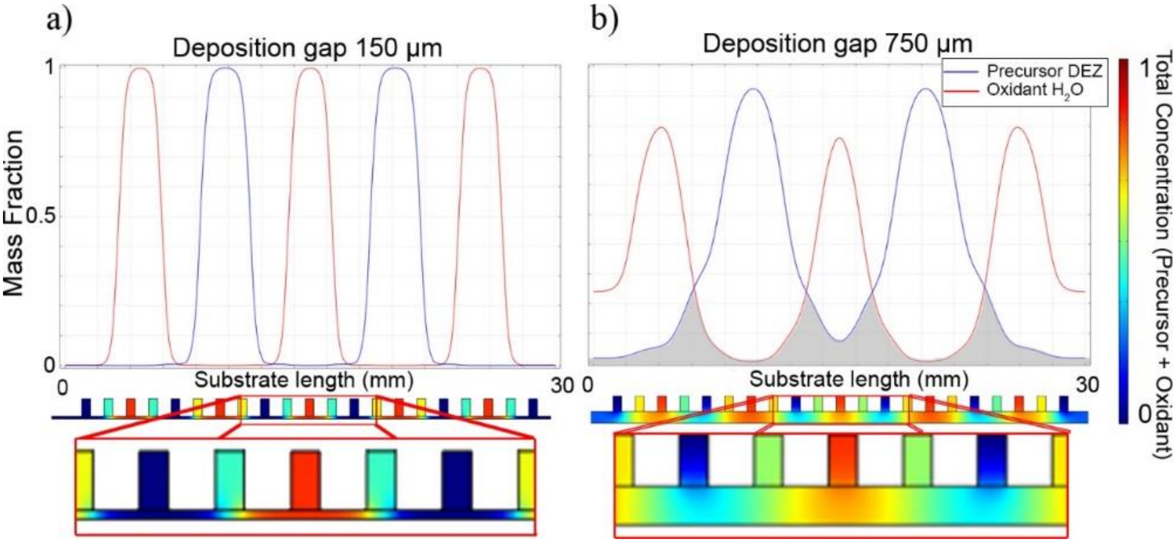

Figure 3-3 *Reactant concentration plot along the immediate region above the substrate for a deposition gap of (a) 150 μm and (b) 750 μm. Under each plot, a 2D plot along the whole geometry of the gap is shown, with a color code that corresponds to the concentration of reactants along the whole gap geometry. They gray-shadowed regions represent the overlapping zones of the two reactants*

In the case of a value of a gap of 150 μm (**Figure 3-3a**), it is possible to see that the concentration is well confined, evidenced by the blue color under each nitrogen outlet. The exhausts contain some amount of precursor concentration mainly diluted and carried by the inert gas in the gas barrier outlet. In this value of gap, the concentration is considered well confined, which means that an ALD-regime is the main growth mechanism for the film deposited. In the other hand, when the gap increases to 750 μm, the concentrated zones (red color) become less confined, making the region just under the nitrogen outlets to have a non-zero concentration, evidenced by the light-blue color on the 2D map. The linear graphs show the concentration on the surface of the substrate, where the amount of “overlap” between the plots of each precursor is indicated by the gray region in **Figure 3-3**.

In order to quantify the overlap for each deposition gap value, we calculated the ratio between the area under the curve of the overlap (where both reactants are present at the same time represented by the gray region in **Figure 3-3**) and the area under the curve of the sum of both concentrations, yielding what we call a “percentage of overlap”.

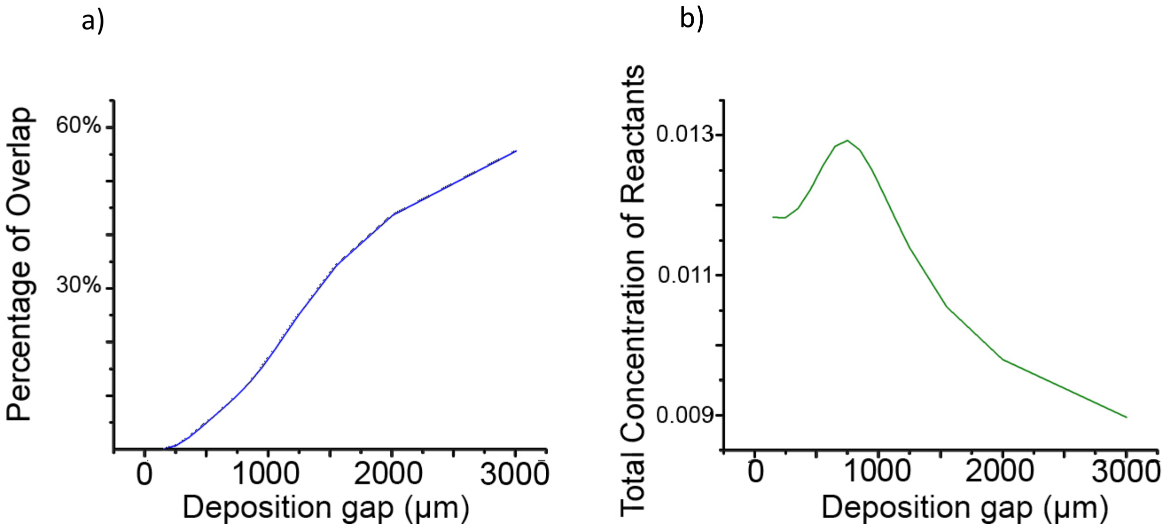

***Figure 3-4**. (**a**) the percentage of overlap, i.e., the percentage in which there exist both co-reactants at the same time, creating thus a CVD regime reaction on the surface of the substrate. (**b**) The total concentration of all the gases (both separated and overlapped) at the immediate area above the substrate vs. head-surface deposition gap.*

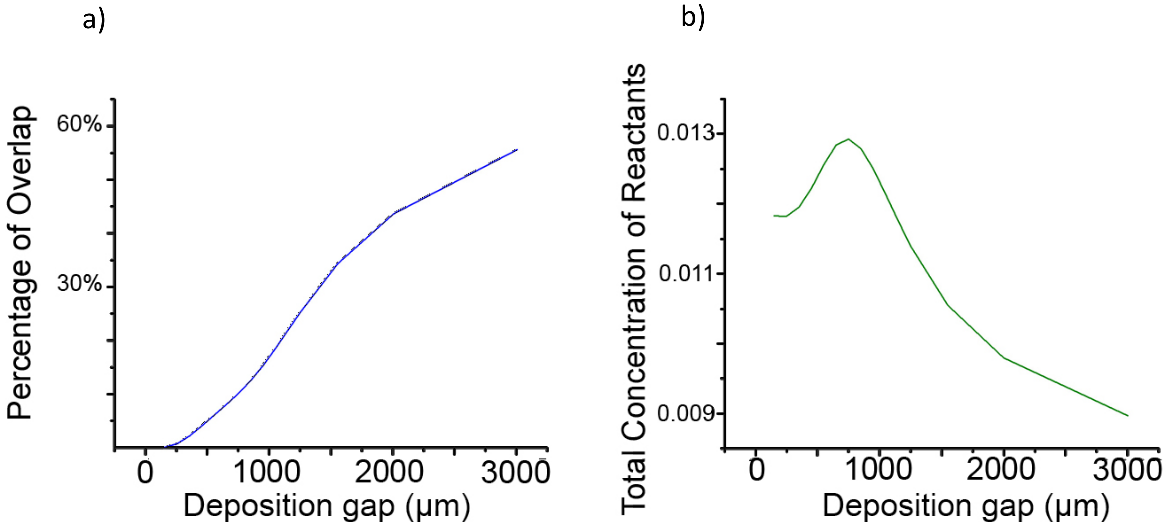

Figure 3-4a shows that, as the gap value increases, the percentage of overlap increases as well. In addition, a change of slope on the growth of the percentage of overlap at a value of around

750 µm is observed. This effect can be explained by looking at the graph in

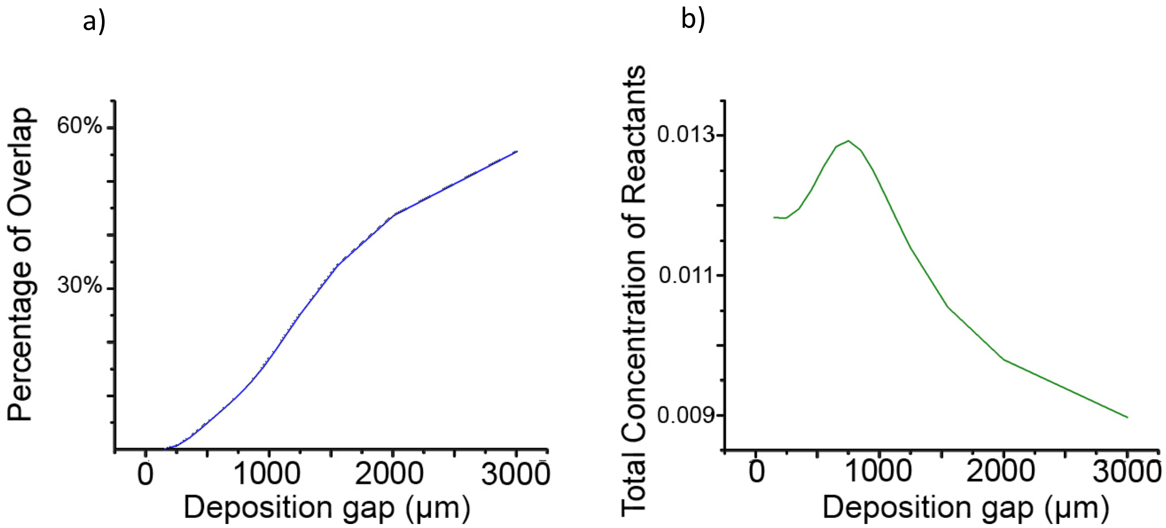

Figure 3-4b, which shows the total concentration of all reactants in the immediate region above the surface of the substrate, as measured by integrating the sum of the concentration of both reactants on the surface of the substrate. For deposition gap levels smaller than 750 µm, the total concentration of reactants above the surface increases. At a value of 750 µm, the plot shows a maximum level. As the deposition gap value increases even further above 750 µm, the plot decreases again.

To explain this, let us remember that the gaseous reactants, besides being directed towards the exhausts slits, they can be directed towards the lateral sides of the system, where there is also atmospheric pressure. Hence, it seems that, as the gap is narrowed, the velocities have a higher component in the parallel direction to the substrate than in the direction perpendicular to it. The former guides the reagents towards the lateral sides of the system, while the latter guides them towards the exhausts. Hence, if the gap is too narrow, the pressure of the system tends to direct the gaseous reactants to the lateral sides; if the gap is too wide, the reactants are also preferentially directed to the sides since their size is also defined by the gap. At a value of 750 µm, the gap is small enough to maintain the reactive gases above the substrate, and it is also not too small to force them towards the lateral outflow.

3.3.3 *Intermixing of Precursors in the Gap*

Once the concentration distribution along the gap is calculated, a surface reaction of the form:

$$\mathrm{DEZ} + \mathrm{H_2O} \xrightarrow{R_{\mathrm{AB}}} \mathrm{CVD\ adsorbed\ film}\,, \qquad (3.10)$$

is calculated with a reaction constant R_{AB} (**equation 3.4**), and using a value for $\mathrm{k_{react}}$ of 10^{-5} $\mathrm{mol \cdot s \cdot kg^{-1} \cdot m^{-1}}$ obtained in reference [120].

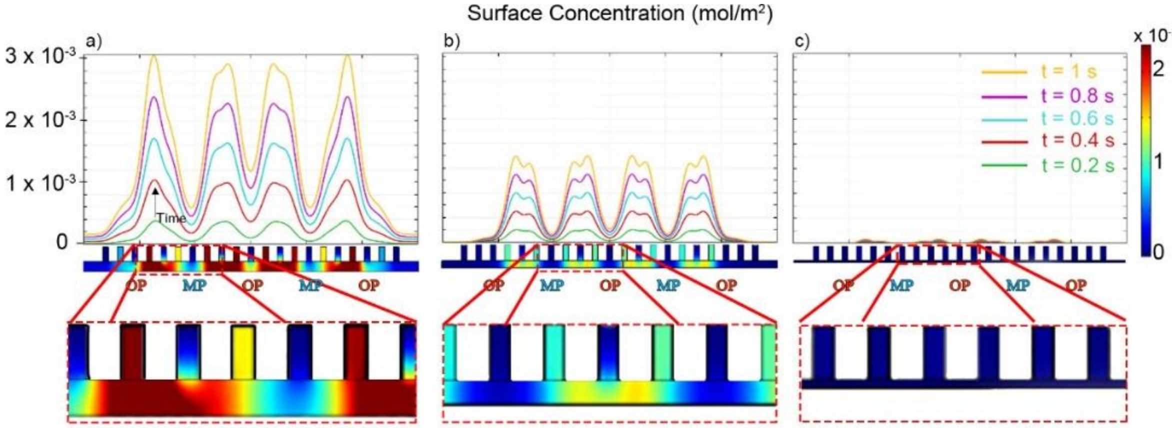

__Figure 3-5__ Results of the CVD surface reaction on the substrate calculated with a time-dependent multiphysics simulation. The plots shown correspond to the surface reaction that results from different gaps. Under each plot, a surface plot of the CVD reaction rate that corresponds to the plot directly above is shown, with OP and MP representing the outlets of the reactants; (__a__) deposition gap of 750 µm, (__b__) deposition gap of 425 µm, and (__c__) deposition gap of 150 µm.

Figure 3-5 shows the result of a simulation for a surface reaction on the surface of the substrate as a function of time up to 1 second. The plots correspond to the surface concentration of the film created due to the presence of a CVD regime in mol·m^{-2} for gap values of 750 µm, 425 µm and 150 µm. Under each plot, a 2D map of the reaction rate R_{AB} is shown for each case. As observed in previous simulations, as the deposition gap increases, the diffusion of reactants presents more “overlap” of reagent concentration, evidenced by the higher reaction rate in certain areas, and leading to a higher CVD component. This in turn yields higher surface concentration as the gap is increased. It is interesting to observe that even when the gap has a value of 150 µm, although relatively smaller compared to the other two cases, a CVD component is still present. Nevertheless, at this gap values, ALD is the primary deposition regime, making the CVD component negligible, as observed in experimental depositions. [1],[7]

To experimentally observe the appearance of the CVD regime with a simple change in gap, depositions of ZnO were made at different values of the gap for the same number of cycles. **Figure 3-6** shows experimental characterizations as evidence of the ability to modify the growth regime in our SALD system. **Figure 3-6a** shows the increase of growth rate per cycle (GPC) as the gap value increases. The values for GPC of ~0.25 nm/cycle for a gap of 150 µm are in accordance with those reported for a self-limited (ALD) growth of ZnO [125]–[127]. The increase of the growth per cycle (GPC) with the gap value confirms the transition from an ALD regime (with small gap values) to a CVD regime (with higher gap values). **Figure 6b** shows the XRD spectra of ZnO films grown with different gap values for the same number of cycles. The peaks correspond to those of crystalline ZnO and one can observe that, as the gap value increases, the intensity of the peaks increases as well, indicating that thicker films are obtained in the same deposition time as the gap is increased.

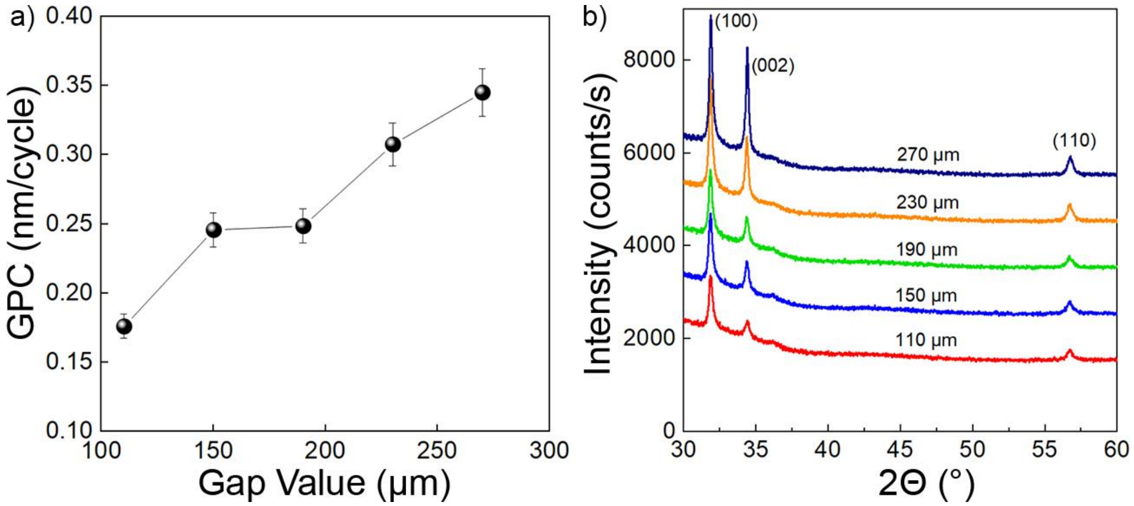

***Figure 3-6**. Experimental results for a deposition of ZnO using di-ethyl zinc (DEZ) and water as co-reactants. (a) Growth per cycle (GPC) evolution with different gap values. (b) X-Ray diffraction patterns for ZnO films grown on glass with different gap values indicated in labels, showing the crystalline peaks corresponding to wurzite ZnO (ICSD #82028). The data for these plots comes from the work performed at LMGP and reported by V. Nguyen [116].*

3.3.3.1 Exhaust Efficiency

In the geometry of our SALD deposition head, although the exhaust of the gas flow consists on an outlet at atmospheric pressure and not a forced exhausts (by e.g. a vacuum pump), it is assumed that gas flow will be directed towards the exhausts pushed/carried by the pressure created by the flow and the close-proximity gap, and that all surplus of reactant concentration is also exhausted properly. As mentioned before, the gaseous spatial separation strongly relies on a well exhausted system where all remnants of the surface chemical reaction are evacuated properly. To ensure this on our SALD system, the exhaust outlets in the deposition head must be sufficiently large in comparison with gas reactant outlet so that the outflow rate is larger or equal than the inflow of reagents. Failure to achieve this either intentionally (by changing the design of the deposition head) or unintentionally (e.g. due to a partial or total blockage of the exhaust slits) may induce a CVD regime even with a small deposition gap.

To quantify how efficient a deposition head is to exhaust gaseous reagents, we define an exhaust efficiency as the efficiency in which the incoming gaseous reactants and by-products are extracted from the reaction zone. Here, such efficiency is calculated by the ratio between the cross-sectional area of the exhaust slits, and that of the gaseous outlets. An ideal ratio would be achieved by a system where the exhaust and the outlet have the same cross-sectional area, allowing for an unhindered flow towards the exhaust slits. In this case, we consider an exhaust efficiency of 100%.

A high exhaust efficiency may be achieved by a properly designed outlet/exhaust area ratio, or, if the geometry requires slits to be smaller, by e.g. properly applying a pumping force in the exhausts, inducing a higher velocity in the exhausts and, thus, the same mass flow through such smaller area. In this thesis, however, we employed a geometrical design to control such efficiency and illustrate the effect of exhaust efficiency.

In the case of the deposition head used in our SALD system, the cross-sectional area of the exhaust slits and of the gaseous outlets are calculated with the shape of the corresponding outlet or slit, shown in **Figure 3-7c**, where the exhaust efficiency is calculated as the ratio between the total area available for exhaust (green area) and the total area available for gas outlet (red area). In the case of the Comsol® simulation, the ratio is controlled by controlling the size between the exhausts and inlet lines, shown in **Figure 3-7a and b**, where the exhaust efficiency is calculated as the ratio between the total length available for exhaust (green line) and the total length available for gas outlet (red line).

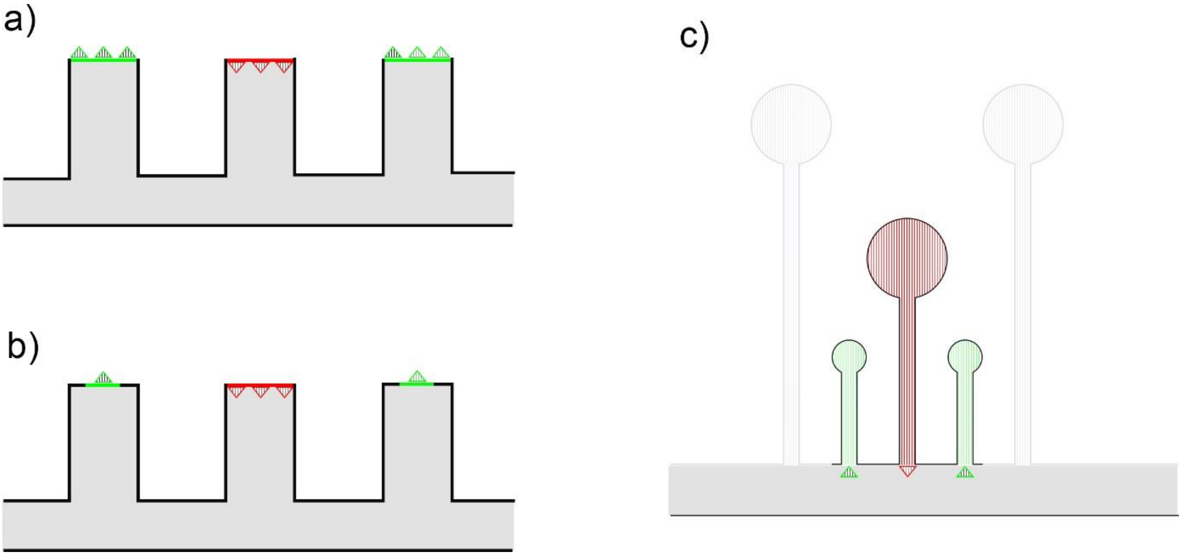

Figure 3-7. Schematic showing the geometry used for the calculation of the exhaust efficiency for the Comsol simulated geometry with a 100% exhaust efficiency (a), a 50 % exhaust efficiency (b), and for the SALD deposition head cross sectional area (c).

Figure 3-8 shows the concentration of the reagents on the surface of the substrate, as well as a 120 second simulation of the surface concentration appearing as a consequence of a CVD-regime; i.e. as a consequence of a gaseous reagent intermixing. In the simulation, the gap was fixed at 150 µm.

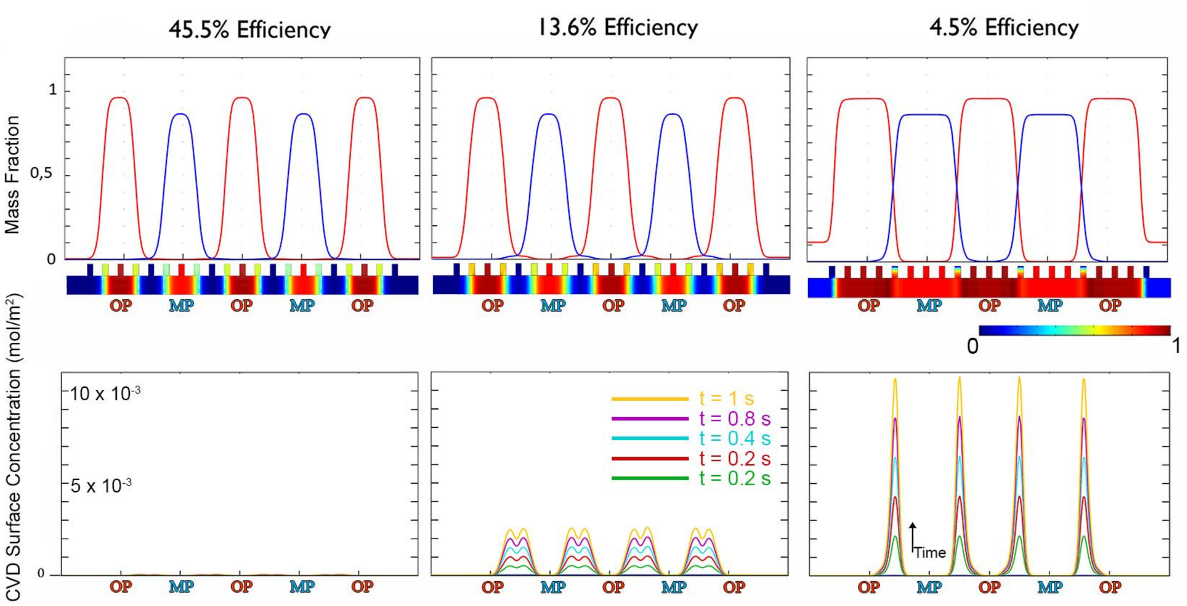

Figure 3-8 CVD regime deposition with different exhaust efficiencies. The exhaust efficiency has a drastic influence on the appearance of CVD regime: with an exhaust efficiency of ~45%, almost no appearance of CVD regime can be observed, at ~13% CVD regime appears in some regions, and at ~4% CVD regime is more pronounced and more localized.

It is possible to see that, as the exhaust efficiency decreases, there is more diffusion of the reactant concentrations, even when the deposition gap is at a "close-proximity" of 150 µm. Interestingly, the diffusion of reactant concentrations has a different behavior in this compared with the case of an increase of the deposition gap: as the exhaust efficiency decreases, the CVD reaction rate appears to be highly localized. This leads to a localized deposition in the CVD regime, and with time, four overlapped regions appear in localized points over the substrate. To try to elucidate what happens when the exhaust efficiency is low, **Figure 3-9** shows the CVD reaction rate calculated along all the gap for the case of an exhaust efficiency of 4.5% presented previously in **Figure 3-8**. **Figure 3-9a** shows the 2D plot of the reaction rate on the gap, i.e. the plot that shows the amount of intermixing of the gaseous reactants. This plot shows that there is indeed intermixing all along the gap, but there are 4 points in which the reaction rate calculated is significantly higher. **Figure 3-9b** shows the reaction rate at the surface of the substrate. Here it is possible to see that, at the difference between the peak and the valley of the plot is around 1 order of magnitude.

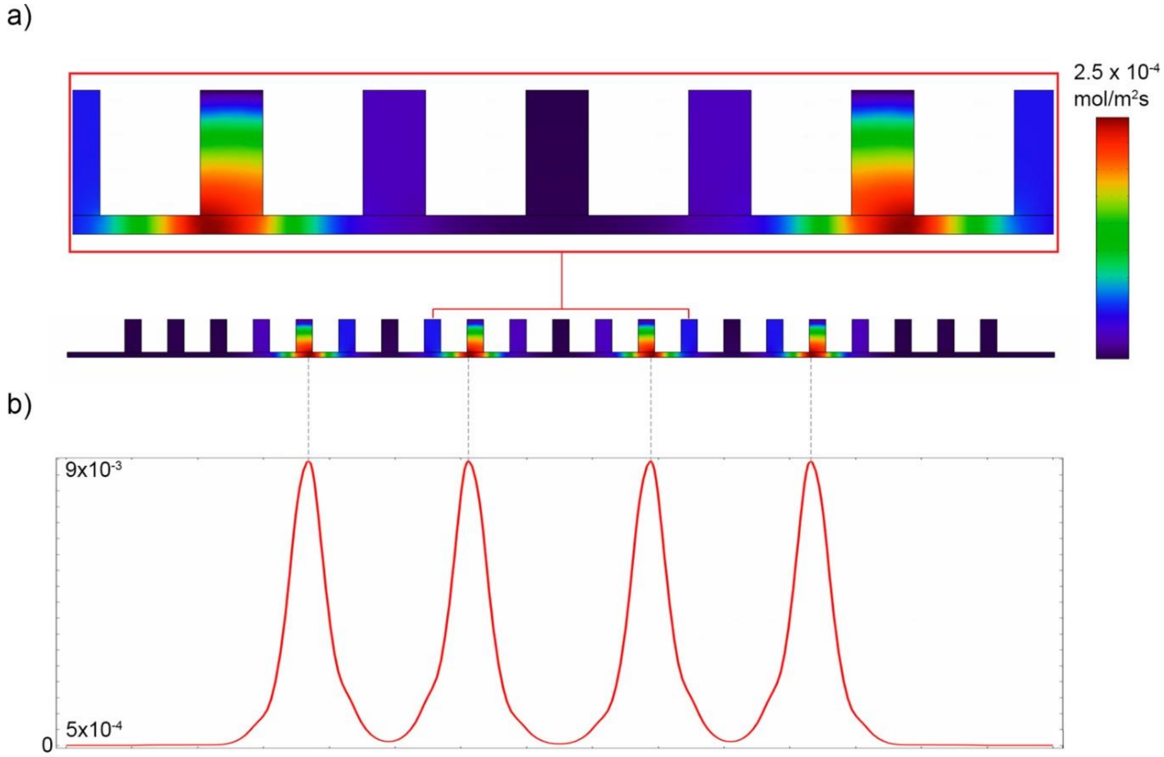

***Figure 3-9**. a) 2D plot of the CVD reaction rate calculated by the Multiphysics simulation. b) linear plot of the CVD reaction rate calculated at the surface of the substrate.*

To verify and understand how the SALD deposition head is performing, an experimental “static mode” deposition was performed. For this, the deposition head was placed at 150 µm and all flows —precursor, oxidant and separation nitrogen— were injected as usual, using 250 sccm, 400 sccm and 750 sccm, respectively. The substrate was not oscillated, which meant that, if any deposition occurred, that would be evidence of the appearance of a CVD component.

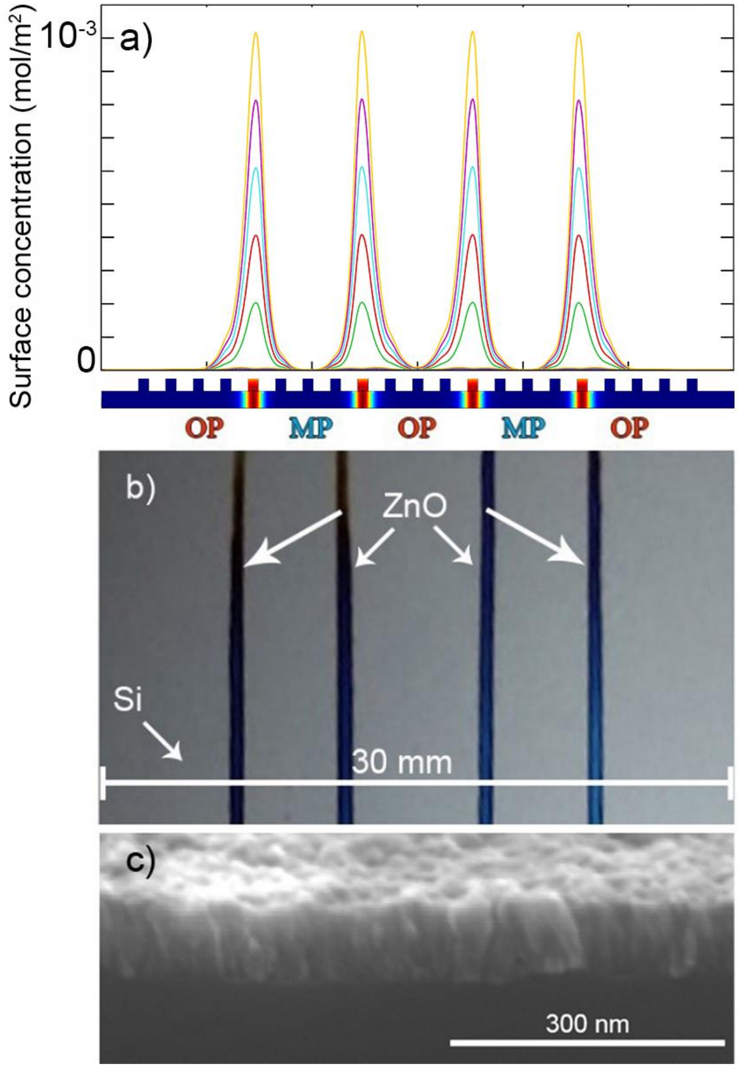

Figure 3-10 *Simulation and experimental result of a static deposition experiment made with the SALD set-up at LMGP: (**a**) CVD deposition simulated for an exhaust efficiency of ~4% shown previously in **Figure 3-8**, and (**b**) optical photography of the pattern obtained after performing an experimental "static deposition" on a Si substrate with DEZ and* H_2O*. (**c**) Scanning electron microscope (SEM) cross-section image showing a ZnO thickness of ~75 nm for one of the lines in the pattern obtained after a 30 s long "static deposition".*

Figure 3-10 shows a "static mode" deposition performed with DEZ as the precursor and water as the oxidant reagent on a silicon substrate for 30 seconds. The measurement shown in **Figure 3-10a** corresponds to the width of the deposition head. Finally, **Figure 3-10c** shows a SEM cross-section image of one of the ZnO lines deposited with the "static mode" experiment. As shown in **Figure 3-10b**, the experimental static mode deposition yields 4 well-defined ZnO lines. This corresponds to the simulated CVD-regime surface concentration performed previously, and shown for easy comparison as well in **Figure 3-10a.** This result would indicate that there is indeed a lack of exhaust in the deposition head. To explain this behavior, we calculated an exhaust/outlet ratio on the physical exhaust slits and gas outlets on the deposition of 10.1%, with the method shown in **Figure 3-7c**. With this value, a simulation was made for an exhaust efficiency of 10% to observe if such localized deposition also occurs. **Figure 3-11** shows that the localized deposition occurs as well for a 10% exhaust efficiency, validating once more the results observed in the experimental static mode deposition.

Furthermore, the depositions obtained in the static mode deposition present an interesting perspective that may be exploited for area selective deposition of materials. If the deposition head presents a low exhaust efficiency, either intentionally or unintentionally, the reaction rate can be increased locally and generate area selective deposition. Therefore, it can be envisaged that, with the correct value of exhaust efficiency and geometry of the deposition head, different patterns can be obtained by locally increasing the reaction rate only in the desired zones. If achieved, this would be a cost-efficient and simple approach to area selective deposition of materials.

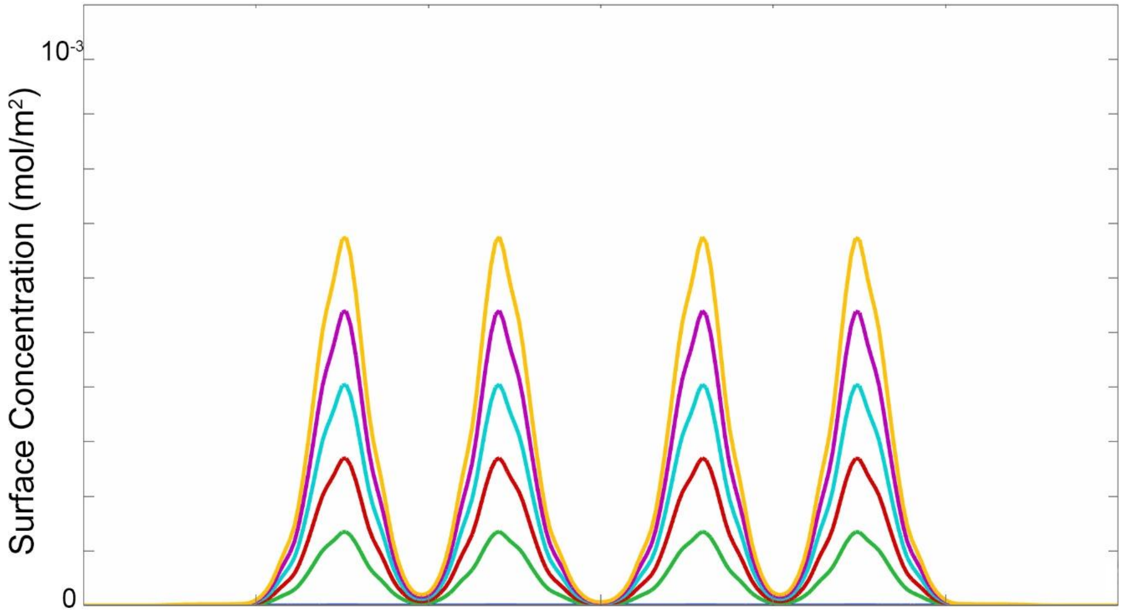

***Figure 3-11**. Surface concentration of a CVD regime deposition for an exhaust efficiency of 10%, corresponding to the exhaust efficiency measured in the deposition head in our SALD system.*

On the other hand, to improve the behavior of the deposition head, we envision either an improvement of the geometry of the deposition head or an induced outflow in the exhausts, i.e. pump in the exhausts, although it will be important to make sure the pump allows for the precursors to interact with the substrate during a long enough time to allow for a surface reaction. In this thesis the effect of a pumping force in the exhaust was, unfortunately, not explored due to the complexity it added both to the SALD system and to the FEM simulation. So, to improve the behavior of the deposition head, here, we study the geometrical approach.

3.4 Tilt and parallelism

Up to now, we have simulated a gap in which the deposition head is perfectly parallel to the substrate surface. Frequently, the alignment of the head is not perfect since our system relies on manual alignment of the deposition head. Hence, the CVD surface reaction simulation was used to assess the influence of a tilt between the substrate and the deposition head. In this case, to simplify the geometry creation, the substrate was chosen as the tilted section, nevertheless, this would be equivalent if the deposition head is the one titled. Since our SALD system uses a "close-proximity" approach where the deposition gap was set to be 150 µm, a slight mis-alignment (a rotation with respect to the deposition head) of 0.3° was created in the substrate, taking as rotation point the mid-point of the substrate.

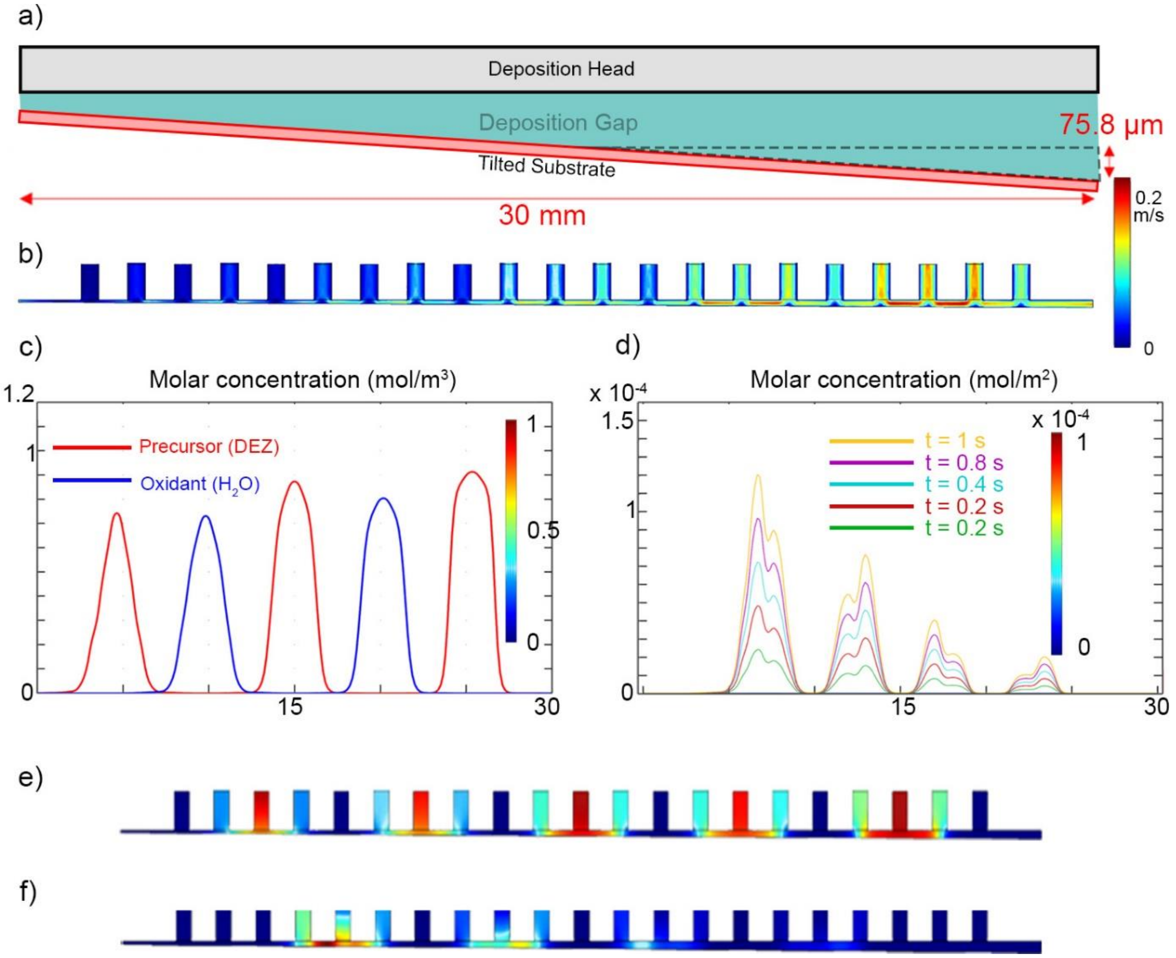

*Figure 3-12 Simulation results for a tilt of 0.3°: (**a**) Schematic of the rotation of the substrate with respect to the deposition head, about its center point, which leads to a difference of ±75.8 µm on each side of the substrate for a 30 mm length head. (**b**) the velocity of the flow is shown; (**c**) concentration of reactants above the surface of the substrate. (**d**) plot of the evolution with time of the surface concentration of a film deposited as a consequence of the appearance of a CVD regime. (**e**) 2D molar concentration distribution of reactants in the gap. (**f**) 2D distribution of the CVD reaction rate along the deposition gap.*

Figure 3-12 shows the results for the simulations done with a tilted substrate. **Figure 3-12a** shows a schematic of the tilt and the geometry of the deposition gap it creates. It can be seen that, with a slight mis-alignment of 0.3°, all the system behaves different than with a perfectly parallel system. Indeed, since the gap is only 150 µm, the slight alignment creates a difference of ~75.8 µm at each side of the gap; around 50% of the intended gap value. The induced mis-alignment creates a difference on the total velocity of the flow as it travels from the gaseous outlets to the exhausts, showing a higher velocity in the section where the deposition gap is higher (**Figure 3-12b**). The molar concentration plot in **Figure 3-12c** and the 2D concentration plot in **Figure 3-12e** show that, despite that in the narrower section of the gap the velocity is lower, the concentration is indeed lower in the same section. However, **Figure 3-12d** shows that the adsorbed film as a consequence of the existence of a CVD regime is actually higher in the narrower section of the gap. This is the case since, in contrast to what was expected, the reaction rate seen in **Figure 3-12f** is higher where the gap is narrower. This seems contradictory to the previously shown conclusion in which the smaller the deposition gap, the less CVD reaction rate there is. However, this may be explained by the increase of the convective mass transfer of the gaseous reagents in the flow in the direction parallel to the substrate caused by the narrowing of the deposition gap. This phenomenon is in accordance with the previously shown plot where the concentration is directed towards the lateral sides of the system (**Figure 3-4**).

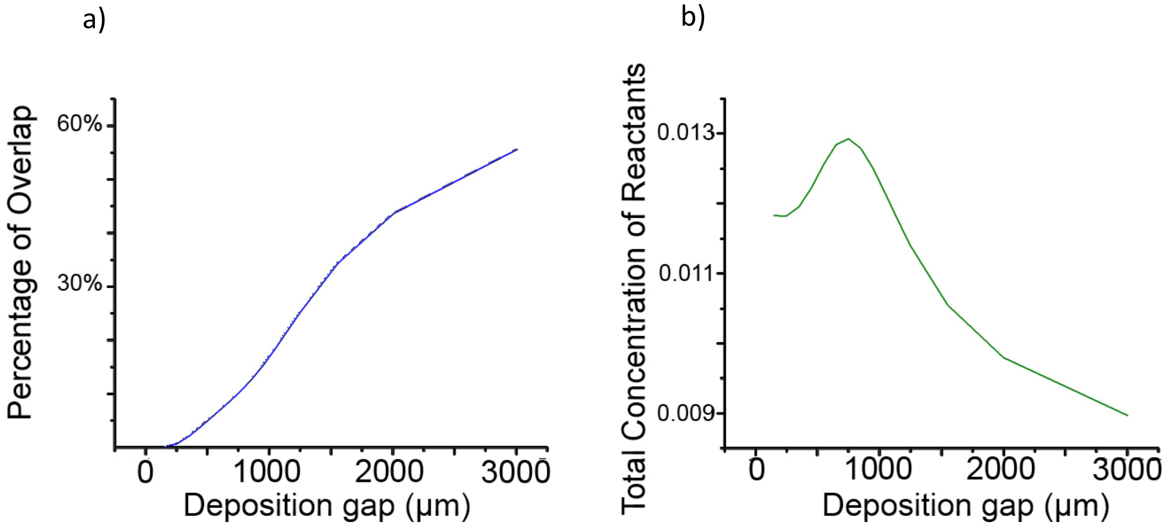

This occurrence of this phenomenon causes a higher chance of intermixing and, thus, increasing the CVD reaction rate. As the deposition gap widens with the tilt, the convective diffusion parallel to the substrate is reduced and hence, the reagents are better directed to the exhausts reducing thus the CVD reaction rate.

As complex as these phenomena can be, it is clear that a slight mis-alignment could cause a non-negligible effect on the deposition and the homogeneity of the films deposited. Hence, it is important when using the current head design to maintain a high precision when aligning the SALD deposition head to the substrate to avoid such inhomogeneities.

3.5 Geometry design for a reduced CVD regime

As a first approach to optimize the geometry for a reduced CVD regime when working at a close-proximity gap, we performed simulations for different sizes of gas barrier width and exhaust slit width, both of which have a value of 0.5 mm in the deposition head. In the simulations, such widths are varied up to 2 mm. **Figure 3-13** shows the results of the simulation of the geometrical study of the nitrogen outlets and exhausts slits. To calculate the total concentration of adsorbed film in the surface after a 1 second simulation, we first perform the same time-dependent simulation as previously. Then, we integrate the resulting CVD surface concentration curve at the end of the simulation (1 second, corresponding to the yellow curves in **Figure 3-13b,c** and **d**), and finally, we divide it by the total width of the geometry created. This way, the calculation considers the increase of the total width of the deposition head as we increase the size of the outlets and slits as shown in the 2D geometries under each plot of **Figure 3-13**.

Figure 3-13a shows a color map of the total concentration of adsorbed film in the surface after a 1 second simulation. It appears that the most influential parameter to decrease the CVD regime deposition is the nitrogen outlet width, although an exhaust width increase also reduces the CVD regime. The results of the time-dependent simulations are shown for the extremes of the color map. In the case where the nitrogen outlet and the exhaust slits have a width of 0.5 mm (**Figure 3-13b**), the concentration of film deposited in CVD regime is the highest. By increasing the size of the exhaust slits to 2 mm, a reduction of CVD regime deposition of ∼22% is achieved (**Figure 3-13c**). On the case where both nitrogen outlets and exhaust slits are 2 mm, a reduction of ∼88% is achieved (**Figure 3-13d**). On the case where only the nitrogen outlet is increased to 2 mm, a reduction of ∼83% is possible (not shown here).

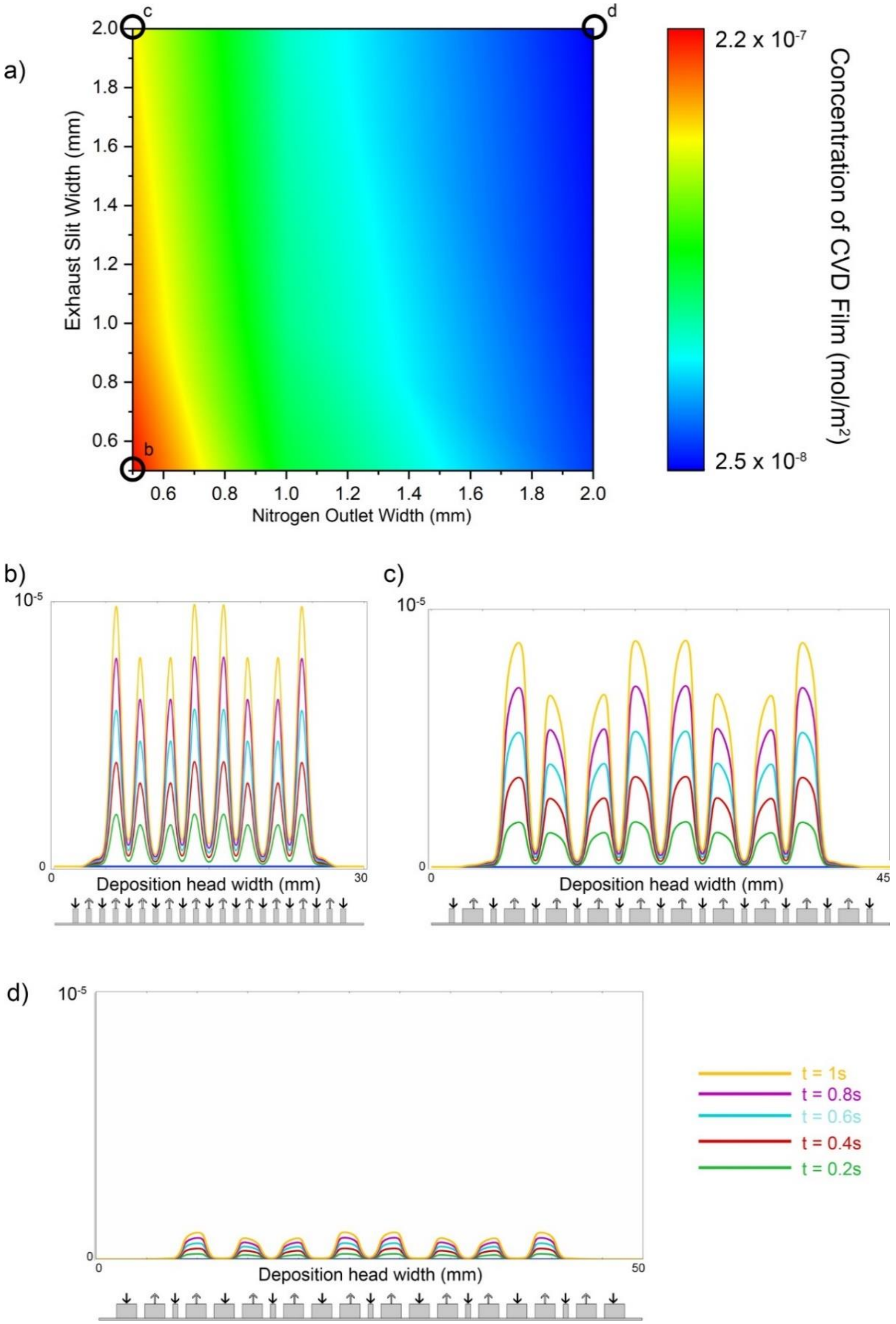

***Figure 3-13**. Geometrical dimension study for the nitrogen outlets and the exhaust slits. a) color map of the total concentration of adsorbed film in the surface after a 1 second simulation. Plot of the evolution of the CVD regime surface concentration with time for a 1 second time-dependent simulation for the cases where the nitrogen width and exhaust width is 0.5 mm (b), where only the exhaust width is increased to 2 mm (c), and where both the nitrogen and the exhaust width is increased to 2 mm (d).*

Given these results, it can be deduced that, if we can decrease the amount of CVD regime in the deposition at a close-proximity, it is also possible that we can increase the deposition gap while maintaining the deposition regime constant. The ability of increasing the deposition gap would be beneficial to decrease the precision needed to maintain an ALD regime, making the system more flexible and more adaptable for non-planar substrates and less sensitive to a tilt.

Figure 3-14 shows the effect of a wider exhaust slit in a substrate that presents a similar tilt of 0.3°. **Figure 3-14a** shows the original case of an exhaust of 0.5 mm wide, as comparison for a system in which the exhaust is 2 mm wide (**Figure 3-14b**). It is clear that, even with a tilt, the change of geometry in the exhaust ports is beneficial to a decrease of a CVD regime, reducing it by around 50%.

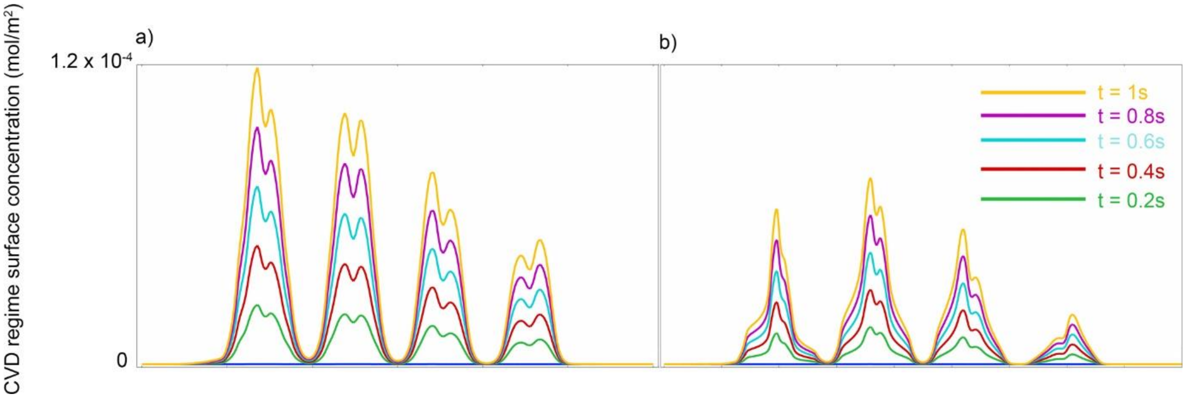

Figure 3-14. Plot of the surface concentration adsorbed in the surface of the substrate as a consequence of a CVD regime for an exhaust width of 0.5 mm (a) and 2 mm (b).

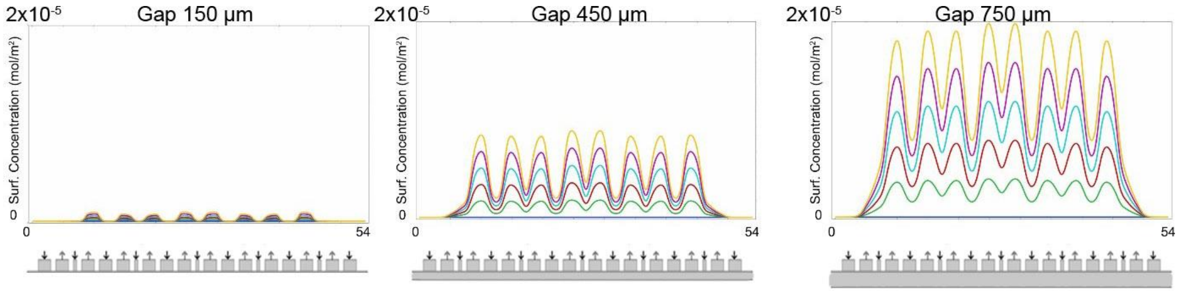

Figure 3-15. Plot of surface concentration adsorbed in the substrate as a consequence of a CVD regime in the deposition gap, for gap values of 150, 450 and 750 µm.

Given that the best results or the decrease of CVD regime in the deposition gap have been obtained with a deposition head in which both the exhaust slits and the inert gas outlet are wider, it is interesting to observe what happens with such geometry at different values of gap. **Figure 3-15** shows the plot for gaps having a value off 150, 450 and 750 µm. It is possible to observe that, despite the low levels of CVD regime with a gap of 150 µm, as the gap increases the CVD regime increases as well, similar as with the original widths of gas slits. Hence, even though the wider slits enhance ALD regime with a close-proximity, it does not impede the appearance of a CVD regime at higher gaps, making it necessary, even for this geometry to work at close-proximity to the substrate.

On the other hand, although the geometry where both the nitrogen outlet and the exhaust slits have a width of 2 mm is the most optimum regarding the amount of CVD regime that appears, one should consider that, to fabricate such geometry, the deposition head must increase its total width. This would consequently cause the need to displace the substrate a larger distance to ensure the substrate is exposed to all the regions, increasing thus the deposition cycle time. Furthermore, if such large slits are used, it would be also important to ensure the homogeneity along the whole area of the deposition by using a properly selected mass in-flow.

In this thesis a deposition head was designed according to the calculations made here using Solid Edge and then fabricated with additive manufacturing techniques in polymeric resin and in metal. The process of design and fabrication will be explained in detail in chapter 4.

3.6 Conclusions

In this chapter, we present the approach we use to simulate some of the phenomena present in the close-proximity SALD system used in LMGP and throughout the work done in this thesis. We confirm that the deposition gap is crucial for a spatial separation of gaseous reagents during deposition since, as the gap increases, the deposition regime transforms into a CVD regime. The control of the deposition gap provides a simple way to control the deposition regime, since it can be changed mechanically even in the middle of depositions, which provides control over the growth mode and, therefore, over the properties of the films deposited, as seen further in the studies performed during this thesis. The SALD technique provides then a simple and versatile way to tune the SALD deposition process by controlling simple parameters in the system.

The simulations here presented were used to understand the influence of other parameters, besides the deposition gap, in the regime of deposition. We studied the efficiency of exhaust as a parameter that may affect the intermixing of gaseous reagents in the deposition gap. We observe that a low exhaust efficiency, which can be induced either by an intentional fabrication or by a non-intentional blockage of the exhausts, causes an interesting phenomenon that causes a well localized deposition. Such localized deposition was validated by a static mode deposition of ZnO on a silicon wafer using DEZ and water as reagents.

The pattern obtained in the static mode depositions here created show promise in selective area deposition of thin films with SALD. Indeed, selective area deposition has shown to be of interest in the scientific community, but the process to achieve this are usually complex and require several steps. The approach here presented provides an interesting potential for a selective area deposition of films, by locally increasing the deposition rate, and achieving it in a relatively simple way.

Additionally, a simulation was performed to visualize the effect of a tilt on the substrate with respect to the deposition head. A tilt of 0.3° was induced in the substrate. It was possible to observe that, even at an ideal close-proximity deposition gap of 150 µm, the CVD regime deposition appeared. Contrary to what was expected, more CVD regime appears at the region where the gap is narrower. This happens because the increase of velocity parallel to the substrate induces a convective mass transfer of the reagents that crosses even the gas barrier, creating a higher intermixing of species in the narrower gap and, therefore, increasing the amount of concentration adsorbed in the surface of the substrate caused by a CVD regime.

Finally, a geometrical study was performed, using the same simulated model. We observe that the geometrical increase of the width to 2 mm of the gas barrier outlets contributes greatly to preventing a CVD regime. In combination with a similar increase in the exhaust slits width, the simulation shows a decrease of the CVD regime concentration of around 88%. This is beneficial both to maintain an ALD regime at close-proximity, and to keep the same deposition regime at higher deposition gap, making the deposition process more flexible and requiring less mechanical precision.

Although many more parameters and combinations of such are still to be simulated, the model here created provides a convenient way to modify parameters and quickly observe the influence on the intermixing of species. Furthermore, the simulation can be improved by including more physics such as heat transfer to the gases, which is neglected here due to the relatively low temperatures used to deposit (around 200 °C). From the chemistry point of view, an ALD surface chemistry would add value to the model since it would allow to optimize the residence time needed for all the active sites in the surface to be occupied, which would in turn allow to optimize the scan speed to reduce the waste of precursors and reduce the cost of deposition. With further work, this 2D model of the cross section of the deposition head can be extended to simulate a closer-to-reality 3D multiphysics simulation, and, if coupled with surface chemistry and even with substrate movement, a whole simulation of the deposition shape and growth per cycle (GPC) could, in theory, be obtained; really interesting as future perspective for simulation of a whole SALD system that can be used as a virtual prototyping for customized deposition of materials.

In the next chapter, we use the knowledge obtained with the simulations here performed to design a new deposition head to deposit Cu_2O. We present the procedure, considerations, and constraints to design a new deposition head that achieves a better exclusive ALD regime deposition and that avoids the complexity of fabrication, installation and maintenance that the deposition head used before this thesis had. In addition, the newly designed head has the convenience of a lower cost of fabrication thanks to the additive manufacturing process used. We also discuss the potential capabilities of the design process and the potential benefits that additive manufacturing provides for further improvements and even customizations of the SALD deposition technique for the application envisaged.

Chapter 4

SALD development for improving the versatility of the instrumentation

Within the material science instrumentation, the development of tools that are capable of fabricating features with nanometric precision has a big importance for the creation of new materials and devices. SALD is one of such tools that allows for nanometric thin films fabrication. In SALD, as explained in chapter 2, the reactions take place in the open air while scanning the substrate back-and-forth under the deposition head. Since the substrate is placed at a close-proximity to the outlets of the deposition head, the flows are confined at the top of the substrate and the chemical reactions occur on the surface of the substrate. The flows of the gas and the separation gap between the deposition head and the substrate are the parameters that control the growth regime of the system, as seen in chapter 3. In the SALD at LMGP, this gap between the substrate and the deposition head is what essentially constitutes the reactor chamber for the SALD, in which the precursors are introduced and extracted, and in which the surface reactions take place. With this in mind, and with the objective of depositing new materials in the SALD system, a new deposition head was fabricated to replace the existing deposition head used for the deposition of ZnO up to the time of this thesis, so as to avoid contamination from different precursors used in the SALD in the process. 3D printing is used for the first time to this purpose.

In the work during this thesis project, a new approach to the design and fabrication of the deposition head was established. A new design was successfully fabricated and it was used for the deposition of Cu_2O. Such head should retain the geometrical characteristics of the original deposition head to ensure that the depositions are comparable. In this chapter, a description of the geometry of the initial SALD deposition head will be shown. Then, the process of the design of a new deposition head will be explained, as well as the requirements of the new deposition head and the constraints present in the system. The two designs used in this thesis will be described. Afterwards, CFD simulations in the 3D geometries made for one of the geometries of the deposition head is presented, and a study on the homogeneity of the flow as a function of some geometrical parameters of the design is shown.

Later, the fabrication procedure by 3D printing will be presented, and the principles of additive manufacturing will be discussed, highlighting the benefits and drawbacks found while fabricating the designs made. Additionally, the limitations of the design and the fabrication process will be discussed. Lastly, the potential applications of the design and fabrication process here presented are discussed and several alternative deposition heads designed and fabricated at LMGP are presented as proof of concepts for the capabilities of the design and fabrication workflow established, as well as for future novel concepts for selective area deposition using SALD.

4.1 Geometry of outlets: how are regions created

The design of the deposition head used in the SALD previous to this thesis project is based on the Kodak design published in [128]. For the deposition head used in LMGP [95], rectangular and parallel slots were designed to create the flows necessary to distribute the reactants along the whole surface of the substrate and induce the surface reaction with the substrate.

***Figure 4-1*a** shows the geometry of the side of the deposition head that is directed towards the substrate to be coated. In this version of the deposition head, the slots used to deliver and extract the different gaseous flows are placed in the bottom side. Such slots have a length of 50 mm and a thickness of 0.5 mm and which will be called “outlets” in this thesis. The outlets are the exit point for the gaseous reagents that travel through an inner channel, which receives such gaseous reagents from the gas panel. They have a simple shape of a cylinder that take the gaseous input of the lateral pieces and convert them to the square shape needed for the substrate deposition. *Figure 4-1*b shows the geometry of a single inner channel.

In order to create the ALD cycles with a linear motion, the output of each contiguous channel in the SALD deposition head is alternated to create the different regions needed (shown in *Figure 4-1*c): metallic precursor region (blue), oxidant region (red), inert gas region (black) and exhaust region (white). In the deposition head originally designed, the channels include 2 metallic precursor channels, 3 oxidant channels, 6 inert gas separation barriers and 11 exhausts in between each channel, as shown in *Figure 4-1*c.

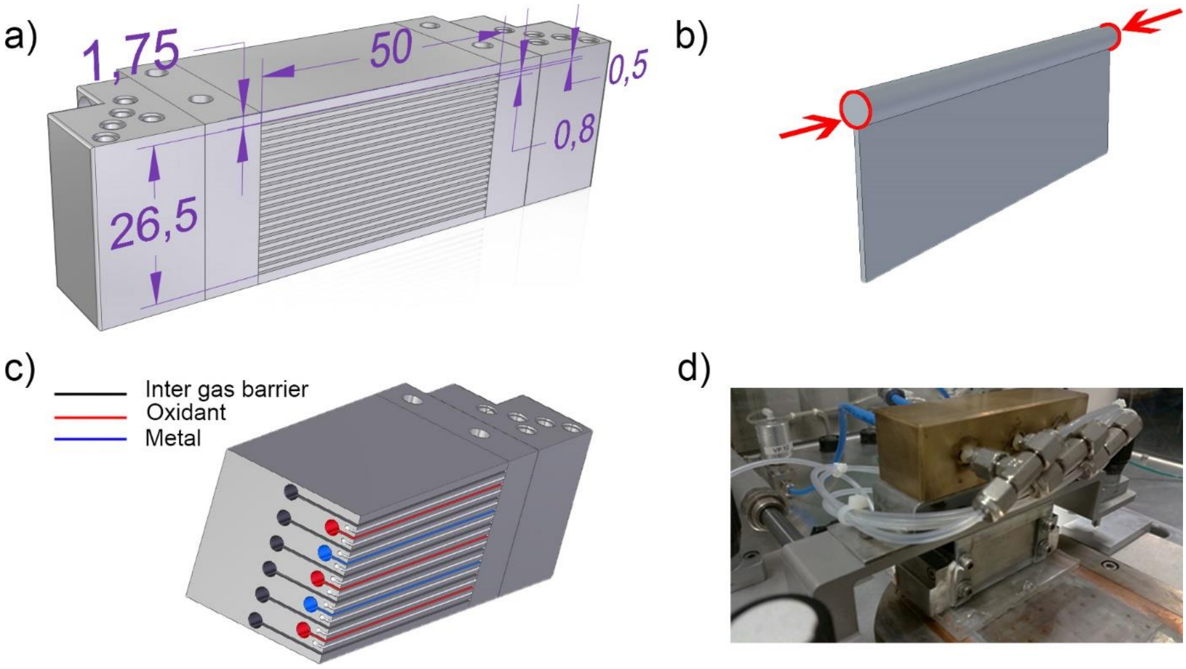

Figure 4-1. Geometry of the deposition head in the SALD previous to the work done in this thesis. a) Dimensions (in mm) of the geometry of the gas outlet side on the deposition head. b) Geometry of the inner path for a single channel. c) Cross-section of the deposition head, with color code on the channels: red for the oxidant channels, blue for the metal channels, black for the inert gas channels, and white for the exhausts*. d) Deposition head installed in the SALD system with all necessary pipes and gas distribution components.*

Every channel in the deposition head uses the two circular sections (shown by red arrows in Figure 4-1b) as input for the gaseous flows. It is important to note that both circular inputs should have the same flow so that the outflow of gas at the bottom end of the channel has as homogeneous flow as possible. For this, the reactive flow of the pipes incoming from the gas panel are divided using a “T” pipe connector to introduce flow into the lateral pieces simultaneously, using plastic piping and sealing the joint at every inlet. The lateral pieces need to be pre-polished to ensure a good surface contact with the main body of the deposition head, and to avoid leaks during its usage.

As the flow in every region outflows from the channel, the exhausts channels provide a path through which the reactive gases can exit the system. Thus, to collect the gaseous species that enter the exhaust channel, a connection to the channels is also used in each of the lateral pieces, and then directed towards a general ventilated exhaust on the SALD.

All this fabrication process needs multiple pieces, multiple pipes to be setup, making the deposition head a complex, costly solution if one is to be made for every material to be deposited. Furthermore, the installation of every head is complex since the pipes may detach with frequent movements. Additionally, the amount of piping also makes the deposition head bigger, thus complicating the manipulation, positioning or changing of the substrate.

To address this issue, and with the idea to fabricate a simpler, cheaper deposition head, the deposition head was re-designed for its replacement in the system.

4.2 Design of the new deposition heads

To address the idea of making the system simpler, it would be more convenient to have all the gas distribution inside the head (in one piece). As explained below, the use of 3D printing allows such complex designs to be fabricated. Hence, for the new design, a monolithic (one-piece) piece was desired. Three inlets should be designed, one for each gaseous reagent needed to create the spatial ALD regions, as well as two exhausts, one for the metallic precursor and one for the oxidant reagent. Finally, the design of the piece should have dimensions that fit in the SALD equipment. This puts a constraint on the total height of the piece to a maximum of 45 mm.

The dimensions of the outlets and exhausts were maintained, since this design has been tested and proven to work. However, all the inner channels which direct the inlets of the gaseous reactants that come from the gas panel to the gas outlets towards the substrate, were redesigned.

4.2.1 *Design workflow*

With the constraints in place, a Computer Aided Design (CAD) software was used to design a three-dimensional model of a monolithic deposition head. **Figure 4-2** shows an illustration of the design workflow used for the creation of the monolithic deposition head. The design workflow involves the modeling of the inner geometry that would work as a path for the gaseous flows from the inlets coming from the gas panel to the outlets that direct the flows towards the surface of the substrate. Once the inner channel was modeled, another piece, used as outer geometry for the new deposition head, was modeled. This piece should have the dimensions determined by the SALD equipment, since this is where the piece had to be ultimately fixed. With the inner gaseous paths and the outer body modeled, an action known in the CAD software as “boolean” is used to subtract the intersection between two three-dimensional bodies. In this case, the inner gaseous paths were subtracted to the outer body, hence creating internal channels in the outer body that follow the geometry of the inner channels initially created. It is important to mention that the model to be subtracted should be over-dimensioned with respect to the outer body to ensure that the outlets and inlets are open as shown in Figure 4-2c.

With the subtracted main body, some final modifications can be made to the deposition head. This can include adaptations for other pipes, external places to attach other pieces such as screws or reshaping geometry to reduce the volume of solid parts in the piece. These three were used on the designs in this thesis, but they are of course not limited to the modifications here mentioned.

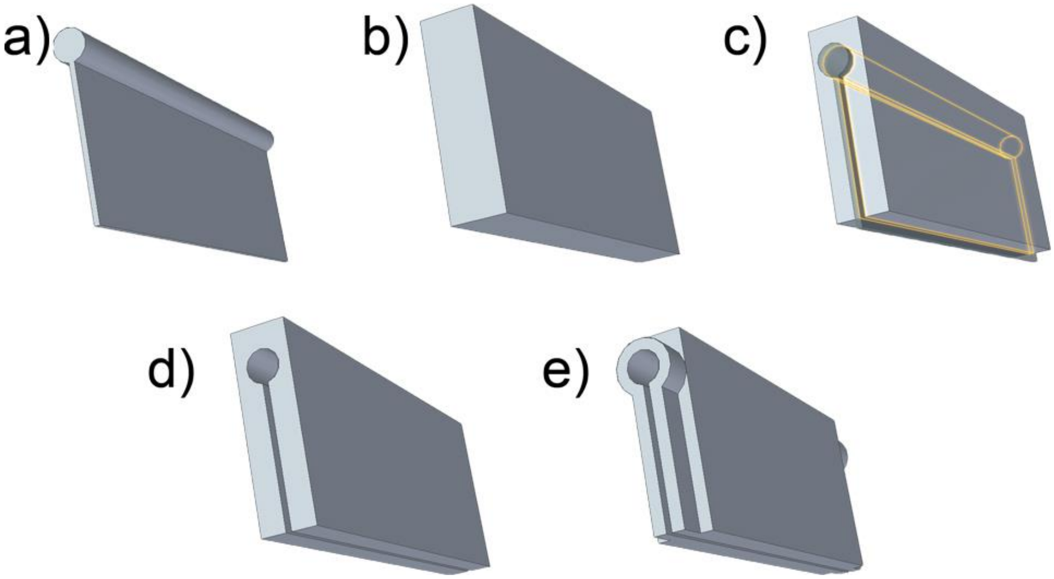

Figure 4-2. *Simplified example for the workflow for the design followed for the deposition head: a) design if the inner channel, b) design of the outer structure of the piece, c) illustration of the intersection between the two geometries created, d) subtraction of the intersection to the outer structure of the piece, e) final modifications to the piece.*

Using this approach, several versions of deposition head were designed before their fabrication was tackled. The first version (V1) of the inner gaseous paths was made with tubular pipes that direct one inlet of gas to the squared outlet at the bottom of the piece. One piece per gaseous reagent was designed, all of them having one inlet and a different number of outlets, the latter defined by the architecture of the head as explained in *Figure 4-1*c.

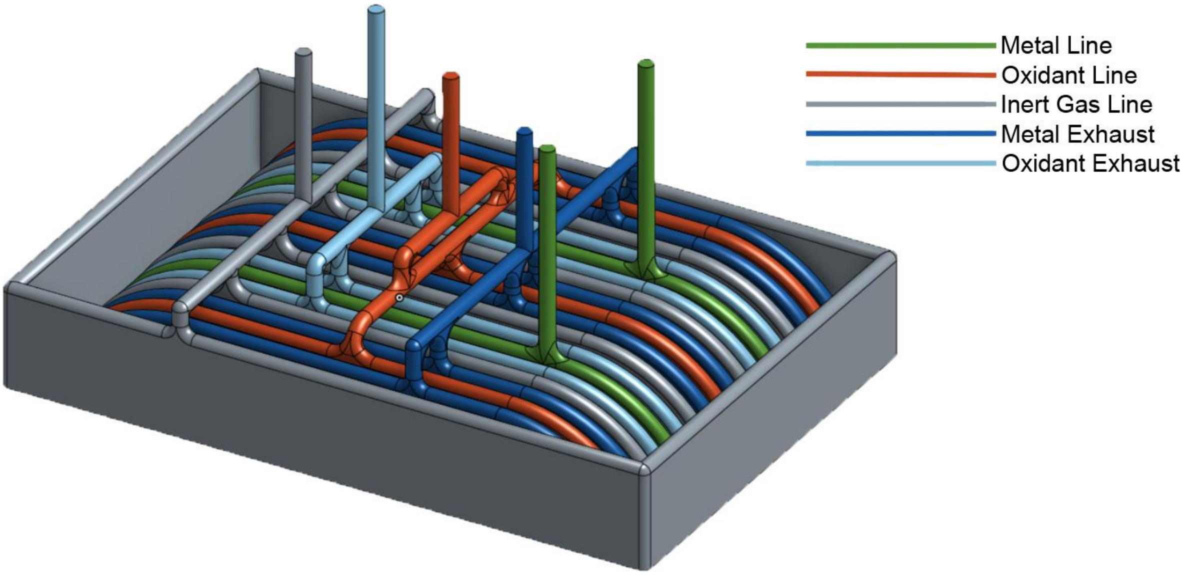

Figure 4-3.*First version for the inner channel structure of what would become the integrated deposition head. This design was later refined and modified as seen in this chapter.*

Figure 4-3 shows the different channel designs in an assembly that contains all the inner channels in the correct place, creating thus the complete structure of the inner channels needed for the SALD process. It is worth noting that the inert gas line includes a squared shape around the other inlets. This was made with the purpose to isolate and define the deposition zone during deposition, and this confinement lines are also present on subsequent versions of the deposition head.

With this design made (V1), it was decided that, even though the flow path of the reactants would be successfully achieved, the path would create pressure drop due to the drastic change of shape from a circle (cross section of the pipe section) to a rectangle (the outlets of the gases), This in turn would cause the flow not to be homogeneous along the whole outlet. So, in order to improve the flow, several versions of the inner gaseous paths were designed until we reached a version that addressed this issue and promoted a more natural path for the gases, thus reducing the pressure drop points and generating a more homogeneous flow, as evidenced by a CFD simulation of the flow presented further in this chapter. After several versions of design, the third iteration was accepted as the most promising and compact deposition head, capable of being 3D printed and adapted for the SALD system at LMGP. Such version, which we call here version 3.7 (V3.7) and which follows the same design approach explained before, can be seen in **Figure 4-4**. Furthermore, the design of each inner channel is shown in **Figure 4-4a-e**.

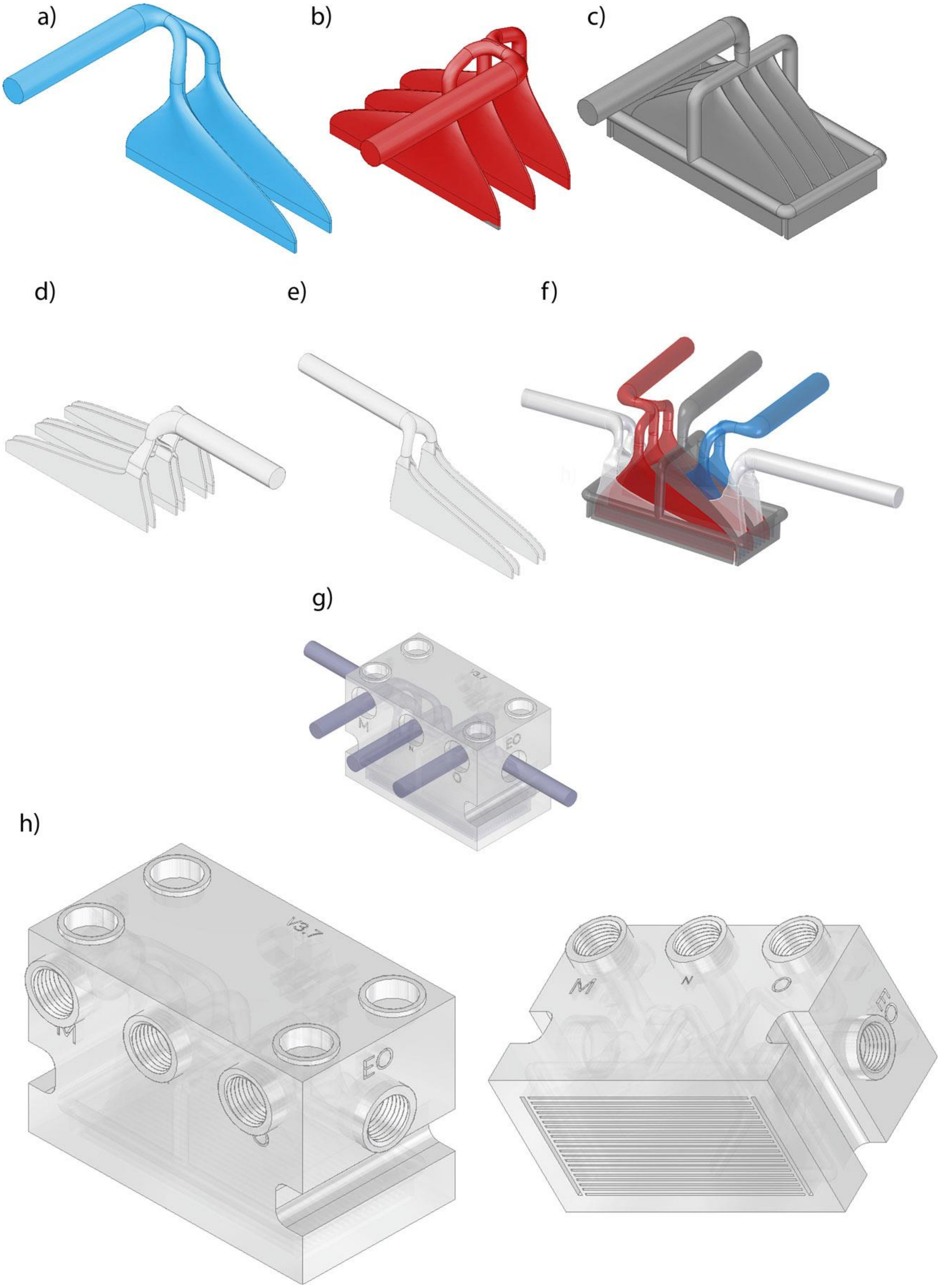

Figure 4-4. *3 dimensional structures used for the design of version 3.7 of the deposition head. The figures show the design of the inner channels for the a) metallic precursor, b) oxidant precursor, c) inert gas used as a barrier, d) exhaust for the oxidant channels, and e) exhaust for the metallic precursor. f) Assembly of all inner channel structures on the correct position relative to each other. g) Outer structure of the final piece with the inner channel assembly on place. h) Final piece for the version 3.7 of the deposition head.*

This version was accepted as one of the most compact and suitable for the deposition of thin films in the SALD. In **Figure 4-5**, the last adaptations made to the deposition head are shown. Three key modifications were performed in the head as last steps to the design. The first modification is a 1/8-inch thread added to the inlets of the gaseous flows (**Figure 4-5a**). This was made to add external quick fit adapters in order to add the ability of a quick change of the deposition head by unplugging the pipes from the gas panel. The second major adaptation are the circular shapes on the top part of the system which act as holders for the screws needed to fix the head to the SALD system (**Figure 4-5b**). The process of adding the necessary screws to the deposition head will be explained further in this chapter. Finally, the third modification involves a removal of certain solid zones with the objective of diminishing the total volume of the piece (in order to save in printing material and time, see **Figure 4-5c** below).

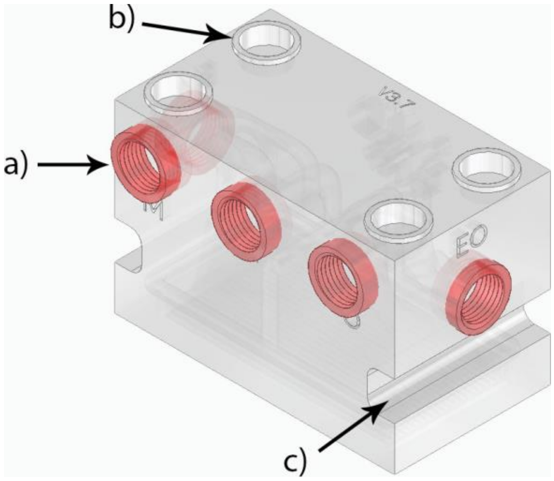

Figure 4-5*. 3D representation of the version 3.7 of the deposition head with the last modifications: a) addition of threads adapted to the pipe connections used at LMGP, b) creation of holes to fix the screws needed to hold the head in place in the SALD system, and c) reduction of volume to decrease the overall usage of material when fabricated.*

With a model of a deposition head that would replace the multiple-piece design with a simple version with only 3 inlets and 2 exhausts, the fabrication of the piece was tackled with the help of additive manufacturing techniques.

4.3 Additive manufacturing

Additive manufacturing (AM), also called 3D printing or rapid prototyping, is part of unconventional manufacturing techniques that allows the fabrication of complex designs that are either not manufacturable or too expensive to manufacture with conventional (subtractive) manufacturing techniques. Additive manufacturing, in general, relies on a layer-by-layer fabrication of certain material that, after the solidification of a certain number of layers, creates the complete geometry. Additive manufacturing has exponentially grown its applicability in countless industries since the principles have been exploited in a cost-efficient way and since the list of materials compatible with AM is increasing continuously. Furthermore, the techniques for additive manufacturing are evolving continuously, offering currently advanced materials with a wide spectrum of hardness, elastic modulus or even chemistry. AM is currently investigated as solution for many technological challenges, and currently, materials such as metals like steel and aluminum [129], ceramics such as zirconia or alumina [130], and even bio-materials for the 3D printing of organs [131] have been 3D printed. For the case of the deposition head for the SALD, the main requirements include the gas tightness (leakproof) for its inner pipes and the resistance to heat up to ~250 °C, since the deposition head is to be placed at a close-proximity to the heated substrate during deposition.

Given these requirements, one of the most common AM techniques called Fused Deposition Modelling (FDM) proved to be unsuitable for the fabrication of the deposition head. This technique is based on a layer by layer deposition of a melted polymeric filament, being the most common the polylactic acid (PLA) filament. This technique is used in a wide variety of applications due to it affordability, although the main one is in decorative applications. However, when this technique was tested for the fabrication of the deposition head, the porosity was shown to cause gas leaks when tested with a flow of nitrogen through the inner pipes of the deposition head. Hence, another technology (also affordable and widely available) was chosen for the fabrication of the deposition for the SALD and is called Stereolithogaphy (SLA).

4.3.1 *Stereolithography*

SLA is a technique based on the photopolymerization of a liquid resin stored in a tank. A print bed is inserted in the resin tank, and a solidified layer is created thanks to a laser that scans a cross section of the piece to print. The solidified layer is created directly on top of the previous layer or, if it is the first layer, directly to the print bed. After the solidification of each layer, the test bed with the printed layers is raised and the resin in the tank re-mixed to homogenize the resin in the tank. The printed layers on the print bed are then lowered again into the resin in the tank for the next layer to be solidified.

A graphical explanation of the process of SLA printing is shown in **Figure 4-6**.

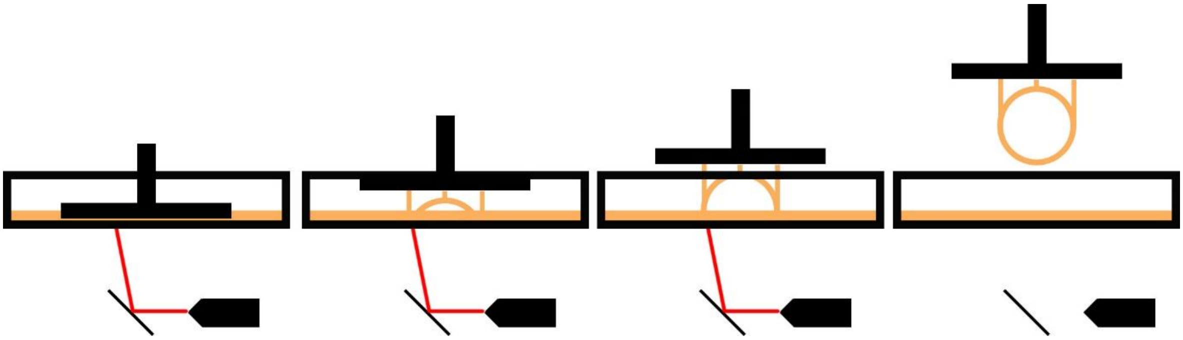

Figure 4-6. *Schematic showing the process of additive manufacturing with SLA technology. Although there are many ways the resin can be exposed to the photopolymerization light (such as LCD and laser projection), the technology at LMGP uses one laser spot to solidify each layer.*

The process of SLA is a widely used method for rapid prototyping. It has been exploited for 3D printing in commercial 3D printers, achieving mechanically resistant models in a fast fabrication time. Moreover, the use of SLA fabrication yields a solid resin piece, perfectly suitable to transport fluids. SLA has been used for novel applications such as microfluidics [132], [133], electrochemistry [134] and medical applications [135]. A deep review of the fundamental methodology of SLA technique and other 3D printing methods can be seen in [136].

On the other hand, as almost any 3D printing technique, the design process must take into account the "imprimability" of the piece. First, as the piece is being printed, it is necessary to make sure that every printed solid is in contact with the print bed to avoid solid pieces to stay on the resin tank. For this, the use of support parts is usually implemented; geometries that connect the free-standing pieces to the print bed. It is possible to define the number and the density of the supports to give the piece a proper printable geometry.

Second, the orientation of the piece needs to be taken into account. The orientation of the piece as it is being printed will determine the number of layers to print and, hence, the duration of the printing process, as well as the surfaces that will enter in contact with the support geometry. This is important since the support geometry actually becomes a part of the piece and it needs to be physically removed from the final geometry. This physical removal of the supports affects the surfaces in which they are in contact with, adding texture to the surface (as seen in **Figure 4-7**). Hence, if a surface needs to be smooth, the piece must be oriented in a way that the supports do not enter in contact with the desired smooth surface.

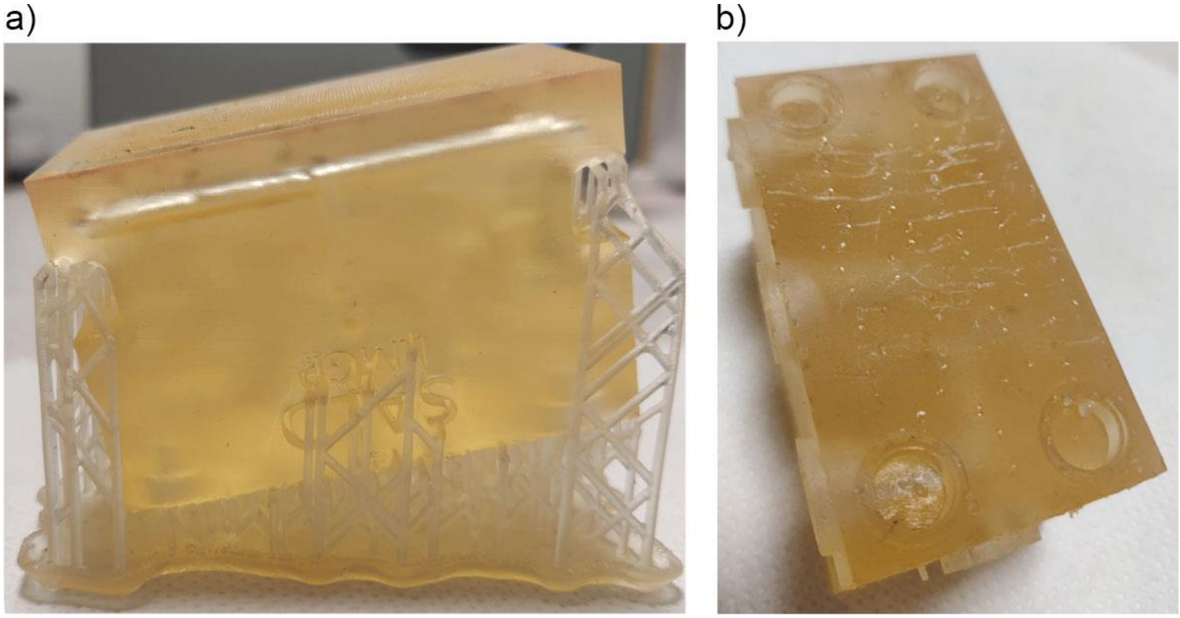

***Figure 4-7**. a) Deposition head printed as it exits the 3D printer containing the supports needed to fabricate the piece. b) Texture on the surface of a 3D printed piece created by the supports. This texture is created as the supports are physically removed from the piece, and it can be removed by polishing of the surface.*

The third consideration when designing pieces for 3D printing relates to the geometry itself. Even though SLA has a theoretical resolution of 25 µm, as mentioned by the 3D printer manufacturers, this resolution usually refers to surface features only. When dealing with geometries such as holes or slits, the resolution is largely reduced by the effect of capillarity of the resin, as the resin is a viscous liquid when not photopolymerized. The real resolution for holes and slits depends on the properties of each resin. This is also an issue when creating the inner geometries of the integrated piece envisioned in this work, where some parts of the inner gaseous paths are small. The consequence of this effect on the 3D printed pieces made in this thesis will be discussed further in this chapter.

To mitigate the problem of lowering the resolution due to the viscosity of the resin, without modifying the created design, two strategies can be proposed. The first consists on changing the resolution of the print, which refers to the thickness of each printed layer. Lowering the resolution may change the surface of the piece but it also reduces the capillarity effect on the slits and holes, making it a simple way to reduce the effect. It is possible that a lower resolution helps by increasing the distance between the solidified layer and the resin tank: as this distance is increased, less confinement of the resin exists, reducing the capillarity effect. The second strategy consists on modifying the orientation of the print: the piece should be oriented in a way that, at each printed layer, the length of the cross section of the slits and holes in the geometry are minimized. This allows for the cross section to be printed as continuously as possible, reducing the change of capillarity effects to occur. An illustration of the latter strategy can be seen in **Figure 4-8**.

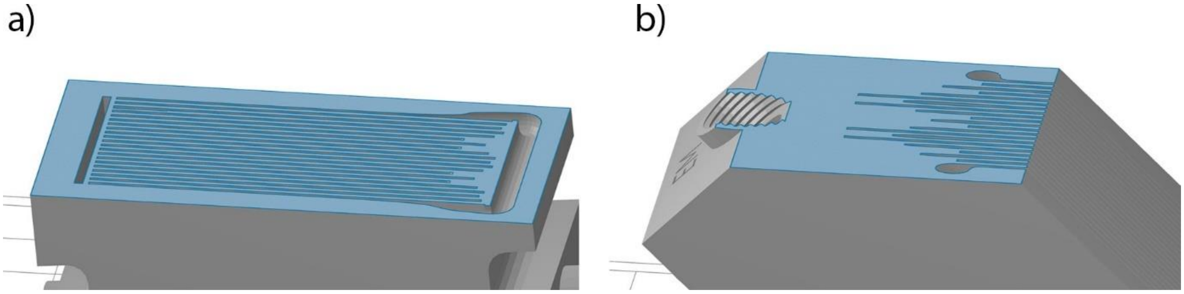

Figure 4-8. *Illustration of the impact on a change of orientation for 3D printing. In both images the blue section corresponds to the layer to be printed at certain point in the printing process. If the orientation causes that the cross-section includes long, narrow shapes (a), the probability of resin being solidified between those shapes due to capillarity increases. Changing the orientation causes the feature to have a smaller length and thus, reducing the risk of undesired capillarity (b).*

Other constraints for the SLA 3D printing of pieces include the size and location of the supports, which ensure that the printed piece stays always on the print bed, or the creation of evacuation holes to allow for resin that may get trapped in the inner geometries to escape properly. Nevertheless, since many of these techniques are common to SLA printing processes, they will not be deeply discussed in this work.

Finally, SLA being a process that requires a layer-by-layer solidification of liquid resin, usually requires post-processing steps on the final piece. First, a cleaning step is needed to remove the excess of liquid resin left on the piece by submerging it in adequate solvent for a pre-defined period of time. Then, in order to ensure the correct mechanical properties of the final piece and ensure a proper solidification of the piece, a UV light bath is recommended for the final piece.

4.3.2 *3D printing setup in LMGP*

During the thesis reported in this work, a 3D printing platform was setup at LMGP. The setup included an SLA 3D printer from Formlabs, model Form 2, and a FDM 3D printer from Ultimaker, model Ultimaker 3 Extended. The former printer was used to carry out the printability tests of the designed pieces. The two resins implemented were the Clear resin and the High Temperature resin, also provided by Formlabs. The high-temperature resin was especially important since the 3D printed pieces were aimed to be used as a functional part of the SALD equipment, which carries out the thin film deposition at temperatures around 200 °C. The high temperature resin resists up to 390 °C, as advertised by Formlabs. The FDM printer at LMGP was used for other additional pieces for the equipment, not directly involved in the deposition process, and thus will not be discussed in this work. A picture of the printing platform is shown in

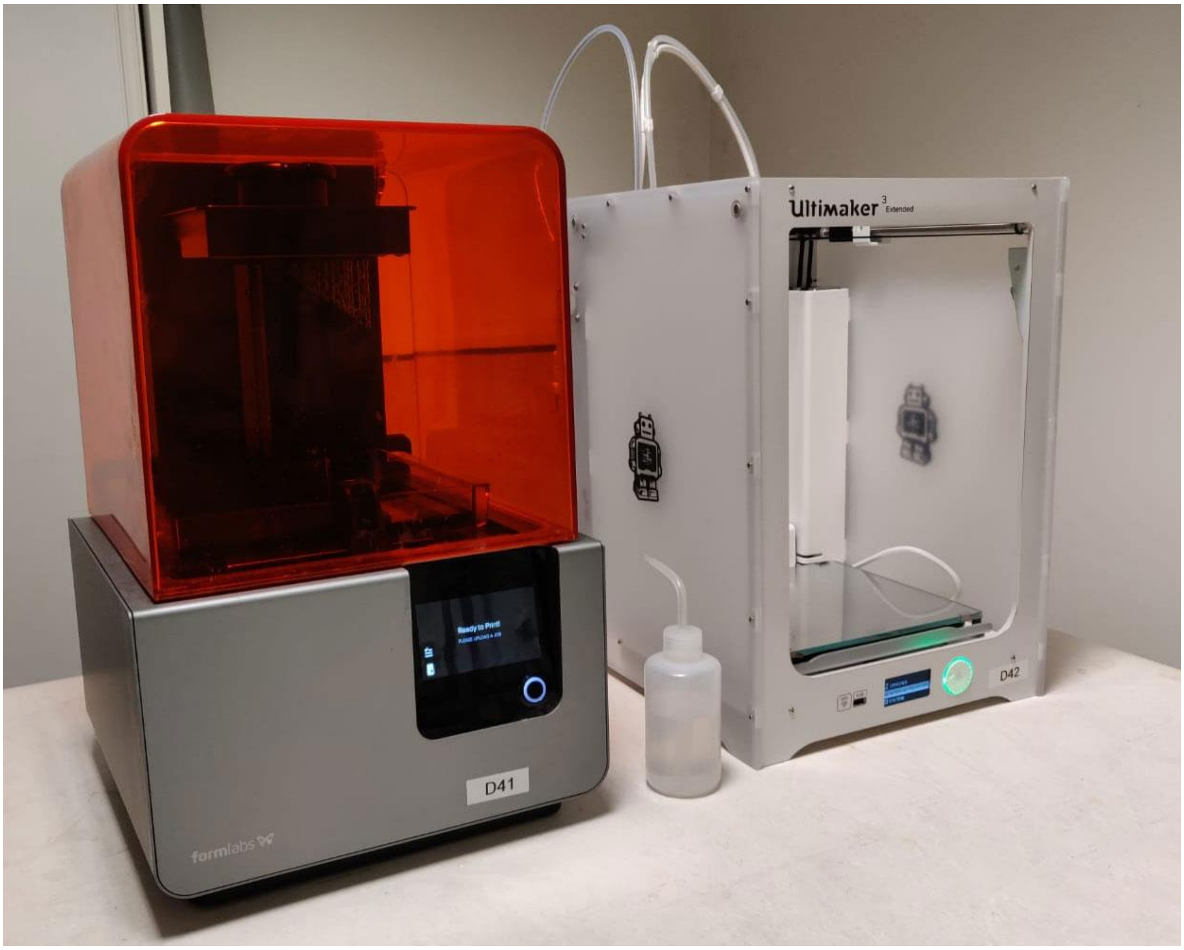

Figure 4-9. *Picture of the 3D printing platform setup at LMGP. On the left, the Form 2 printer from Formlabs. On the right, the Ultimaker 3 Extended from Ultimaker.*

Printability tests were made with the version 3.7 of the integrated deposition head described before as a proof of concept for the inner gaseous paths and the whole integrated deposition head concept.

For the 3D printing of the concept of deposition head, two different resins were used: the clear resin, which is the standard resin in the catalog of the resin supplier Formlabs, and a high-temperature resin, also provided by Formlabs and suited specially to sustain high-temperatures. These two resins have the advantage that they are transparent even when solidified, allowing for a better visual inspection of the quality of the printed piece.

4.3.3 *Results on fabrication*

The orientation of the piece and the position of the supports used to print the integrated deposition head is shown in **Figure 4-10a**. After a printing process with a resolution (layer height) of 0.025 mm, the print with the clear resin was a success. **Figure 4-10b** shows the printed piece as it exits from SLA printer and the supports are mechanically removed and the piece is submerged in isopropyl alcohol for around 10 minutes (as per the recommendations of the resin supplier). The final piece is visually inspected to ensure that the gaseous outlets are correctly printed. To further test the limitations of the 3D printing resolution with SLA, a variation to the outlets was performed. This time, instead of having rectangular outlets, we include perpendicular features that turn the rectangular outlets into a "shower" shaped outlet, with squared holes measuring 0.5 mm per side. **Figure 4-10c** shows the result for the SLA print of the integrated deposition head version 3.7 with a "shower" feature in the outlets after the post-processing of the pieces (removal of supports and cleaning in isopropyl alcohol).

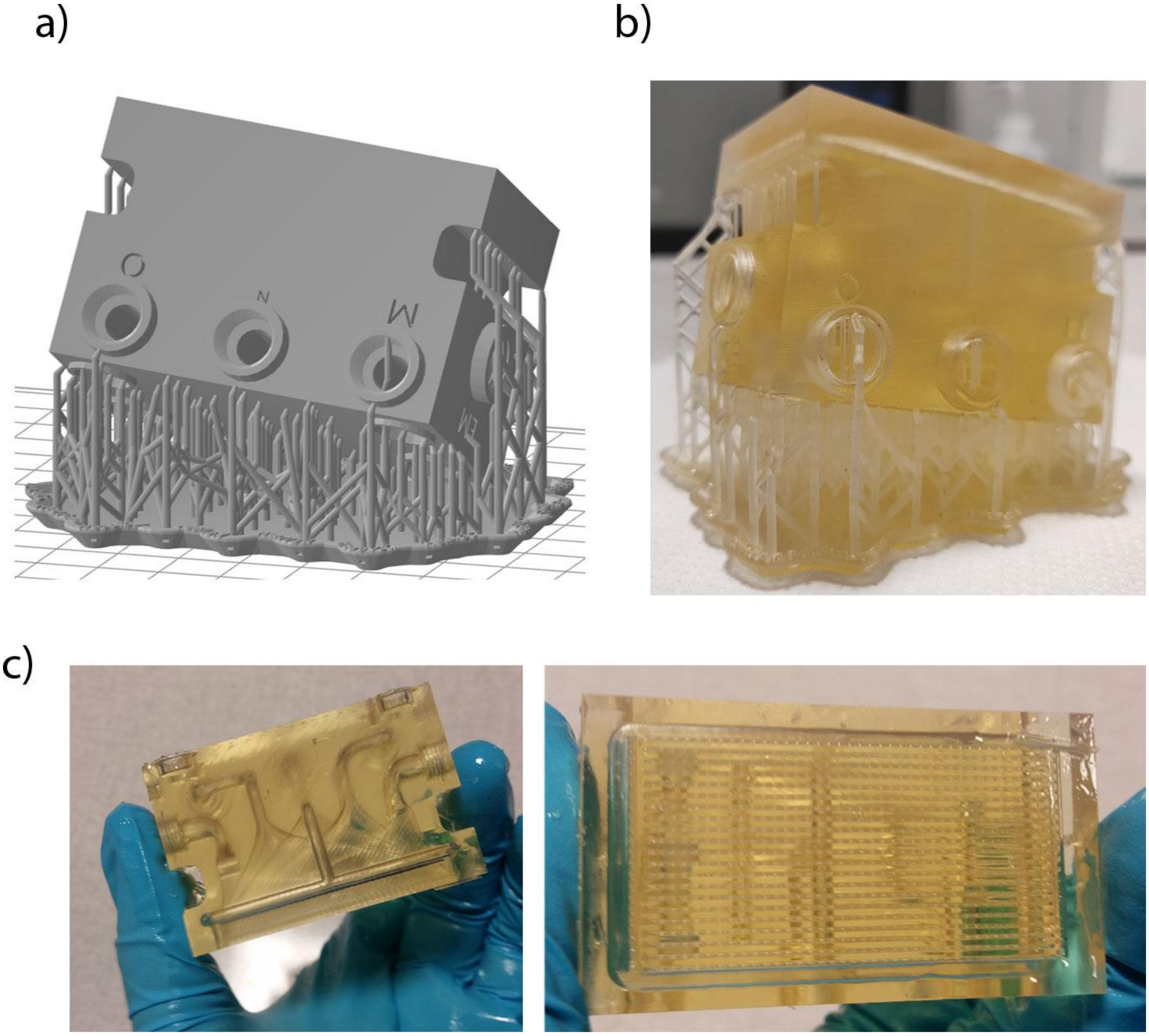

Figure 4-10. a) Orientation of the version 3.7 of the deposition head used for printing, along with the necessary supports. b) 3D Printed head as it leaves the printer. c) Side view and bottom view of the of the successfully 3D printed piece with the supports removed.

As seen in **Figure 4-10c**, the outlets of the deposition are well printed and corresponds to the geometries of the designed deposition head. The "shower" head also presents a correct fabrication of holes in the whole piece and, although it is difficult to observe in the picture, by using a flow of air each gas inlet was tested to ensure that the flow exited from the correct outlets in the deposition head. SLA proved to be a suitable solution to the fabrication of the integrated deposition head. This is the first time 3D printing is used to fabricate compact deposition heads with tuned gas distribution channels and outlets.

Once the piece was successfully printed, mechanical pieces to adapt the plastic tubes from the gas panel were screwed in place and sealed with silicone paste. Furthermore, since fixing the piece in the equipment of the SALD was needed, an additional step was introduced. Since it was not possible , to print standard M4 threads, due to the limits of resolution in the 3D printer, conventional screws with the correct size were placed in the holes in the top of the piece (previously designed) and then the holes were filled manually with liquid resin. After this, UV light was shined on the liquid resin, causing it to photopolymerize, thus fixing the screws in place. **Figure 4-11** shows a schematic of the process.

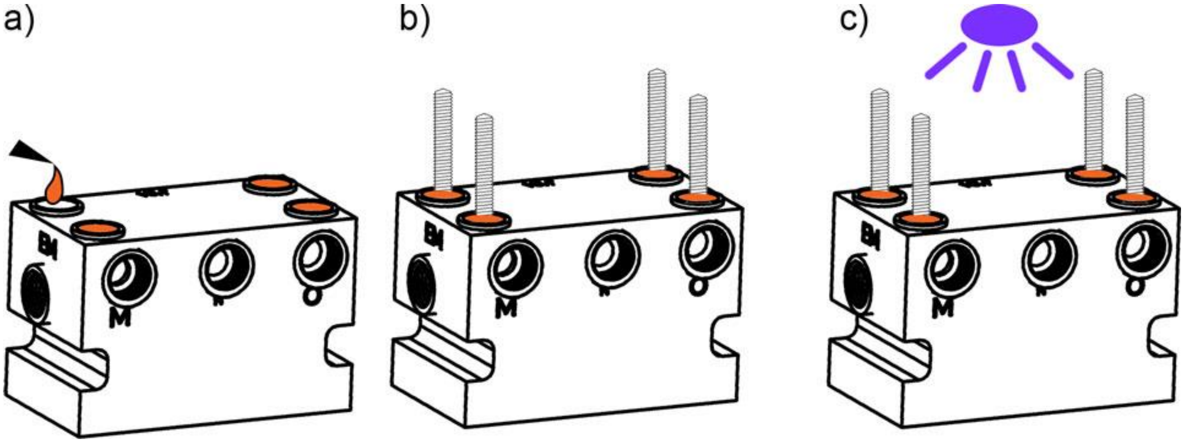

Figure 4-11*. Schematic of the process for the fixation of the screws on the deposition head. a) A drop of liquid resin is inserted in the required place. b) The screws are submerged in the liquid resin, taking care to hold them as straight as possible. c) Exposition to UV light for 15 to 30 minutes, depending on the amount and type of resin used.*

With these steps, the final version of the deposition head was successfully fabricated and it was ready for installation on the SALD system. In general, the fabrication process of a new deposition head was successfully established and tested. This allows for a fast exploration of the geometries in the deposition head, some of which will be explained here. Furthermore, this also enables for a faster adaptation cycle in the SALD for the study of other materials in the future, avoiding contamination from previous materials deposited, and without the complexity that the previous deposition head presented. From the design process, which has as a priority the channels in which the gaseous reagents will travel through, the deposition head was designed considering additive manufacturing as a viable, low-cost manufacturing technique. If we take into account the cost and the volume of the material used, each deposition head has a cost of around 50 euros, considerably lower than the previous multi-piece metallic deposition head, which had a fabrication cost of around 1,000 euros. The version 3.7 of the integrated deposition head as installed in the SALD equipment can be seen in **Figure 4-12**.

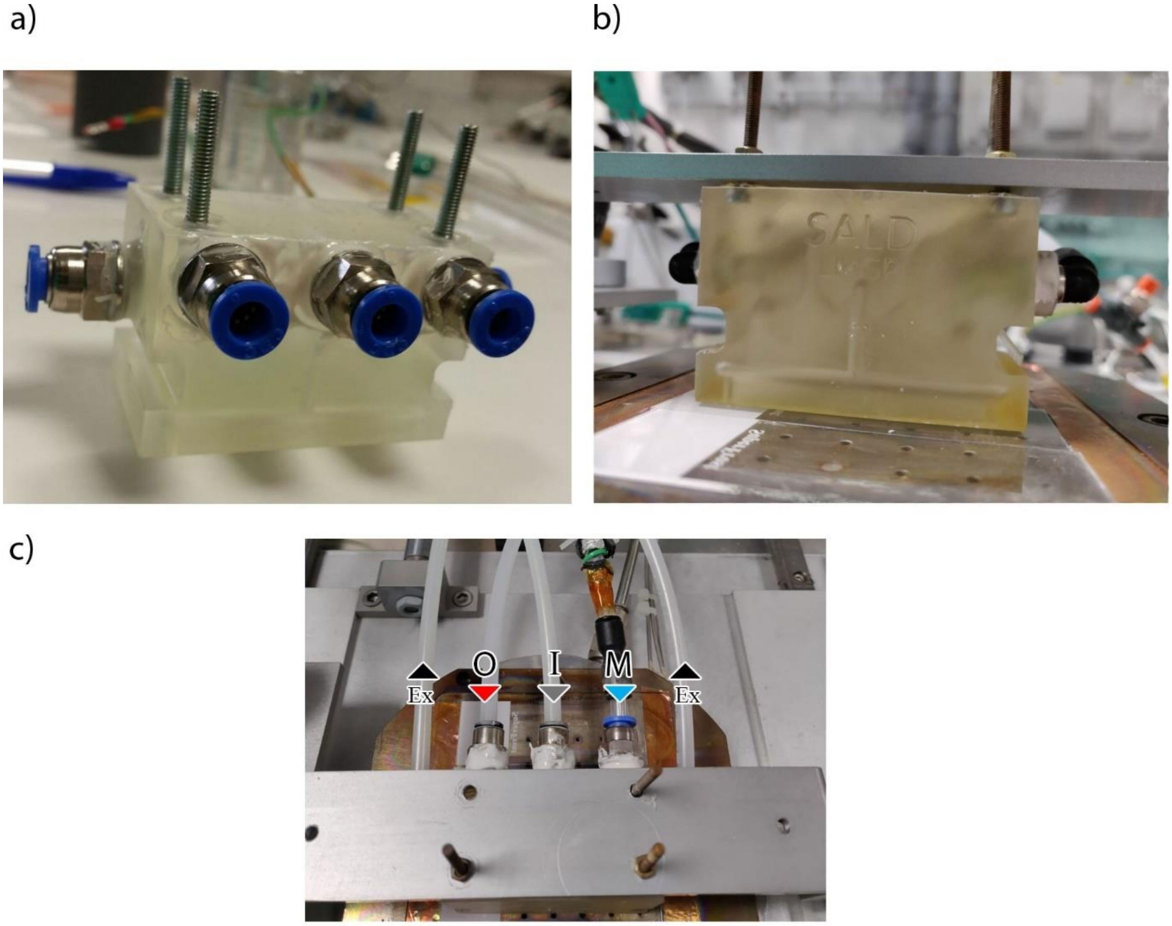

Figure 4-12. *Printed deposition head with a) external pipe adapters installed and fixing screws in place and b) installed on the SALD system. d) Top view of the installed printed deposition head showing 3 inlets for*

After the printing of the design was validated, another test was performed with the same print parameters but using the high temperature resin. Unfortunately, even though the print on the clear resin was a success, when trying a print with the high-temperature resin, the print was successful only when the resin tank was new. This happens since when a print has been performed in with the high-temperature resin, as its solidification requires a higher laser power and longer exposition to the laser beam, the process damages the transparent bottom of the resin tank. This process is known as “clouding” of the resin tank and effectively reduces the print resolution as more layers are printed. **Figure 4-13a** shows the effect of printing around 700 layers with the high-temperature resin. As this happens, the printing process of the deposition head with this resin results in not well open gaseous outlets as seen in **Figure 4-13c** and **d**, which can be compared to well printed outlets in **Figure 4-13b.** Multiple approaches were explored, including changing the orientation or the resolution of the print, but the only successful approach consisted on using a new resin tank, since this surprisingly happened even when the print was being performed in a not "clouded" zone in the resin tank. This is of course not ideal and, along with the homogeneity studied explained soon after, led to the design of a new head.

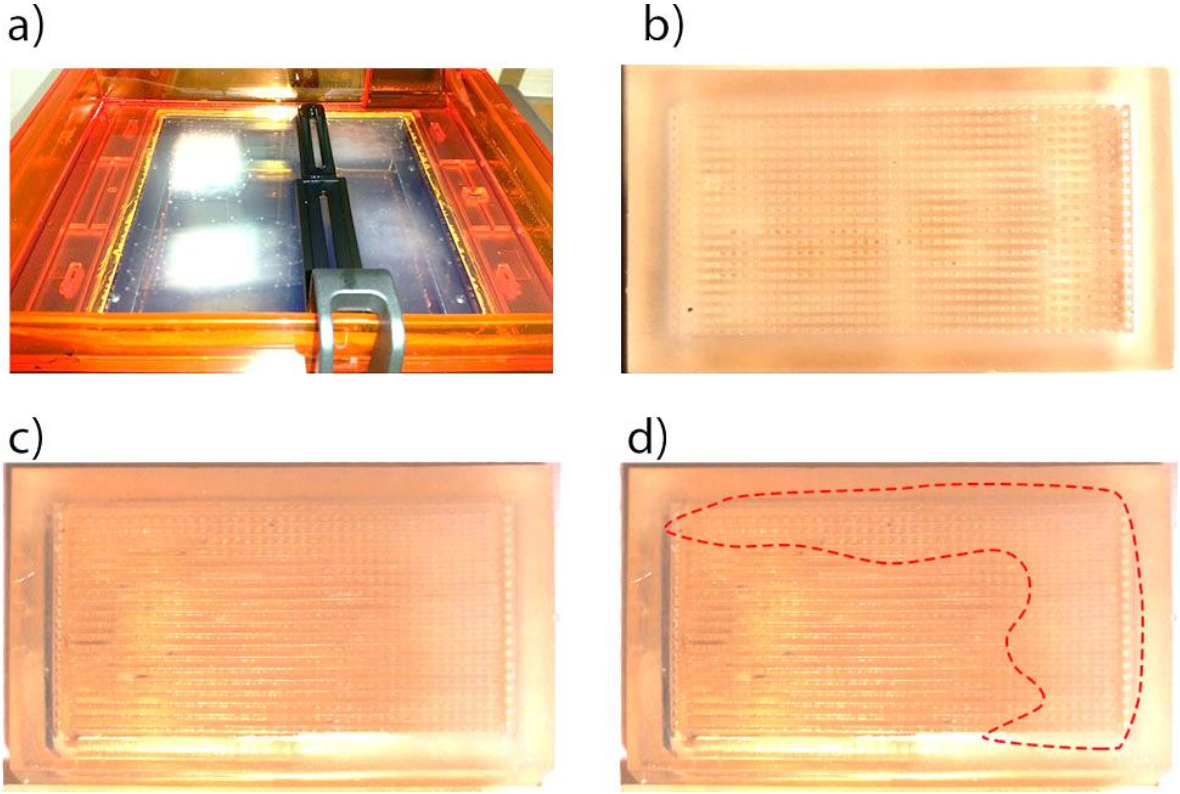

Figure 4-13. *Failure of 3D prints in high-temperature resin head. a) Picture of the tank after a print of the V3.7 of the deposition head with high-temperature resin. The white zones in the transparent bottom of the tank are a result of the damage created by the laser as it scans every layer. This is known as "clouding". b) Bottom view of a well-printed deposition head. c) A bottom view of a deposition head in which the holes for the gas outlets are not well printed. The zone in which it was well printed is outlined with a red, dotted line in (d).*

4.4 Homogeneity tests

During this thesis project, once the V3.7 of the deposition head was ready to use and was installed in the system, the deposition and characterization of Cu_2O thin films started. The results of the Cu_2O deposition will be discussed in chapter 5. Nevertheless, the performance of the integrated deposition head was in parallel and continuous study and development. More specifically, the flow of gases was simulated with CFD tools to ensure the homogeneity of the outlet flow. Using Comsol Multiphysics, a CFD simulation of nitrogen flowing through the corresponding cross section of the inner channels of the deposition head was performed. **Figure 4-14** shows the result of the velocity profile through one of the geometries of the channel.

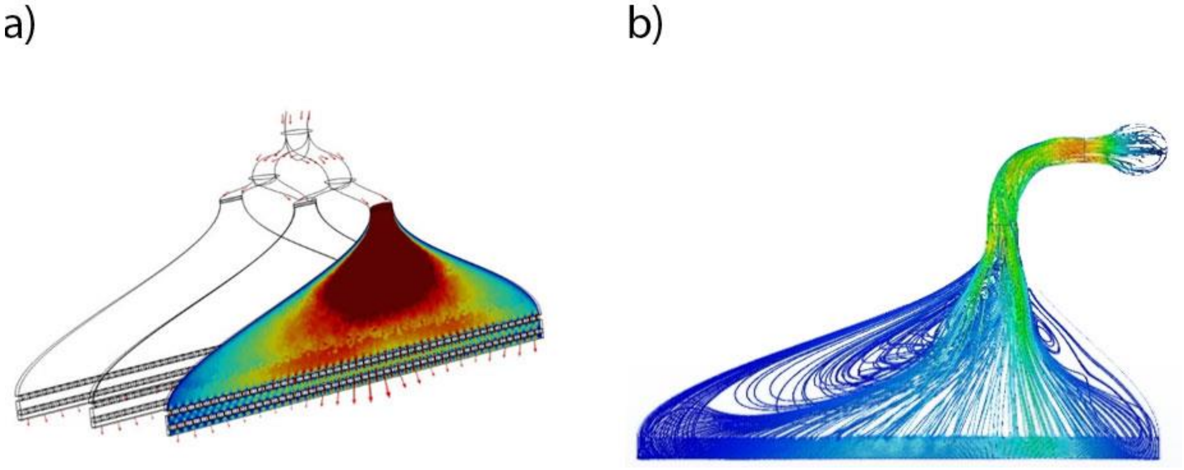

***Figure 4-14**. Comsol simulation for a) the inner channels corresponding to the oxidant (three outlets) and b) an inner channel for the metal channels (lateral view). Note how in (a) the arrows, which represent the velocity at the output, are not homogeneous. In (b) the velocity streamlines also represent a different velocity at the zone of the outlets.*

As seen in **Figure 4-14a**, the velocity profile of the flow is not homogeneous along the whole outlet. Indeed, although the pipe has an increase of the cross-sectional area of the channel to induce a spread of the flow in the expansion section of the channel, the velocity at the outlet presents a difference on the velocity output, with a maximum magnitude centered just below the injection of the flow into the expansion area. This effect is effectively reduced when the substrate is placed as at the close-proximity required for the SALD deposition but since the pressure influences the deposition rate, as seen in chapter 3, the non-homogeneous profile this shape induces was not desired.

Hence, although the version 3.7 of the deposition head achieved good results in terms of Cu_2O deposition (which will be presented on chapter 5), a new design for the deposition head was envisaged. However, for this design, CFD was included in the design workflow to validate the homogeneity of the flow.

4.5 Combination of both ideas

For the new design, it was decided, to ensure a homogeneous flow, to explore a more basic geometry in the outlet of the channel. Even though the integration of the deposition head into one single piece was kept, such idea was combined with the previous cylinder-box shape, found in the original multi-piece deposition head (***Figure 4-1*****b**).

With the dimensions extracted from the CFD analysis, a new design of inner channels for the deposition head was created. Following the same design workflow as designed in **Figure 4-4**, a new design was finished, which was called version 6.1. In the case of V6.1, two main changes were added to the deposition head. First, the geometry of the outlets was modified. It was decided that the width of the outlets of the gaseous reagents was extended to 0.75 mm, to avoid the issue of the reduction of print resolution with the high-temperature head mentioned before. Also, the width of the exhausts was modified independently to the reagent outlets, in order to allow for a better exhaust efficiency, also following the conclusions of the gaseous reagents intermixing explained on chapter 3. Second, the new cylinder-box geometry was used for the outlets, ensuring also a homogeneous flow, according to the CFD performed for this geometry. Finally, to simplify the printing and optimization, the number of channels was modified to one metal precursor, two oxidant outlets, 4 gas barriers and 2 lateral gas barriers, to confine the film deposition. **Figure 4-15** shows the process of fabrication of the V6.1 deposition head.

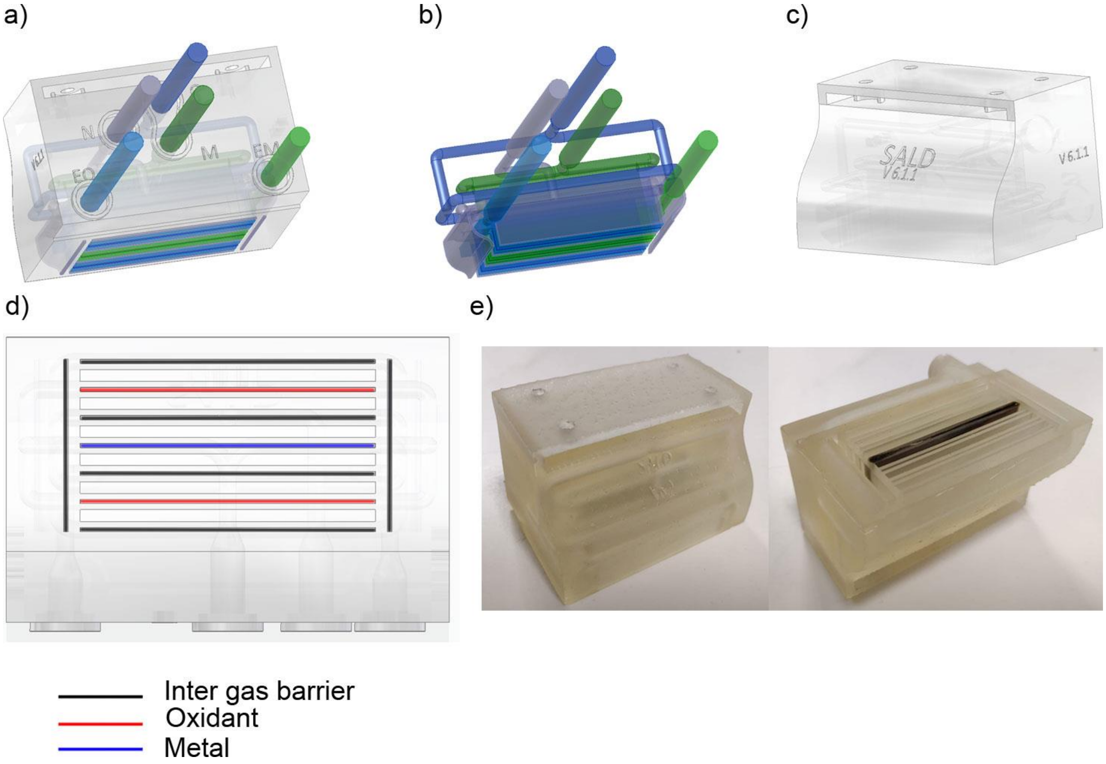

***Figure 4-15**. Design process of the latest integrated deposition head fabricated (version 6.1). a) Outer structure of the piece with b) inner channel structure. c) Final design of the version 6.1. d) Bottom view of the design showing the gas outlets and exhausts. e) Printed deposition head with inlet pipes and protection for the zones exposed to heat. The black line in the middle of (d) corresponds to the metallic precursor, in this case used with copper precursor, which causes a deposition with black color in the exhaust.*

The version 6.1 was successfully printed in both clear and high-temperature resin, and no faults on the print were observed: the gaseous outlets are well printed and the openings are well defined. Moreover, in this design, the previously added threads (**Figure 4-5**) and the post-print adding of fixing screws were replaced. The former was approached by a design on the inlets that allows to fix the pipes directly to the deposition head, and sealed with silicone. The latter was addressed by changing the design of the upper fixation. (**Figure 4-15c**)

The version 6.1 of the deposition head was also used for depositions of Cu_2O during this thesis, and the result will be also shown in chapter 5. Furthermore, as it will be shown also in chapter 5, the homogeneity of the deposited layers as well as the definition of the deposited area was greatly improved with this design. This was expected since the increase of the exhausts improves the removal of reagent remnants and by-products, hence promoting the exclusivity of ALD regime in the process.

This deposition head offers a solution to the homogeneity problem in the SALD deposition. Nevertheless, the alignment of the deposition head to obtain the close-proximity is difficult to obtain since the resin has the tendency to deform at the temperatures of deposition. Hence, it was decided that, to improve even further the homogeneity and to help obtain a better alignment in the close-proximity gap, a metallic version of the version 6.1 of the integrated deposition head was to be 3D printed. The metal 3D print process was obtained by Initial SAS (www.initial.fr), which provided an aluminum 3D deposition head of great quality. The dimensions are well respected, and the inner channels are well printed as per the flow tests performed. In this case, visual inspection of the inner channels is not possible since the deposition head is not transparent. The metallic version of the deposition head is shown in **Figure 4-16**.

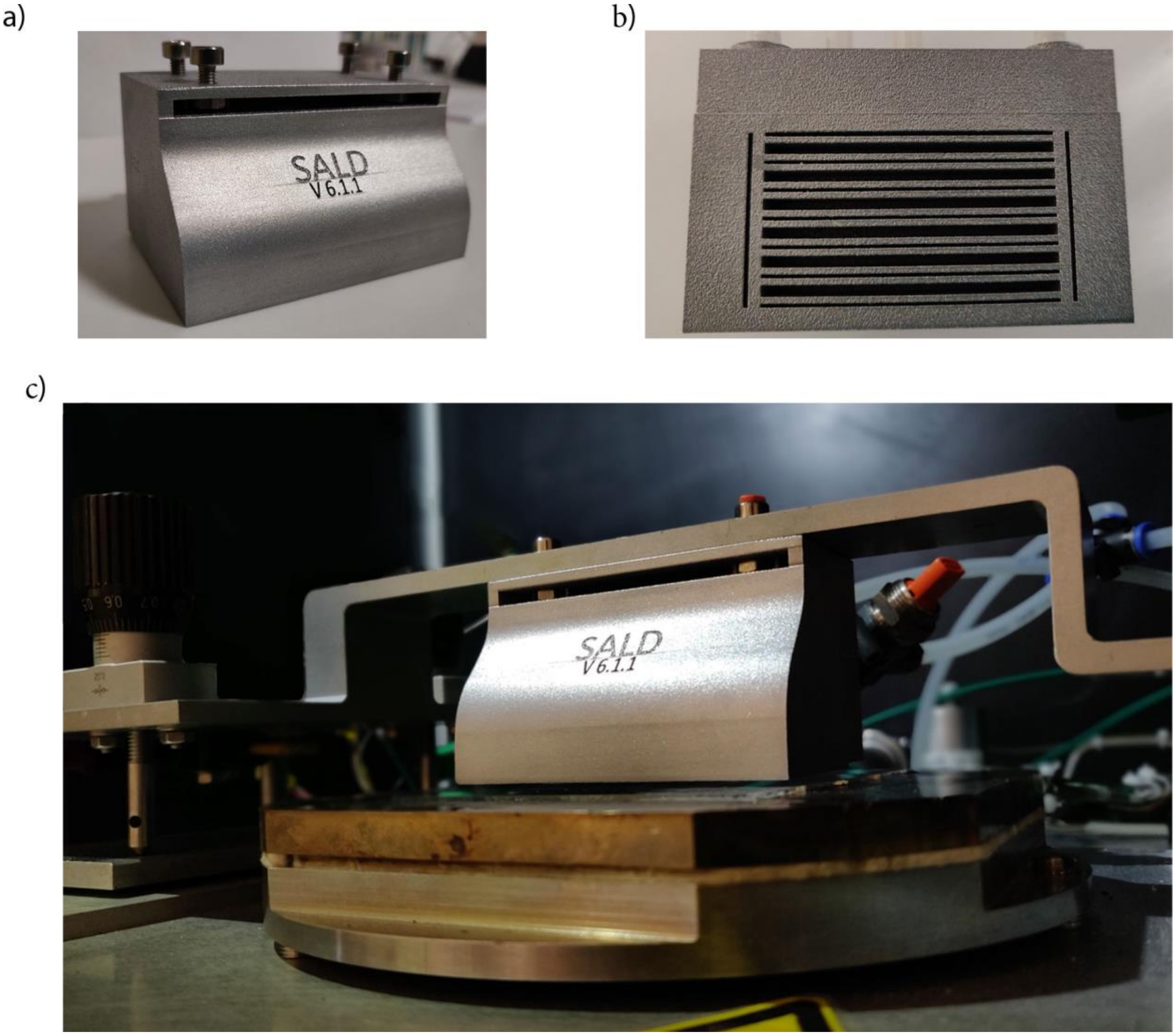

Figure 4-16*. Version 6.1 of the integrated deposition head 3D printed in aluminum. a) Front view, b) bottom view, and c) installed on the SALD system*

During this thesis the three versions of deposition head were used to deposit Cu_2O. Even though the deposition characteristics is different for each deposition head, the results were consistent enough to be comparable and study the Cu_2O thin films, as it will be discussed in chapter 5.

4.6 Miscellaneous designs towards novel concepts for area selective deposition

As the 3D printing of the deposition head was explored, the capabilities of the design workflow setup were explored for other designs that could exploit the advantage of the capabilities of 3D printing, ultimately leading to the capability of performing area selective deposition.

As mentioned in chapter 1, area selective deposition is an important challenge for thin film deposition and specially for ALD depositions. ASD is a patterning technique that allows for a bottom-up approach for nanoscale fabrication. If achieved, ASD would allow for a decrease on the number of steps in lithography in the semiconductor industry, potentially saving costs related to such processes [137]. In this work, the combination of customized 3D printed deposition heads with SALD, along with the static deposition approach presented in chapter 3, present a promising path towards scalable and cost-efficient ASD. For this, four different variations were designed as proof of concept for future designs.

4.6.1 *Smaller gaseous outlets*

One of the first applications for the flexibility of the design is the modification of the length of the gas outlets. In this case, it was desired to test the ability for deposition in smaller area, so, a deposition head with the same architecture of the version 6.1 but with length reduced to 25 mm was fabricated and it is shown in **Figure 4-17**.

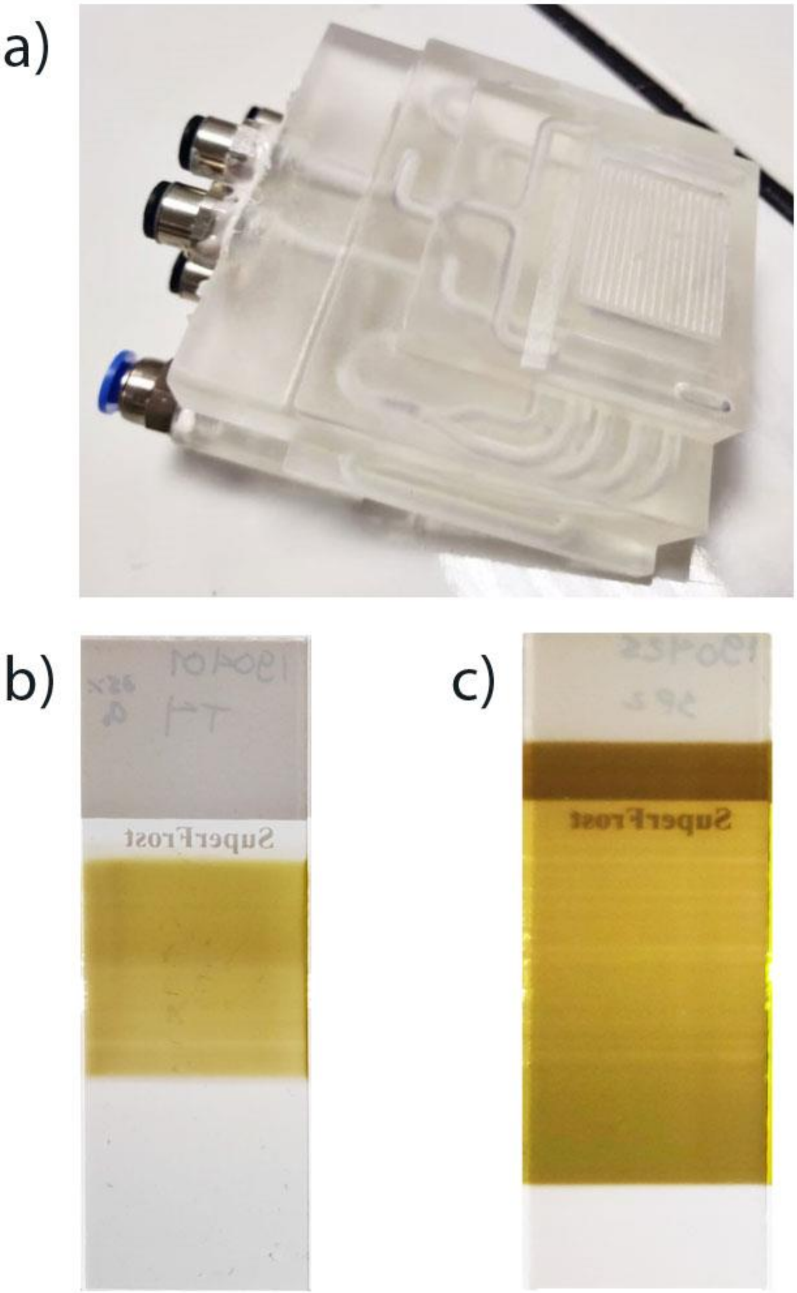

***Figure 4-17**. a) Picture of a variation of the deposition head, in which the outlets have a length of 30 mm (smaller than the original 50 mm) b) Picture of a deposition of Cu_2O with a deposition head with 30 mm outlet length. c) Picture of a deposition made with a deposition head with 50 mm outlet length, for comparison. Both depositions were made on standard microscope glasses (75 by 25 mm)*

The depositions with this head were successfully carried out in smaller area. However, for this it is important that the parameters are well adapted to the new design since the flows and concentrations of the reagents may be affected by this change. Still, the idea is a proof that simple changes like geometrical changes can be done with minimum effort, allowing for a more flexible deposition process.

4.6.2 *Inert Gas Protection Added*

A further tested idea was the addition of inert gas outlets in the deposition head. In this case, it was desired that, during the SALD deposition of air-sensitive materials, the exposure of the substrate to the air should be minimized. For this, several outlets were added to each side of the deposition head that would deliver inert gas, thus enlarging the surface of the deposition head with an inert gas flow to protect the substrate as it scans through the different regions from exposure to the atmosphere.

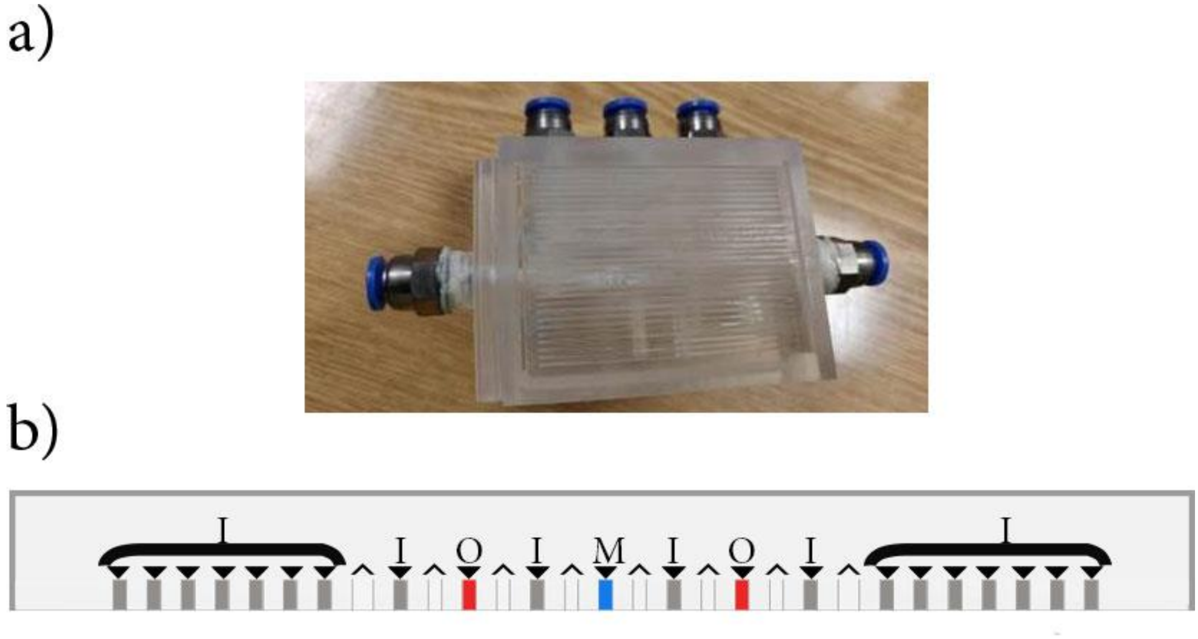

Figure 4-18. a) Deposition head fabricated with extra inert gas outlets. b) Schematic of the deposition head designed with extra inert gas outlets showing the outlets of inert gas (I), the metal line (M), the oxidant line (O), and the exhausts (upward arrows).

The design was created, and the piece was fabricated successfully, despite the complexity of the inner channels it required. To test, thin films of ZnO were deposited to prove the functionality of the head. This head thus provides a proof of concept of the fabrication of a complex geometry. The fabricated design is shown in **Figure 4-18**.

4.6.3 *De-phased Depositions*

A further idea explored involved the deposition of subsequent thin films, in different locations. In this case, the fabricated deposition head consisted of the same gaseous outputs with one extra output added for another metallic precursor. Furthermore, the gaseous outlets are shifted from each other so as to deposit layers in different zones in the substrate. This deposition head allows for the deposition of a multilayer architecture without the need to change any part of the system, and only by controlling the valves in the gas panel. **Figure 4-19** shows an image and a schematic of the design.

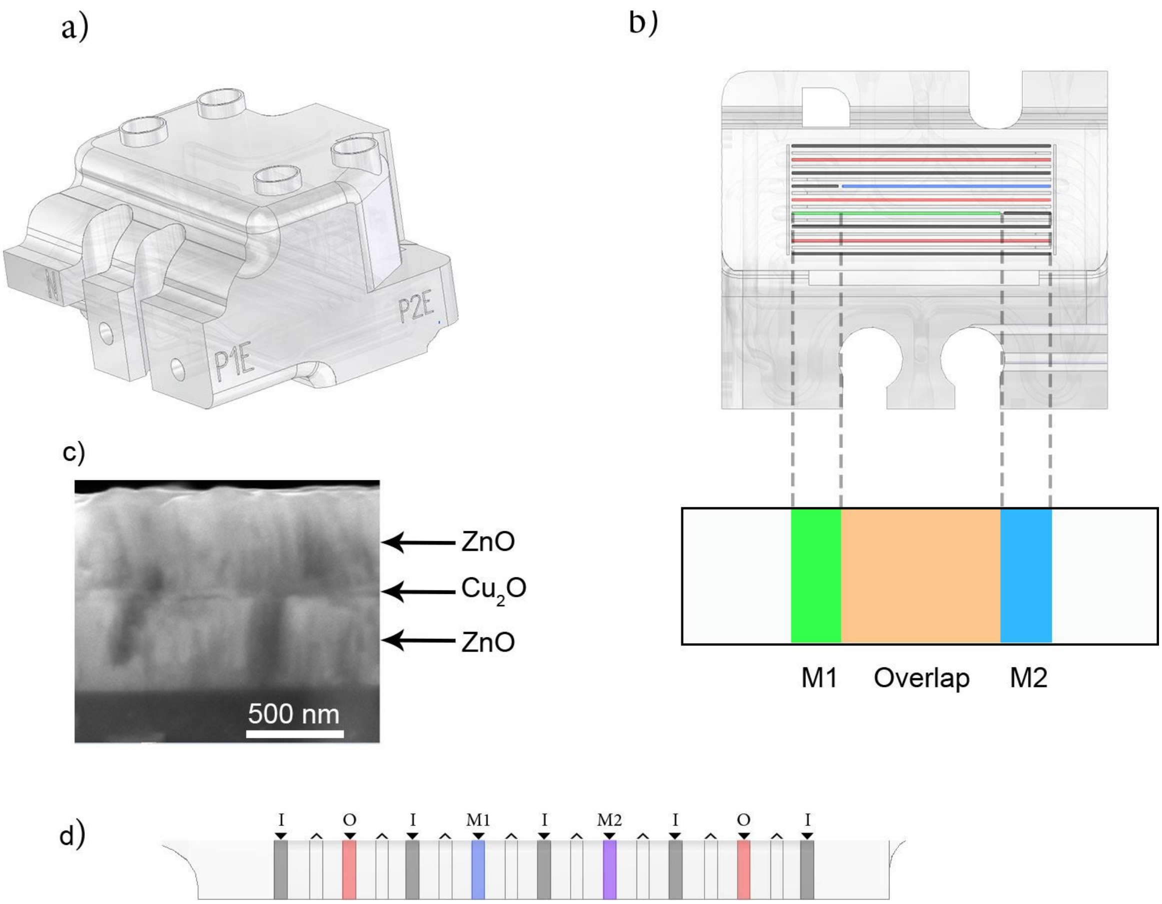

Figure 4-19. *Deposition head with two different metallic precursors. a) Quasi-isometric view of the design. b) Bottom view of the design. Here, the deposition head has two different exhausts for each metal precursor: one metallic outlet (M1) is positioned at a different position of the next metallic outlet (M2), causing three zones in the deposition: one with only M1, a zone in which both M1 and M2 are present, and one with only M2. This can be used with a continuous flow, or alternating the flow on each metallic outlet. c) SEM image showing the stack of layers deposited with this deposition head with DEZ as M1 and Cu(hfac)TMVS as M2 to obtain ZnO and Cu_2O, respectively. d) Cross section of the head, showing the gas outlets for the inert gas (I), the oxidant (O), 2 outlets for different metallic precursors (M1 and M2), and exhausts with an upward arrow.*

This deposition head was used to deposit subsequent layers of ZnO and Cu_2O.

As it can be seen, the deposition of the multilayers was a success and, although the thickness achieved with the Cu_2O was not high, it provided the proof that the multilayered deposition was possible. This idea can of course be expanded to multiple materials and to larger areas, getting closer to the concept of deposition of full devices with the same instrumentation and in a continuous in-line, large area fabrication. For this, the deposition of other materials should be mastered in the SALD, multiple precursor containers should be installed, and further automation of the gas panel should be performed to optimize the process.

4.6.4 *SALD Pen*

Finally, the concept of the deposition head was disrupted to create a so-called SALD Pen. The SALD Pen concept consists on gaseous channels that, instead of having a rectangular shape, form concentric circular outputs, each outlet surrounding the previous one. This was done to fabricate a deposition head that could deposit materials in a line, regardless of the direction of scan of the substrate. **Figure 4-20** shows the design of the SALD Pen.

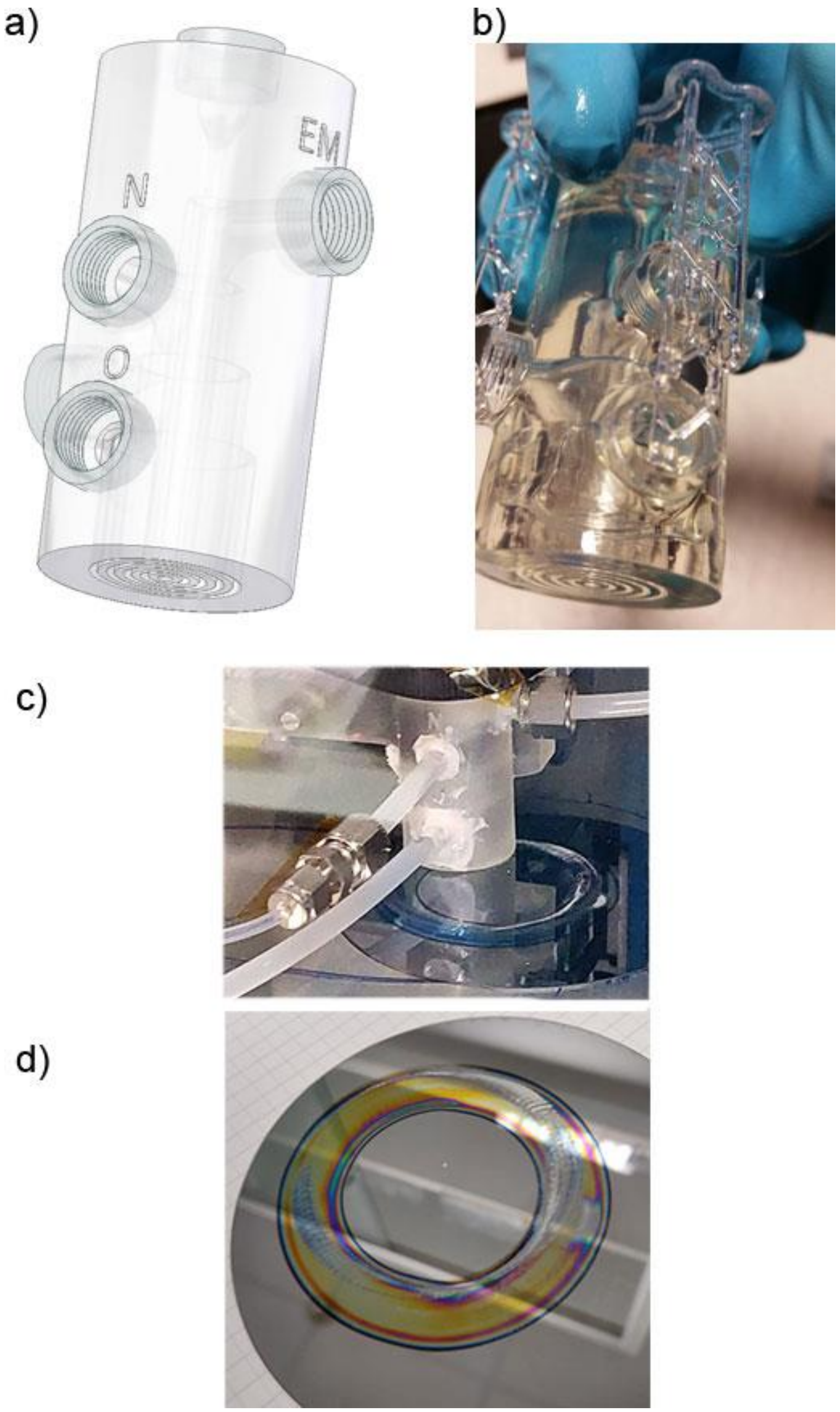

***Figure 4-20**. a) Design of the conceptual SALD Pen, in which the flows are separated concentrically. b) 3D printed SALD Pen as a test for its "imprimability". The design has not been tested during this thesis but further work at LMGP will verify the usability of this concept.c)the SALD Pen installed in a 3-axis table, scanning a circular shape on top of a 100 mm Si wafer. d) Deposition of a ZnO circular pattern achieved with a circular motion of the SALD Pen above the Si substrate.*

With this head, instead of a rectangular deposition, the deposition would consist on a simple line. This allows, with the help of a 2-dimensional patterned movement, to deposit in any shape or pattern desired. This is an interesting concept to the selective area deposition of SALD thin films and it would be interesting to fabricate mask-less patterned substrates. **Figure 4-20c** shows the deposition of ZnO obtained with a circular motion of the SALD on top of a 100 mm Silicon wafer. Although this is a preliminary test of the capabilities of the SALD Pen, it shows high potential for free-form depositions with materials compatible with SALD techniques. The circular film here shown shows imperfections evidenced by white parts and a “scratched” section. Such imperfections were caused by the same head during the movement, since the system hasn’t been optimized for parallelism between the SALD Pen and the substrate surface. Apart from the imperfections, the ZnO film has a rather homogeneous thickness all along the circular deposition, and it is believed that the thickness (which would indicate the spatial resolution of the deposition) can be enhanced by a better control of the gas outflow, as well as on a higher resolution 3D printed part. Finally, it should be mentioned that the circular shape was chosen given its simplicity of programming in the motion controller and that, with the SALD Pen installed and optimized, the deposition of arbitrary shapes would be straight-forward.

4.7 Conclusions and perspectives

As shown in this chapter, the process of design and fabrication of deposition heads that consist of a monolithic piece was created and setup at the LMGP laboratory. The design workflow allows for the design of an endless variety of variations for the deposition head, depending on the user’s needs. This gives unique advantages for the SALD system such as reducing the cost of fabrication and optimization of the deposition heads. Furthermore, different designs may be explored with this workflow, giving extra functionalities to use of deposition head. Such workflow is compatible with the fabrication of large-area deposition heads, which are in turn compatible with large-area deposition techniques such as roll-to-roll systems. Additionally, the workflow for the fabrication of 3D printed heads is useful for unconventional applications that allow for complex and low-cost fabrication. The workflow used in this thesis was also used for the development of additional pieces such as a plasma reactor (in collaboration with the laboratory GREMI, in the framework of an ANR project), which was based on the version 3.7 of the deposition head presented previously, and that can be adapted to the deposition head V3.7 for in-line plasma enhances SALD [138].

Further improvements of the design workflow should include a workflow that is closer to the simulation tools to predict the flow on the designed piece. This is especially important as larger area deposition designs are made since the homogeneity of the sample could be compromised and the design should ensure a correct flow. On the other hand, since the design-fabrication process can be done quickly, the design process may be adapted for each precursor, taking into account their physical characteristics such as viscosity and volatility.

Once all the tools and modifications needed in the SALD system were obtained, the deposition of Cu_2O thin films was performed in the SALD system. For the material, we concentrated our efforts on the fabrication and characterization of the microstructural, electronical and optical properties of the films. In the next chapter, the experimental results of the deposition and their characterization is shown, both as an interesting material, but also as validation of all the optimization performed in the SALD equipment done in this thesis.

Chapter 5

Cu_2O Thin Film Deposition

During this thesis, the SALD system at LMGP was modified and upgraded to include new heating control systems, new precursor bubblers and an optimized, monolithic deposition head that can be easily installed for studying new materials. The latter allows for low-cost screening of different geometries of the deposition head and the gap. Hence, the final part of this thesis is the testing of such SALD instrumentation upgrades for the deposition of Cu_2O thin films.

5.1 Cu_2O Precursors

Within the CVD and ALD processes, the research of the deposition of metallic copper for metal interconnection applications has led to the development of various types of copper-containing organometallic precursors. In particular, the copper(I) β-diketonate compounds are among the most common. Such compounds have the form of $Cu^I(\beta - diketonate)L$, where L represents a molecule used to stabilize the compound [139].

The chemical reaction that happens inside the CVD or ALD chamber is as follows. First, the precursor molecule $Cu^I(\beta - diketonate)L$ is adsorbed on the surface of the substrate. Then, thanks to the energy given by the heated substrate, the adsorbed species decompose following the equation:

$$Cu^I(\beta - diketonate)L_{ads} \longrightarrow Cu^I(\beta - diketonate)_{ads} + L_{(g)} \, , \qquad (1)$$

In which the stabilizing ligand L is desorbed in a gaseous form. Finally, in the case that this precursor, used to fabricate metallic copper films, a disproportionation reaction happens as follows:

$$2\, Cu^I(\beta - diketonate)_{ads} \longrightarrow 2Cu^{II}(\beta - diketonate)_{2_{(g)}} + Cu^0 \, , \qquad (2)$$

Desorbing gaseous $Cu^{II}(\beta - diketonate)_2$. This allows to incorporate metallic copper into the growing film. This whole mechanism is explained in [140] and [141], and it assumes no gas-phase reaction, which is perfectly adapted to ALD depositions.

Here, however, with the aim to deposit Cu_2O films, an extra mechanism is proposed. In the presence of water and enough thermal energy, the decomposition of the$Cu^I(\beta - diketonate)_{ads}$ molecule in Equation (1) can be decomposed as follows:

$$2\, Cu^I(\beta - diketonate)_{ads} + H_2O \longrightarrow Cu_2O_{ads} + 2\, H(\beta - diketonate)_{(g)}\,, \qquad (3)$$

Thus, incorporating Cu_2O to the growing thin film, and desorbing gaseous $H(\beta - diketonate)$ species. A similar mechanism is proposed in [142], where the $Cu^I(\beta - diketonate)_{ads}$ reacts with hydrogen to produce $H(\beta - diketonate)$ species, supported by its observation with a mass spectrometer.

With respect to the precursors used in this work, the β-diketonate compound that has been found to yield a relatively high vapor pressure and high deposition rate (although for copper metallization) is the molecule 1,1,1,5,5,5-hexafluoroacetylacetonate, also referred to as (hfac) [140]. On the other hand, as for the stabilizing L molecule, among those found to provide better stability to the precursor are vinyltrimethylsilane (TMVS) [143]–[145], trimethilphosphine (PMe_3) [146], and 1,5-cyclooctadiene (COD) [147]. In this thesis, due to the stability they provide, and due to the availability at the LMGP, precursors with the ligands TMVS and COD were used to carry out Cu_2O depositions. Two different copper(I) β-diketonate compounds were thus used as precursors for the Cu_2O thin films in this work. In both precursors the β-diketonate is hfac. The one containing TMVS will be called Cupraselect (after the commercial name used by Air Products), and the latter one will be called CuCOD. Cupraselect is a yellow/green liquid with a boiling point at 55 °C, while CuCOD is a bright yellow solid (powder) with a melting point of 85 °C. Figure 5-1 shows the chemical structure for these precursors.

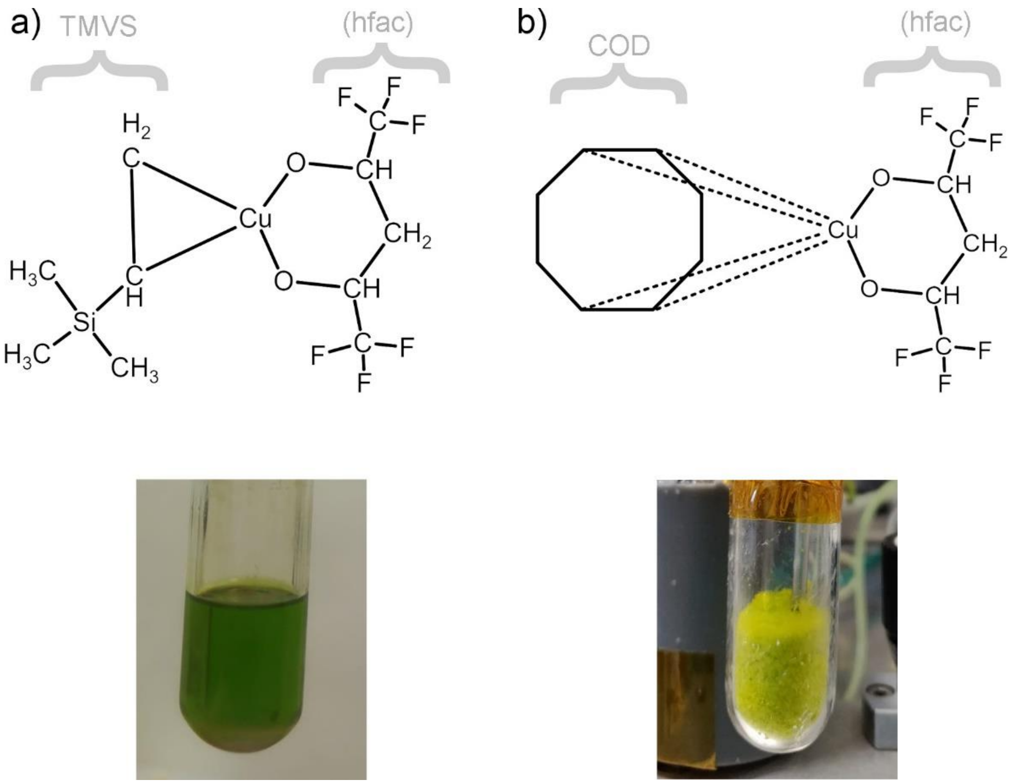

Figure 5-1. Chemical structure and photography of each precursor: Cu(hfac)TMVS (a) and Cu(hfac)COD (b).

For these precursors, Equation (3) seems to be supported by reference [142], where the authors report that one of the products of the decomposition of the Cupraselect precursor in a CVD reactor is indeed $H(hfac)$.

Regarding the volatility of the precursors, diethylzinc (DEZ), a common precursor used to deposit ZnO in CVD and ALD reactors, and used at LMGP with the SALD system, is taken as a point of comparison. The reported values of vapor pressure of DEZ range from 105 mTorr [148] to 262 mTorr [124] at 25 °C. Considering these values, the vapor pressure of the Cu_2O precursors used here is considerably low, having a value of 60 mTorr for the Cupraselect precursor [149] and 0.5 mTorr for the CuCOD precursor [141] at the same temperature. This low volatility may be due to the high molecular weight of the copper precursors that have a value of 370.8 g/mol for the Cupraselect precursor and 378.8 g/mol [150] for the CuCOD precursor [151]; values that are high compared with the molecular weight of DEZ, which is of 123.5 g/mol [152]. Given these values, and to improve the delivery of precursor to the substrate, heating is needed to increase the precursor concentration extracted from the bubblers, justifying then the installation of heating systems in the new bubblers of the SALD system. However, it is important to note that, for the Cupraselect precursor, increasing the temperature decreases its stability [149], phenomenon that will be studied further in this chapter.

To address the relatively low volatility of the precursors here used, the Cu_2O dedicated bubblers installed in the SALD system were enhanced with a heated bubbler system that heats the precursor and the pipes that carry the gaseous reactants, up to the inlet of the deposition head. This allows for the increase of volatility of the precursor and, thus, the extraction of a higher concentration of precursor to the carrier gas. It would be ideal that the deposition head was heated as well, but, due to technical complexity, this was not done during this thesis.

5.2 SALD Cu_2O depositions: initial material properties

The conditions for the deposition of Cu_2O were tested and Cu_2O was successfully deposited. For the first tests, the Cupraselect precursor was selected for the deposition of the thin films. This was the case given that the precursor is in liquid form, which makes it compatible with a "conventional" bubbler on the SALD system, in which the created bubblers were based upon. In addition, Cupraselect had already been used to deposit Cu_2O by SALD [36], [113].

With the bubblers in place and the version 3.7 of the deposition head installed (discussed in chapter 4), the SALD system was setup with the parameters shown in Table 5-1. The values on each of the gaseous outputs of the deposition head were chosen so that they provide an equilibrated flow and that the phenomena present on the deposition gap were as close as possible both to the real head, and to the simulations made in Comsol and presented in chapter 3. The scan speed of 50 mm/s was used to maintain similar motion parameters as previously tested for ZnO depositions. Before the actual deposition, several SALD oscillations were made to allow for the gas pipes and the deposition head to become saturated with the precursor molecules, allowing for a successful delivery of reagent concentration to the substrate. Such saturation is performed with a dummy lime-glass substrate, which is used to observe film formation, thus indicating delivery of reagents to the substrate. After this saturation cycles were performed, the lime-glass substrate was installed on the support, and the deposition of Cu_2O started.

***Table 5-1**. Deposition parameters for initial Cu_2O depositions with Cupraselect precursor.*

Precursor Flow [SCCM]	**Precursor Dilution Flow [SCCM]**	**Precursor %**	**Water Flow [SCCM]**	**Water Dilution Flow [SCCM]**	**Water %**
150	100	60%	100	275	26.67%

Bubbler Temperature	**Substrate Temperature**	**Scan speed**
60 °C	170 °C	50 mm/sec

After 750 SALD oscillations (which corresponds to 3000 ALD cycles), the deposition of a Cu_2O film was successfully achieved. The film presents a transparent, yellow color, characteristic of Cu_2O when the thickness of the film is in the order of tens of nanometers. Figure 5-2a shows a cross-sectional SEM image of the Cu_2O layer deposited, showing a homogeneous and flat film with a thickness of 55 nm. Figure 5-2b shows an optical photography of the Cu_2O film deposited on the glass substrate. It can be seen that the layer is homogeneous along the whole substrate as judging by the color of the film and by the SEM cross section image of the film.

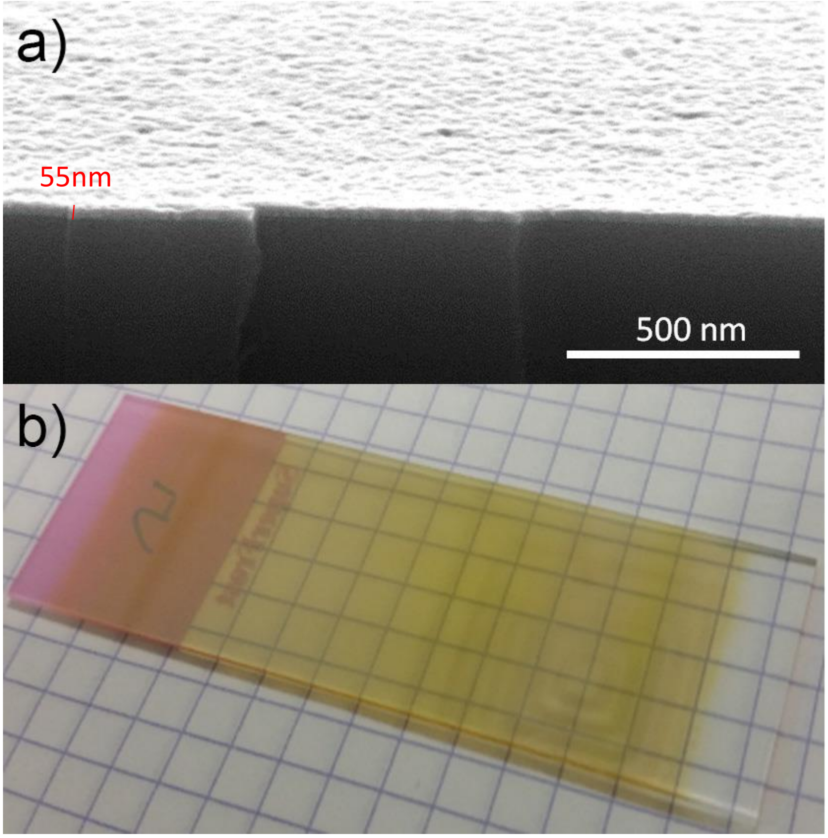

Figure 5-2. *a) Cross sectional SEM image of a Cu_2O layer deposited on a glass substrate. b) Optical photography of a 55 nm thin film of Cu_2O deposited with SALD on a glass substrate.*

5.2.1 *Topography analysis of the deposited Cu_2O film*

To characterize the surface of the Cu_2O layer, XRR measurements and subsequent fitting were performed. After the fitting of the signal observed (shown in Figure 5-3a), the thickness was confirmed to be 55 nm, with a roughness of 2.4 nm and a density of 5.7 $g\cdot cm^{-3}$, which is close to the theoretical value of 6 $g\cdot cm^{-3}$. Figure 5-3b shows an AFM measurement of the surface showing a roughness of 4.8 nm with a grain size of ~60-80 nm (Figure 5-3c).

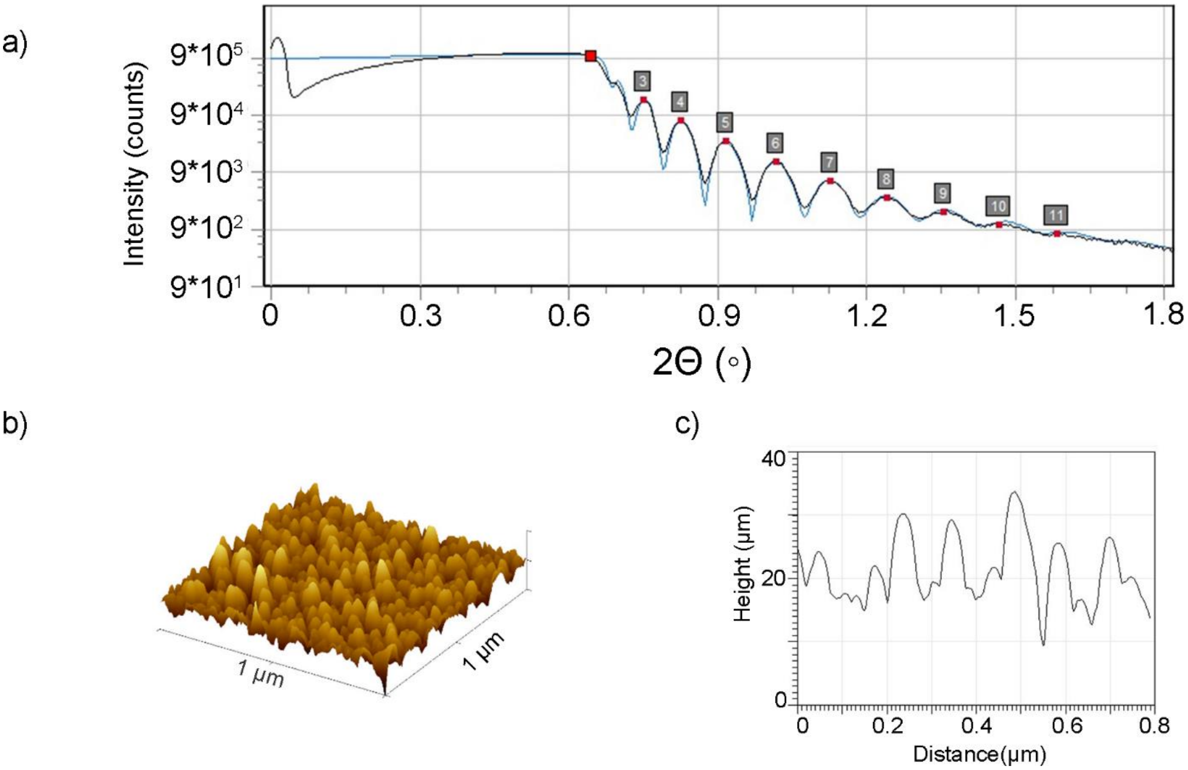

***Figure 5-3**. a) XRR measurement and fit of the first Cu_2O layer deposited with SALD. b) AFM micrograph of the surface of the Cu_2O layer showing a roughness of ~4 nm and c) corresponding profile of the AFM micrograph, showing a grain size of around 60-80 nm.*

The thickness measured by XRR and SEM corresponds to a growth per ALD cycle (GPC) of 0.03 nm/cycle, which is in accordance with the conventional ALD growth of Cu_2O thin films [153], [154], and similar GPC as well for a previous SALD report [36]. However, there are multiple parameters to consider that may affect the growth rate of the thin film, as it will be detailed further in this work.

5.2.2 *Raman spectroscopy: vibrational fingerprint of Cu_2O*

In order to confirm the existence of the Cu_2O phase, Raman spectroscopy was used to compare this film with a reference of powder Cu_2O measured previously at LMGP. Raman spectroscopy was used given its ability to perform non-destructive analysis, while giving a clear fingerprint of the material scanned. Figure 5-4 shows the Raman spectrum of the layer previously shown in Figure 5-2, as well as a Raman spectrum of powder Cu_2O as reference, measured with a wavelength of 488 nm.

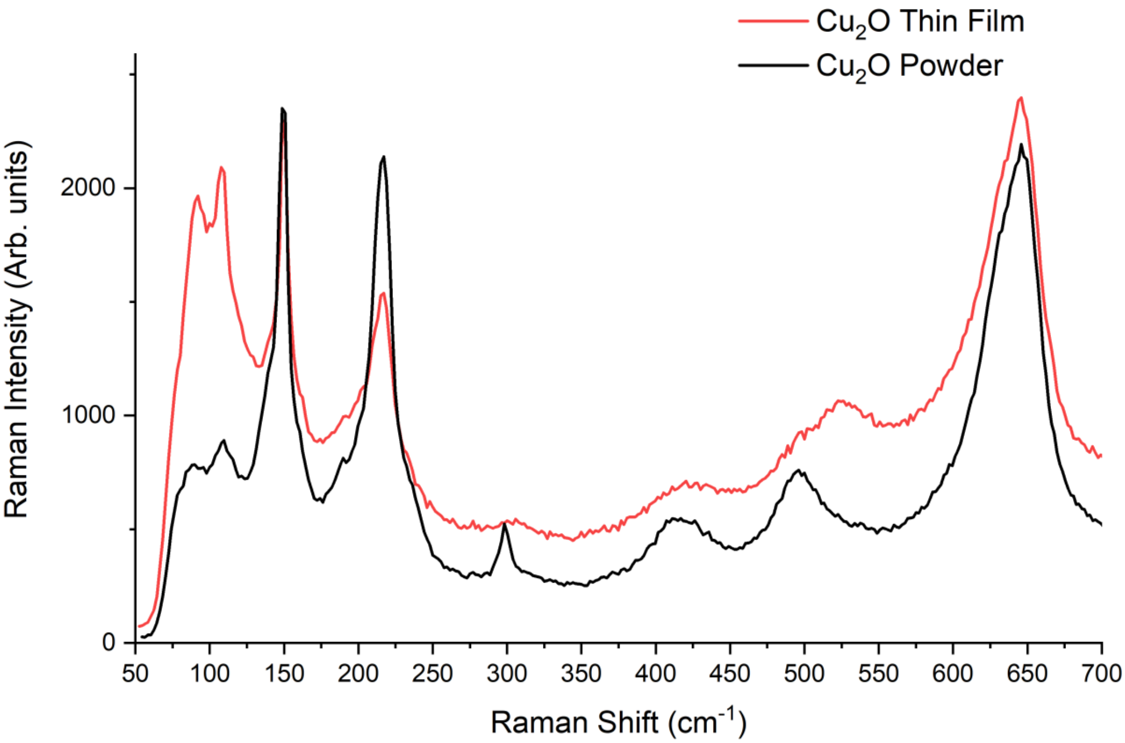

Figure 5-4. *Raman spectra of the Cu_2O thin film deposited with SALD (in red) and the reference powder Cu_2O, taken at LMGP.*

The peaks observed in Figure 5-4 correspond well to the Cu_2O powder reference at LMGP for most of the peaks as listed Table 5-2, which shows a summary of the peaks present in the Raman spectra of Cu_2O found in literature.

Different types and synthesis procedures of Cu_2O are presented, ranging from a 20 µm single crystal [155], a Cu_2O annealed microcrystal [156], chemical synthesis [157], hydrothermal synthesis of microcubes and microspheres [158], electrochemical deposition [159], exploding wire nanoparticle synthesis [160] and thermal oxidation [161].

***Table 5-2**. Literature review of the appearance of Raman peaks for Cu_2O in diverse morphologies, and comparison with LMGP powder Cu_2O reference and the peaks found in this work.*

	Wavenumber for Cu_2O Peaks (cm^{-1})								
Vibrational Mode	**Ref** [155]	**Ref** [156]	**Ref** [157]	**Ref** [158]	**Ref** [159]	**Ref** [160]	**Ref** [161]	**LMGP Powder**	**This work**
Raman mode	86	-	-	98	-	-	-	89	91
$\Gamma12^-$	110	109	-	-	-	105	109	108	107
$\Gamma15^-$ (LO)/V_O	152	154	164	154	150	147	154	150	150
Cu_2O crystals	-	218	219	218	220	219	218	216.5	216.5
$2\Gamma15^-$	-	-	-	-	-	298	308	298.2	306.5
$4\Gamma12$	-	-	413	408	417	410	436	414	421
$\Gamma25^+$	515	515	-	524	-	535	515	496	523
$\Gamma15$ (TO)	633	-	628	620	625	636	635	645	645
2nd $\Gamma15^-$ (LO)	662	665	-	-	-	-	665		

Visible in Table 5-2, one of the peaks that is common to all the references here cited is the peak centered at ~150 cm^{-1}. This peak, henceforth called V_O peak is one of the most characteristic peaks of Cu_2O, and it also appears in the Raman spectrum of the Cu_2O deposited with the SALD system. This peak has the benefit that no other peaks corresponding to other vibrational modes in the Cu_2O or CuO crystal are close to it, making it easily identifiable. The mode of this peak corresponds to the $\Gamma15^-$ longitudinal optical (LO) vibrational (phonon) mode in the Cu_2O lattice. In some reports such mode is attributed to the vibration, and hence existence, of oxygen vacancies [157], [159]. Since in this work the presence of oxygen during deposition of the Cu_2O films is studied, this peak will be useful for understanding the influence of oxygen in the Cu_2O growth.

As for the peak at ~300 cm^{-1}, some reports [160], [161] attribute it to a 2nd order vibration of the $\Gamma15^-$ ($2\,\Gamma15^-$), while others attribute it to the existence of CuO, along with peaks at ~342 cm^{-1} and ~627 cm^{-1} [157], [159], [162]. The latter coincides also with the $\Gamma15^+$ vibrational mode in Cu_2O and, for this reason, the peak that can identify the existence of CuO is the one appearing at ~342 cm^{-1}. Along this thesis, and for simplicity, the usage of the term “CuO peak” will refer to such peak.

One of the biggest challenges for Cu_2O deposition with any method is the presence of CuO phase in the film. This is not desirable for electronic applications since these two materials have considerably different band gap. Considering the fact that Raman spectroscopy is one of the most sensitive to CuO identification, it is worth to note that in the above Raman spectra (and for all depositions done in this work), no CuO peak is visible, suggesting a deposition in which any CuO quantity present in the film would be below the detection limit of Raman spectroscopy.

5.2.3 *Electrical conductivity and annealing*

To characterize the electrical conductivity of the Cu_2O film, 4-point probe (4PP) measurements were performed on its surface. The measured sheet resistance of the film is 49 MΩ, which, with a thickness of 55 nm, corresponds to a resistivity of 260.8 Ω·cm. This value of resistivity is also within the order of magnitude of Cu_2O deposited by different methods, as shown in Table 1-1, and compares well with previous reports on the deposition of Cu_2O by SALD using the same precursor [36].

In order to investigate the source of the conductivity in the Cu_2O thin film, the sample was annealed at 250 °C for 1 hour and let to cool down naturally to room temperature. Figure 5-5a shows the sheet resistance as a function of the annealing temperature of the Cu_2O film. Figure 5-5b shows the Arrhenius plot of the resistivity versus the temperature for the cooling down section of the annealing.

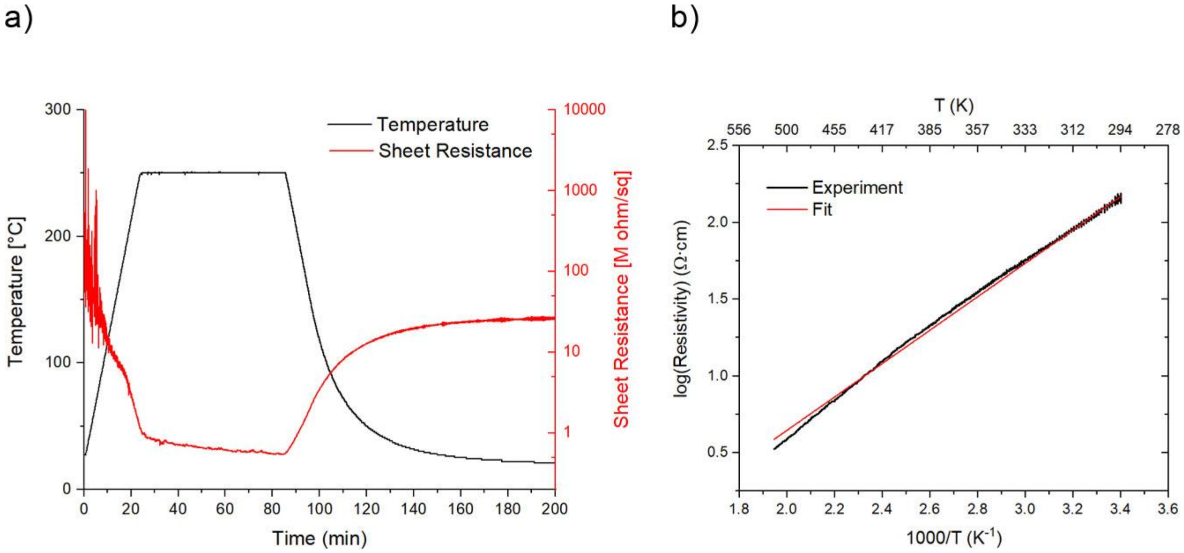

Figure 5-5. *a) Annealing graph of the Cu_2O layer deposited with SALD. b) Arrhenius plot for the cooling down of the annealing part, along with a linear fit to extract an energy of activation of 1.08 eV.*

It can be seen that the conductivity of Cu_2O film improves after annealing. The sheet resistance measured decreases with the increase of the temperature and even when the temperature remains constant at 250 °C. This suggests that defects responsible for p-type charge carriers, which in the case of Cu_2O are attributed to copper vacancies (V_{Cu}), are being thermally activated. Moreover, since the resistivity improves during the temperature plateau and after annealing to approximately 20 Ω·cm, it would be reasonable to think that some reorganization in the polycrystalline film and possibly, formation of additional V_{Cu} happens. This could be possible by oxygen interaction or its in-diffusion since the annealing was carried out in open air. Continuing the analysis, from the Arrhenius plot, the activation energy of V_{Cu} (and possibly their formation) is calculated from the slope to 1.08 eV. This value is high but it is consistent with the values corresponding to the vacancy formation enthalpy calculated for oxygen-rich environments, using the Heyd–Scuseria–Ernzerhof Density Functional Theory (DFT-HSE) and reported in [163].

This analysis sheds light to the possibility that, as deposited with the conditions used for the Cu_2O film, the activation of V_{Cu} defects is not complete at room temperature or not sufficient density of this defect is generated. Hence, if films with higher density of V_{Cu} are deposited, the resistivity should reasonably decrease. Moreover, the oxygen-rich atmosphere in the SALD system (the film is exposed to air on every oscillation) appears to have a benefit on the conductivity of the film, phenomenon that will be explored during the depositions and that will be presented further in the current chapter.

5.2.4 *Effect of Scan speed*

As the sample in the SALD reactor oscillates back and forth under the deposition head, the effect of the speed on which it moves, the scan speed, is a parameter that can be easily modified and it allows for a control on the residence time of the sample in each region of the SALD reagents. Here, three different speeds were screened, and the parameters measured are shown in Figure 5-6.

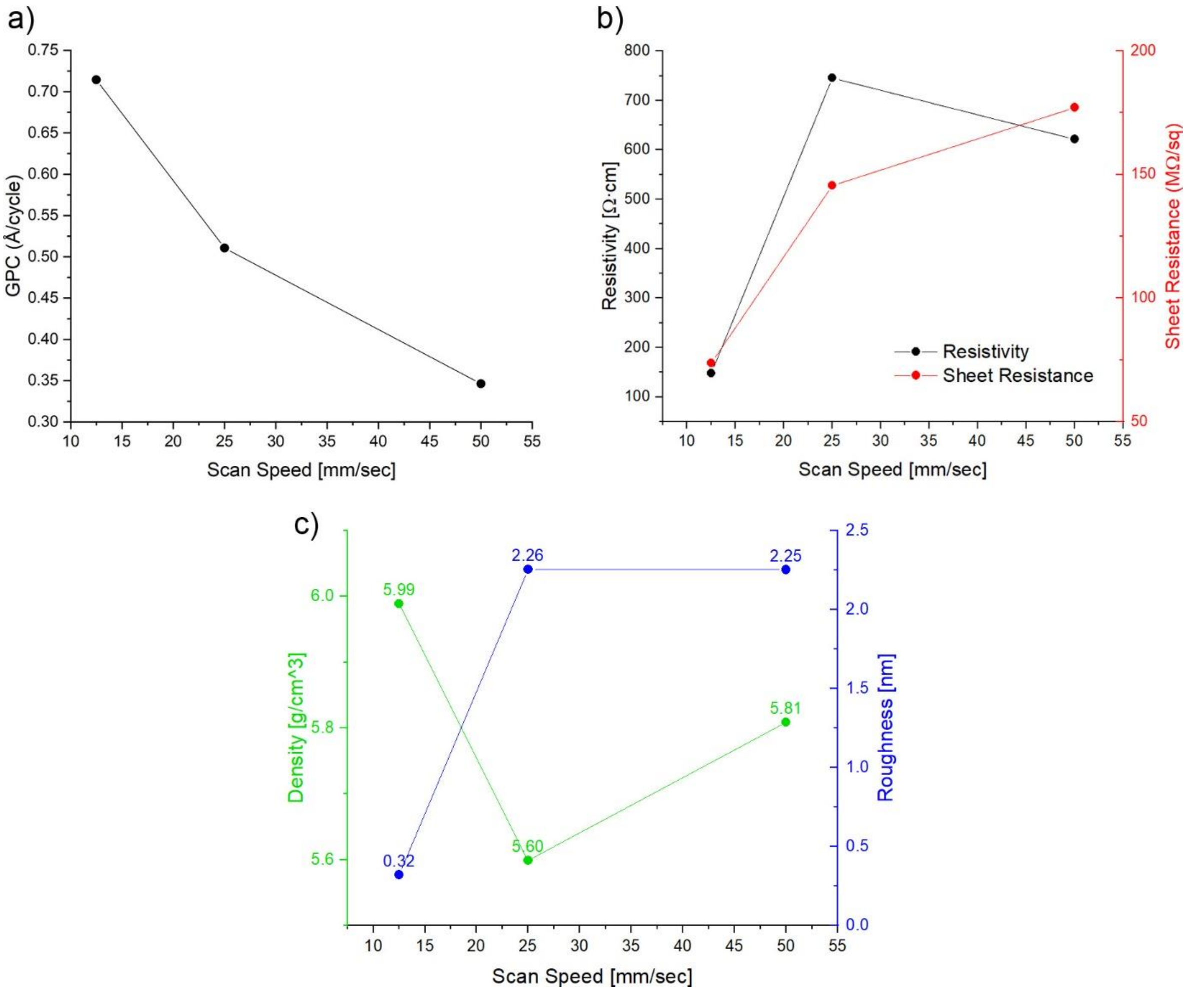

Figure 5-6. *GPC (a), Resistivity (b), Density and roughness (c), plots as a function of the scan speed of the SALD.*

As seen in Figure 5-6, the scan speed affects the properties of the Cu_2O films deposited. Figure 5-6b shows the resistivity and the sheet resistance of the samples deposited. The graph suggests that, at low scan speeds, the film is more conductive, probably due to the higher density and lower roughness of the deposited film (shown in Figure 5-6c), which may be positively impacted since lower speeds may allow for a better surface chemical reaction at every cycle, thus, creating a more compact film.

On the other hand, Figure 5-6**Figure 5-6.** GPC (a), Resistivity (b), Density and roughness (c), plots as a function of the scan speed of the SALD.a shows the GPC of the deposition for each speed. Contrary to what was expected, it can be easily seen that lower speeds increase the GPC. Since ALD relies on a surface saturation, increasing the residence time (by lowering the scan speed) should not increase the GPC. The unexpected result suggests that the chemical reaction in each reactant region does not saturate the substrate and, what is even more impacting for the film properties, the remnants of the reagents may not be removed properly. Thus, it is possible to conclude that lower scan speeds are beneficial for the layer morphological and electronic properties. Nevertheless, lower scan speeds affect the deposition time since, for a lower scan speed, the time per cycle increases as well. Still, this parameter is relatively simple to control, and it may lead to better material properties.

5.3 Effect of the deposition gap on the Cu_2O properties: ALD vs CVD regime

Another of the important parameters to optimize and following the (finite element method) FEM study presented in chapter 3, is the gap between the substrate and the deposition head. According to the simulations presented previously in this work, as the deposition gap increases, the intermixing of the gaseous reagents increases as well, gradually shifting the deposition mode from an ALD mode, which is enabled by small values of deposition gap (~ 150 µm), to a CVD mode, as the deposition gap increases.

To test the effects on the deposition gap, two different depositions of Cu_2O films were made at different values of gap and their electrical and microstructural properties were characterized.

5.3.1 *Morphology*

Figure 5-7 shows SEM images of two Cu_2O films deposited at 190 °C with a balanced flow of gases and an optimized flow through the bubbler. The number of SALD oscillations for both samples was 1000, which, since the process used the V3.7 of the deposition head, the equivalent number of ALD cycles is 4000. Regarding the distance from the substrate to the deposition head, a gap of 1000 µm (CVD regime) was used for the sample presented in Figure 5-7a, while a gap of 150 µm (ALD regime) was used for the sample presented in Figure 5-7b. As it can be seen, the microstructure of the layers shows slightly different morphology on each of the depositions made. For the CVD regime deposition, bigger and more faceted grains can be seen, while for an ALD regime deposition the diameter of the grain seem smaller.

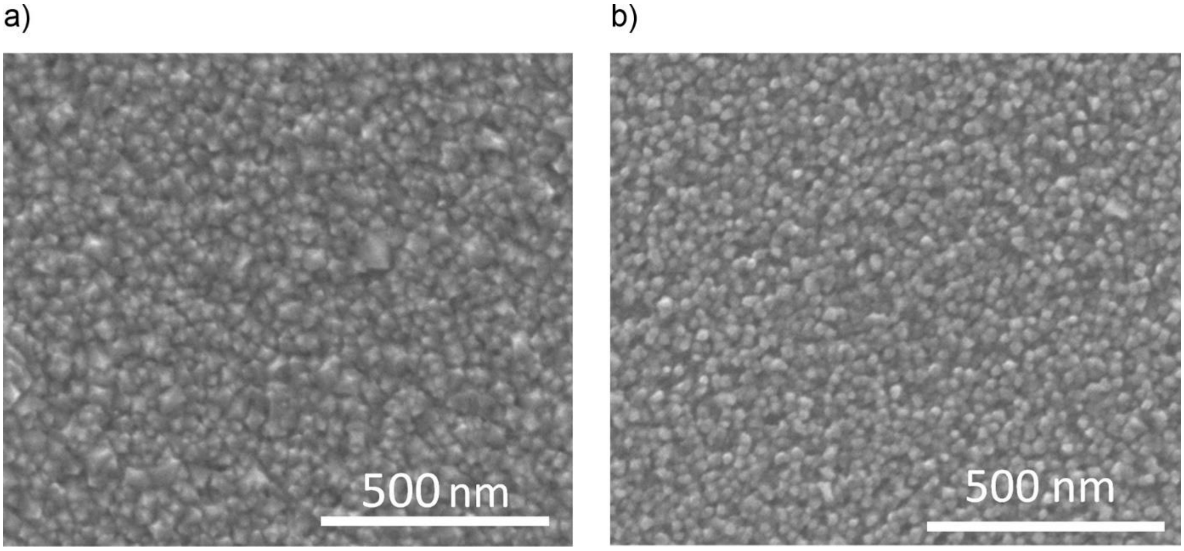

Figure 5-7. *SEM images of Cu_2O films deposited in CVD regime using a gap of 1000 µm (a) and ALD regime using a gap of 150 µm (b).*

For the deposition with a CVD regime, the GPC was 0.0225 nm/cycle, while for the deposition with an ALD regime, the GPC was 0.0125 nm/cycle. Hence, since the GPC is different for each deposition, the thickness of the sample was not the same and its thickness was estimated by AFM measurements on the edge of an etched part of the layer to 90 nm and 50 nm, respectively. As predicted in chapter 3, the growth per cycle was higher when performing depositions at a high gap, since a CVD regime leads to a non-self-limited surface reaction, causing a higher reaction rate and, thus, increasing the GPC.

Nevertheless, XRD was performed on each sample since the morphology had a different appearance, and it was desired to investigate if the change of the shape of the grain was due to the thickness or due to a change on the properties of the material.

5.3.2 *Texture and Electrical Conductivity*

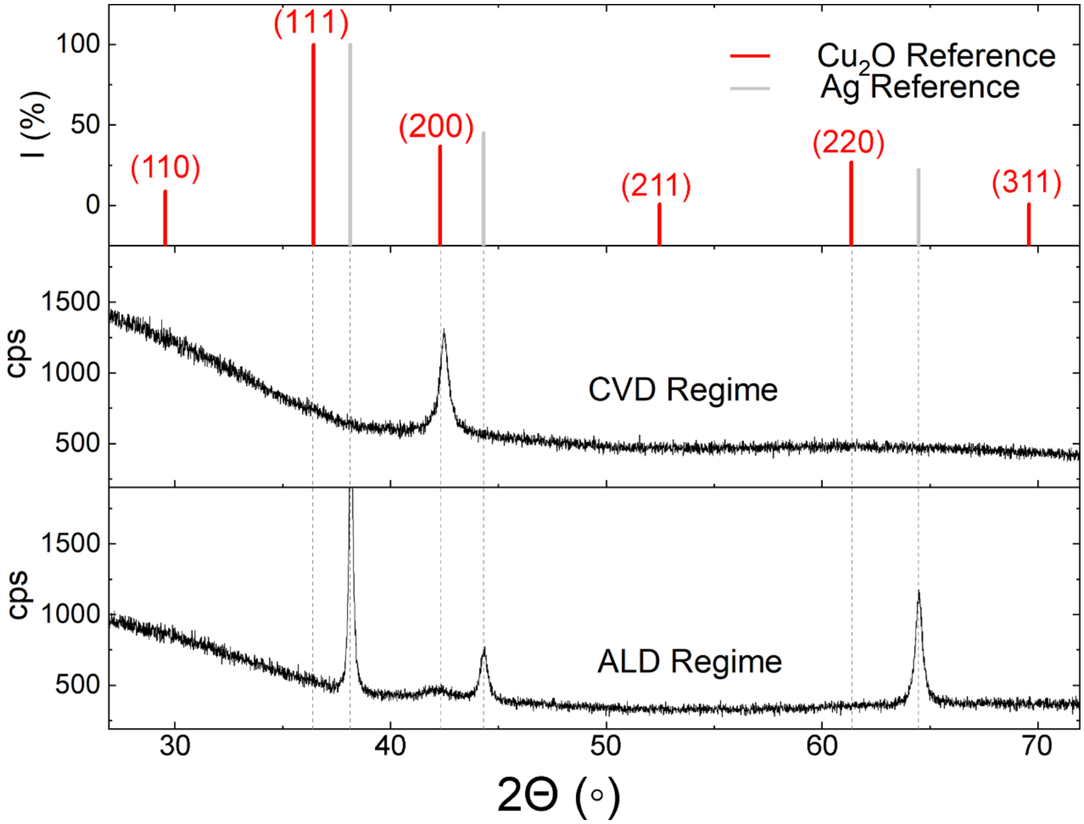

Figure 5-8. *XRD patterns for Cu$_2$O thin films deposited in CVD and ALD regime, compared with the reference peaks (in red). The appearance of Ag peaks (in gray) is due to the contacts applied to the substrate in order to characterize electrical properties.*

Figure 5-8 shows the XRD patterns in Bragg-Brentano configuration for the samples grown with a CVD and an ALD regime. Since the sample had been prepared for electrical measurements, the peaks of Ag also appear on the diffraction pattern.

It is possible to see in the diffraction pattern of the layer grown in a CVD regime that the layer presents a well crystallized Cu$_2$O phase with a preferred (200) orientation. Note, that this peak is slightly shifted to higher angles, suggesting some lattice distortion due to the polycrystalline phase, the presence of vacancies or stress in the lattice. On the other hand, the XRD pattern of the layer grown in an ALD mode suggests that the layer deposited was less crystallized, with a slightly visible peak at the same (200) reference position for the Cu$_2$O. It should be noted however that the change on intensity of the peak may be due to the change of thickness of the deposited film.

To continue with the characterization of both layers, the resistivity of the layers was estimated with a 4PP sheet resistance measurement. Table 5-3 shown the characteristics of the layers grown in each mode.

Table 5-3. Comparison of CVD and ALD regime for the Cu_2O films deposited.

Deposition Gap	SALD Oscillations	Growth Mode	Layer Thickness (AFM)	Resistivity (4PP at LMGP)
˜150 um	1000	ALD Regime	˜50 nm	9.3 Ω.cm
˜1000 um	1000	CVD Regime	˜90 nm	33.1 Ω.cm

The measurements made suggest that for the layer grown in an ALD regime, the conductivity was one order of magnitude lower than for the CVD sample, even though the thickness of the layer was not the same. However, due to the thickness difference, another deposition with the same deposition parameters as the ALD regime was made, and the number of cycles was defined to yield a layer of approximately 90 nm of thickness (comparable with the film grown with a CVD regime). This would allow to verify that the difference on the XRD patterns for the CVD and ALD mode is not just an effect of the thickness of the layers.

However, since the depositions at this point had a promising outcome with respect to the conductivity, it was desired that one deposition process should coat two samples at the same time, so that more destructive and non-destructive characterization could be performed. The SALD technique provides a straightforward method to achieve this: by increasing the length of the back-and-forth scanning movement (the scanning distance), two samples can be coated at the same time by placing them next to each other and scanning them under the deposition head gaseous outlets. This modification to the process was successfully performed in the SALD. However, the fact that the scanning distance is increased, exposes each sample a longer time to the atmosphere. Thus, it is interesting to see how this would affect the Cu_2O deposition.

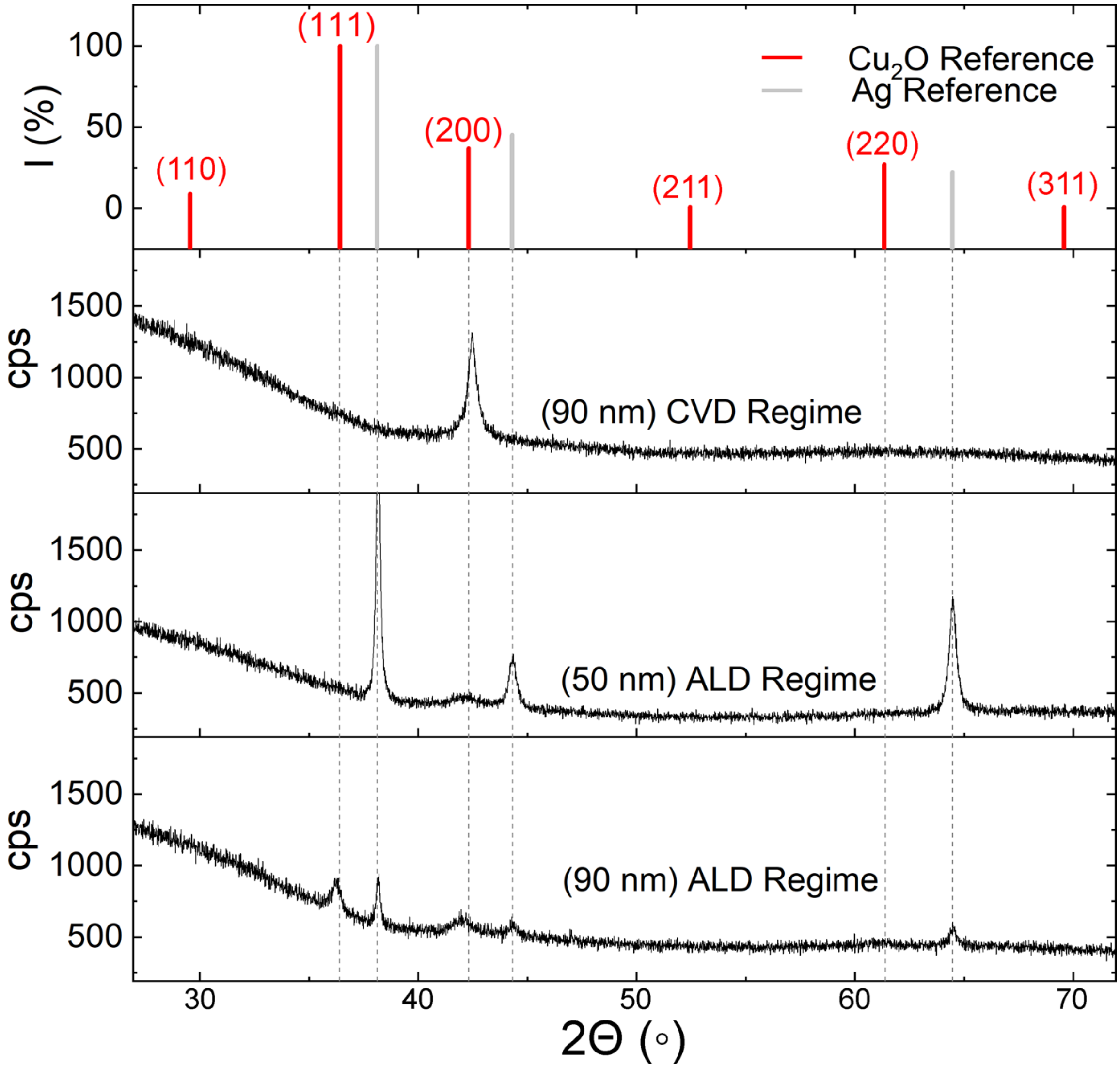

Figure 5-9. *XRD patterns that include Cu$_2$O thin films grown in CVD regime, as well as two films grown in ALD regime using different number of cycles.*

Figure 5-9 shows the XRD patterns for the two previous samples deposited, the CVD regime sample with 90 nm thickness, the ALD regime sample with 50 nm thickness (called henceforth “ALD-50” sample), along with the sample deposited with an ALD regime for 1000 SALD oscillations, leading to a thickness of around 90 nm, as measured by AFM (called henceforth “ALD-90” sample).

It is clearly seen that the ALD-90 sample is less crystallized than the sample deposited with a CVD regime, as seen by the (200) XRD peak. On the other hand, the position and intensity of the (200) peak in ALD-90 nm sample is comparable to the same peak in the ALD-50 sample, which has a slightly less intensity that may be due to the thickness of the layers. However, even more apparent is the appearance of the (111) XRD peak on the ALD-90 layer, which presents an even higher intensity that the (200) peak for the same layer, indicating a polycrystalline character of this sample. The appearance of the (111) peak cannot be only explained by the fact that the Cu_2O layer is thicker, since in the ALD-50 layer, the peak was not present whatsoever. Thus, given that all other parameters were the same in the deposition, the appearance can be attributed to the difference on the scanning distance during the deposition and, hence, the increased exposure of the layer to the atmosphere.

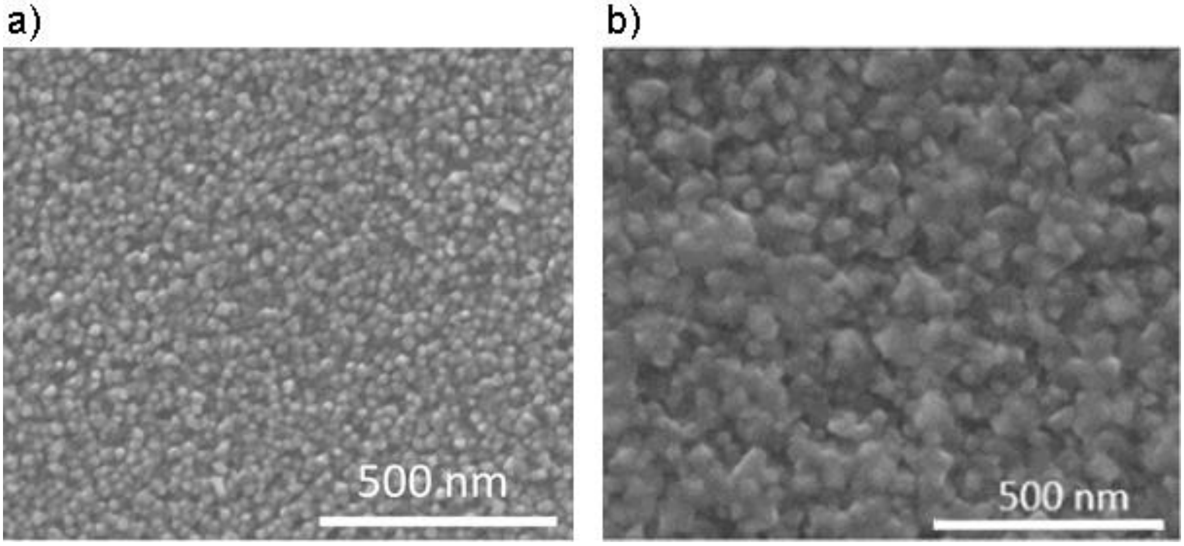

Figure 5-10. SEM pictures of the Cu_2O thin films corresponding to the sample a) ALD-50, which is 50 nm thick and b) ALD-90, which is 90 nm thick.

Figure 5-10 shows SEM images taken for the sample ALD-50 (Figure 5-10a) and ALD-90 (Figure 5-10b). The images show a clear and obvious difference on the morphology of the film that, given that the shape of the grains is completely different, does not arise due to the thickness of the film. It seems that the grains are bigger and are, in fact more randomly oriented in the sample ALD-90. This probably suggests that exposure to the atmosphere allows for some crystalline reorganization in the atomic layer, giving rise to the XRD diffractogram previously shown.

According to 4PP measurements, the ALD-90 layer presents a resistivity of 3 Ω.cm, even more conductive than the ALD-50 sample. Nevertheless, to better compare the electrical conductivity of ALD-50 and ALD-90 layers, Hall effect measurements were made to obtain the mobility, charge carrier concentration and resistivity at different temperatures

5.3.3 *Hall measurements*

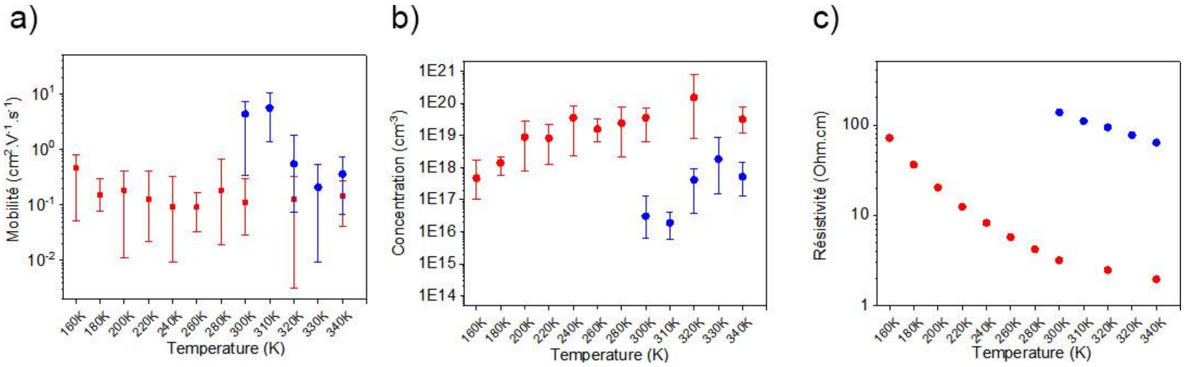

Figure 5-11. *Hall effect measurements for samples ALD-50 (blue) and ALD-90 (red), showing the charge carrier mobility (a), charge carrier concentration (b) and the resistivity (c) as a function of the temperature.*

Figure 5-11 shows the Hall effect measurement of the ALD-50 (in blue) and ALD-90 (in red). The former sample is measured at room temperature and above (from 300 K to 340 K), and the latter is measured at wider temperature range (from 160 K to 340 K, *in-situ*). It is interesting to note that the ALD-50 sample presents a higher resistivity than the one measured with 4PP at LMGP. The difference between 4PP and Hall effect measurements can be due to the known fact that the Hall measurements in a Van der Pauw configuration can be misleading for materials in which the mobility is not homogeneous in the grain and at the grain boundaries [164]. This effect, according to the XRD patterns previously shown (Figure 5-9), is most probably present with the measurements of the Cu_2O layers, since they are polycrystalline. This is more pronounced for thinner layer, with higher boundary to grain area ratio. Nevertheless, since the measurements are made on layers of the same material, they can be used here to compare both layers deposited with an ALD regime.

Looking at the graphs, one can see that charge carrier mobility is lower for ALD-90 sample at approximately room temperature and rather constant as a function of the temperature. Concerning the charge carrier concentration, it increases for both samples, but significantly for ALD-90 one even up to 10^{20} carriers/cm^{-3}, which is one of the highest values reported [67]. Regarding the resistivity, it decreases as the temperature increases. This is in accordance to the analysis made in section 2.3. The ALD-90 sample has a resistivity almost two orders of magnitude lower than the ALD-50 sample. This low resistivity is possibly produced by the high carrier concentration of the ALD-90 sample (two to three orders of magnitude higher at room temperature), which in turn, decreases the charge carrier mobility.

These characterizations suggest that the presence of oxygen is beneficial to the deposition of Cu_2O with high conductivity, since the sample that has better conductivity properties was exposed to the open-air atmosphere at each oscillation of the SALD deposition. This phenomenon will be discussed further in this chapter.

To study the source of the change of carrier concentration of the ALD-50 and ALD-90 sample, XPS measurements were performed on the sample.

5.3.4 *Chemical state characterization (XPS)*

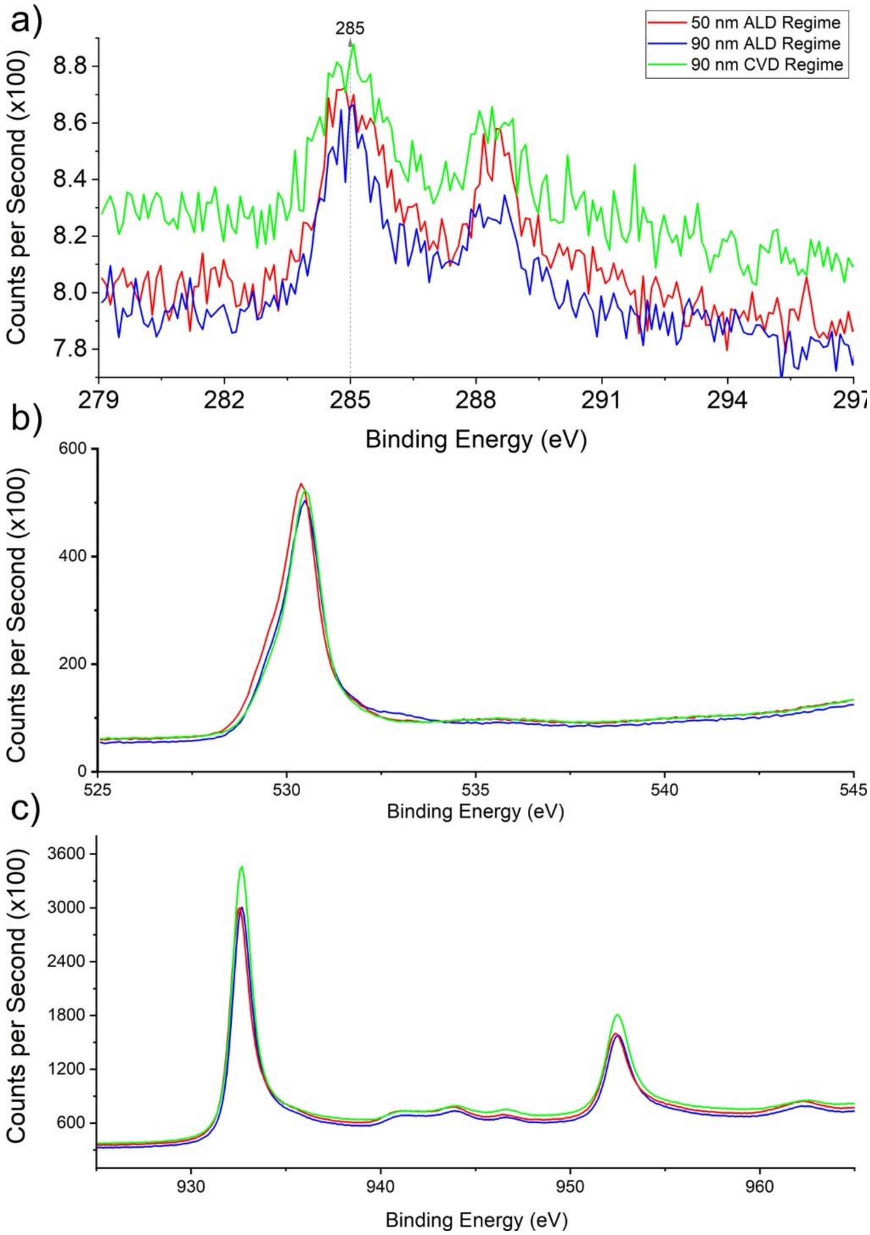

Figure 5-12. *XPS measurements for the Cu_2O thin films showing the spectrum of surfacic C 1S (a), bulk O 1S (b), and bulk Cu 2P (c).*

Figure 5-12 shows the XPS spectra for the surface content of C 1S used for zero-correction of the spectra, the bulk content of O 1S and the bulk content of Cu 2P peaks of the sample deposited in a CVD regime, the ALD-50 and the ALD-90 samples. It seems that the XPS spectra for the three samples are quite similar, although the correction with respect to the peak of carbon was difficult to obtain since the reference peak of carbon was almost not present. Despite that, the O 1S peak suggests that the atomic concentration of oxygen atoms is similar for all three layers, while the Cu 2P doublet suggests a higher atomic concentration of copper in the layer deposited with a CVD regime. Furthermore, the satellite peaks at approximately 945 eV and 965 eV suggest that there exists a certain amount of Cu2+, but such amount is similar for all three layers as well. Such Cu2+ can be the result of CuO being present in the film.

The study of the influence of oxygen exposure of the sample during SALD deposition is an important parameter to study. However, during the experiments done up to this point, the liquid copper precursor used (Cupraselect precursor) presented difficulties on its stability.

5.4 Stability of the precursors: the instability of Cupraselect and effects on the Cu_2O films

One of the main works of this thesis was the fabrication of bubblers to contain the liquid precursor used for Cu_2O depositions, with a technique borrowed from the PICVD approach. Although this task was successfully performed, the chemical stability of the precursor was not ideal. Furthermore, it seems that the bubbler did not properly avoid the leakage of air into the bubbler causing that the precursor reacted prematurely inside the bubbler. Figure 5-13a shows the bubbler filled with the Cupraselect precursor, while Figure 5-13b shows the same bubbler 48 hours later. These pictures clearly show the lack of stability of the precursor inside the bubbler.

To study the effect of this instability on the films, depositions made at the same day of refilling the bubbler, 17 days later, and 48 days after the precursor refilling were analyzed with XRD and SEM to observe microstructural changes. Later, electrical characterization with 4PP measurements was also made.

5.4.1 *Morphology and Crystallography*

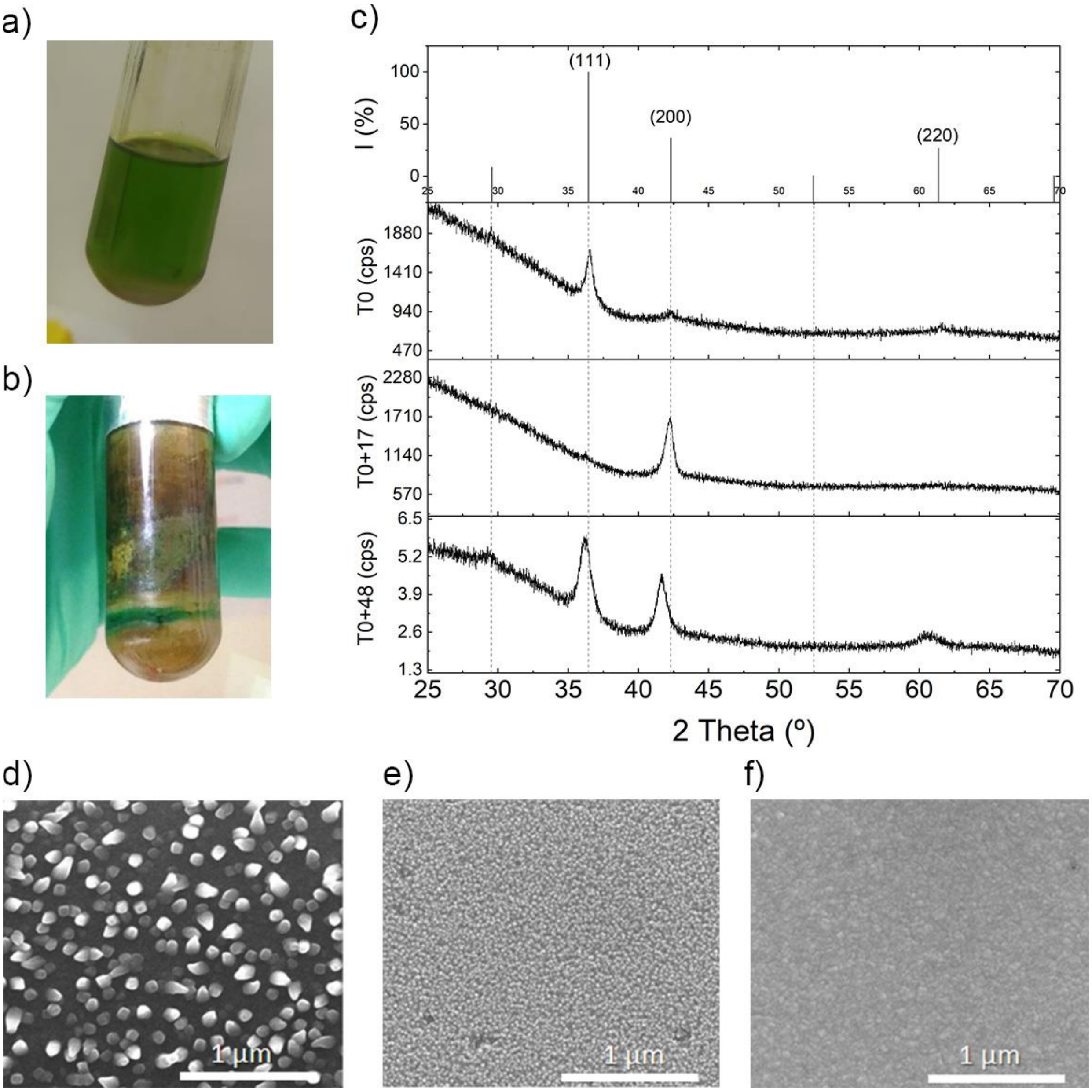

***Figure 5-13**. The stability of the Cupraselect precursor is not ideal. The image shows the precursor at the moment the bubbler has been refilled (a), and the same precursor after 48 hours during which the precursor was used to carry out depositions and thus was heated and cooled several times. (b). The XRD patterns of the thin films deposited with the bubbler at different lapses of time after the bubbler was filled (c). SEM images showing the surface topography of the Cu$_2$O layers deposited 0 (d), 17 (e), and 48 (f) days after the bubbler was refilled.*

Figure 5-13c shows the XRD patterns for samples deposited at 190 °C with equivalent flow and scanning parameters, at the day of refilling the bubbler (T0), 17 days after refilling the bubbler (T0+17) and 48 days after refilling the bubbler (T0+48). It is worth noting that during such 48 days, the precursor went through heating and cooling cycles needed for the deposition of the films. Interestingly, the instability of the precursor influenced the orientation of the Cu_2O layer deposited, showing a (111) preferred orientation for the sample deposited at the moment of refilling, a (200) preferred orientation for the sample deposited 17 days after refilling the bubbler, and a (111) and (200) orientations in polycrystalline ratio for the sample deposited 48 days after refilling the bubbler. More interestingly, the sample deposited at the same day of refilling the bubbler presented an unexpected morphology in the film, showing nano-sized vertical features, similar to nanorods (Figure 5-13d). Such nanorods have a diameter of approximately 60 nm, which is similar to the grain size of the Cu_2O layers previously deposited. As the precursor continues to age, the morphology of the films changes as well, going to faceted grains (Figure 5-13e) with the deposition 17 days after refilling, and then to possibly smoother layer (Figure 5-13f) with the deposition 48 days after the bubbler refilling. During this work, it has not been possible to identify the mechanism by which such nanorods are obtained, which would be very interesting since such nanostructured films could have applications in photoelectrochemical water splitting and other optoelectronic applications due to the increase of surface area in the Cu_2O. Further studies on this line is currently being carried out in the group.

5.4.2 *Electrical Conductivity*

A plot of the resistivity values obtained for the different films is shown in Figure 5-14 (note that the scale of the resistivity is in MΩ.cm). Comparing the samples deposited after some days of the precursor refilling, the resistivity of the film (calculated with an estimated thickness from the GPC measured with previous depositions), it seems that, as the precursor passes more time inside the bubbler, the electrical properties of the films deposited are enhanced, going from approximately 33 MΩ.cm for the sample that was deposited at the same day that the bubbler was refilled, to 700 KΩ.cm, with a precursor that stayed 48 days inside the bubbler. This effect may be due to the change on chemistry within the bubbler. It seems that, when the precursor reaches equilibrium with the gas in the bubbler, the orientation of the copper oxide changes from (111) to (200) to a mixture of both, giving it different morphologies and enhancing the conductivity for the latter one.

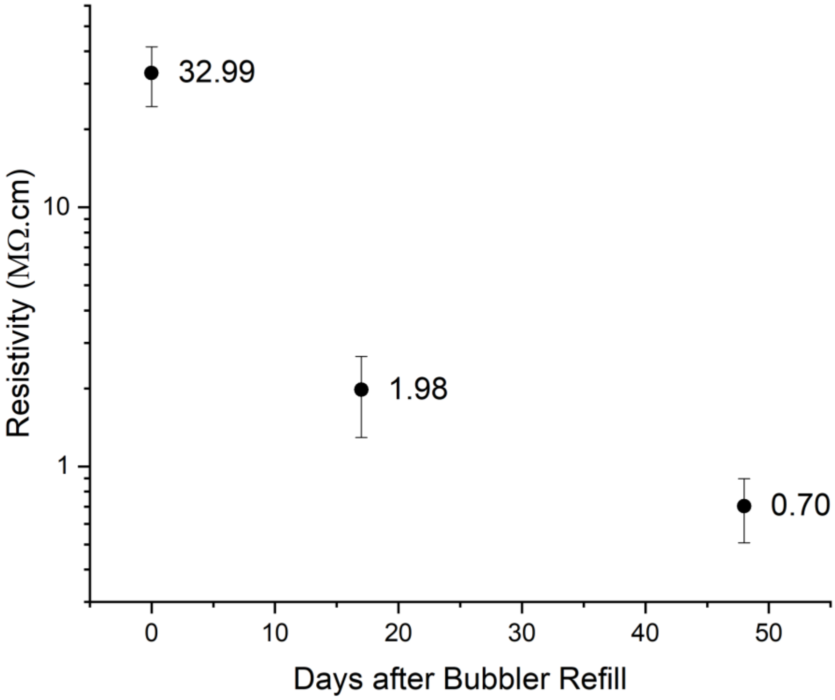

Figure 5-14. *Resistivity as a function of the time that that has passed after the Cupraselect bubbler was refilled.*

5.4.3 *Precursor Concentration and Film Thickness Over Time*

Besides the apparent chemical instability of the precursor, the GPC achieved is also not stable throughout depositions in the same day. Figure 5-15a shows the XRD pattern and Figure 5-15b shows the corresponding photographical pictures of samples deposited on the same day, with the exact same conditions, one after another for 500 SALD oscillations (2000 ALD cycles). In the first deposition made, it is possible to see on the XRD pattern that the Cu_2O has certain level of crystallization, but the thickness of the layer is small (Figure 5-13b-1). The subsequent deposition presents the same orientation of the Cu_2O growth, but the layer thickness is higher, as shown by the photographic picture (Figure 5-13b-2). As subsequent depositions of Cu_2O continue, the thickness achieved with the same number of oscillations increases as well. This is expected since it is known that, for the SALD system at LMGP, certain level of saturation in the inner walls of the gas lines is needed to deliver precursor concentration to the sample successfully. However, with the Cupraselect precursor, after the 4th consecutive deposition (i.e., after 2000 SALD oscillations shown in Figure 5-13b-3 to 5), the thickness of the deposited film decreases once more. This behavior suggests that the reactive molecule concentration in the liquid precursor is not constant and, after certain concentration has been extracted from it, such concentration decreases significantly. However, after 24 hours in which the precursor is stored, it seems to have had enough time to regenerate the reactive molecule, and the surface reaction can happen again. It seems that the time that the precursor needs to reach equilibrium with the reactive molecules is longer that the rate of consumption of such reactive molecules during the SALD process. This is verified by the fact that, 24 hours after the behavior shown in Figure 5-13 happens, the deposition of Cu_2O can occur normally, only to repeat the depletion of the reactive molecule once more.

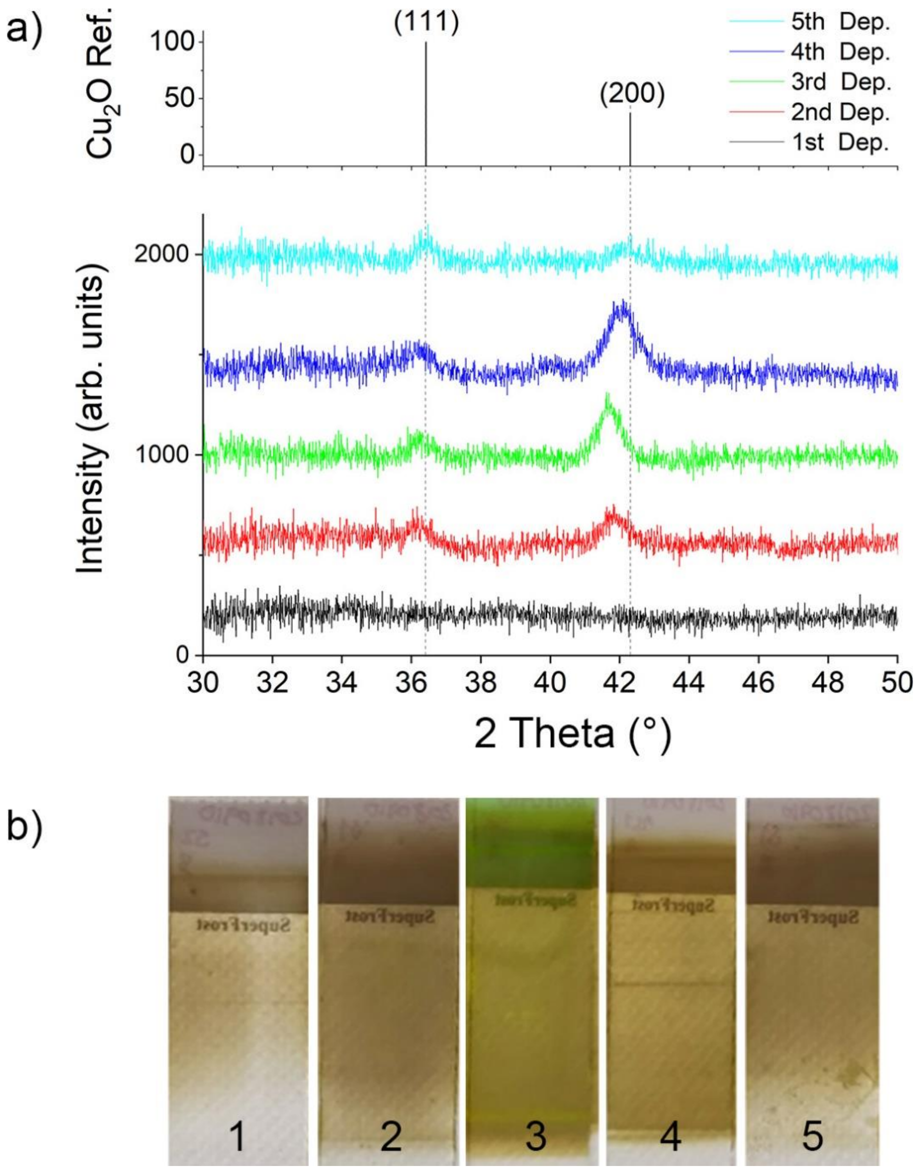

Figure 5-15. a) XRD patterns of the Cu_2O layers deposited subsequently on the same day, showing similar orientations that vary with respect to their intensity. b) Optical photographs of the layers deposited subsequently, with numbers 1 to 5 showing the order in which they were deposited.

Given the lack of stability of the Cupraselect precursor, both in the long term (after several tenths of days) and in the short term (after 24 hours), the depositions of Cu_2O layers were made using the CuCOD, which, after the optimization of the precursor regarding the sealing and temperature of the bubbler, was found to have a better stability and reproducibility on the depositions. The new precursor was found to have a stable GPC at 220 °C on the substrate surface.

5.5 Oxygen-rich depositions: tuning the properties of the Cu_2O films

5.5.1 *Oxygen*

With the study of the conductivity done in the Cu_2O previously deposited, the scanning distance is a parameter that seemed to greatly influence the electrical properties of the Cu_2O films. Indeed, the scan speed is directly related to the time that the substrate is exposed to the atmosphere after each SALD oscillation, since the required distance to scan the whole substrate is longer than the width of the deposition head. This behavior suggests that the exposure to the oxygen in the atmosphere during the deposition of the layer has a potential benefit to the electrical conductivity of the Cu_2O.

Hence, in order to study the effect of oxygen on the deposition of Cu_2O in the SALD, gaseous O_2 was introduced in the inert gas channel that originally was used to create the "purge" region of the SALD. In fact, the purge section had now two purposes: besides removing the remnants and by-products of the surface reaction from the sample surface, now, the introduced oxygen would also react with the adsorbed surface at each SALD oscillation. The amount of oxygen introduced is a percentage of the total inert gas flow (N_2) introduced on the deposition head, which in this case is 600 SCCM.

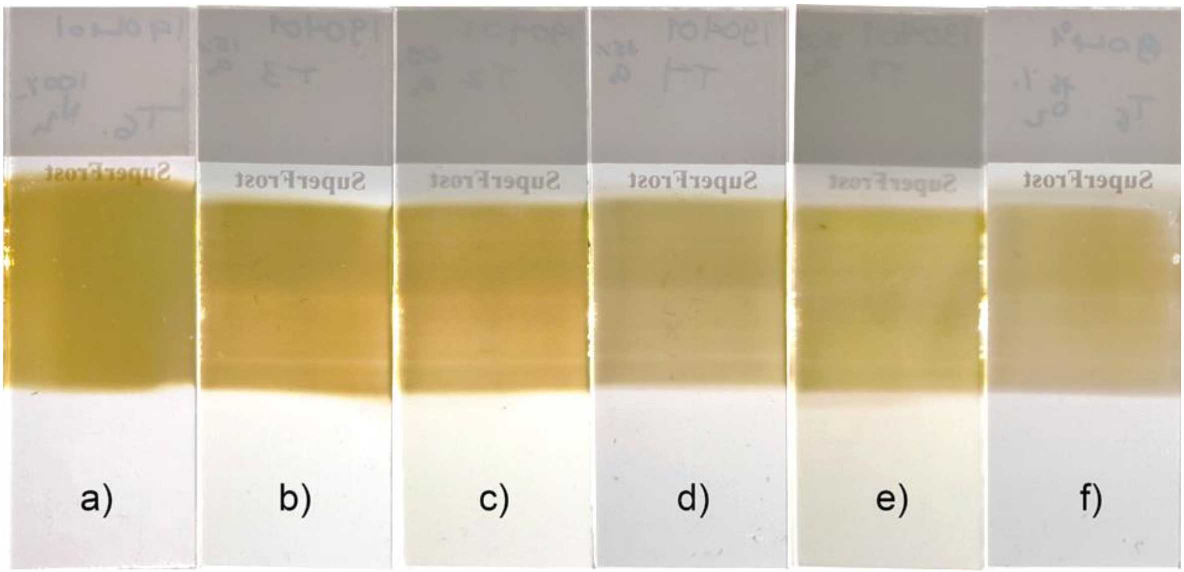

Figure 5-16. *Deposition of Cu_2O thin films with 0% (a), 15% (b), 25% (c), 35% (d), 50% (e), and 75% (f) of O_2 added to the inert gas outlet of the deposition head.*

Figure 5-16 shows a series of deposition made with the CuCOD for 500 cycles each. The CuCOD precursor presented a much better reproducibility on the deposition it achieved, and on the long-term stability. The size of the deposition was smaller than usual because, at this stage, a design of the deposition head, based on the V6.1 but with smaller outlets (30 mm long, instead of 50 mm long) and shown in Figure 4-17, was used. Such new head had as objective to proof that the size and shape of the deposition can be easily modified with a simple change on the geometry of the deposition head (as explained in chapter 4). The new deposition head was fabricated with the same material as the previous ones, and the quality of deposition was tested to have the same quality of previous films. For the study of oxygen influence in the deposition of Cu_2O, the scanning distance was set such that the sample was exposed as little as possible to the atmosphere, so as to ensure that the film reacted with the oxygen introduced, rather than with the oxygen present in the atmosphere. For these experiments, only the oxygen amount in the inert gas inlet was varied, all other parameters were kept constant.

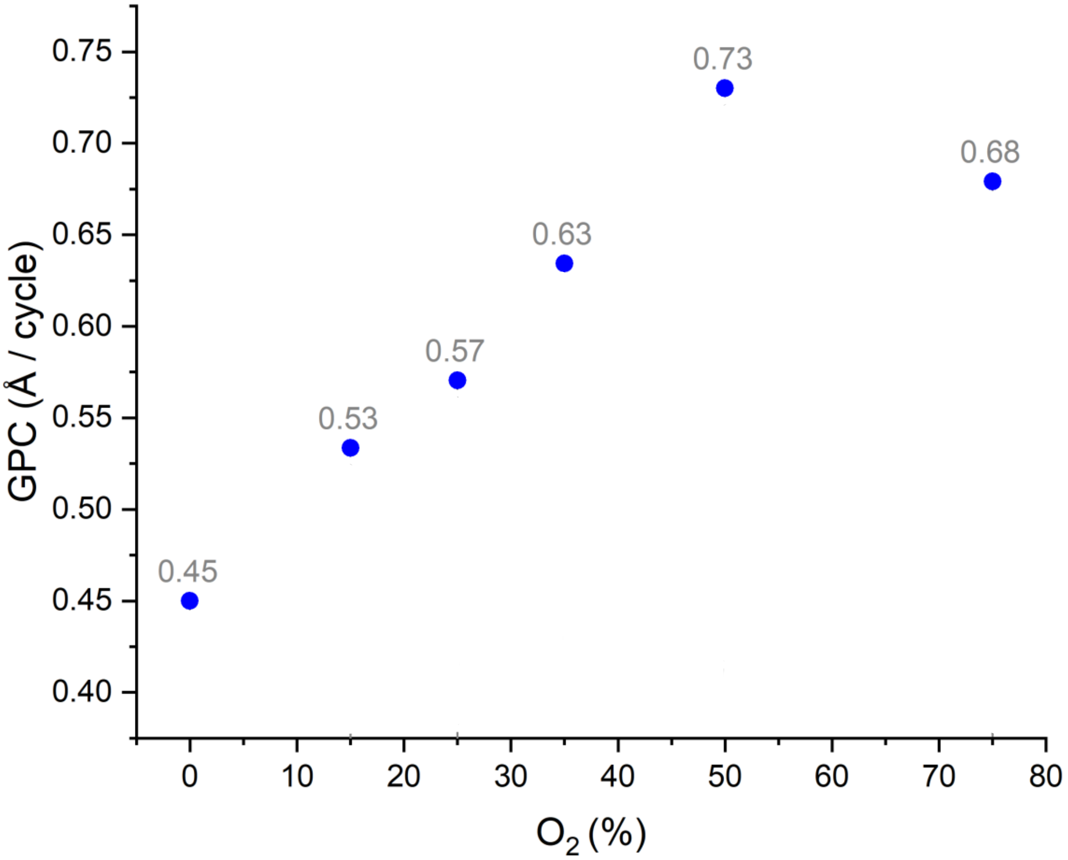

Figure 5-17. *GPC values as a function of the amount of oxygen added to the inert gas outlet of the deposition head.*

Figure 5-17 shows the GPC of the Cu_2O deposition with different amounts of oxygen introduced in the process, as measured with the thickness obtained with a spectroscopic ellipsometer at LMGP.

It can be seen that the introduction of oxygen increases the GPC of the Cu_2O from 0.045 nm/cycle to 0.053 nm/cycle just by introducing 15% of oxygen in the inert gas line of the deposition head. The GPC with no oxygen in the deposition process is equivalent to the GPC obtained with the Cupraselect. This corresponds an increase of 18.6% of the GPC with respect with the deposition that has no oxygen in the process. The GPC presents this increase until the percentage of oxygen in the inert gas line is 75%, case in which the GPC decreases slightly. This effect can be explained by looking at the morphology of the films deposited. The SEM pictures of the films shown in Figure 5-18 shows that the topography is affected by the inclusion of oxygen. It seems that the layer deposited using a 15% of oxygen has the least roughness in its surface. As the concentration of oxygen is increased the roughness is amplified, and a three-dimensional structure is favored. In the case of the deposition with a 75% oxygen flow, it is possible that the enhanced 3-dimensional growth explains the decrease of the GPC of the deposition, since a 3-dimensional growth would require more matter, and thus the thickness of the film is sacrificed.

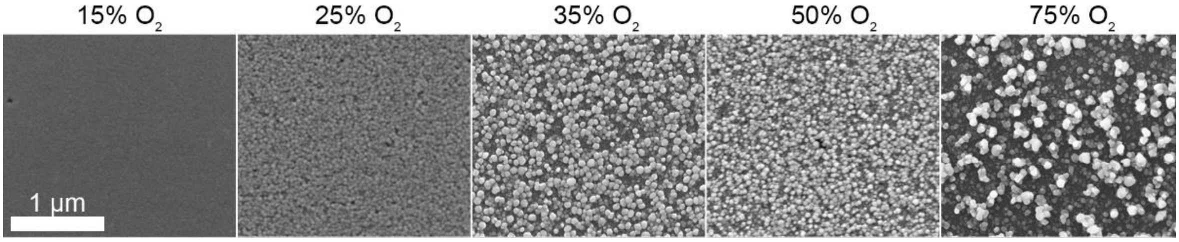

Figure 5-18. *SEM images showing the morphology change as the concentration of oxygen during the deposition of Cu_2O increases.*

To identify the differences of the films deposited, electrical characterization using 4PP measurements were made. Care was taken on measuring on the section that was not exposed to the atmosphere during the scanning movements of the SALD oscillation. Furthermore, the thickness of the layer was measured using a 4-wavelength ellipsometer (see chapter 2 for details). The thickness of each layer is shown in Table 5-4.

Table 5-4. *Thickness of the layers with different oxygen addition to the inert gas outlet of the deposition head, as measured with ellipsometer.*

Oxygen Percentage (%)	Ellipsometer Thickness (nm)
0	45.01
15	53.37
25	57.04
35	63.44
50	73.02
75	67.91

Figure 5-19 shows the electrical measurements on the samples with different amount of oxygen in the deposition process.

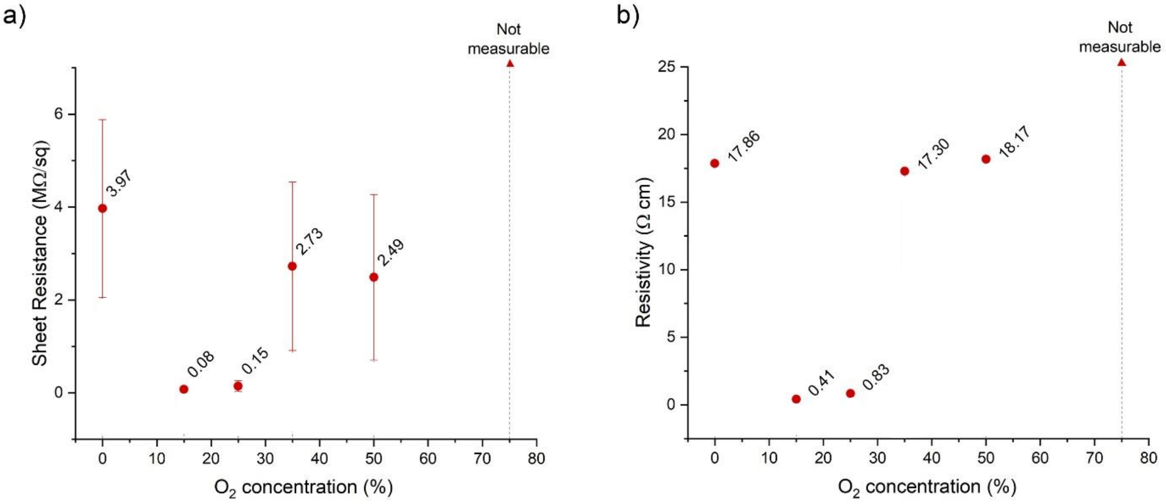

Figure 5-19. *Sheet Resistance (a) and resistivity (b) of the Cu_2O film as a function of the amount of oxygen added to the inert gas outlets of the deposition head during deposition.*

Interestingly, the introduction of oxygen influences positively the conduction of the deposited Cu_2O films, reaching a maximum of conductivity for the sample with 15% oxygen in the inert gas line. The resistivity is on the similar order of magnitude of the sample ALD-90, shown previously. This confirms the fact that the exposure to oxygen during the SALD deposition of Cu_2O is the parameter that originates the high conductivity in the film. However, for the case of the sample deposited with 75% of oxygen in the inert gas line, the sheet resistance was not measurable with a Keithley 2000 multimeter, since the resistance measured surpassed the limit of measurement of the device. This means that too much of oxygen during the process can also hinder the conductivity of the film, even though it increases the deposition rate at the same value of deposition gap; i.e. at depositions in ALD regime.

To compare the different depositions, the total transmission in the UV-vis-nIR spectrum for each sample was measured, and the Tauc plot was derived from it.

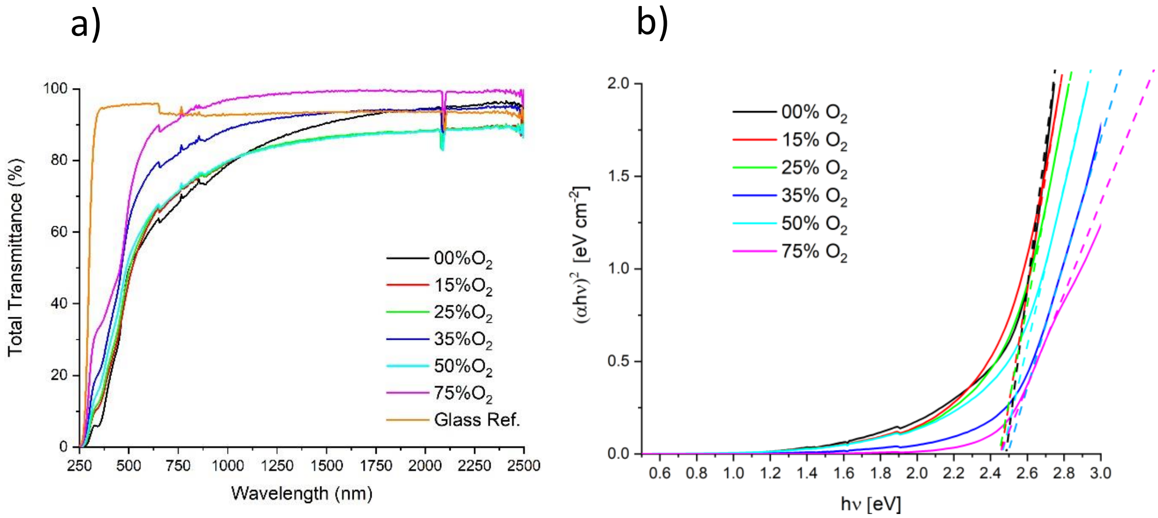

Figure 5-20. *Total transmission spectrum (a) and its derived Tauc plot (b) for the Cu_2O layers deposited with different amount of oxygen to the inert gas outlet of the deposition head.*

Figure 5-20 shows the total transmission spectrum (Figure 5-20a) and the Tauc Plot (Figure 5-20b) of the samples deposited with different amounts of oxygen in the process. It is important to note that the thickness of each layer is different. From the Tauc plot, it is possible to see that all the optical bandgaps values have a value from 2.45 eV to 2.5 eV. These values are in accordance with the bandgap of Cu_2O, and no important difference can be seen between the samples deposited with different amounts of oxygen during the SALD process. Furthermore, in the total transmission plot (Figure 5-20a), a reference from the glass substrate is shown as reference. It is quite interesting to note that it seems that the Cu_2O deposition indeed enhances the transmission in the infrared wavelengths. Such phenomenon is quite puzzling, and no explanation was found for such behavior. It is also important to note that the jump at 650 nm, present in all plots, is due to the change of the sensor in the spectrophotometer.

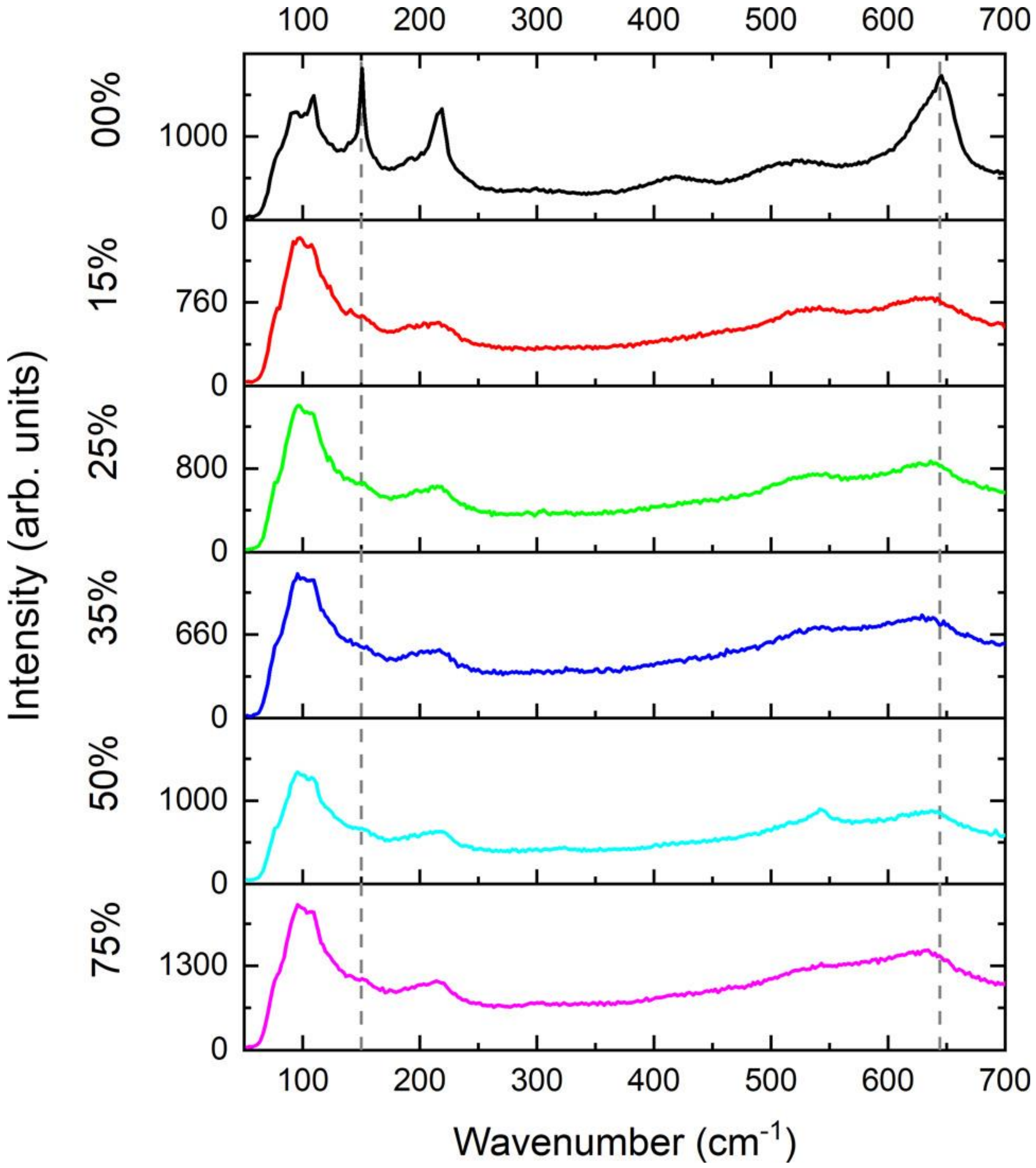

***Figure 5-21**. Raman spectra of the Cu_2O layers deposited with different amounts of oxygen in the inert gas outlet of the deposition head during deposition.*

Raman spectroscopy measurements were made to dig deeper on the material properties of the Cu_2O deposited with oxygen insertion in the SALD process. Figure 5-21 shows the Raman spectra of the different samples. It is apparent that the reference sample (with 0% oxygen added) differs from the samples deposited with any amount of oxygen. The peak at 150 cm^{-1}, which corresponds to a $\Gamma 15^-$ vibration and which is attributed to the existence of oxygen vacancies, effectively disappears from the spectrum.

Finally, XRD measurements were made on the films to observe the crystallographic structure of the films deposited with oxygen during the deposition. Figure 5-22 shows the XRD patterns for the films deposited with 15%, 50% and 75% of oxygen flow. Although the film with 75% oxygen has the least thickness, the XRD pattern shows a better crystallization on the (111) orientation of Cu_2O. Interestingly, the XRD pattern for the sample deposited with 15% oxygen flow shows a less crystalized film, with a peak that presents a left-shift, which indicates the presence of stress in the lattice. Indeed, it has been shown that tension in the lattice causes an improvement on the conductivity of the film, due to the overlapping of 2p orbitals of Cu_2O, and allowing for a better charge carrier transport.

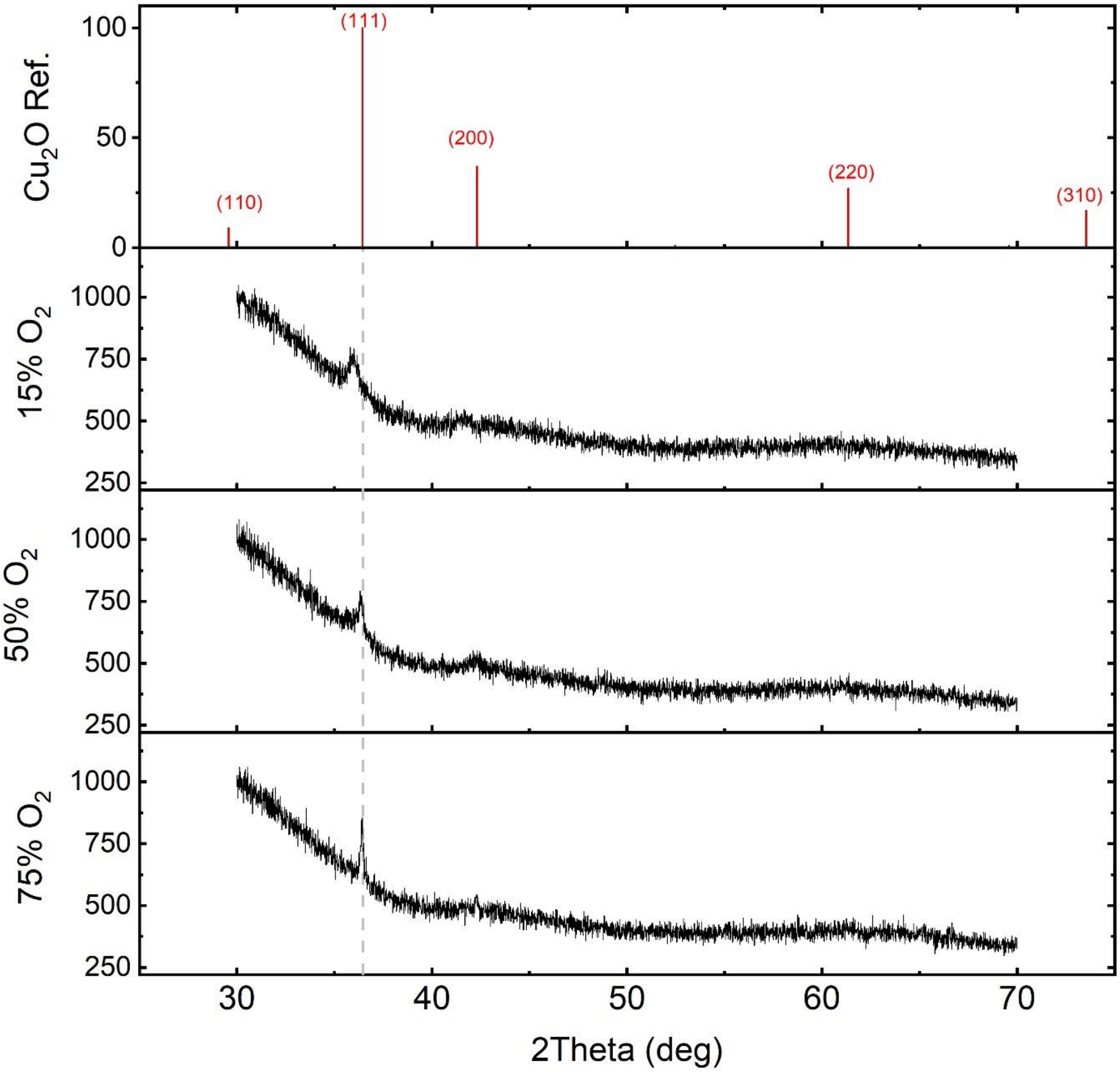

Figure 5-22. *XRD patterns for Cu_2O films deposited with 15%, 50% and 75% of oxygen during the SALD deposition, as compared to the Cu_2O reference peaks.*

It is important to note the difference of the sample deposited with 50% oxygen. It is possible to see a difference in the total transmission (Figure 5-20), the morphology (Figure 5-18) and thickness (Table 5-4), with respect of all other samples. This may have been due to uncontrolled deposition conditions, or possibly even not clean substrates.

Given that the inclusion of oxygen during the deposition of Cu_2O films, it is interesting to vary the SALD deposition parameters once more to find the deposition process that yields the best conductivity in the films. Thus, two parameters were re-tested, this time with the inclusion of 15% oxygen in the process: the gap between the deposition head and the substrate, and the scan speed of the oscillations during the deposition.

5.5.2 *Deposition Gap*

It is interesting to study the effect of the gap again for two reasons. The first reason is to make sure that reproducibility of the SALD deposition can be achieved. Previously, we showed that ALD regime yields better conductivity than CVD regime and that the exposure of the sample to the oxygen present in the atmosphere yields a good conductivity in the film. These depositions will confirm the phenomenon and confirm the versatility of the SALD system of working on both modes. The second reason is to study the diffusion of the atmosphere's oxygen into the gap. Finally, the change of the deposition gap also induces a change on the flow velocities, and it is important to see the effects of such change in the deposition regime and in the film properties. This is important since the SALD is currently working in open-air configuration and the understanding of the interaction with the atmosphere is crucial to control the deposition of Cu_2O.

Figure 5-23 shows Cu_2O films made at 220 °C, with 15% oxygen in the inert gas line. The depositions were made with a gap of 150 µm (a), 250 µm (b), 450 µm (c), and 650 µm (d). It is clear that the border of the deposition is less confined as we increase the value of the gap, consistent with the FEM simulations shown in chapter 3. Moreover, in the sample deposited at 150 µm, it seems that the layer is more affected by the imperfections on the deposition head provoking the horizontal lines, since in the film deposited at 250 µm the layer seems more homogeneous.

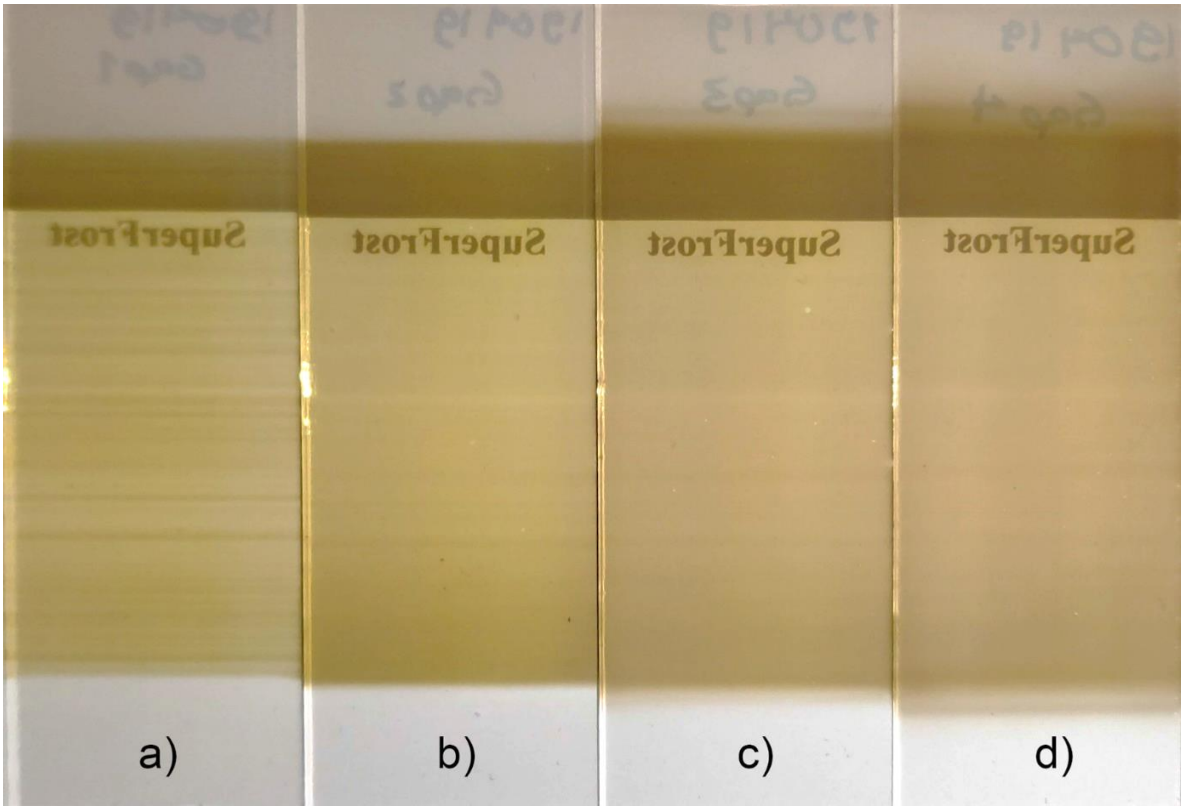

Figure 5-23. *Optical photographs for Cu_2O layers deposited with a gap of 150 µm (a), 250 µm (b), 450 µm (c), and 650 µm (d).*

Furthermore, to compare the topography of the deposited films, Figure 5-24 shows SEM images taken for the layers deposited with different deposition gaps.

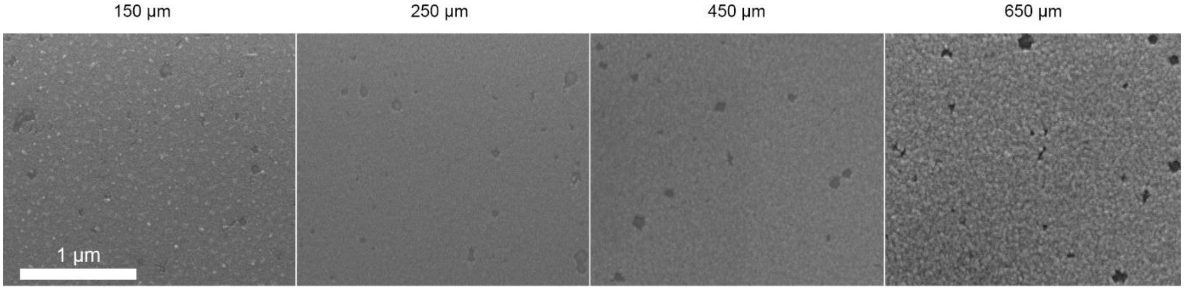

Figure 5-24. *SEM images for the films deposited with different deposition gaps.*

Figure 5-24 shows the SEM pictures for the samples deposited at different value of deposition gap. The thickness of the layers was measured by a cross-section image made with an SEM for each film and the values are shown in Table 5-5. It is possible to see that the morphology of the films presents a different roughness that may correspond to the thickness of the sample. For the film deposited with a gap of 650 µm, the texture of the surface of the film has a higher roughness, with grains of similar size and shape.

Additionally, regardless of the deposition gap, it seems that the inclusion of oxygen creates films with pinholes of around 100 nm, which is the first time that this has been observed in the depositions made in this work, and it will require further study.

Table 5-5. *Thickness of the Cu_2O films deposited with different deposition gaps as measured by cross-section SEM images.*

Gap (µm)	SEM Thickness (nm)
150	36
250	29
450	33
650	37

Furthermore, Figure 5-25 shows a plot of the GPC in function of the deposition gap used during the deposition of the films. It seems that at a deposition gap of 150 µm the GPC is indeed higher than a deposition gap of 250 µm, which is contrary what was expected. A possible explanation of this behavior is proposed in the discussion section, further in this chapter.

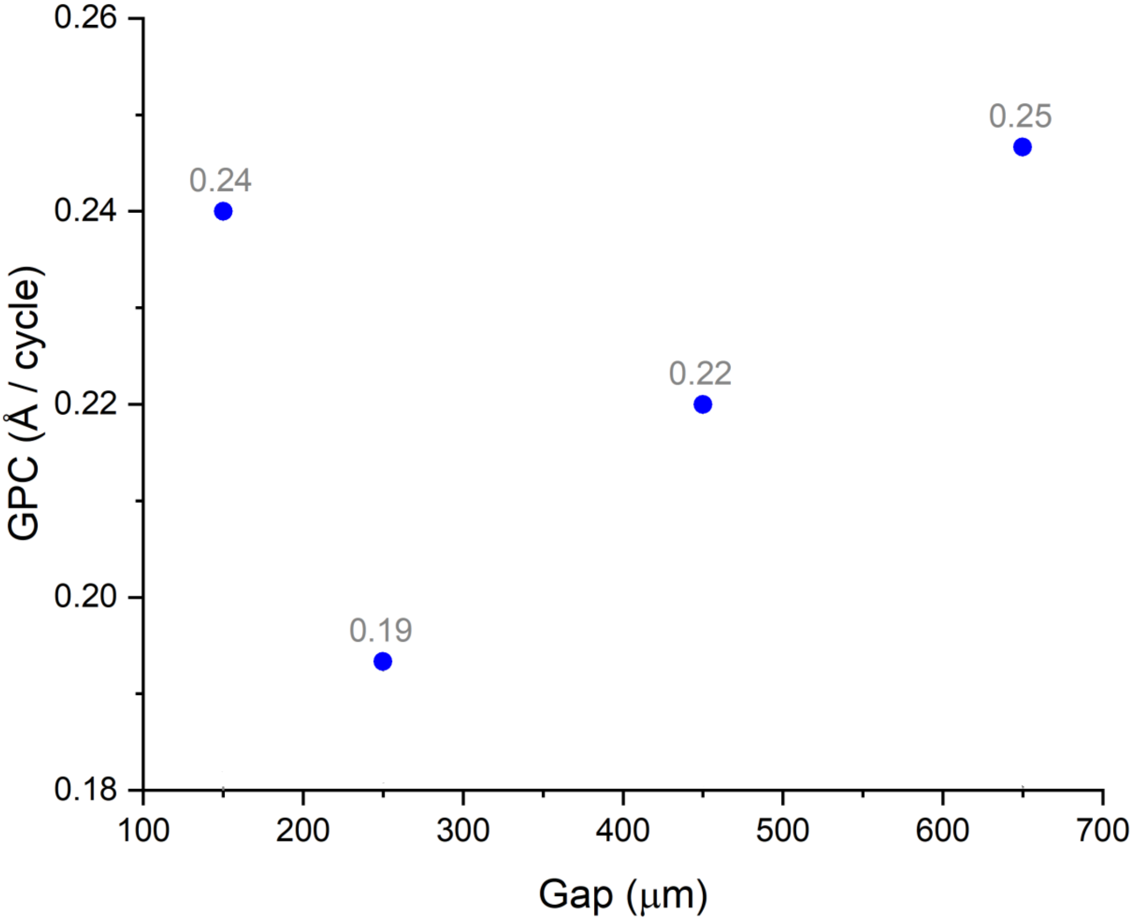

Figure 5-25. *Plot of the GPC in function of the deposition gap value used during the deposition of Cu_2O films.*

With the thickness measurements, the sheet resistance was measured with 4PP method, and the resistivity was calculated. Figure 5-26 shows these values for the different value of deposition gap.

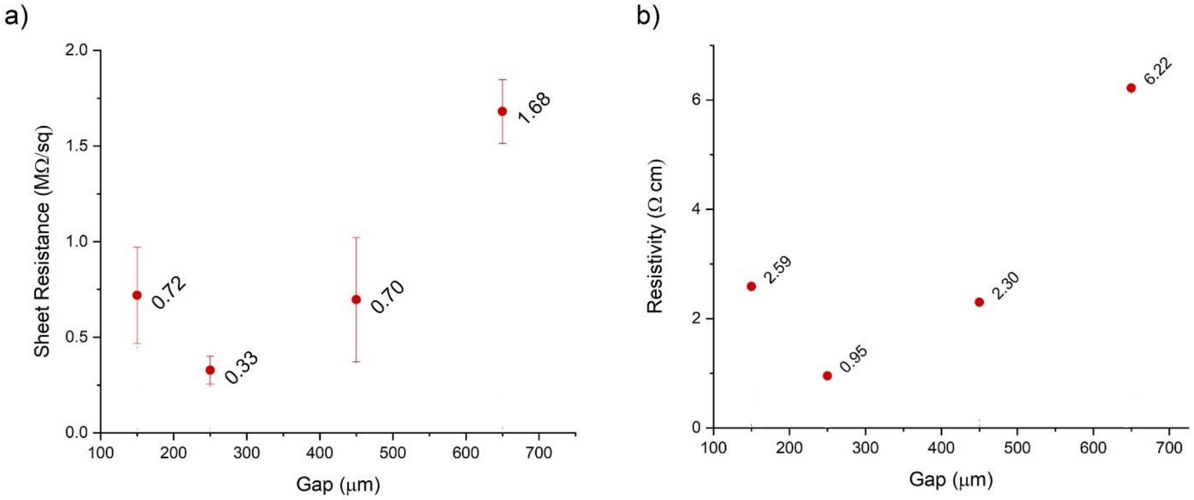

Figure 5-26. *Sheet Resistance (a) and resistivity (b) of the Cu_2O film as a function of the value of the deposition gap.*

As it can be seen, the resistivity of the deposited Cu_2O film decreases slightly when increasing the gap from 150 µm to 250 µm. This is an interesting behavior and it suggests that, as mentioned before, the simultaneous benefits of working in an ALD regime, with enough gap to enhance the diffusion of air in the atmosphere creates a deposition in which oxygen vacancies are minimized, while the quality of the film (density, roughness and homogeneity) still are governed by the ALD regime. As the gap is increased, even though the diffusion of the air in the atmosphere is increased, so is the diffusion of reactive species in the gap, causing, as shown in chapter 3, the appearance of a CVD regime, which decreases the quality of the film and, thus, decreasing its conductivity. On the other hand, a smaller gap induces higher velocities in the flow due to the Bernoulli's effect, which may induce a higher convective diffusivity in the gap and hence a higher chance of CVD regime appearance.

XRD measurements were made to the films to study the crystallographic orientation of the films and the XRD patterns shown in Figure 5-27 indicate the typical peak shift on the (111) orientation peak, while the intensity changes depending on the thickness of the film.

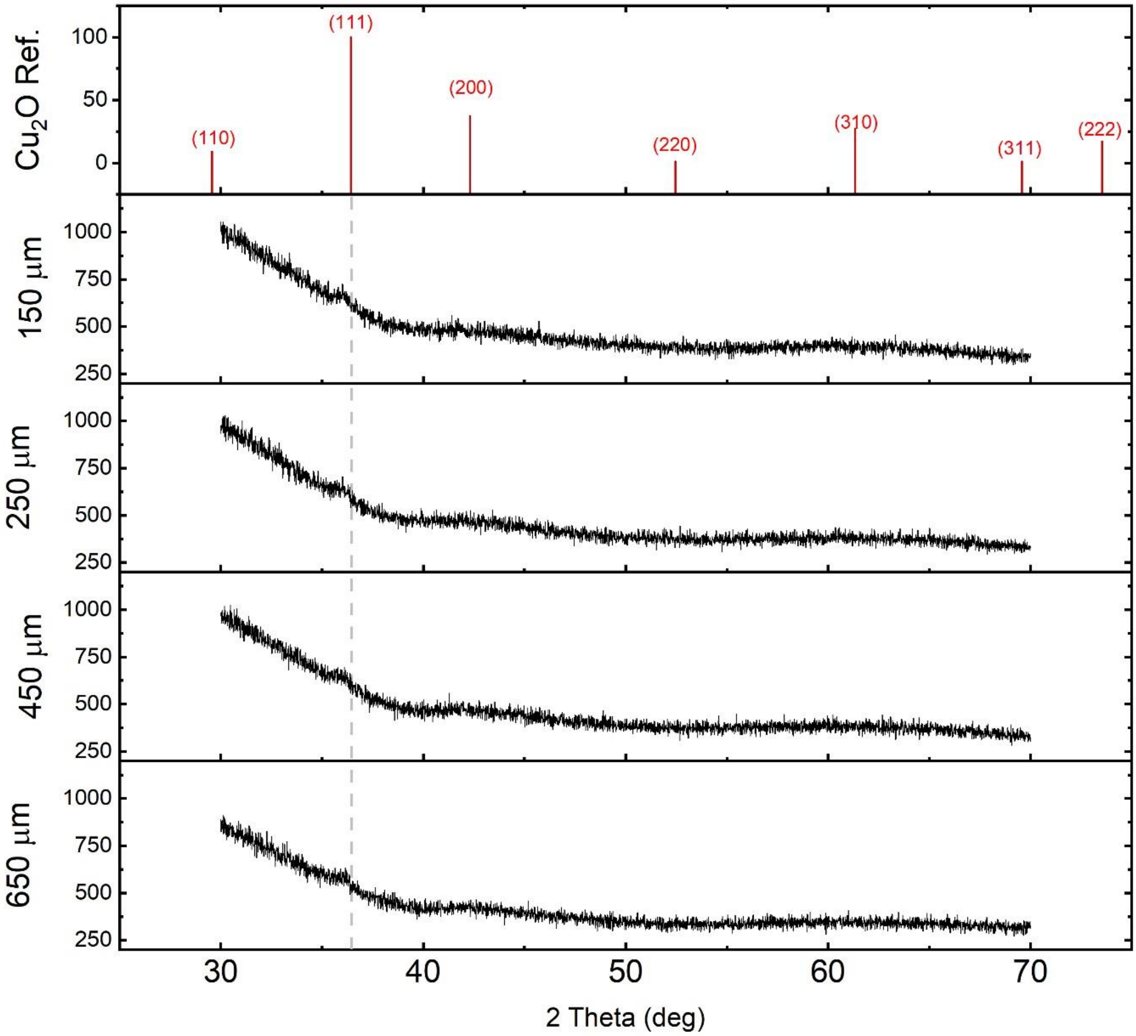

Figure 5-27. *XRD patterns for the Cu$_2$O films deposited with different deposition gap values.*

5.5.3 *Speed*

To study the effect of the scan speed, depositions of 750 SALD oscillations were made with a gap of 200 µm. Once more, 15% oxygen was introduced in the inert gas line and the scan speed were set to 25 (a), 50 (b), 100 (c), 150 (d), and 225 (e) mm/sec. Figure 5-28. Optical photographs for Cu2O layers deposited with different values of scan speeds 25 (a), 50 (b), 100 (c), 150 (d), and 225 (e) mm/sec.

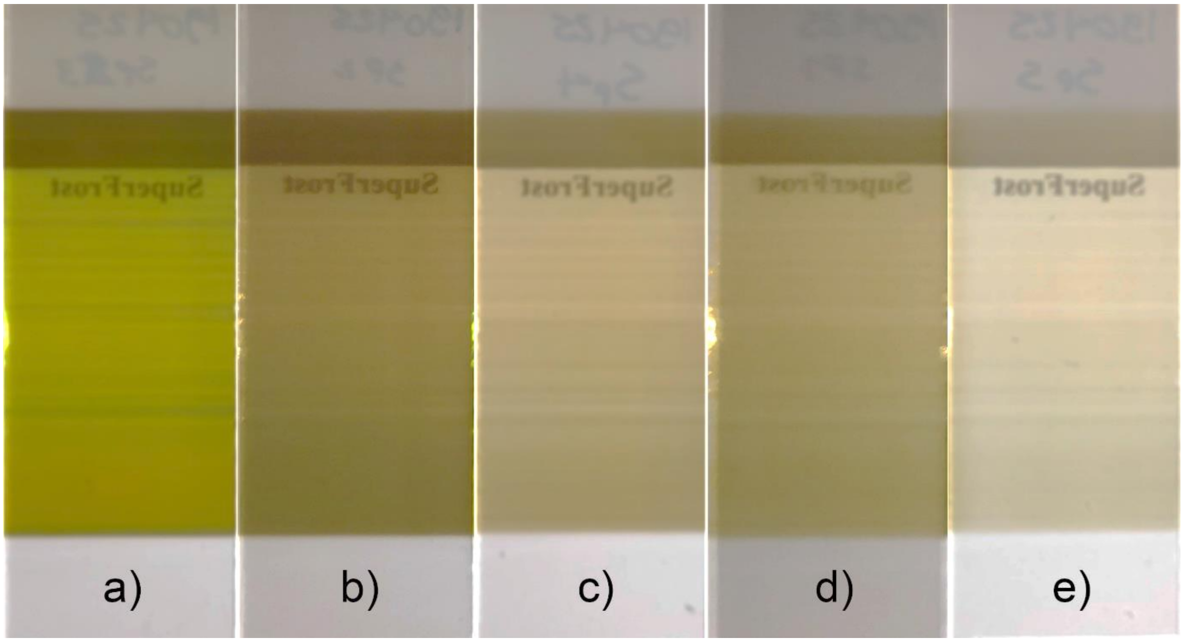

Figure 5-28. *Optical photographs for Cu_2O layers deposited with different values of scan speeds 25 (a), 50 (b), 100 (c), 150 (d), and 225 (e) mm/sec.*

SEM images of the surface of the film are shown in Figure 5-29 with no significant difference on topography on the films. The interesting observation occurs in the sample deposited at 56 mm/s where it seems that the film deposition didn't reach a full coverage on the substrate, most probably due to the limited exposure time of the substrate to the reactant regions, as well as a mass transport limited process due to the concentration of the precursor in the carrier gas. This indicates that for the decrease of the time of oscillation in the SALD, the concentration should also be optimized to ensure the delivery of sufficient concentration of reactive molecules to the surface of the substrate.

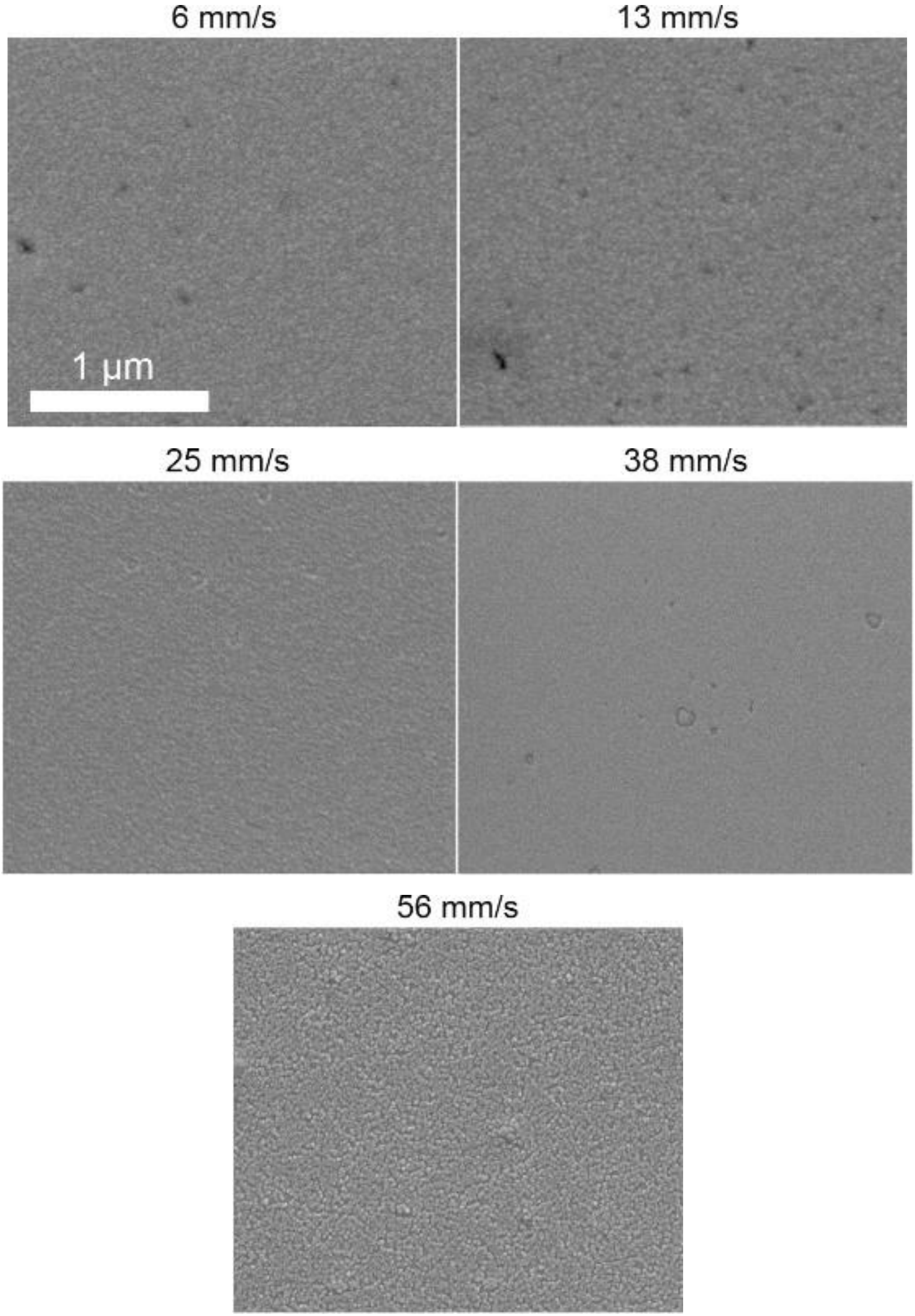

Figure 5-29. SEM images of the Cu_2O layers deposited with different scanning speeds.

As done previously, the thickness was measured by cross-section SEM images and Table 5-6 shows the thickness of the samples deposited at different scan speeds.

Table 5-6. *Thickness of the Cu_2O films deposited with different scan speeds as measured by cross-section SEM images.*

Speed (mm/sec)	SEM Thickness (nm)
6	81
13	27
25	22
38	19
56	~5

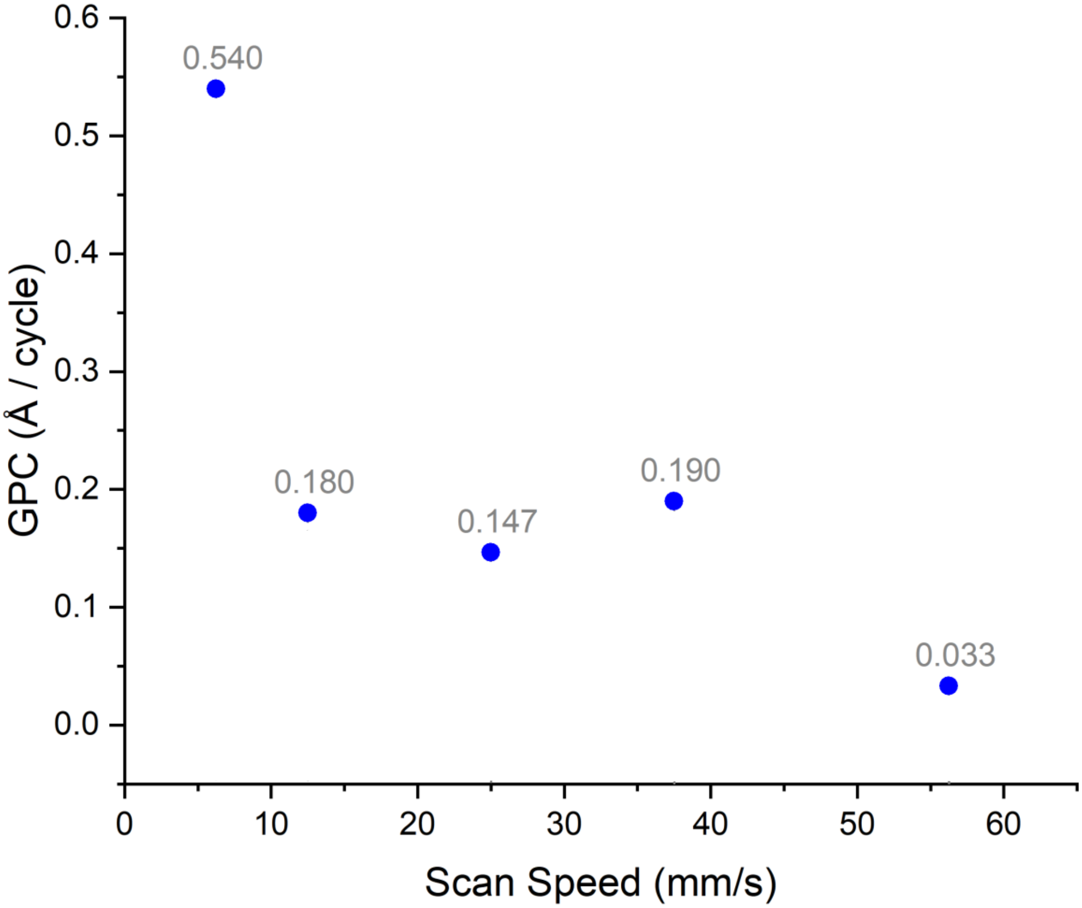

Figure 5-30. *Plot of the GPC in function of the scan speed of the substrate under the SALD deposition head.*

Although they are not shown in this report, the color of the thicker samples is consistent with the color observed for samples of similar thickness deposited on the SALD previously during this thesis. The sheet resistance measured with 4PP technique at LMGP, while the resitivity for each sample was calculated with the thickness measured with cross-sectional SEM images. Figure 5-30 shows a plot of the GPC as a function of the scan speed of the substrate under the deposition head. It is possible to see that at low speed, the GPC has the highest value achieved with Cu_2O with CuCOD in this thesis. This may indicate that the speeds used until now may not be enough to ensure surface coverage of the substrate, which would be expected due to the low reactivity of the molecule. In the case of a speed of 6 mm/s, a high GPC can be obtained but the cycle duration would then be increased, decreasing the growth rate. Regarding the electrical conductivity of the samples deposited, 4PP measurements were done on each sample, and the measurements of sheet resistance and resistivity of the films deposited are shown in Figure 5-31.

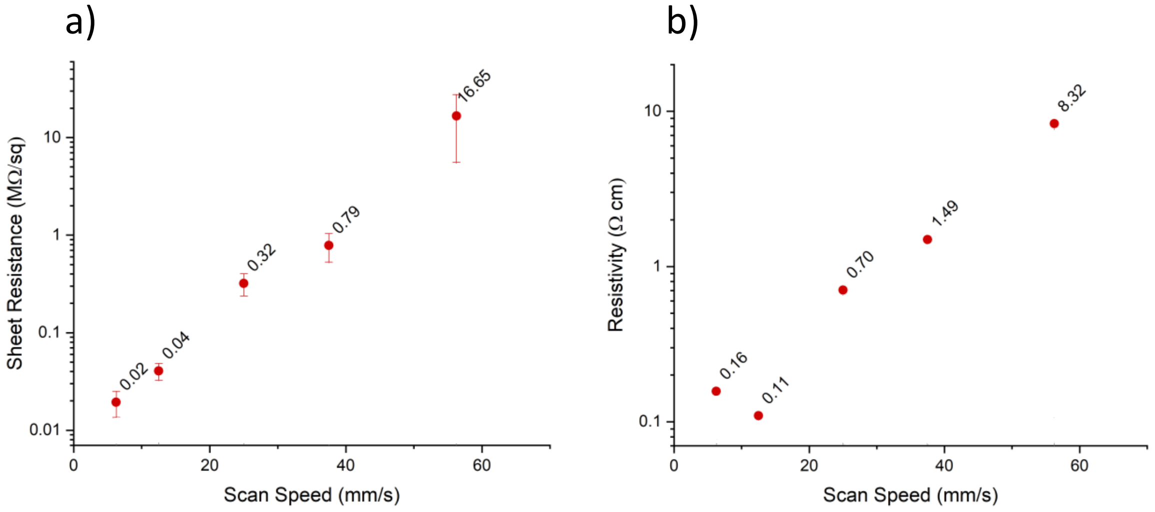

Figure 5-31. Sheet Resistance (a) and resistivity (b) of the Cu_2O film as a function of the scan speed.

It can be seen that the speed of 13 mm/s yields the best conductivity for the deposited Cu_2O film. Even taking into account the thickness, resistivity as low as 0.11 Ω.cm could be achieved, which is one of the lowest resistivity seen in Cu_2O thin films both in this thesis and in literature. Furthermore, it is interesting to note that even though a scan speed of 6 mm/s yields the highest GPC, a scan speed of 13 mm/s yields a similar GPC than higher scan speeds, but can achieve a higher conductivity on the thin films.

After characterizing the conductivity of the films deposited, the XRD patterns of the layers deposited with different speeds were obtained. It is apparent that the thicker sample deposited at 6 mm/s presents a well-defined diffraction (111) peak in the pattern, which intensity decreases as the scan speed increases. Besides the intensity of the peak, which corresponds to the thickness of the layer, all observable peaks present the characteristic shift, possibly indicating the existence of stress in the lattice of the Cu_2O. This is consistent with the XRD patterns previously shown for samples deposited with 15% of oxygen flow.

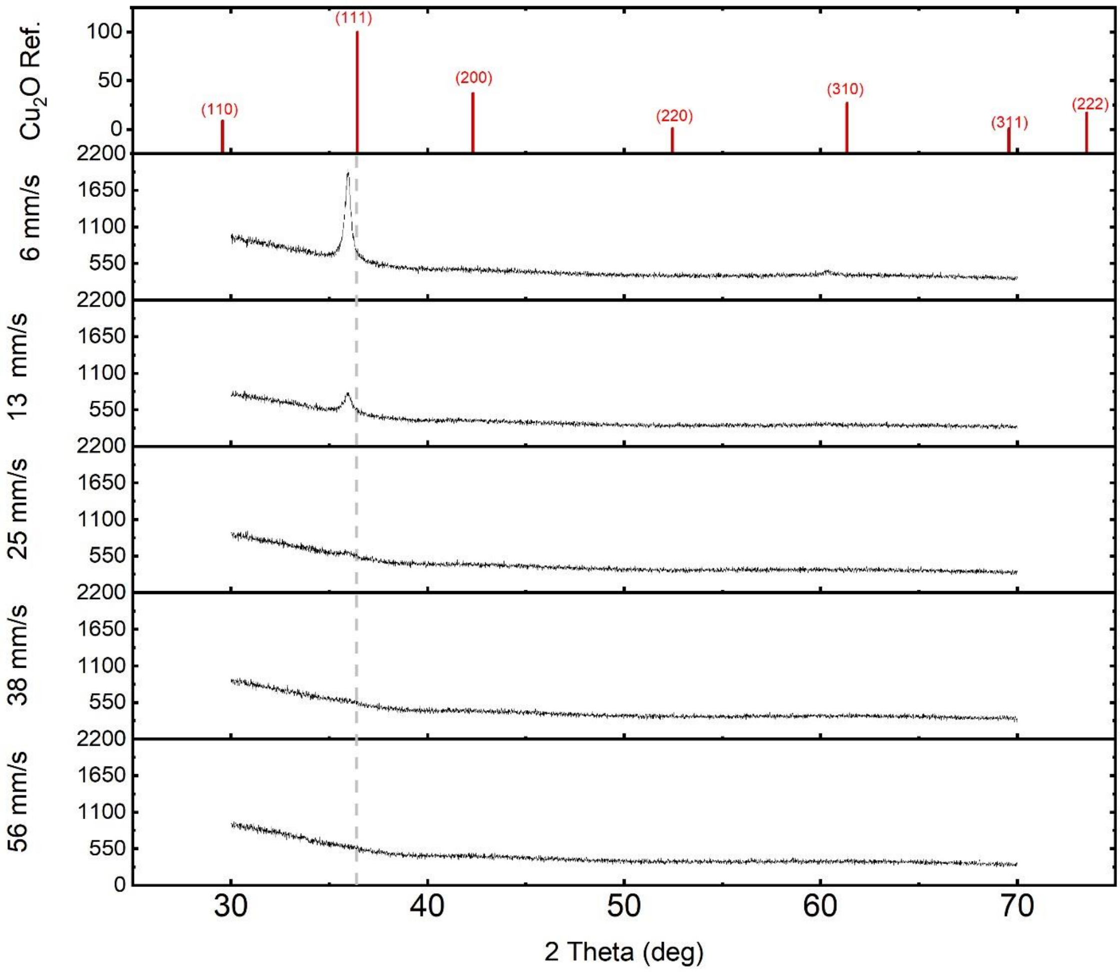

Figure 5-32 *XRD patterns of the Cu_2O films deposited with different scanning speeds. 25 (a), 50 (b), 100 (c), 150 (d), and 225 (e) mm/sec.*

5.5.4 *Water And Oxygen*

Finally, it is interesting to understand the role in the SALD process of the oxidant element that in our setup can be oxygen or water. To investigate this, 4 different Cu_2O samples were deposited varying the mixing of O_2 and water in the SALD deposition process. Figure 5-33 shows Cu_2O samples deposited with: 0% concentration of water and 0% percent concentration of oxygen, i.e. only N_2 flow in the output (sample a), 0% concentration of water and 15% concentration of oxygen (sample b), 83% water and 15% oxygen (sample c), and once more, with 0% water and 15% oxygen (sample d). The latter sample was deposited only to verify that the effects of introducing water on the gas panel was reversible and that the sample (sample b) was reproducible.

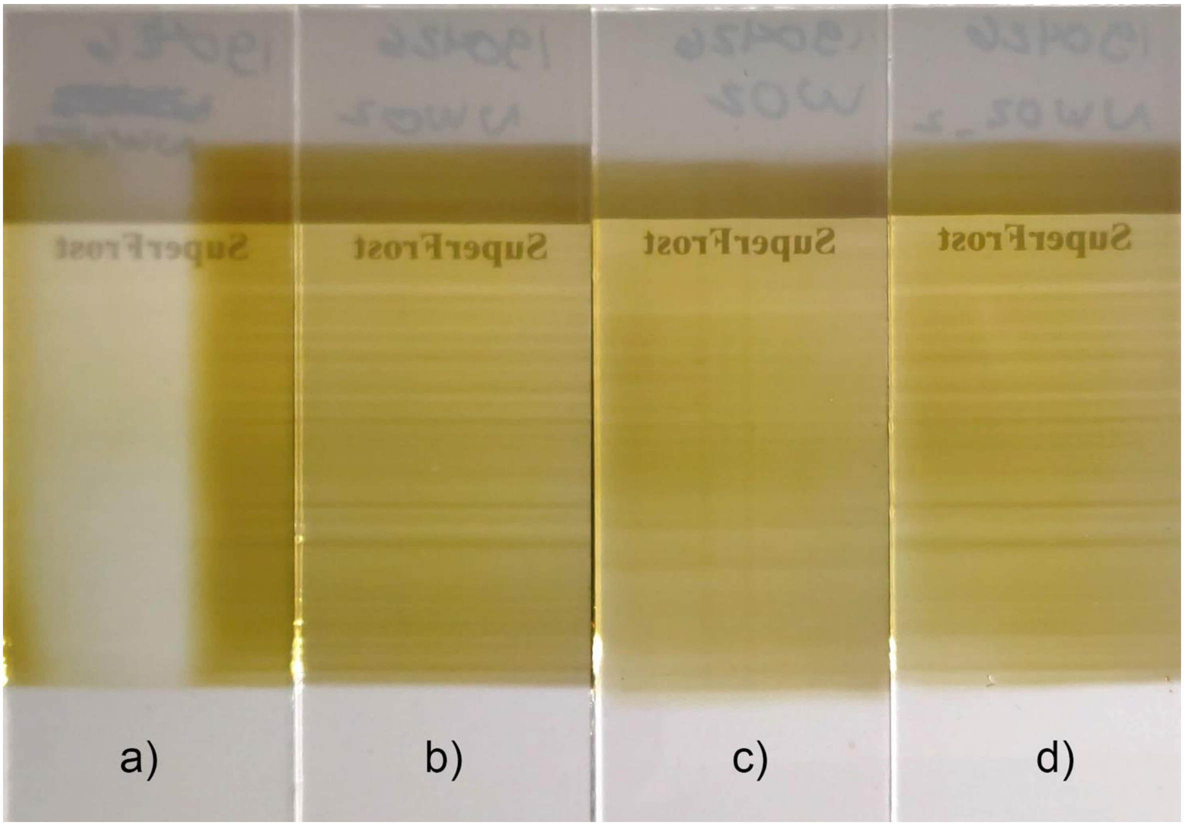

Figure 5-33. *Optical photographs for Cu_2O layers deposited with different values of oxygen and water during deposition: 0% concentration of water and 0% percent concentration of oxygen (a), 0% concentration of water and 15% concentration of oxygen (b), 83% water and 15% oxygen (c), and once more, with 0% water and 15% oxygen (d).*

Figure 5-34 shows SEM images of the surface of the sample deposited with 83% of water during the deposition and the sample deposited with 0% water during the deposition. Although the conductive properties of the film are influenced by the inclusion of water, the topography seems unaffected.

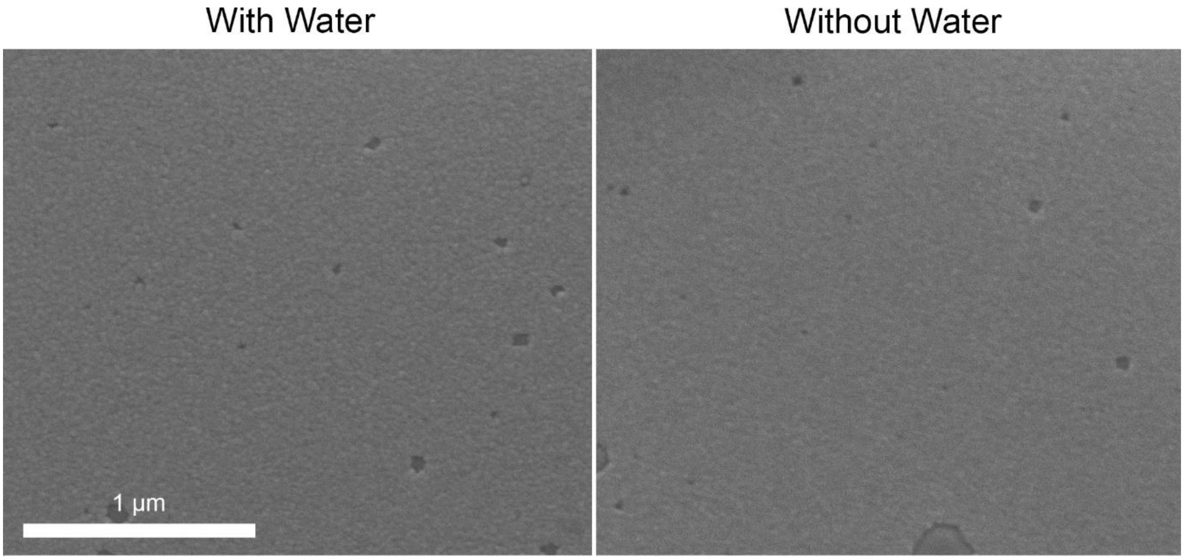

Figure 5-34. *SEM images of Cu_2O films deposited with 15% of oxygen and 83% of water (a) and 15% oxygen and 0% water (b).*

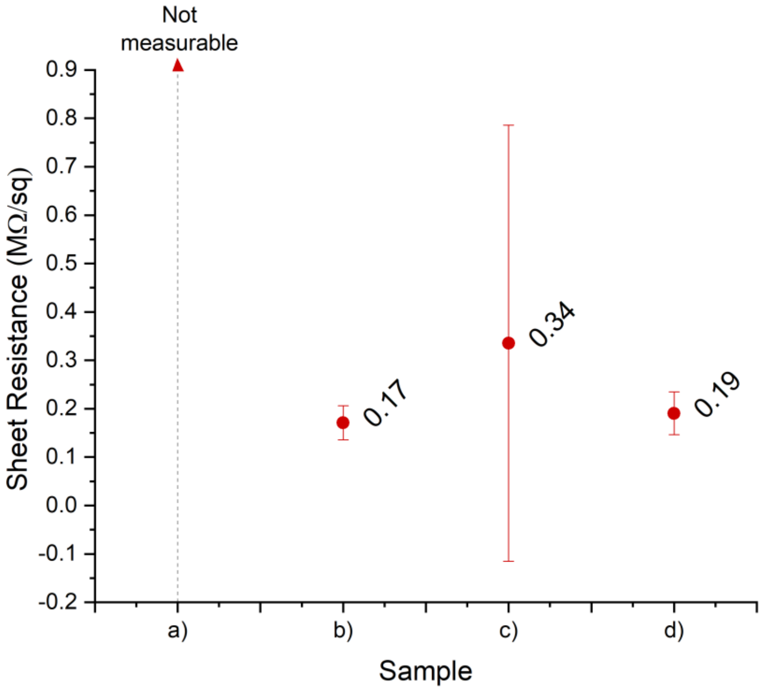

Figure 5-35 *Sheet Resistance of the Cu_2O film as a function of a) no water and no oxygen, b) no water and 15%oxygen, c) 83% water and 15% O_2, d) no water and 15% oxygen (once more).*

Figure 5-35 shows the sheet resistance measured with 4PP at LMGP for each deposition previously mentioned. The sample with no water and no oxygen was not taken into account in the resistance measurements since the sample is not homogeneous and, in fact, the zone that remains under the deposition head at all times (i.e., that is not exposed to the atmosphere during the deposition) is too thin to measure resistance with the equipment at LMGP. Nevertheless, this sample was important to make sure that the water presence in the system indeed causes a surface chemical reaction since, without it, the layer cannot grow and, actually, it is possible that the small amount that has been deposited on the zones never exposed to the atmosphere took place due to the diffusion of the atmosphere's humidity diffusion into the gap.

Regarding the samples with oxygen and/or water, it is interesting to note that, even though the water causes a complete surface reaction on the surface to create the layers of Cu_2O, it seems that the presence of oxygen achieves indeed a better conductivity of the deposited Cu_2O films. Even more, these depositions suggest that the homogeneity of the conductivity in the film is in fact hindered by the presence of water in the process, phenomenon that was confirmed in these depositions by the sample (d), in which water was removed, and the conductivity of the film presented a more homogeneous conductivity along the whole film, as evidenced by the lower variance of the conductivity measurements.

Once more, XRD patterns of the films deposited show the usual shift on the (111) peak of the Cu_2O. Furthermore, with such patters, shown in Figure 5-36, it is possible to see that the intensity of the peak of the sample without water is slightly higher, possibly indicating a thicker layer. It makes sense then that the sheet resistance for such layer is lower and it may be reasonable to conclude that the inclusion of water actually decreases the GPC of the process.

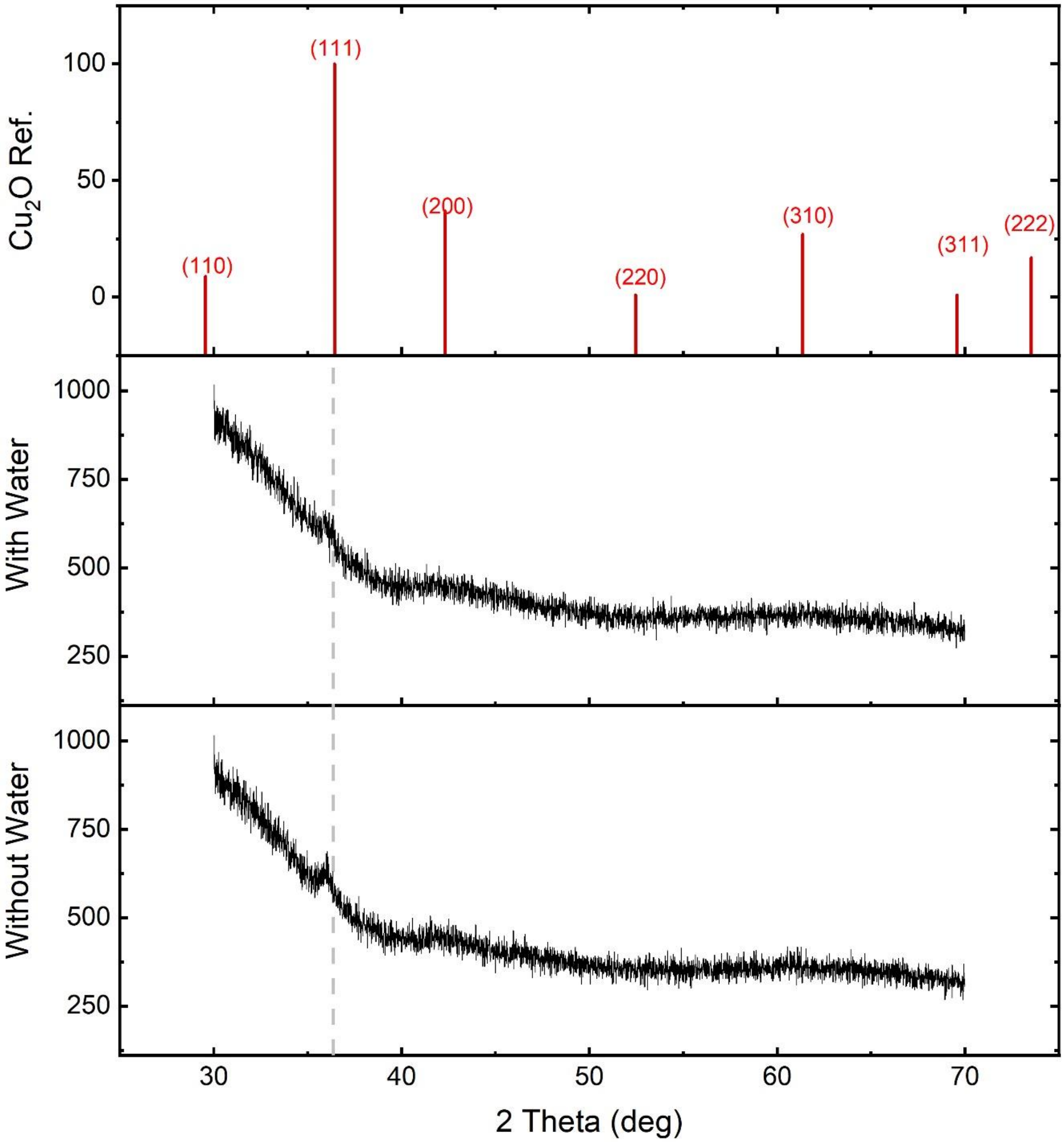

Figure 5-36. *XRD patterns of Cu$_2$O films deposited with 15% oxygen and 83% water (a) and 15% oxygen and 0% water.*

5.6 Discussion of experimental results

In this work, thin films of Cu$_2$O were successfully deposited on glass substrates using the SALD system along with the bubblers and heaters fabricated during this thesis, following the guidelines that FEM simulations offered and, finally, making use of the enhanced, monolithic 3D printed deposition heads designed and fabricated also in this doctoral thesis.

All depositions were made with the glass slide moving orthogonally to the deposition head as shown in Figure 5-37. Furthermore, all substrates went to an exposure to the atmosphere at every SALD oscillation. However, it is interesting to note that with the addition of oxygen in the SALD flows, the inhomogeneities on the conduction on the film disappeared as visibly apparent in Figure 5-33.

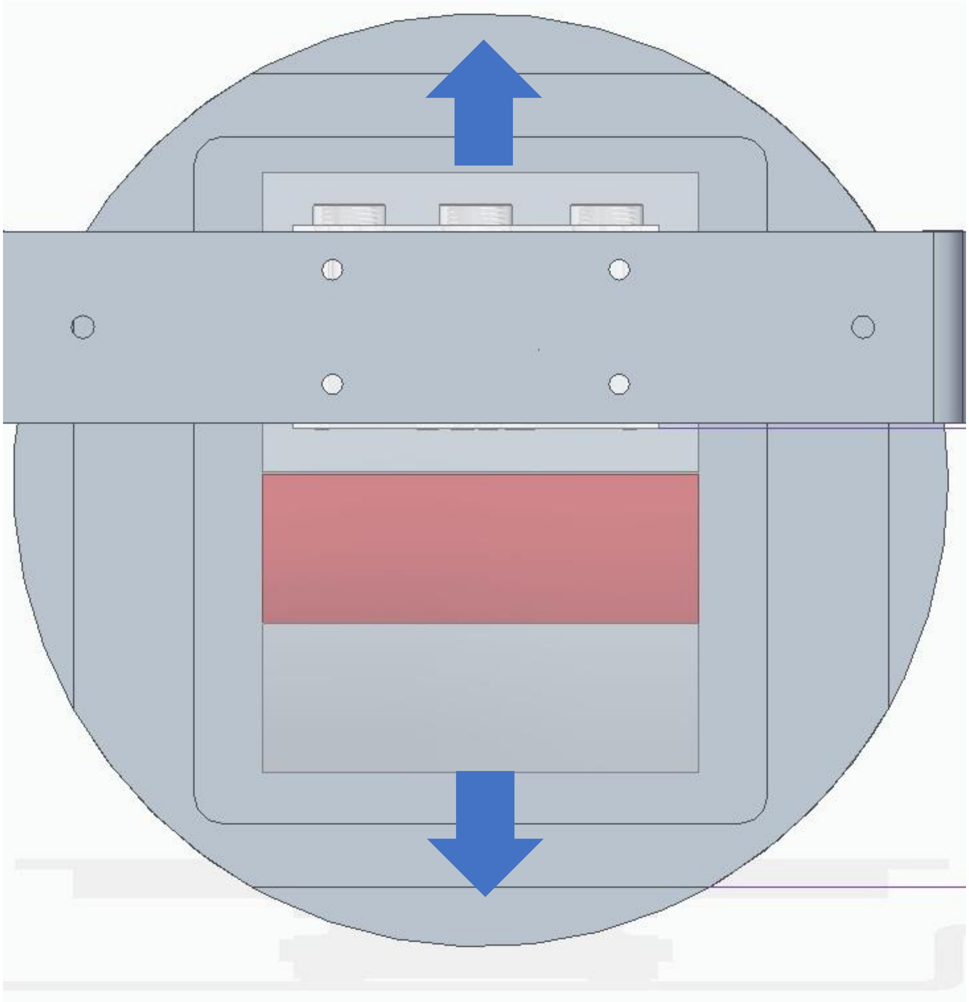

Figure 5-37. *Schematic showing the direction of scanning for the samples deposited in this thesis with blue arrows. The red square represents the position in which the substrates were positioned.*

The two precursors used here form part of the $Cu^{I}(\beta - diketonate)L$ precursors commonly used in CVD metallic copper depositions due to their volatility and high deposition rates. Here, an alternative chemical mechanism is proposed, in which, in presence of water, the $\beta - diketonate$ is attached to a hydrogen atom and released as gaseous $H(\beta - diketonate)$. A similar mechanism has been proposed in [142], which is evidence of the possibility of such mechanism. Although in this work it has not been confirmed quantitively, and doing so would be important for future works, the deposition of high purity and crystalline Cu_2O is evidence of such mechanism. For the deposition process, two different precursors were used, one using TMVS and another using COD as the stabilizing ligand and (hfac) as a $\beta - diketonate$ compound for both precursors.

SALD deposition of Cu_2O yields layers that are characterized by the same benefits of conventional ALD films: high density, low roughness and crystalline growth. The deposition with SALD is comparable to alternative chemical methods, with the added benefit of the soft process that ALD provides, and the low-cost, industrial compatibility and quick cycle time that SALD offers. Furthermore, SALD offers the possibility of tuning the deposition, and hence the film properties, by simple changes in the system; avoiding costly tailoring of organometallic precursors.

SALD deposits flat Cu_2O thin films with a roughness of ~3 nm, and a density of ~5.8 g/cm3, which is close to the theoretical bulk density. The thin films can be deposited with nanometric control by defining the number of oscillations that the substrate will scan under the deposition head. Even though the precursors are not as volatile as other precursors used in ALD such as diethylzinc, the deposition conditions were tuned for each precursor. The growth rate obtained is in the order of magnitude of 0.3 Å/cycle, comparable with reported values of Cu_2O ALD depositions. However, given the fast cycle scanning of SALD, the growth rates are in the order of ~2 nm/min, two orders of magnitude higher than the less than 25 pm/min obtained with conventional ALD in [154], [165]

5.6.1 *Stability of Precursors: Cupraselect vs CuCOD*

During this thesis, two different precursors were tested to deposit Cu_2O thin films. Although both are usable for the deposition of crystalline and homogeneous Cu_2O films, it seems that the stability of the Cupraselect is not good when heated. Heating was needed for both precursors here used, Cupraselect and CuCOD, since their vapor pressure at room temperature is too low comparing with other precursors like DEZ. However, it seems that the Cupraselect precursor is not stable both in a short term, i.e. in approximately 24 hours, decreasing the growth rate of the deposition as time passes, nor in the long term, i.e. in approximately 48 days, where the deposition rate of the process and properties of the deposited Cu_2O films changes considerably.

The 24 hours instability may be attributed to the decrease of concentration of the reactive species of the precursor. As the precursor heats up, the $Cu^I(hfac)TMVS$ molecule may be decomposed following Equation (1) but, as the bubbler creates an isolated space, the released $TMVS$ cannot escape, allowing it to react again with the $Cu^{II}(hfac)_2$ that remained in the precursor as the temperature is decreased and the precursor is left to rest (overnight). Once this happens, the original chemical structure of the precursor is regained, and depositions can be achieved once more. Although this mechanism could explain the observations during experiments, the mechanism here proposed still needs to be verified and validated.

Regarding the long-term instability, this may be explained by the disproportionation reaction shown in Equation (2), where metallic copper is deposited. This can be verified by the presence of orange (copper color) deposition on the bubbler after some days. Furthermore, in this work, it is proposed that, as the precursor is heated for several days, as the disproportionation reaction product $Cu^{II}(hfac)_2$ is created and not exhausted (due to the closed bubbler), in presence of moisture in the air, the following reaction occurs:

$$Cu^{II}(hfac)_2 + H_2O \longrightarrow CuO + 2\,H(\beta - diketonate)_{(g)}\,, \qquad (6)$$

Since CuO is black, this explains the black solid deposit on the bubbler after several weeks of usage in the SALD (see Figure 5-13). It is expected then that the Cupraselect precursor chemically changes inside the bubbler due to both the intrinsic instability of the precursor at high temperatures, as reported before [149], and due to the lack of proper sealing of the bubbler to the atmosphere's moisture.

Although there is little evidence of such mechanisms occurring, and indeed the mechanism behind its instability hasn't been widely reported, the Cupraselect precursor is known to be thermally unstable [166], [167].

On the other hand, the reason for the appearance of the nano-sized shapes seen in the deposited film when using a just re-filled precursor bubbler (Figure 5-13d) remains unknown, and it would be interesting to understand the reaction mechanism that leads to such shapes. Indeed, somewhat similar growth mode has been previously reported, where oxidation of copper foils using a thermogravimetric apparatus leads to the appearance of "whiskers" on the film, depending on the oxidation temperature and the presence of water in the oxidizing gas [168]. Still, the mechanism leading to such shapes needs to be studied further to find ways to fabricate such morphologies that could be promising for increasing the surface area in the substrate; important feature in e.g. photovoltaics or photoelectrochemical water splitting.

When using the CuCOD precursor, such instabilities were not seen and the depositions, besides being of comparable quality and properties of the ones made with Cupraselect precursor, they also seemed to be more reproducible and stable in the long-term. This was the case since, when using this precursor, the bubbler was improved by using proper rubber seals and stainless steel industrial-grade sealing joints. The usage of CuCOD led to high quality Cu_2O films and allowed for a systematic study of the material. Interestingly, the use of CuCOD led to depositions of films with mainly a (111) crystalline orientation. Further studies would be needed to understand of the underlying phenomenon that causes this preference.

5.6.2 *Deposition Gap in the SALD*

As expected, given the FEM simulations presented on chapter 3, by easily changing the gap on the SALD system, the deposition can be tuned to deposit in a CVD or an ALD regime. ALD regime has the advantage of a denser film with low roughness and nanometric thickness control. The ALD regime, as is the case for conventional ALD, leads to high quality depositions that have low roughness and with good electrical conductivity, making highly conductive Cu_2O thin films possible.

The GPC of the process can be finely tuned by changing the value of the gap. Nevertheless, the electrical properties of the film may be affected, and the confinement of the gases may not be properly achieved. Furthermore, as the SALD works in open air, the diffusion of moisture and oxygen in the atmosphere also play a more important role when the deposition gap is large.

As the deposition gap was increased, major improvements on the conductivity of the layer were observed. Such changes were consistent with a change of growth orientation, which shows that a less crystallized layer with a mixture of (111) and (200) orientation presents a higher conductivity. However, this was later attributed to the exposure of the substrate to the atmosphere as the substrate scans back-and-forth under the deposition head.

Analyzing Hall effect measurements, it can be seen that, for the conductive samples, when the sample exposure to the atmosphere is limited (sample ALD-50), the carrier concentration is lower than when the sample is exposed to the atmosphere (sample ALD-90), while the mobility is higher for the former, and lower for the latter. This is a known phenomenon in which a high carrier concentration causes low mobility due to ionized impurity scattering [94].

On the other hand, it is possible that the increase of GPC observed for a deposition gap of 150 µm with respect to a gap of 250 µm happens due to the increase of convective diffusion of the concentration in the deposition gap, which would induce a CVD regime even with low values of deposition gaps. Although the simulations made in this work don't shown such behavior, it is possible that the diffusivity of the precursors within the carrier gas is higher due to the molecular weight of the precursors. Indeed, simulations were made with the molecular weight of DEZ, which is substantially lower than the molecular weight of the copper precursors here used. Hence, the higher flow velocities of the gases in a narrow gap may induce a higher convective diffusion, hence causing a higher CVD regime for smaller gaps.

5.6.3 *Inclusion of Oxygen during the SALD deposition of Cu_2O*

In order to add oxygen during the deposition process of Cu_2O films, some flow of gaseous O_2 was introduced in the slot assigned for the inert gaseous outlet in the deposition head. The results of the depositions show that the addition of oxygen in the inert gas region affects positively the conductivity of the deposited Cu_2O films. It seems that 15% of oxygen (with respect to the total outlet in the inert gas region) yields to the best conductivity in the film. Also, the GPC of the process is increased as the amount of oxygen introduced is increased.

The Tauc plots for the layers deposited with different amount of oxygen show optical bandgap values from 2.4 to 2.5 eV, confirming that the material of the films deposited is similar. Additionally, Raman spectroscopy shows two main things. First, the layers with oxygen are much less crystallized than the layer deposited without oxygen in the process, as judging by the broad peaks corresponding to the Cu_2O Raman vibrations. Second, the Raman peak at a wavenumber of 150 cm^{-1} corresponding to a $\Gamma 15^-$ vibration, effectively disappears. As this peak is attributed to oxygen vacancies [RefCuO1, RefCuO2], the disappearance of such peak suggests that more oxygen is present in the film (hence decreasing the amount of oxygen vacancies in the lattice).

Since the inclusion of oxygen improved the deposition, three studies were made to find a strategy to improve the conductivity of the Cu_2O thin films using the SALD system parameters: 1) study of the deposition gap, 2) effect of the scan speed and, 3) simultaneous presence of water and oxygen.

Out of these series of depositions, we show the main conclusions drawn:

5.6.3.1 Water introduction in the process increase mobility but, in presence of oxygen, hinders the conductivity:

The Cu_2O depositions done in ALD regime present high conductivity, as evidenced by the low resistivity values measured. This happens due to the inherent properties of ALD depositions, which enhance the density and homogeneity if the film. However, it is possible that the water as an oxidizing agent in the process is not sufficient for the surface reaction, leading to a high amount of oxygen vacancies present in the film, thus leading to poor conductivity as evidenced by films with a sheet resistance higher than 120 MΩ/sq.

Wang, et. al. [168] have reported the oxidation behavior of copper. According to their reported mechanism, the presence of water vapor on the oxidation process of the copper plays an important role on substituting copper vacancies of the lattice with positively charged hydrogen atoms (H^+), hence effectively decreasing the conduction mechanism of the Cu_2O, which is known to be via the V_{Cu}'s.

5.6.3.2 The oxidation of the Cu_2O layer exclusively by oxygen in the gas panel improves conductivity.

The deposition made with 15% oxygen were measured to be considerably more conductive that the ones without presence of oxygen. This suggests that the oxygen enhances the charge carrier creation, phenomenon that was also suggested in the literature.

The mechanism of formation can be described as follows [168]:

$$\frac{1}{4} O_{2(g)} + Cu_{Cu}^{X} \xrightarrow{\qquad} V_{Cu} + h + \frac{1}{2} O_{O}^{X} \;, \tag{7}$$

Which confirms that the presence of oxygen enhances in fact the creation of copper vacancies and, thus increasing the charge carrier concentration. In the case of the precursors used in this work, and given that the surface contains $Cu^{II}(hfac)_2$, the reaction may be proposed as follows

$$O_{2(g)} + 4\, Cu^{II}(hfac)_2 \xrightarrow{\qquad} V_{Cu} + h + 2Cu_2O + 8\,(hfac)_2 \tag{8}$$

If this mechanism is true, then it is important to get rid of the highly reactive $(hfac)_2$. This fact leads to the next conclusion.

5.6.3.3 An optimized gap value is needed

It seems that when the deposition gap is too small (~150 µm), when oxygen is present in the film, the conductivity is lower than when the gap is slightly larger (~250 µm). This suggests that, in order to improve even further the charge carrier generation in the film, a small quantity of water is needed. In this case, such quantity is provided by the diffusion of water from the atmosphere given the deposition gap. It may be possible, then, that, in the presence of water, the following reaction occurs:

$$2\,(hfac)_2 + 2\,H_2O \xrightarrow{\qquad} 4\,H(hfac) + O_2, \tag{9}$$

allowing for the reactive species to be eliminated and generating even more oxygen for the charge carrier generation.

This mechanism is still to be verified by studying the by-products of the surface reaction in situ on the SALD, interesting for the future developments of Cu_2O deposition in the SALD, since the open-air technique allows for a relatively simple in-situ gaseous characterization such as Fourier Transform Infrared Spectroscopy (FTIR), and the deposition head provides a convenient was to extract the remnants and by-products of the deposition.

5.6.3.4 Too much oxygen during the deposition process decreases the conductivity.

The depositions made with high concentration of oxygen presented a decrease of conductivity and, for the case of the deposition in which 75% of the flow in the inert gas outlet was oxygen, a change on the shape on the Tauc plot was observed.

These observations suggest that the mechanism corresponds to the one reported in [168]. According to such report, the partial pressure of oxygen affects the oxidation of the copper in the layer. It is reported that at an oxygen partial pressure smaller than a given equilibrium concentration, the creation of Cu_2O is favored, whereas at oxygen partial pressure higher than such equilibrium concentration, CuO is formed on the outer layer of the film.

It seems then that too much oxygen in the process may induce the generation CuO as impurities in the film, causing for the conduction mechanism to be hindered. Although this unfortunately was not proved in this work, this may be a possible explanation on the decrease of conductivity and the change on the total transmittance (and hence the Tauc plot) when more than 15% of oxygen is added to the SALD deposition of Cu_2O (Figure 5-20).

5.6.3.5 The slow scan speed and diffusion on the film.

The slow scan speed allows for a better diffusion of the oxygen and reactants through the film, which allows for a better charge carrier creation through the whole bulk.

It seems that the scan speed allows for a better deposition of thin films. If we take into account that the mechanism reported in [168] relies on a diffusion of oxygen, the increase of conductivity as the scan speed decreases may be explained by the increase of residence time by the substrate in each gaseous reactant region, which gives more time for the oxygen to diffuse into the whole Cu_2O film when scan speeds are slow.

5.7 Conclusions and perspectives

The deposition of Cu_2O was achieved and the properties of the film were successfully controlled by relatively simple changes in the deposition process, allowing for a faster screening of deposition conditions. Much work is nevertheless needed to confirm the phenomena here presented. As interesting perspectives for future work would be the confirmation of the absence of oxygen vacancies in the films with 15% oxygen, possibly with XPS measurements. Characterizing also a series of samples with varied oxygen concentration by XPS, would allow for confirmation of stoichiometry change and so, V_{Cu} defect density influence on conduction mechanism. Alternatively, a detailed study on film microstructure after annealing would also shed some light for conduction mechanism. The in-situ characterization of the surface reaction by-products is also an interesting task that should be tackled to confirm the reaction mechanisms here presented. Further tests with different amounts of water concentration in the deposition should be screened as well, to define the optimum amount of humidity in the deposition needed to achieve the best conductivity. Finally, Hall effect measurements should be done to quantitatively measure the mobility and carrier concentration of the layers deposited with oxygen, which would provide much more information than only 4PP measurements.

Much of the characterization not done here was due to the limited time for the work but, with the optimization done in the SALD and the changes made to the system, the deposition can be done rather quickly and easily, taking advantage of the quick and high quality depositions that SALD offers. Nevertheless, it was demonstrated here that SALD can tune the properties in a cheap and relatively simple way, allowing for a faster screening of conditions, depending on the application desired. Cu_2O was shown to achieve unprecedented conductivity, aided by the open-air work mechanism of the SALD. Further work should include the creation of electronic devices that take advantage of the conductivity and the fast deposition rates that the SALD can achieve.

General Conclusions and Perspectives

Spatial Atomic Layer Deposition (SALD) is an alternative technique to Atomic Layer Deposition (ALD) that provides the ability to deposit nanometric thin films with comparable properties than those obtained by ALD. Based on the same fundamental physical and chemical principles, SALD offers in addition the potential for industrialized high throughput fabrication and processing of nanometric thin films, interesting especially for the development of novel electronic devices that have unconventional properties such as flexibility or transparency.

The SALD system has numerous ways of being implemented, since its main mechanism of deposition relies on the spatial, rather than temporal, separation of the reagents needed to perform a surface chemical reaction at the surface of the substrate. Out of all these approaches, the close-proximity approach, used in the LMGP and along this thesis, has been demonstrated for the deposition of high quality, conformal and homogeneous thin films, comparable with other thin film deposition techniques such as (MO)CVD, PLD or Spray Pyrolysis. On the other hand, SALD also provides alternatives to techniques such as RF Magnetron Sputtering and conventional ALD, where highly conductive films can be achieved but the cost of the fabrication method makes its industrialization a complex matter.

Nevertheless, despite the high-quality depositions it has achieved, the close-proximity SALD deposition method is just in its infancy with respect of the potential applications, variations and developments it can offer. While it has proved successful depositions with different materials, the library of materials is relatively short and the optimal conditions for their successful deposition are still to be tested and defined. For this, the different properties of the precursors used in the deposition procedure must be considered. On the other hand, envisioning industrial fabrication of thin films, the mechanical components of the SALD system must also be designed considering the requirements for quality, homogeneity and reproducibility of the depositions. Industrial-compatible thin film fabrications must be designed to achieve large area depositions with a high-throughput. SALD is a promising candidate to accomplish such task, having already been used in production of large area surface for high throughput depositions. However, a precise control of the depositions is needed to exploit all its benefits. Particularly, the fluid mechanics phenomena occurring within the system and its impact in the material properties must be elucidated so that reproducibility can be obtained. On the other hand, the usage of costly components must be avoided when possible, and hence, a careful design of the components must be considered. Finally, as the SALD deposition mechanism relies on a displacement of the substrate through different reactant regions, it is important to ensure the precision of such displacement, or, at least, to control its impact on the final deposition properties.

In this thesis project, an approach to the development, study and optimization of the close-proximity SALD system at LMGP is presented. Such optimizations and enhancements were guided by the requirements of the deposition of one of the few oxides that present a p-type semiconductor behavior, and that has potential applications in transparent electronics, photovoltaics and photoelectrochemical water splitting: cuprous oxide (Cu_2O).

This work was divided in several sections that present the work done in the SALD and in the Cu_2O thin films. In the first chapter of the present report, an overview of the scientific literature is presented, both regarding the SALD deposition method, and the Cu_2O material properties achieved by different deposition methods. Regarding the Cu_2O material, the main electrical and optical properties of the Cu_2O are presented and literature regarding its p-type conduction mechanism is discussed. Furthermore, a general overview and comparison of the different Cu_2O fabrication methods is shown, considering the conductivity of the Cu_2O films they can achieve. Afterwards, to consider the industrial compatibility of Cu_2O as a thin film component in electronic devices, SALD is presented as a promising candidate. Since SALD is indeed a derivation of the conventional ALD deposition method, a brief explanation of ALD and a comparison against SALD is presented. Multiple approaches to achieve the “spatial” attribute of SALD are presented, out of which the close-proximity approach is shown as the strategy used in multiple thin-film fabrications previously published by the LMGP.

In the second chapter, the methods and materials used in this thesis are presented. First, the SALD system is presented in detail, as well as the changes made to add the capability to deposit Cu_2O thin films. Such changes consist mainly on a temperature-controlled bubbler that had to be designed and implemented in the automation system of the SALD, taking care that the temperature had to be precisely controlled, not to induce instability to the chemicals inside the bubbler, and to ensure a proper delivery of the volatilized reagents onto the surface of the substrate, avoiding its condensation at any point in the gas delivery panel. Furthermore, one of the main components of the SALD system is presented: the deposition head. Such component is key to achieve the phenomena that accomplish the spatial separation of reagents required for SALD. Also, in chapter 2, the techniques and instruments used for the characterization of the thin films deposited with the SALD are presented, including SEM, XRD, XRR, Raman Spectroscopy, UV-Vis-nIR, 4 Point Probe, Van der Pauw and Hall-effect measurements.

Given the importance of the deposition head in the SALD system and the gap it creates due to its close-proximity to the substrate, a study of the fluid mechanics in such gap is presented in chapter 3. For this, using Comsol Multyphysics® software, a CFD simulation was performed and coupled with diffusion of concentrated species and surface chemical reactions, to simulate the intermixing of species in the deposition gap. It was shown that changing the value of the deposition gap induces a rapid change in the intermixing in the gas phase of the gap, allowing for a tuning on the deposition regime from an ALD deposition, with a slower but more controlled growth rate that yields a dense and conductive film, to a CVD-like regime in the deposition, where the growth rate increases at the expense of the quality of the film. Also, the exhaust efficiency of the deposition head was shown to have an impact on the intermixing of the species. It was shown that, with a low exhaust efficiency, a localized surface reaction rate on the substrate appears, leading to localized lines of deposition. This is of special interest for area selective deposition, which has been shown to be complex, since the approach here presented provides a simple and innovative way to locally increase the deposition rate, and it is the first time that ASD is shown to work with spatial CVD or ALD.

Continuing with the simulations made, several geometrical parameters were studied. The tilt on the deposition head was shown to have an important effect on the deposition regime, causing inhomogeneities along the deposition, and justifying the need of precision mechanisms that can control the position and movements of the deposition head to the micrometric level. Furthermore, the geometry of the deposition head slits was studied and it was shown that, by changing the width of the gas outlets and/or the gas exhausts, it is possible to envision a deposition head in which the deposition regime can be controlled for longer ranges of deposition gap value, making the SALD deposition method more flexible and, possibly, less constraining regarding the mechanical precision needed.

Chapter 3 provides a convenient strategy to systematically study and optimize the geometry of the deposition head slits to tune the deposition regime in a customizable form. With the use of CFD, different deposition head slit architecture can be studied and, by creating virtual prototypes, a faster optimized thin-film deposition can be achieved.

In this work, the knowledge obtained by the CFD simulations was implemented for the design of a deposition head specifically fabricated for the Cu_2O thin film depositions. Furthermore, since the fabrication of a new deposition head as designed previously to this work required costly and complex processes, a full process for the fabrication of a low-cost and low-complexity deposition head was established in LMGP, which included its mechanical design via the CAD software Solid Edge®, along with its fabrication via additive manufacturing. Such process is detailed in chapter 4 of the present work.

The design of the new deposition head reduced some of the complexity of the previous deposition head. As a main property, the new deposition head was intended to be designed as a single piece with no assembly process needed. For this, the design starts with the definition of the architecture of the slits for the gaseous outlets or exhausts. Once defined, the inner path for the gases was designed, considering that the inlets for the deposition head had, in our case, a circular shape with a defined diameter. The inner path of the gases was designed so that the circular input to the head was transformed to a rectangle-shaped outlet that would be in close-proximity to the substrate. This design is flexible, and the same method can be applied for virtually any size, although each design should be validated for a homogeneous gas distribution along the squared outlet, with the help of CFD tools, as mentioned before. Once these paths are designed, the outer design of the deposition head must be made. The outer shape is dependent on the physical space available in the system, as well as the range of displacement of the substrate beneath the deposition head. Also, it is desired that such geometry has the least volume as possible so that the cost of the material needed for its fabrication is reduced as much as possible. Once both parts are designed, a subtraction operation is performed to "hollow" the gaseous paths from the outer shape, thus creating the deposition head. Final designs and adaptations are added to the design, such as adapters for screws or parts used to hold the piece in place, before its fabrication.

For the fabrication, since with conventional fabrication methods it is impossible or costly to fabricate the inner channels required for the new deposition head, additive manufacturing, also known as 3D printing, was used. In this case, a stereolithography (SLA) 3D printing in polymeric resin was performed for the fabrication of prototypes of the new deposition head, that were successfully tested in the SALD system. Once one of the designs was validated and tested for the deposition of Cu_2O, such design was printed by an external provider with Selective Laser Sintering (SLS) of metallic powders, to obtain an aluminum 3D-printed SALD deposition head. This last deposition head provided unprecedented deposition control in its homogeneity and in the control of the deposition area, it allowed for a better gap alignment with the substrate and provided a heat-resistant deposition head for Cu_2O thin films.

The tasks presented in chapter 4 were tested in this work and can be replicated for the quick fabrication of new deposition heads, allowing for the introduction of new materials to the SALD system, avoiding the contamination of the films due to other materials deposited. Furthermore, the 3D design and printing of the deposition head provides a wide spectrum of possibilities thanks to the flexibility of additive manufacturing. In the case of this doctoral thesis, the geometry of the deposition head was customized in the width of the slits in it. But the 3D printing technology allows for a design with any number, shape and architecture of slits and exhausts in the deposition head. This consequently can be exploited for the area selective deposition of materials using the same principle of the SALD, coupled with a well-designed deposition head and the proper automation for such task. Also, in chapter 4, some of the preliminary designs that exploit a more complex architecture and design were presented, including a multi-layer deposition head, and a free-form SALD "Pen", which has been recently obtained interesting preliminary results in the LMGP. With these, it is possible to envisage free-form depositions of high-quality thin films, and even whole device printing systems, without sacrificing the benefits of the SALD technique. These results provide only the starting point of a whole new paradigm of deposition methods that may allow for the deposition of nanostructured multilayer stacks and even whole printed devices in an additive manner.

Finally, in chapter 5, with all the changes and adaptations made to the SALD system, the deposition of Cu_2O thin films was used as a test for the SALD adaptations and studied and optimized to obtain highly conductive Cu_2O transparent p-type thin films. For this, two different copper(I) β-diketonate precursors were tested, one of which presented instable depositions. Using the more stable precursor, it was possible to demonstrate that, with the addition of 15% of oxygen during the deposition, the resistivity of the thin films was decreased up to 2 orders of magnitude. It is suggested that the inclusion of oxygen during deposition of Cu_2O enhances the creation of copper vacancies (V_{Cu}), while the inclusion of enough moisture in the surface reaction allows for a full chemical reaction, of the remaining β-diketonate in the surface, allowing to increase the oxygen in the surface and, thus generating charge carriers in the film.

Although the mechanism here proposed would require further experimental validation and the phenomena suggested need to be elucidated, when the deposition conditions were properly combined with the scan speed of the substrate displacement and the proper value of gap, Cu_2O films with a resistivity of down to ∼0.5 Ω.cm were obtained. This shows that, by performing simple changes to the system (the deposition gap), to the deposition head (the width of the slits), and/or to the deposition flows (the inclusion of a small percentage of oxygen in the flow), it is possible to tune the properties of the Cu_2O films deposited, to obtain a high-mobility and low carrier concentration, or vice versa, and even obtain highly conductive films without the inclusion of dopants in the film.

With the adaptations done to the SALD system, Cu_2O is now optimized for further study of the conduction phenomena, as well as for its implementation in devices as a p-type semiconductor. Furthermore, the whole process for such adaptations can be replicated to allow the deposition of high-quality and tunable thin films of other materials.

The present work provides one of the first steps towards the implementation of a deposition system that can be easily modified to tune the properties to the thin films fabricated. The SALD system here optimized, as well as the Cu_2O films here deposited are the beginning of a series of iteration with the aim to improve both the deposition process of the SALD to include more complex and versatile thin film processing, and the study of the conductivity mechanisms in the Cu_2O thin films and their integration into electronic devices.

With its industrialization in mind, the SALD system must be tested in large-area scale depositions. This includes either the fabrication of a deposition head that allows for the deposition on a larger area, or the modification of the deposition process to deposit in a continuous way either on a rigid substrate or using a roll-to-roll deposition. Regarding the deposition head, multiple perspectives can be seen concerning its design and fabrication via 3D printing. Deposition heads that allow for the deposition of multiple materials in the same deposition scanning, deposition heads that allow free-form thin film deposition and large-area deposition heads, are among some of the variations that 3D design and printing could offer. However, such design can be modified in any number of ways, and the design here presented is just the start of the path towards a complex, functional and fully customizable deposition head. For that, the simulations here presented can be further improved. Here, the simulation of the deposition head consisted on a two-dimensional simulation that corresponds to the cross-sectional geometry of the deposition head. If large-area depositions are envisaged, it would be useful to further develop a three-dimensional simulation in order to precisely simulate the flow along the whole deposition head, thus ensuring homogeneity in the whole film deposited. This would also be of great help when defining the gas flows needed for a large-area deposition, by ensuring that the needed parameters are achievable within a reasonable complexity and cost. Furthermore, a 3D simulation would indeed be capable of simulating the whole deposition process, allowing to spot potential areas of improvement in the deposition process. Additionally, if coupled with more chemical-oriented simulations, the simulations would allow to customize also the deposited material properties, allowing a holistic virtual prototyping of the SALD system for the prediction of important parameters such as the film properties or the GPC of the deposition process.

Finally, with the SALD capabilities of depositing Cu_2O, the next step is to apply the high conductive properties to develop devices such as the hole transport layer (HTL) in solar cells or as an electrode for solar photoelectrochemical water splitting devices. For this, the interface of the layers of a device must be tuned, which could potentially be achieved with SALD by properly controlling the deposition conditions in the system.

Eventually, with a catalog of sufficient size of materials optimized for SALD deposition, and with the proper automation and control of the system, a full cycle of printed electronic devices, fully industrial compatible and with a high throughput can be envisaged. The work presented here provides new approaches towards such objective.

References

[1] T. Minami, "Transparent conducting oxide semiconductors for transparent electrodes," *Semicond. Sci. Technol.*, vol. 20, no. 4, pp. S35–S44, Mar. 2005.

[2] A. Dabirian *et al.*, "Tuning the Optoelectronic Properties of ZnO:Al by Addition of Silica for Light Trapping in High-Efficiency Crystalline Si Solar Cells," *Adv. Mater. Interfaces*, vol. 3, no. 3, p. 1500462, 2016.

[3] C. Guillén and J. Herrero, "TCO/metal/TCO structures for energy and flexible electronics," *Thin Solid Films*, vol. 520, no. 1, pp. 1–17, Oct. 2011.

[4] M. H. Ani, F. Helmi, S. H. Herman, and S. Noh, "Resistive switching of Cu/Cu2O junction fabricated using simple thermal oxidation at 423 K for memristor application," *IOP Conf. Ser. Mater. Sci. Eng.*, vol. 290, p. 012088, Jan. 2018.

[5] E. L. Runnerstrom, A. Llordés, S. D. Lounis, and D. J. Milliron, "Nanostructured electrochromic smart windows: traditional materials and NIR-selective plasmonic nanocrystals," *Chem. Commun.*, vol. 50, no. 73, pp. 10555–10572, Aug. 2014.

[6] M. Morales-Masis, S. D. Wolf, R. Woods-Robinson, J. W. Ager, and C. Ballif, "Transparent Electrodes for Efficient Optoelectronics," *Adv. Electron. Mater.*, vol. 3, no. 5, p. 1600529, 2017.

[7] K. Ellmer, "Past achievements and future challenges in the development of optically transparent electrodes," *Nat. Photonics*, vol. 6, no. 12, pp. 809–817, Dec. 2012.

[8] H. Ohta and H. Hosono, "Transparent oxide optoelectronics," *Mater. Today*, vol. 7, no. 6, pp. 42–51, Jun. 2004.

[9] Z. Wang, P. K. Nayak, J. A. Caraveo-Frescas, and H. N. Alshareef, "Recent Developments in p-Type Oxide Semiconductor Materials and Devices," *Adv. Mater.*, vol. 28, no. 20, pp. 3831–3892, 2016.

[10] K. H. L. Zhang, K. Xi, M. G. Blamire, and R. G. Egdell, "P-type transparent conducting oxides," *J. Phys. Condens. Matter*, vol. 28, no. 38, p. 383002, Jul. 2016.

[11] H. Kawazoe, M. Yasukawa, H. Hyodo, M. Kurita, H. Yanagi, and H. Hosono, "P-type electrical conduction in transparent thin films of CuAlO2," *Nature*, vol. 389, no. 6654, pp. 939–942, Oct. 1997.

[12] G. Hautier, A. Miglio, G. Ceder, G.-M. Rignanese, and X. Gonze, "Identification and design principles of low hole effective mass p-type transparent conducting oxides," *Nat. Commun.*, vol. 4, p. 2292, Aug. 2013.

[13] B. S. Li, K. Akimoto, and A. Shen, "Growth of Cu2O thin films with high hole mobility by introducing a low-temperature buffer layer," *J. Cryst. Growth*, vol. 311, no. 4, pp. 1102–1105, Feb. 2009.

[14] K. Matsuzaki, K. Nomura, H. Yanagi, T. Kamiya, M. Hirano, and H. Hosono, "Epitaxial growth of high mobility Cu2O thin films and application to p-channel thin film transistor," *Appl. Phys. Lett.*, vol. 93, no. 20, p. 202107, Nov. 2008.

[15] Y. Wang *et al.*, “Electronic structures of Cu2O, Cu4O3, and CuO: A joint experimental and theoretical study,” *Phys. Rev. B*, vol. 94, no. 24, p. 245418, Dec. 2016.
[16] D. W. H. Rankin, “CRC handbook of chemistry and physics, 89th edition, edited by David R. Lide,” *Crystallogr. Rev.*, vol. 15, no. 3, pp. 223–224, Jul. 2009.
[17] “Rare Earth Elements—Critical Resources for High Technology | USGS Fact Sheet 087-02.” [Online]. Available: https://pubs.usgs.gov/fs/2002/fs087-02/. [Accessed: 10-Aug-2019].
[18] Y.-N. Kim, H.-G. Shin, J.-K. Song, D.-H. Cho, H.-S. Lee, and Y.-G. Jung, “Thermal Degradation Behavior of Indium Tin Oxide Thin Films Deposited by Radio Frequency Magnetron Sputtering,” *J. Mater. Res.*, vol. 20, no. 6, pp. 1574–1579, Jun. 2005.
[19] S. Rühle *et al.*, “All-Oxide Photovoltaics,” *J. Phys. Chem. Lett.*, vol. 3, p. 3755−3764, Dec. 2012.
[20] T. Dimopoulos, “Chapter 11 - All-Oxide Solar Cells,” in *The Future of Semiconductor Oxides in Next-Generation Solar Cells*, M. Lira-Cantu, Ed. Elsevier, 2018, pp. 439–480.
[21] Y. Ievskaya, R. L. Z. Hoye, A. Sadhanala, K. P. Musselman, and J. L. MacManus-Driscoll, “Fabrication of ZnO/Cu2O heterojunctions in atmospheric conditions: Improved interface quality and solar cell performance,” *Sol. Energy Mater. Sol. Cells*, vol. 135, pp. 43–48, Oct. 2015.
[22] T. Minami, Y. Nishi, and T. Miyata, “High-Efficiency Cu2O-Based Heterojunction Solar Cells Fabricated Using a Ga2O3 Thin Film as N-Type Layer,” *Appl. Phys. Express*, vol. 6, no. 4, p. 044101, Mar. 2013.
[23] T. Minami, Y. Nishi, and T. Miyata, “Efficiency enhancement using a Zn1− x Ge x -O thin film as an n-type window layer in Cu2O-based heterojunction solar cells,” *Appl. Phys. Express*, vol. 9, no. 5, p. 052301, Apr. 2016.
[24] C. Zuo and L. Ding, “Solution-Processed Cu2O and CuO as Hole Transport Materials for Efficient Perovskite Solar Cells,” *Small*, vol. 11, no. 41, pp. 5528–5532, Nov. 2015.
[25] E. Ruiz, S. Alvarez, P. Alemany, and R. A. Evarestov, “Electronic structure and properties of Cu2O,” *Phys. Rev. B*, vol. 56, no. 12, pp. 7189–7196, Sep. 1997.
[26] M. M. Islam, B. Diawara, V. Maurice, and P. Marcus, “Bulk and surface properties of Cu2O: A first-principles investigation,” *J. Mol. Struct. THEOCHEM*, vol. 1–3, no. 903, pp. 41–48, 2009.
[27] J. Deuermeier *et al.*, “Visualization of nanocrystalline CuO in the grain boundaries of Cu2O thin films and effect on band bending and film resistivity,” *APL Mater.*, vol. 6, no. 9, p. 096103, Sep. 2018.
[28] J. Deuermeier *et al.*, “Highly conductive grain boundaries in copper oxide thin films,” *J. Appl. Phys.*, vol. 119, no. 23, p. 235303, Jun. 2016.
[29] B. K. Meyer *et al.*, “Chapter Six - The Physics of Copper Oxide (Cu2O),” in *Semiconductors and Semimetals*, vol. 88, B. G. Svensson, S. J. Pearton, and C. Jagadish, Eds. Elsevier, 2013, pp. 201–226.
[30] P. A. Korzhavyi and B. Johansson, “Literature review on the properties of cuprous oxide Cu2O and the process of copper oxidation,” Swedish Nuclear Fuel and Waste Management Co., SKB-TR--11-08, 2011.
[31] S. Astronomiche and F. Biccari, “Defects and Doping in Cu 2 O,” no. 688774, 2009.

[32] D. O. Scanlon, B. J. Morgan, and G. W. Watson, “Modeling the polaronic nature of p-type defects in Cu2O: the failure of GGA and GGA + U.,” *J. Chem. Phys.*, vol. 131, no. 12, p. 124703, 2009.

[33] H. Raebiger, S. Lany, and A. Zunger, “Origins of the p-type nature and cation deficiency in Cu2O and related materials,” *Phys. Rev. B*, vol. 76, no. 4, p. 045209, Jul. 2007.

[34] S. K. Baek, Y. H. Kwon, J. H. Shin, H. S. Lee, and H. K. Cho, “Low-Temperature Processable High-Performance Electrochemically Deposited p-Type Cuprous Oxides Achieved by Incorporating a Small Amount of Antimony,” *Adv. Funct. Mater.*, vol. 25, no. 32, pp. 5214–5221, 2015.

[35] J. W. Hodby, T. E. Jenkins, C. Schwab, H. Tamura, and D. Trivich, “Cyclotron resonance of electrons and of holes in cuprous oxide, Cu2O,” *J. Phys. C Solid State Phys.*, vol. 9, no. 8, pp. 1429–1439, Apr. 1976.

[36] D. Muñoz-Rojas *et al.*, “Growth of 5 cm2V − 1s − 1 mobility , p-type Copper (I) oxide (Cu2O) films by fast atmospheric atomic layer deposition (AALD) at 225 ° C and below,” *AIP Adv.*, vol. 2, no. 4, p. 042179, 2012.

[37] Y. Ebisuzaki, “Preparation of Monocrystalline Cuprous Oxide,” *J. Appl. Phys.*, vol. 32, no. 10, pp. 2027–2028, Oct. 1961.

[38] H. Liu *et al.*, “Cu2O Thin Films: The Role of Humidity in Tuning the Texture and Electrical Properties of Cu2O Thin Films Deposited via Aerosol-Assisted CVD (Adv. Mater. Interfaces 3/2019),” *Adv. Mater. Interfaces*, vol. 6, no. 3, p. 1970020, Feb. 2019.

[39] S. Ishizuka, T. Maruyama, and K. Akimoto, “Thin-Film Deposition of Cu2O by Reactive Radio-Frequency Magnetron Sputtering,” *Jpn. J. Appl. Phys.*, vol. 39, no. 8A, p. L786, Aug. 2000.

[40] C. Hilsum, “Simple empirical relationship between mobility and carrier concentration,” *Electron. Lett.*, vol. 10, no. 13, pp. 259–260, Jun. 1974.

[41] D. B. M. Klaassen, “A unified mobility model for device simulation—I. Model equations and concentration dependence,” *Solid-State Electron.*, vol. 35, no. 7, pp. 953–959, Jul. 1992.

[42] Ø. Nordseth, “Silicon-Based Tandem Solar Cells,” *Laboratory Journal – Business Web for Users in Science and Industry*, Jun. 2017.

[43] T. P. White, N. N. Lal, and K. R. Catchpole, “Tandem Solar Cells Based on High-Efficiency c-Si Bottom Cells: Top Cell Requirements for >30% Efficiency,” *IEEE J. Photovolt.*, vol. 4, no. 1, pp. 208–214, Jan. 2014.

[44] C. Malerba, F. Biccari, C. Leonor Azanza Ricardo, M. D’Incau, P. Scardi, and A. Mittiga, “Absorption coefficient of bulk and thin film Cu2O,” *Sol. Energy Mater. Sol. Cells*, vol. 95, no. 10, pp. 2848–2854, Oct. 2011.

[45] B. Balamurugan and B. R. Mehta, “Optical and structural properties of nanocrystalline copper oxide thin films prepared by activated reactive evaporation,” *Thin Solid Films*, vol. 396, pp. 90–96, 2001.

[46] W. G. J. H. M. van Sark, A. Meijerink, and R. E. I. Schropp, “Solar Spectrum Conversion for Photovoltaics Using Nanoparticles,” *Third Gener. Photovolt.*, Mar. 2012.

[47] F. Ran, M. Taniguti, H. Hosono, and T. Kamiya, “Analyses of Surface and Interfacial Layers in Polycrystalline Cu2O Thin-Film Transistors,” *J. Disp. Technol.*, vol. 11, no. 9, pp. 720–724, Sep. 2015.

[48] K. Matsuzaki, K. Nomura, H. Yanagi, T. Kamiya, M. Hirano, and H. Hosono, “Effects of post-annealing on (110) Cu2O epitaxial films and origin of low mobility in Cu2O thin-film transistor,” *Phys. Status Solidi A*, vol. 206, no. 9, pp. 2192–2197, 2009.

[49] E. Fortunato *et al.*, “Thin-film transistors based on p-type Cu2O thin films produced at room temperature,” *Appl. Phys. Lett.*, vol. 96, no. 19, p. 192102, May 2010.

[50] “Design of p-CuO/n-ZnO heterojunctions by rf magnetron sputtering | DORA Empa.” [Online]. Available: https://www.dora.lib4ri.ch/empa/islandora/object/empa:5861. [Accessed: 28-Apr-2019].

[51] T. Minami, Y. Nishi, and T. Miyata, “Impact of incorporating sodium into polycrystalline p-type Cu2O for heterojunction solar cell applications,” *Appl. Phys. Lett.*, vol. 105, no. 21, p. 212104, Nov. 2014.

[52] Y. H. Ko, G. Nagaraju, S. H. Lee, and J. S. Yu, “Facile preparation and optoelectronic properties of CuO nanowires for violet light sensing,” *Mater. Lett.*, vol. 117, pp. 217–220, Feb. 2014.

[53] L. Wang *et al.*, “Enhancing the efficiency of ZnO/Cu2O inorganic nanostructure solar cells simply by CdS quantum dots,” *Sol. Energy Mater. Sol. Cells*, vol. 130, pp. 387–392, Nov. 2014.

[54] W. L. (余温雷) Yu *et al.*, “Diversity of electronic transitions and photoluminescence properties of p-type cuprous oxide films: A temperature-dependent spectral transmittance study,” *J. Appl. Phys.*, vol. 117, no. 4, p. 045701, Jan. 2015.

[55] “Electrospray deposition and characterization of Cu_2O thin films with ring-shaped 2-D network structure.” [Online]. Available: https://www.jstage.jst.go.jp/article/jcersj2/122/1425/122_JCSJ-T14010/_article/-char/ja/. [Accessed: 28-Apr-2019].

[56] J. Li *et al.*, “Engineering of optically defect free Cu_2O enabling exciton luminescence at room temperature,” *Opt. Mater. Express*, vol. 3, no. 12, pp. 2072–2077, Dec. 2013.

[57] “Copper oxide quantum dot ink for inkjet-driven digitally controlled high mobility field effect transistors - Journal of Materials Chemistry C (RSC Publishing).” [Online]. Available: https://pubs.rsc.org/en/content/articlelanding/2013/tc/c3tc00869j#!divAbstract. [Accessed: 28-Apr-2019].

[58] “Magnesium-doped cuprous oxide (Mg:Cu2O) thin films as a transparent p-type semiconductor - Resende - 2016 - physica status solidi (a) - Wiley Online Library.” [Online]. Available: https://onlinelibrary.wiley.com/doi/full/10.1002/pssa.201532870. [Accessed: 28-Apr-2019].

[59] J.-D. Kwon *et al.*, “Controlled Growth and Properties of p-Type Cuprous Oxide Films by Plasma-Enhanced Atomic Layer Deposition at Low Temperature,” *Appl. Surf. Sci.*, vol. 285P, pp. 373–379, Aug. 2013.

[60] X. Zou, G. Fang, L. Yuan, M. Li, W. Guan, and X. Zhao, “Top-Gate Low-Threshold Voltage Cu2O Thin-Film Transistor Grown on SiO2/Si Substrate Using a High-κHfON Gate Dielectric,” *IEEE Electron Device Lett.*, vol. 31, no. 8, pp. 827–829, Aug. 2010.

[61] S. Jeong and E. S. Aydil, “Structural and electrical properties of Cu2O thin films deposited on ZnO by metal organic chemical vapor deposition,” *J. Vac. Sci. Technol. A*, vol. 28, no. 6, pp. 1338–1343, Sep. 2010.

[62] H. Kim *et al.*, “Highly-conformal p-type copper(I) oxide (Cu2O) thin films by atomic layer deposition using a fluorine-free amino-alkoxide precursor,” *Appl. Surf. Sci.*, vol. 349, pp. 673–682, Sep. 2015.

[63] S. Y. Kim *et al.*, “p-Channel oxide thin film transistors using solution-processed copper oxide,” *ACS Appl. Mater. Interfaces*, vol. 5, no. 7, pp. 2417–2421, Apr. 2013.

[64] W. Yu *et al.*, “Enhanced Fröhlich interaction of semiconductor cuprous oxide films determined by temperature-dependent Raman scattering and spectral transmittance,” *J. Raman Spectrosc.*, vol. 44, no. 1, pp. 142–146, 2013.

[65] A. H. Jayatissa, K. Guo, and A. C. Jayasuriya, “Fabrication of cuprous and cupric oxide thin films by heat treatment,” *Appl. Surf. Sci.*, vol. 255, no. 23, pp. 9474–9479, Sep. 2009.

[66] S. S. Jeong, A. Mittiga, E. Salza, A. Masci, and S. Passerini, “Electrodeposited ZnO/Cu2O heterojunction solar cells,” *Electrochimica Acta*, vol. 53, no. 5, pp. 2226–2231, Jan. 2008.

[67] C.-L. Chu, H.-C. Lu, C.-Y. Lo, C.-Y. Lai, and Y.-H. Wang, “Physical properties of copper oxide thin films prepared by dc reactive magnetron sputtering under different oxygen partial pressures,” *Phys. B Condens. Matter*, vol. 404, no. 23, pp. 4831–4834, Dec. 2009.

[68] S. Eisermann *et al.*, “Copper oxide thin films by chemical vapor deposition: Synthesis, characterization and electrical properties,” *Phys. Status Solidi A*, vol. 209, no. 3, pp. 531–536, 2012.

[69] T. Ikenoue, T. Kawai, R. Wakashima, M. Miyake, and T. Hirato, “Hole mobility improvement in Cu2O thin films prepared by the mist CVD method,” *Appl. Phys. Express*, vol. 12, no. 5, p. 055509, Apr. 2019.

[70] S. Jeong and E. S. Aydil, “Structural and electrical properties of Cu[sub 2]O thin films deposited on ZnO by metal organic chemical vapor deposition,” *J. Vac. Sci. Technol. Vac. Surf. Films*, vol. 28, no. 6, p. 1338, Sep. 2010.

[71] J.-D. Kwon *et al.*, “Controlled Growth and Properties of p-Type Cuprous Oxide Films by Plasma-Enhanced Atomic Layer Deposition at Low Temperature,” *Appl. Surf. Sci.*, vol. 285P, pp. 373–379, Aug. 2013.

[72] T. Kosugi and S. Kaneko, “Novel Spray-Pyrolysis Deposition of Cuprous Oxide Thin Films,” *J. Am. Ceram. Soc.*, vol. 81, no. 12, pp. 3117–3124, 1998.

[73] L. Bergerot, C. Jiménez, O. Chaix-Pluchery, L. Rapenne, and J.-L. Deschanvres, “Growth and characterization of Sr-doped Cu2O thin films deposited by metalorganic chemical vapor deposition,” *Phys. Status Solidi A*, vol. 212, no. 8, pp. 1735–1741, Aug. 2015.

[74] J. Resende *et al.*, “Resilience of Cuprous Oxide under Oxidizing Thermal Treatments via Magnesium Doping,” *J. Phys. Chem. C*, vol. 123, no. 14, pp. 8663–8670, Apr. 2019.

[75] K. Akimoto, S. Ishizuka, M. Yanagita, Y. Nawa, G. K. Paul, and T. Sakurai, “Thin film deposition of Cu_2O and application for solar cells,” *Sol. Energy*, vol. 80, pp. 715–722, 2006.

[76] A. O. Musa, T. Akomolafe, and M. J. Carter, “Production of cuprous oxide, a solar cell material, by thermal oxidation and a study of its physical and electrical properties,” *Sol. Energy Mater. Sol. Cells*, vol. 51, pp. 305–316, 1998.

[77] S. K. Baek, Y. H. Kwon, J. H. Shin, H. S. Lee, and H. K. Cho, “Low-Temperature Processable High-Performance Electrochemically Deposited p-Type Cuprous Oxides Achieved by Incorporating a Small Amount of Antimony,” *Adv. Funct. Mater.*, vol. 25, no. 32, pp. 5214–5221, Aug. 2015.

[78] D. Muñoz-Rojas, V. H. Nguyen, C. M. de la Huerta, C. Jiménez, and D. Bellet, “Spatial Atomic Layer Deposition,” *Chem. Vap. Depos. Nanotechnol.*, Jan. 2019.

[79] P. W. May and Y. A. Mankelevich, “From Ultrananocrystalline Diamond to Single Crystal Diamond Growth in Hot Filament and Microwave Plasma-Enhanced CVD Reactors: a Unified Model for Growth Rates and Grain Sizes,” *J. Phys. Chem. C*, vol. 112, no. 32, pp. 12432–12441, Aug. 2008.

[80] A. Yanguas-Gil, *Growth and Transport in Nanostructured Materials: Reactive Transport in PVD, CVD, and ALD*. Springer International Publishing, 2017.

[81] R. W. Johnson, A. Hultqvist, and S. F. Bent, “A brief review of atomic layer deposition: from fundamentals to applications,” *Mater. Today*, vol. 17, no. 5, pp. 236–246, Jun. 2014.

[82] P. Uprety, B. Macco, M. M. Junda, C. R. Grice, W. M. M. Kessels, and N. J. Podraza, “Optical and electrical properties of H2 plasma-treated ZnO films prepared by atomic layer deposition using supercycles,” *Mater. Sci. Semicond. Process.*, vol. 84, pp. 91–100, Sep. 2018.

[83] A. Rezk and I. Saadat, “High-Performance ALD Al-Doped ZnO Thin-Film Transistors Grown on Flexible Substrates,” *IEEE Electron Device Lett.*, vol. 40, no. 2, pp. 240–242, Feb. 2019.

[84] M. Bosund, D. E. M. Salmi, and R. Peltonen, “Atomic layer deposition into ultra-high aspect ratio structures with a stop-flow ALD reactor,” p. 2.

[85] R. Vallat, R. Gassilloud, B. Eychenne, and C. Vallée, “Selective deposition of Ta2O5 by adding plasma etching super-cycles in plasma enhanced atomic layer deposition steps,” *J. Vac. Sci. Technol. A*, vol. 35, no. 1, p. 01B104, Nov. 2016.

[86] “(Invited) Area Selective Atomic Layer Deposition As an Emerging Process for Advanced Nanofabrication.” [Online]. Available: http://ma.ecsdl.org/content/MA2019-01/23/1186.short. [Accessed: 27-Apr-2019].

[87] “Fifteen Nanometer Resolved Patterns in Selective Area Atomic Layer Deposition—Defectivity Reduction by Monolayer Design - ACS Applied Materials & Interfaces (ACS Publications).” [Online]. Available: https://pubs.acs.org/doi/abs/10.1021/acsami.8b13896. [Accessed: 27-Apr-2019].

[88] S. F. Nelson, C. R. Ellinger, and D. H. Levy, “Improving Yield and Performance in ZnO Thin-Film Transistors Made Using Selective Area Deposition,” *ACS Appl. Mater. Interfaces*, vol. 7, no. 4, pp. 2754–2759, 2015.

[89] X. Liu *et al.*, “Metalorganic chemical vapor deposition of Al2O3 using trimethylaluminum and O2 precursors: Growth mechanism and crystallinity,” *J. Cryst. Growth*, vol. 408, pp. 78–84, Dec. 2014.

[90] G. Z. Wang, Y. Wang, M. Y. Yau, C. Y. To, C. J. Deng, and D. H. L. Ng, “Synthesis of ZnO hexagonal columnar pins by chemical vapor deposition,” *Mater. Lett.*, vol. 59, no. 29, pp. 3870–3875, Dec. 2005.

[91] E. Ahvenniemi *et al.*, “Review Article: Recommended reading list of early publications on atomic layer deposition—Outcome of the ‘Virtual Project on the History of ALD,’” *J. Vac. Sci. Technol. Vac. Surf. Films*, vol. 35, no. 1, p. 010801, Jan. 2017.

[92] D. Muñoz-Rojas, V. H. Nguyen, C. Masse de la Huerta, S. Aghazadehchors, C. Jiménez, and D. Bellet, “Spatial Atomic Layer Deposition (SALD), an emerging tool for energy materials. Application to new-generation photovoltaic devices and transparent conductive materials,” *Comptes Rendus Phys.*, vol. 18, no. 7, pp. 391–400, Sep. 2017.

[93] D. Muñoz-Rojas and J. MacManus-Driscoll, "Spatial atmospheric atomic layer deposition: a new laboratory and industrial tool for low-cost photovoltaics," *Mater. Horiz.*, p. Doi:10.1039/c3mh00136a, 2014.

[94] V. H. Nguyen, U. Gottlieb, A. Valla, D. Muñoz, D. Bellet, and D. Muñoz-Rojas, "Electron tunneling through grain boundaries in transparent conductive oxides and implications for electrical conductivity: the case of ZnO:Al thin films," *Mater. Horiz.*, vol. 5, no. 4, pp. 715–726, Jul. 2018.

[95] V. H. Nguyen *et al.*, "Deposition of ZnO based thin films by atmospheric pressure spatial atomic layer deposition for application in solar cells," *J. Renew. Sustain. Energy*, vol. 9, no. 2, p. 021203, Mar. 2017.

[96] H. Choi *et al.*, "Fast spatial atomic layer deposition of Al2O3 at low temperature (<100 °C) as a gas permeation barrier for flexible organic light-emitting diode displays," *J. Vac. Sci. Technol. Vac. Surf. Films*, vol. 34, no. 1, p. 01A121, Jan. 2016.

[97] P. Poodt, A. Lankhorst, F. Roozeboom, K. Spee, D. Maas, and A. Vermeer, "High-speed spatial atomic-layer deposition of aluminum oxide layers for solar cell passivation," *Adv. Mater.*, vol. 22, no. 32, pp. 3564–7, Aug. 2010.

[98] S. Franke *et al.*, "Alumina films as gas barrier layers grown by spatial atomic layer deposition with trimethylaluminum and different oxygen sources," *J. Vac. Sci. Technol. A*, vol. 35, no. 1, p. 01B117, Dec. 2016.

[99] P. Poodt *et al.*, "Spatial atomic layer deposition: A route towards further industrialization of atomic layer deposition," *J. Vac. Sci. Technol. Vac. Surf. Films*, vol. 30, no. 1, p. 010802, 2012.

[100] D. MUÑOZ-ROJAS, "Dépôt par couche atomique spatiale (SALD)," *Ref : TIP958WEB - "Innovations technologiques,"* 10-Nov-2016. [Online]. Available: https://www.techniques-ingenieur.fr/base-documentaire/innovation-th10/innovations-en-materiaux-avances-42186210/depot-par-couche-atomique-spatiale-sald-re262/. [Accessed: 11-Aug-2019].

[101] "Spatial Atomic Layer Deposition | IntechOpen." [Online]. Available: https://www.intechopen.com/books/chemical-vapor-deposition-for-nanotechnology/spatial-atomic-layer-deposition. [Accessed: 28-Apr-2019].

[102] L. David H., "Process for atomic layer deposition," 7,413,982, 19-Aug-2008.

[103] D. H. Levy, D. Freeman, S. F. Nelson, P. J. Cowdery-Corvan, and L. M. Irving, "Stable ZnO thin film transistors by fast open air atomic layer deposition," *Appl. Phys. Lett.*, vol. 92, no. 19, p. 192101, May 2008.

[104] P. Poodt, R. Knaapen, A. Illiberi, F. Roozeboom, and A. van Asten, "Low temperature and roll-to-roll spatial atomic layer deposition for flexible electronics," *J. Vac. Sci. Technol. Vac. Surf. Films*, vol. 30, no. 1, p. 01A142, Dec. 2012.

[105] K. Ali and K.-H. Choi, "Low-Temperature Roll-to-Roll Atmospheric Atomic Layer Deposition of Al2O3 Thin Films.," *Langmuir ACS J. Surf. Colloids*, Nov. 2014.

[106] E. Dickey and W. A. Barrow, "High rate roll to roll atomic layer deposition, and its application to moisture barriers on polymer films," *J. Vac. Sci. Technol. Vac. Surf. Films*, vol. 30, no. 2, p. 021502, Jan. 2012.

[107] W. M. M. (Erwin) Kessels and M. Putkonen, "Advanced process technologies: Plasma, direct-write, atmospheric pressure, and roll-to-roll ALD," *MRS Bull.*, vol. 36, no. 11, pp. 907–913, Nov. 2011.

[108] X. Jiang and S. F. Bent, “Area-Selective ALD with Soft Lithographic Methods: Using Self-Assembled Monolayers to Direct Film Deposition,” *J. Phys. Chem. C*, vol. 113, no. 41, pp. 17613–17625, Oct. 2009.

[109] L. Hoffmann, “Spatial atomic layer deposition of electrically (non-)conductive gas diffusion barriers,” Wissenschaftliche Abschlussarbeiten » Dissertation, Universität Wuppertal, Fakultät für Elektrotechnik, Informationstechnik und Medientechnik » Elektrotechnik » Dissertationen, 2018.

[110] L. Hoffmann *et al.*, “Atmospheric pressure plasma enhanced spatial atomic layer deposition of SnOx as conductive gas diffusion barrier,” *J. Vac. Sci. Technol. A*, vol. 36, no. 1, p. 01A112, Dec. 2017.

[111] L. Hoffmann *et al.*, “Spatial Atmospheric Pressure Atomic Layer Deposition of Tin Oxide as an Impermeable Electron Extraction Layer for Perovskite Solar Cells with Enhanced Thermal Stability,” *ACS Appl. Mater. Interfaces*, vol. 10, no. 6, pp. 6006–6013, Feb. 2018.

[112] L. Hoffmann *et al.*, “Gas Diffusion Barriers Prepared by Spatial Atmospheric Pressure Plasma Enhanced ALD,” *ACS Appl. Mater. Interfaces*, vol. 9, no. 4, pp. 4171–4176, Feb. 2017.

[113] D. Muñoz-Rojas and J. MacManus-Driscoll, “Spatial atmospheric atomic layer deposition: a new laboratory and industrial tool for low-cost photovoltaics,” *Mater. Horiz.*, vol. 1, no. 3, pp. 314–320, Apr. 2014.

[114] K. Musselman *et al.*, “Rapid open-air deposition of uniform, nanoscale, functional coatings on nanorod arrays,” *Nanoscale Horiz*, vol. 2, Feb. 2017.

[115] R. L. Z. Hoye, D. Muñoz-Rojas, K. P. Musselman, Y. Vaynzof, and J. L. MacManus-Driscoll, “Synthesis and Modeling of Uniform Complex Metal Oxides by Close-Proximity Atmospheric Pressure Chemical Vapor Deposition,” *ACS Appl. Mater. Interfaces*, p. 150515102727002, 2015.

[116] V. H. Nguyen, “Development of transparent electrodes by vacuum-free and low cost deposition methods for photovoltaic applications,” *PhD Tesis Grenoble INP Oct 2018*, no. https://tel.archives-ouvertes.fr/tel-01992223, Oct. 2018.

[117] J. Tauc, “Optical properties and electronic structure of amorphous Ge and Si,” *Mater. Res. Bull.*, vol. 3, no. 1, pp. 37–46, Jan. 1968.

[118] P. M. Hemenger, “Measurement of High Resistivity Semiconductors Using the van der Pauw Method,” *Rev. Sci. Instrum.*, vol. 44, no. 6, pp. 698–700, Jun. 1973.

[119] C. Masse de la Huerta, V. H. Nguyen, J.-M. Dedulle, D. Bellet, C. Jiménez, and D. Muñoz-Rojas, “Influence of the Geometric Parameters on the Deposition Mode in Spatial Atomic Layer Deposition: A Novel Approach to Area-Selective Deposition,” *Coatings*, vol. 9, no. 1, p. 5, Jan. 2019.

[120] D. Dobkin and M. K. Zuraw, *Principles of Chemical Vapor Deposition*. Springer Netherlands, 2003.

[121] R. L. Z. Hoye *et al.*, “Research Update: Atmospheric pressure spatial atomic layer deposition of ZnO thin films: Reactors, doping, and devices,” *APL Mater.*, vol. 3, no. 4, p. 040701, 2015.

[122] J. van Deelen, A. Illiberi, B. Kniknie, H. Steijvers, A. Lankhorst, and P. Simons, “APCVD of ZnO:Al, insight and control by modeling,” *Surf. Coat. Technol.*, vol. 230, pp. 239–244, Sep. 2013.

[123] D. Pan, T.-C. Jen, and C. Yuan, "Effects of gap size, temperature and pumping pressure on the fluid dynamics and chemical kinetics of in-line spatial atomic layer deposition of Al2O3," *Int. J. Heat Mass Transf.*, vol. 96, pp. 189–198, May 2016.

[124] M. Fulem *et al.*, "Vapor pressure of metal organic precursors," *J. Cryst. Growth*, vol. 248, pp. 99–107, Feb. 2003.

[125] J. Lim and C. Lee, "Effects of substrate temperature on the microstructure and photoluminescence properties of ZnO thin films prepared by atomic layer deposition," *Thin Solid Films*, vol. 515, no. 7, pp. 3335–3338, 2007.

[126] D. Pal, A. Mathur, A. Singh, J. Singhal, and S. Chattopadhyay, "Photoluminescence of Atomic Layer Deposition Grown ZnO Nanostructures," *Mater. Today Proc.*, vol. 5, no. 3, Part 3, pp. 9965–9971, 2018.

[127] E. Rauwel *et al.*, "Oxide Coating of Alumina Nanoporous Structure Using ALD to Produce Highly Porous Spinel," *Chem. Vap. Depos.*, vol. 18, no. 10-12, pp. 315–325, 2012.

[128] D. H. Levy, D. Freeman, S. F. Nelson, P. J. Cowdery-Corvan, and L. M. Irving, "Stable ZnO thin film transistors by fast open air atomic layer deposition," *Appl. Phys. Lett.*, vol. 92, no. 19, p. 192101, May 2008.

[129] W. E. Frazier, "Metal Additive Manufacturing: A Review," *J. Mater. Eng. Perform.*, vol. 23, no. 6, pp. 1917–1928, Jun. 2014.

[130] J. Wilkes, Y.-C. Hagedorn, W. Meiners, and K. Wissenbach, "Additive manufacturing of ZrO2-Al2O3 ceramic components by selective laser melting," *Rapid Prototyp. J.*, Jan. 2013.

[131] A. A. Zadpoor and J. Malda, "Additive Manufacturing of Biomaterials, Tissues, and Organs," *Ann. Biomed. Eng.*, vol. 45, no. 1, pp. 1–11, Jan. 2017.

[132] R. Amin *et al.*, "3D-printed microfluidic devices," *Biofabrication*, vol. 8, no. 2, p. 022001, Jun. 2016.

[133] N. P. Macdonald, J. M. Cabot, P. Smejkal, R. M. Guijt, B. Paull, and M. C. Breadmore, "Comparing Microfluidic Performance of Three-Dimensional (3D) Printing Platforms," *Anal. Chem.*, vol. 89, no. 7, pp. 3858–3866, Apr. 2017.

[134] A. Ambrosi and M. Pumera, "3D-printing technologies for electrochemical applications," *Chem. Soc. Rev.*, vol. 45, no. 10, pp. 2740–2755, May 2016.

[135] M. P. Chae, W. M. Rozen, P. G. McMenamin, M. W. Findlay, R. T. Spychal, and D. J. Hunter-Smith, "Emerging Applications of Bedside 3D Printing in Plastic Surgery," *Front. Surg.*, vol. 2, 2015.

[136] J.-Y. Lee, J. An, and C. K. Chua, "Fundamentals and applications of 3D printing for novel materials," *Appl. Mater. Today*, vol. 7, pp. 120–133, Jun. 2017.

[137] A. J. M. Mackus, M. J. M. Merkx, and W. M. M. Kessels, "From the Bottom-Up: Toward Area-Selective Atomic Layer Deposition with High Selectivity," *Chem. Mater.*, vol. 31, no. 1, pp. 2–12, Jan. 2019.

[138] F. Zoubian *et al.*, "Development and characterization of an atmospheric pressure plasma reactor compatible with spatial ALD," *J. Phys. Conf. Ser.*, vol. 1243, p. 012002, May 2019.

[139] C. Cavallotti, V. Gupta, C. Sieber, and K. F. Jensen, "Dissociation reactions of CuI(hfac)L compounds relevant to the chemical vapor deposition of copper," *Phys. Chem. Chem. Phys.*, vol. 5, no. 13, pp. 2818–2827, Jun. 2003.

[140] "Dissociation reactions of Cu I (hfac)L compounds relevant to the chemical vapor deposition of copper - Physical Chemistry Chemical Physics (RSC Publishing)

DOI:10.1039/B300895A.” [Online]. Available: https://pubs.rsc.org/en/content/articlehtml/2003/cp/b300895a. [Accessed: 18-Jul-2019].

[141] M. J. Hampden-Smith and T. T. Kodas, “Chemical vapour deposition of copper from (hfac)CuL compounds,” *Polyhedron*, vol. 14, no. 6, pp. 699–732, Mar. 1995.

[142] T. Fujii, S. Arulmozhiraja, M. Nakamura, and Y. Shiokawa, “Chemistry of Cu deposition by Cu(hfac)(tmvs) monitored by Li+ ion attachment mass spectrometry,” *J. Appl. Phys.*, vol. 100, no. 8, p. 084912, Oct. 2006.

[143] J. a. T. Norman, B. A. Muratore, P. N. Dyer, D. A. Roberts, and A. K. Hochberg, “NEW OMCVD PRECURSORS FOR SELECTIVE COPPER METALLIZATION,” *J. Phys. IV*, vol. 02, no. C2, pp. C2-271-C2-278, Sep. 1991.

[144] D. Yang, J. Hong, D. F. Richards, and T. S. Cale, “Nucleation and film growth during copper chemical vapor deposition using the precursor Cu(TMVS)(hfac),” *J. Vac. Sci. Technol. B Microelectron. Nanometer Struct. Process. Meas. Phenom.*, vol. 20, no. 2, pp. 495–506, Mar. 2002.

[145] S. K. Kwak, K. S. Chung, I. Park, and H. Lim, “Substrate and pretreatment dependence of Cu nucleation by metal–organic chemical vapor deposition,” *Curr. Appl. Phys.*, vol. 2, no. 3, pp. 205–211, Jun. 2002.

[146] T. T. Kodas, H.-K. Shin, K.-M. Chi, M. J. Hampden-Smith, J. D. Farr, and M. Paffett, “Selective low-temperature chemical vapor deposition of copper from (hexafluoroacetylacetonato)copper(I)trimethylphosphine, (hfa)CuP(Me)3,” *Adv. Mater.*, vol. 3, no. 5, pp. 246–248, 1991.

[147] S. L. Cohen, M. Liehr, and S. Kasi, “Selectivity in copper chemical vapor deposition,” *Appl. Phys. Lett.*, vol. 60, no. 13, pp. 1585–1587, Mar. 1992.

[148] “Physicochemical properties of dimethylzinc, dimethylcadmium and diethylzinc - Kuniya - 1991 - Applied Organometallic Chemistry - Wiley Online Library.” [Online]. Available: https://onlinelibrary.wiley.com/doi/abs/10.1002/aoc.590050419. [Accessed: 18-Jul-2019].

[149] P. Garrou, C. Bower, and P. Ramm, *Handbook of 3D Integration, Volume 1: Technology and Applications of 3D Integrated Circuits*. John Wiley & Sons, 2011.

[150] T. M. Besmann, *Proceedings of the Thirteenth International Conference on Chemical Vapor Deposition*. The Electrochemical Society, 1996.

[151] K. M. Chi, H.-K. Shin, M. J. Hampden-Smith, E. N. Duesler, and T. T. Kodas, “The chemistry of β-diketonate copper(I) compounds—III. The synthesis of (β-diketonate) Cu(1,5-COD) compounds, the solid state structure and disproportionation of hexafluoroacetylacetonato (1,5-cyclooctadiene)copper(I), (hfac)Cu(1,5-COD),” *Polyhedron*, vol. 10, no. 19, pp. 2293–2299, Jan. 1991.

[152] PubChem, “Diethylzinc.” [Online]. Available: https://pubchem.ncbi.nlm.nih.gov/compound/11185. [Accessed: 02-Oct-2019].

[153] C. de Melo *et al.*, “Semi-Transparent p-Cu2O/n-ZnO Nanoscale-Film Heterojunctions for Photodetection and Photovoltaic Applications,” *ACS Appl. Nano Mater.*, Jun. 2019.

[154] D. Dhakal *et al.*, “Atomic layer deposition of ultrathin Cu2O and subsequent reduction to Cu studied by in situ x-ray photoelectron spectroscopy,” *J. Vac. Sci. Technol. A*, vol. 34, no. 1, p. 01A111, Oct. 2015.

[155] K. Reimann and K. Syassen, “Raman scattering and photoluminescence in Cu2O under hydrostatic pressure,” *Phys. Rev. B*, vol. 39, no. 15, pp. 11113–11119, May 1989.

[156] A. Compaan, “Surface damage effects on allowed and forbidden phonon raman scattering in cuprous oxide,” *Solid State Commun.*, vol. 16, no. 3, pp. 293–296, Feb. 1975.

[157] W. Wei, B. Xu, and Q. Huang, “Controllable Synthesis and Catalytic Property of Novel Copper Oxides (CuO and Cu2O) Nanostructures,” *Int. J. Mater. Sci. Appl.*, vol. 5, no. 1, p. 18, Jan. 2016.

[158] R. Kumar, P. Rai, and A. Sharma, “Facile synthesis of Cu2O microstructures and their morphology dependent electrochemical supercapacitor properties,” *RSC Adv.*, vol. 6, no. 5, pp. 3815–3822, Jan. 2016.

[159] M.-C. Huang *et al.*, “Temperature dependence on p-Cu2O thin film electrochemically deposited onto copper substrate,” *Appl. Surf. Sci.*, vol. 301, pp. 369–377, May 2014.

[160] A. Sahai, N. Goswami, S. D. Kaushik, and S. Tripathi, “Cu/Cu2O/CuO nanoparticles: Novel synthesis by exploding wire technique and extensive characterization,” *Appl. Surf. Sci.*, vol. 390, pp. 974–983, Dec. 2016.

[161] H. Solache-Carranco, G. Juárez-Díaz, J. Martínez-Juárez, and R. Peña-Sierra, “Estudio de la cristalización de Cu2O y su caracterización por difracción de rayos X, espectroscópica Raman y fotoluminiscencia,” *Rev. Mex. Física*, vol. 55, no. 5, pp. 393–398, Oct. 2009.

[162] Q. Zhang *et al.*, “CuO nanostructures: Synthesis, characterization, growth mechanisms, fundamental properties, and applications,” *Prog. Mater. Sci.*, vol. 60, pp. 208–337, Mar. 2014.

[163] L. Y. Isseroff and E. A. Carter, “Electronic Structure of Pure and Doped Cuprous Oxide with Copper Vacancies: Suppression of Trap States,” *Chem. Mater.*, vol. 25, no. 3, pp. 253–265, Feb. 2013.

[164] F. Werner, “Hall measurements on low-mobility thin films,” *J. Appl. Phys.*, vol. 122, no. 13, p. 135306, Oct. 2017.

[165] T. Iivonen *et al.*, “Atomic Layer Deposition of Photoconductive Cu2O Thin Films,” *ACS Omega*, vol. 4, no. 6, pp. 11205–11214, Jun. 2019.

[166] M. Zhang, A. Kobayashi, T. Koide, A. Sekiguchi, O. Okada, and N. Hosokawa, “Optimization of copper CVD film properties using the precursor of Cu(hfac)(tmvs) with variations of additive content,” in *Proceedings of the IEEE 1999 International Interconnect Technology Conference (Cat. No.99EX247)*, 1999, pp. 170–172.

[167] M. Zhang, A. Sekiguchi, O. Okada, A. Itsuki, and K. Ogi, “Chemical Vapor Deposition of Copper Thin Film Using a Novel Precursor of Allyloxytrimethylsilyl Hexafluoroacetylacetonate Copper(I),” *Jpn. J. Appl. Phys.*, vol. 40, no. 8R, p. 4825, Aug. 2001.

[168] J.-P. Wang and W. D. Cho, “Oxidation Behavior of Pure Copper in Oxygen and/or Water Vapor at Intermediate Temperature,” *ISIJ Int.*, vol. 49, no. 12, pp. 1926–1931, 2009.